UNIVERSITÉ DU LUXEMBOURG

DISSERTATION

Defence held on 25/05/2023 in Esch-sur-Alzette

to obtain the degree of

DOCTEUR DE L'UNIVERSITÉ DU LUXEMBOURG

EN BIOLOGIE

by

Pauline Mencke

Born on 23rd of November 1993 in Stuttgart-Bad Cannstatt (Germany)

EXAMINATION OF ROLE AND FUNCTION OF DJ-1 IN PARKINSON'S DISEASE AND GLIOBLASTOMA

Dissertation defence committee

Prof. Dr. Rejko Krüger, dissertation supervisor
Professor, University Luxembourg

Prof. Dr. Michel Mittelbronn, Chair
Professor, University Luxembourg

Assoc. Prof. Dr. Johannes Meiser, internal expert
Assoc. Professor, University Luxembourg

Prof. Dr. Lena Burbulla
Professor, Ludwig-Maximilians-University Munich, Germany

Prof. Dr. Ulrike Naumann
Professor, University Tübingen, Germany

Prof. Dr. Wim Vandenberghe
Professor, UZ Leuven, Belgium

Assistant Prof. Dr. Guido Bommer
Assistant Professor, Catholic University of Louvain, Belgium

Dissertation defence committee

Prof. Dr. Rejko Krüger, dissertation supervisor

Professor, University Luxembourg

Prof. Dr. Michel Mittelbronn, Chair

Professor, University Luxembourg

Assoc. Prof. Dr. Johannes Meiser, internal expert

Assoc. Professor, University Luxembourg

Prof. Dr. Lena Burbulla

Professor, Ludwig-Maximilians-University Munich, Germany

Prof. Dr. Ulrike Naumann

Professor, University Tübingen, Germany

Prof. Dr. Wim Vandenberghe

Professor, UZ Leuven, Belgium

Assistant Prof. Dr. Guido Bommer

Assistant Professor, Catholic University of Louvain, Belgium

Table of contents

Abbreviations

Abbreviation	Explanation
CRISPR	Clustered Regularly Interspaced Short Palindromic Repeats
GBM	Glioblastoma
GSH	glutathione
GSSG	oxidized glutathione
iPSC	induced pluripotent stem cells
OE	overexpression
OXPHOS	oxidative phosphorylation
PARK7	Parkinson Disease Protein 7
PCR	polymerase chain reaction
PD	Parkinson's disease
mRNA	precursor mRNA
NAC	N-acetylcysteine
qPCR	real-time PCR
ROS	reactive oxygen species
shCtrl	small hairpin RNA control
shRNA	small hairpin RNA
smNPCs	small molecule neural precursor cells
TCA cycle	tricarboxylic acid cycle
WT	wildtype

Summary

In the last years, there is increasing evidence for an inverse association between the risk of developing Parkinson`s disease (PD) and cancer. In fact, it was shown by several epidemiological studies that there is an inverse correlation for gene expression in PD and cancer: genes that are down-regulated in PD can be up-regulated in cancer and vice versa[1,2]. However, there are some exceptions where a direct correlation for gene expression in PD and cancer can be observed as it was shown that the downregulation of the PD-associated Parkin gene promotes cell proliferation in pancreatic cancer[3].

Parkinson´s disease (PD) is a neurodegenerative disease that is characterized in the first place by three cardinal symptoms: tremor, rigidity and bradykinesia resulting from loss of dopaminergic neurons in the substantia nigra pars compacta[4]. Currently, there is no cure for PD and no treatment that will stop the progress of the disease. Nonetheless, symptoms can be treated e.g., with Levodopa. Most primary PD cases are idiopathic and familial PD caused by known mutations in different genes is rather rare[5]. Much research has been done to unveil mechanisms underlying the pathology of PD. Nonetheless, due to the complexity and heterogeneity of PD, the etiology is not yet fully understood. So far, the association of PD and cancer was mainly focusing on the most common cancers like lung, colorectal or prostate cancer. Despite that, PD-associated genes can also be involved in rather rare cancer types like Glioblastoma (GBM). In fact, high expression of PD-associated genes play an important role in tumor proliferation and migration of glioma cells due to their influence on cell cycle and apoptosis[6]. Similar to PD, there is no cure for and a gap in knowledge of GBM, a highly aggressive brain tumor that is associated with high morbidity and mortality. Current treatment for GBM includes surgical resection if feasible prior to radiotherapy and/or chemotherapy[7]. Nevertheless, a deeper understanding of the pathogenesis of GBM and mechanisms of tumor resistance is necessary to manage and treat these tumors more efficiently. The origin of GBM is still unsolved and for many years, astrocytes were claimed to be the cells of origin for GBM. Currently, neural stem cells and oligodendrocyte precursor cells are also considered to be involved in gliomagenesis[8].

It was shown that two identical mutations in one gene can cause either neuronal cell death in PD when present in the germline or increased cell survival in cancer in case it is present in somatic cells[9]. This intriguing relationship between PD and cancer reveals a new perspective to the well-known opposing cell fates of neuronal degeneration and cell death in PD and the uncontrolled proliferation as well as enhanced resistance to death observed in cancer cells[10].

In the scope of the present study, we analyzed the effect of the loss of DJ-1 in PD-patient-derived astrocytes using isogenic cell models and the role of DJ-1 in different GBM cell lines. We further examined inverse modulatory effects of DJ-1 upregulation in PD cells and DJ-1 downregulation in GBM cells and characterized the role of this protein in both diseases. We found that DJ-1 deficient astrocytes show an impairment in metabolism and cell growth, decreased glutathione (GSH), and increased oxidized glutathione (GSSG) levels, and an increase in reactive oxygen species (ROS) and apoptosis. Importantly, DJ-1 deficient astrocytes showed an increased immune response upon stimulation, as seen by increased cytokine expression and release. We assessed the functional relevance of the altered immune response by analyzing the migration behavior of human T-cells towards the astrocytes upon stimulation and found that DJ-1 deficient astrocytes attract more T-cells and that knockdown of DJ-1 in the T-cells is increasing the migration of the T-cells towards the astrocytes even more. All these phenotypes could be rescued by glutamine or N-acetylcysteine (NAC) supplementation, leading to the hypothesis that increased ROS levels in the DJ-1 deficient astrocytes cause a reduction of tricarboxylic acid (TCA) cycle flux and eventually increased cytokine release. Consistently, we observed that DJ-1 overexpression astrocytes have an increased metabolic activity and cell growth. Concordantly with the results in the DJ-1 overexpression astrocytes, we saw that knockdown of DJ-1 in the GBM cells is decreasing the TCA cycle flux and cell growth.

Taken together, our results highlight that DJ-1 levels modulate metabolism, growth and immune response in astrocytes and the growth and metabolic activity of GBM cells. This is the first study analyzing PD-patient-derived DJ-1 deficient isogenic astrocytes and the first study comparing phenotypes of DJ-1 overexpression astrocytes and DJ-1 knockdown GBM cells to investigate common pathways of neurodegeneration and cancer.

Manuscript I

Bidirectional Relation Between Parkinson's Disease and Glioblastoma Multiforme

Mencke et al. 2020

Status:

Published in Frontiers in Neurology 20.08.2020

Preface

I contributed to the following review by drafting all paragraphs except for the paragraph EPIDEMIOLOGY OF PD AND CANCER, which was written by Dr. Sugier and Dr. Elbaz.

The whole manuscript was reviewed by Prof. Dr. Krüger, Dr. Hanss, Dr. Boussaad and by Dr. Sugier and Dr. Elbaz.

Bidirectional Relation Between Parkinson's Disease and Glioblastoma Multiforme

Pauline Mencke[1]*, Zoé Hanss[1], Ibrahim Boussaad[1], Pierre-Emmanuel Sugier[2], Alexis Elbaz[2] and Rejko Krüger[1,3,4]*

[1] Translational Neuroscience, Luxembourg Centre for Systems Biomedicine, University of Luxembourg, Luxembourg, Luxembourg, [2] Institut de Statistique de l'Université de Paris, Paris, France, [3] Parkinson Research Clinic, Centre Hospitalier de Luxembourg (CHL), Luxembourg, Luxembourg, [4] Transversal Translational Medicine, Luxembourg Institute of Health (LIH), Luxembourg, Luxembourg

Cancer and Parkinson's disease (PD) define two disease entities that include opposite concepts. Indeed, the involved mechanisms are at different ends of a spectrum related to cell survival - one due to enhanced cellular proliferation and the other due to premature cell death. There is increasing evidence indicating that patients with neurodegenerative diseases like PD have a reduced incidence for most cancers. In support, epidemiological studies demonstrate an inverse association between PD and cancer. Both conditions apparently can involve the same set of genes, however, in affected tissues the expression was inversely regulated: genes that are down-regulated in PD were found to be up-regulated in cancer and vice versa, for example p53 or *PARK7*. When comparing glioblastoma multiforme (GBM), a malignant brain tumor with poor overall survival, with PD, astrocytes are dysregulated in both diseases in opposite ways. In addition, common genes, that are involved in both diseases and share common key pathways of cell proliferation and metabolism, were shown to be oppositely deregulated in PD and GBM. Here, we provide an overview of the involvement of PD- and GBM-associated genes in common pathways that are dysregulated in both conditions. Moreover, we illustrate why the simultaneous study of PD and GBM regarding the role of common pathways may lead to a deeper understanding of these still incurable conditions. Eventually, considering the inverse regulation of certain genes in PD and GBM will help to understand their mechanistic basis, and thus to define novel target-based strategies for causative treatments.

Keywords: Parkinson's disease, glioblastoma multiforme, pleiotropy, cancer, neurodegeneration

CANCER AND NEURODEGENERATION

The Inverse Association of Parkinson's Disease and Cancer

There is now accumulating evidence for an inverse association between Parkinson's Disease (PD) and cancer (1–3). Studies suggest that people affected by a neurodegenerative disorder have a reduced incidence for most cancers (4, 5). Molecular studies showed that there is an inverse correlation of the expression of shared genes in PD and cancer: genes down-regulated in PD can be up-regulated in cancer and vice versa (6, 7). These inversely correlated gene expression may affect the same pathways in opposite ways, either involving genetic or environmental factors

(5, 8, 9). Shared genetic pathways deregulated in opposite ways are a major focus, particularly those favoring apoptosis and cell proliferation, influencing cell cycle control, DNA repair, and kinase signaling (4). Common mechanisms such as chronic inflammation (10) and immunosenescence, and common risk factors like diabetes and obesity, have been implicated in both conditions (11, 12).

Parkinson's Disease

PD is a neurodegenerative disease characterized by three cardinal motor symptoms: tremor, rigidity and bradykinesia resulting from loss of dopaminergic neurons in the *substantia nigra pars compacta* (13). PD affects 1–2% of the population over 60 years (14). Age of onset before the age of 40 is seen in <5% of the cases in population-based cohorts, which is typical of familial cases of PD with underlying genetic cause like mutations in *SNCA, Parkin, PINK1, DJ-1, LRRK2, ATP13A* (**Table 1**). Monogenic forms of PD are rare. In general, genetic factors are claimed to be involved in 5–10% of the cases (14). Histopathological hallmarks of PD are proteolytic inclusions called Lewy bodies (LB) and Lewy neurites containing α-synuclein (47). Cellular hallmarks of PD are an impairment of proper functioning of molecular and organelle degradation pathways like the ubiquitin–proteasome system and autophagy (48). In particular, the process of removing defective mitochondria from the cells is known to be impaired in PD (49). This process is a special form of autophagy, called mitophagy (50), and is regulated by the PD-linked proteins PINK1 and Parkin (51). The impairment of autophagy, lysosomal and mitochondrial function in PD can lead to the accumulation of α-synuclein and defective mitochondria (52) and, ultimately, to neurodegeneration. The diagnostic of PD is mostly a clinical diagnosis as it is based on neurological tests when the PD patients already show motor symptoms. Due to the complexity and heterogeneity of PD, the etiology is not yet fully understood. Therefore, there is no cure for PD and no treatment that will stop the progress of the disease and treatment is only symptomatic, e.g., levodopa therapy. This is why it is important to investigate underlying mechanisms of PD to stratify causative treatments.

Glioblastoma Multiforme

Glioblastoma multiforme (GBM) is the most malignant tumor of the central nervous system. GBM tumors are most likely developing from astrocytes (53). Based on their histological and clinical features, astrocytomas are classified into four different subtypes according to the WHO classification: Pilocytic astrocytoma, diffuse astrocytoma, anaplastic astrocytoma, and GBM. Pilocytic and diffuse astrocytoma are characterized by a rather low growth rate, while anaplastic astrocytoma and GBM show common uncontrolled proliferation and diffuse tissue penetration (54). GBM is characterized by poor prognosis, low survival rates, and extremely limited opportunities for therapy. Symptoms of GBM are rather unspecific like increased intracranial pressure, including headache and focal or progressive neurologic deficits. Seizures are the presenting symptom in 25% of patients and can occur at a later stage of the disease in 50% of patients (55). Malignant gliomas are the third leading cause of cancer death for people aged between 15 and 34, accounting for 2.5% of the global cancer death toll. GBM has a maximum incidence in patients aged more than 65 years, and is mainly affecting the cerebral hemispheres (54). A cellular hallmark of GBM and all cancers is the so-called Warburg effect which describes the phenomenon that cancer cells use aerobic glycolysis to produce ATP (56). GBM cells are characterized by increased glucose uptake and lactate production (57). GBM cells also use oxidative phosphorylation (OXPHOS) (57). The hypoxic GBM tumor environment allows the constant expression of hypoxia inducible factors 1 alpha and 2 alpha (HIF-1α, HIF-2α). Hypoxia and hypoxia-stabilized HIFs regulate GBM metabolism by stabilizing genes involved in metabolism like the glucose transporters GLUT1 and GLUT3, thereby sustaining an increased glucose uptake of the GBM cells (57). Also, the enzyme catalyzing the first step in glycolysis, hexokinase, is hypoxia/HIF regulated (57). As for PD, the diagnosis of GBM is typically made when first symptoms occur and rely on clinical examination and neuroimaging methods. However, mostly both diseases are diagnosed at an advanced stage of tumor growth or neurodegeneration, respectively. Treatment strategies of GBM are based on a multidisciplinary approach. Current standard therapy is a combination of maximal safe surgical resection of the tumor and subsequent radiation and chemotherapy with temozolomide (Temodar®), an oral alkylating agent. However, even with advances in surgical resection, the prognosis for GBM patients remains poor, with a median survival of 15 months (55).

COMMON GENES IN PD AND GBM

A common set of genes like the tumor suppressor p53, epidermal growth factor and its receptor EGF(R), the glyoxalase and deglycase DJ-1 and biological processes are deregulated in opposite directions in PD and GBM (6). Particularly, there is evidence that PD-associated genes are involved in GBM pathogenesis (**Table 1**). A summary of publications examining and exhibiting the involvement of PD-associated genes in GBM is shown in **Table 1**. Consistent with PD-associated genes being involved in GBM, it is important to note that mutations in the same gene can behave differently if they are germline or somatic mutations. For example, mutations in *PARK2* affecting the Parkin protein can cause neuronal cell death in PD if they are present in the germline, or increased cell survival in GBM if they are present in somatic cells like astrocytes (**Figure 1**). (25). Pathways that are affected in PD and GBM are overlapping but are regulated inversely by alternatively regulated genes. These pathways are regulating cell proliferation and cell metabolism as well as mitochondrial clearance (1). In the following, examples for inversely regulated pathways in PD and GBM are illustrated and the role of commonly involved genes in both diseases in the regulation of these pathways will be outlined.
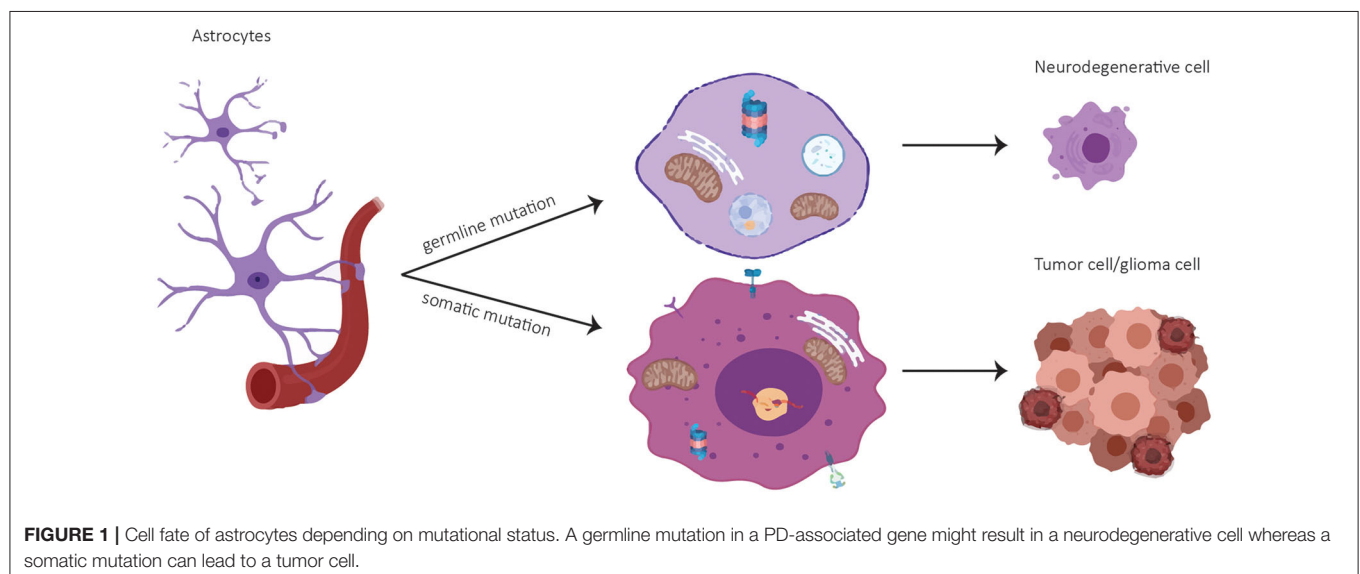
Pro-Survival Signaling

Pro-survival signaling is one of the most important pathways regulating and sustaining cell proliferation. Once dysregulated, uncontrolled cell proliferation can lead to tumorigenesis. This is why cell proliferation and apoptosis need to be in a tight equilibrium, which is well controlled by many mediators.

TABLE 1 | Overview PD-genes in GBM.

PD-associated gene	GBM	Function	Involvement in disease
PARK1 (SNCA)	(15–23)	Important role in maintaining an adequate supply of synaptic vesicles in presynaptic terminals	Meningioma: (24) PARK1 was shown to contribute to malignant progression of tumors
PARK2 (Parkin)	(25–33)	Regulation of autophagy, important for mitochondrial maintenance	Autophagy pathway
PARK5 (UCHL1)	(21, 34)	Hydrolase activity, removes and recycles ubiquitin molecules from degraded proteins Ligase activity, links together ubiquitin molecules for use in tagging proteins for disposal	Degrades not needed proteins UCHL1 acts as a colorectal cancer oncogene via activation of the β-catenin/TCF pathway through its deubiquitinating activity (35)
PARK6 (PINK1)	(23, 36, 37)	Regulation of autophagy, important for mitochondrial maintenance	PINK1 is a Negative Regulator of Growth and the Warburg Effect in Glioblastoma
PARK7 (DJ-1)	(38–41)	ROS scavenger, antioxidative role, cyto-protective	Pro-tumor survival, mitochondrial dysfunction
PARK8 (LRRK2)	Somatic mutations [The Cancer Genome Atlas (TCGA)] (42)	GTPase and kinase function LRRK2 has been associated with a diverse set of cellular functions and signaling pathways including mitochondrial function, vesicle trafficking together with endocytosis, retromer complex modulation and autophagy	LRRK2 mutation carriers have a pos. correlation with cancer incidence (43)
PARK9 (ATP13A2)	Somatic mutations [The Cancer Genome Atlas (TCGA)]	P5 subfamily of ATPases which transports inorganic cations as well as other substrates	ATPase that plays a role in intracellular cation homeostasis and the maintenance of neuronal integrity
PARK15 (FBXO7)	(44)	F-box protein Phosphorylation-dependent ubiquitination	Oncogenic properties of FBXL10, but also tumor suppression by FBXL10 has been reported (45, 46)

FIGURE 1 | Cell fate of astrocytes depending on mutational status. A germline mutation in a PD-associated gene might result in a neurodegenerative cell whereas a somatic mutation can lead to a tumor cell.

P53—The Master Controller of Cell Proliferation and Its Regulation in PD and GBM

One key player in the regulation of cell proliferation is the tumor suppressor p53. p53 is upregulated in PD, but downregulated in GBM (**Figure 2A**) (58–60).

p53 inhibits cell proliferation by both blocking cell cycle progression and promoting apoptotic cell death (**Figure 2A**). This way, p53 provides a clear prevention from stem cell tumor growth and thereby GBM development. p53 itself is also regulated via several stress signals occurring during malignant progression like genotoxic damage, oncogene activation, loss of normal cell contacts, and hypoxia (**Figure 2A**). This leads to a model where growth inhibitory functions of p53 are normally held dormant, to be unleashed only in nascent cancer cells (61). In PD, the level of p53 and its activity in neurons can increase not only as a result of oxidative stress and DNA damage, but
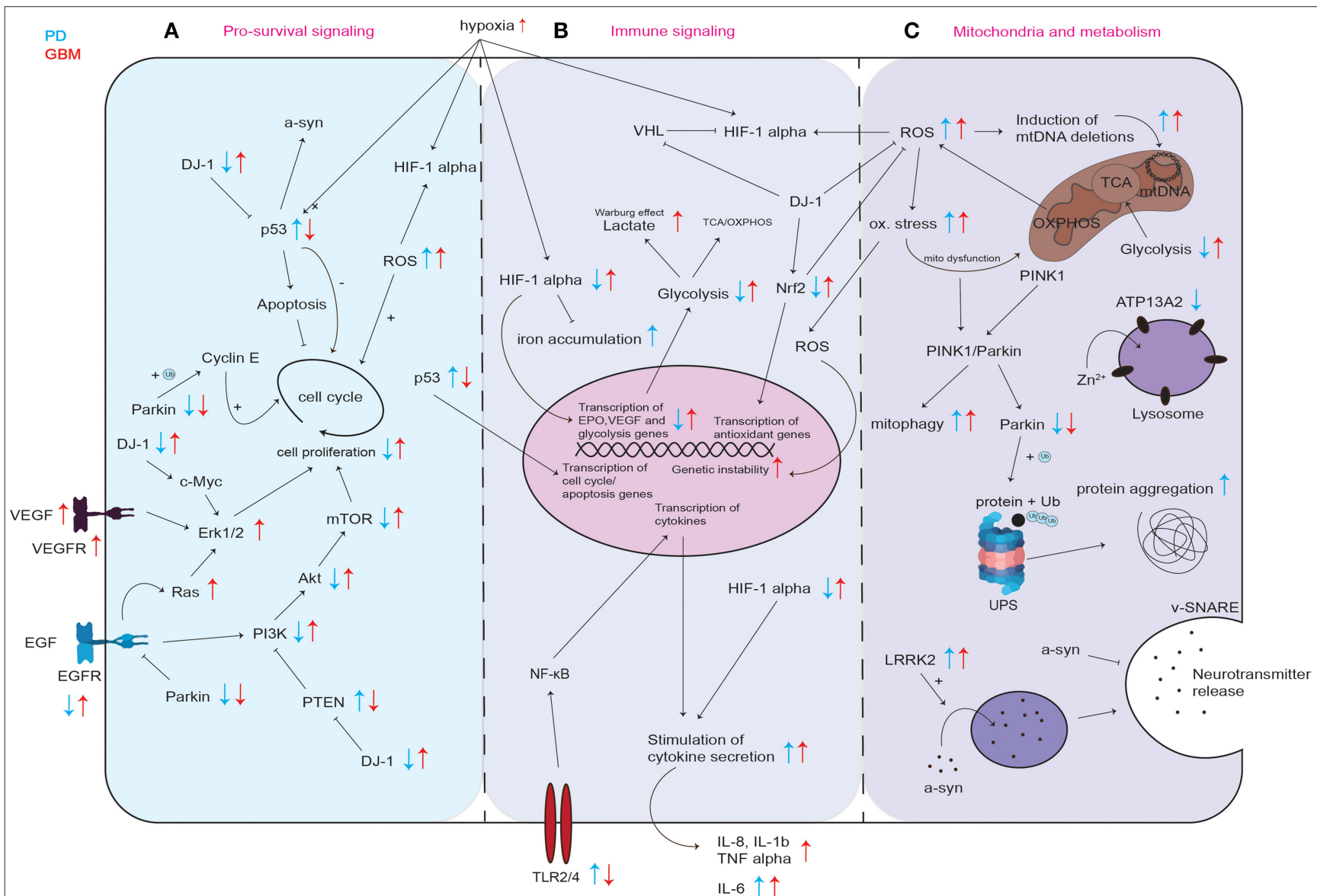
FIGURE 2 | Graphical representation of common cellular pathways described in literature to be dysregulated in PD and GBM. Dysregulation (up- or downregulation) of mediators and proteins of commonly involved mediators and proteins in PD and GBM is illustrated with blue and red arrows, while blue arrows correspond to the situation in PD, red arrows indicate the regulation in GBM. Differential regulation of discussed mediators regarding pro-survival signaling **(A)** immune signaling **(B)** and their involvement in mitochondria and metabolism **(C)**. UPS, ubiquitin proteasome system; ox. stress, oxidative stress; mito dysfunction, mitochondrial dysfunction.

also due to aberrant regulation of its expression for example by mutated or incorrectly cleaved proteins involved in the process of neurodegeneration (58). An increase in p53 expression and its activation results in enhanced expression of genes that are responsible for apoptosis and/or cell cycle arrest and may trigger neuronal cell death (58). In line, Mogi et al. found increased levels of p53 protein in the nigrostriatal dopaminergic region in PD patients compared to controls (62). It was shown that p53 regulates α-synuclein expression since the α-synuclein promoter harbors a p53 responsive element (63). Therefore, an increase in p53 in PD could not only lead to increased apoptosis induction but also to an increase in expression of potentially dysfunctional α-synuclein and to its subsequent aggregation (63). Kato et al. found that DJ-1 inhibits the transcriptional activity of p53 (**Figure 2A**) (64). Loss of DJ-1 protein in PD could thereby lead to increased expression of p53 target genes leading to cell death. In GBM, p53 is frequently downregulated or inactivated by mutations leading to a reduction in apoptosis induction (**Figure 2A**) (65) and p53 inactivation positively correlates with GBM tumor invasiveness (66). Zheng et al. showed that central nervous system (CNS)-specific deletion of p53 and Phosphatase And Tensin Homolog (PTEN) in the CNS of mice leads to a high-grade malignant glioma phenotype resembling human GBM (67). These results are in line with the data found at The Cancer Genome Atlas in the exploration mode when looking at the TCGA-GBM data set, which reports PTEN, p53 and EGFR as the most frequently mutated tumor suppressor genes in GBM (https://portal.gdc.cancer.gov).

EGFR Signaling in PD and GBM

EGFR is downregulated in PD and upregulated in GBM (**Figure 2A**). EGFR activates the phosphoinositide 3-kinase (PI3K)-Akt pathway (**Figure 2A**). The PI3K/Akt signaling pathway is known as one of the most important kinase cascades that mediates crucial cellular functions such as survival, proliferation, migration, and differentiation (68). Activated receptor tyrosine kinases (RTKs) like EGFR activate PI3K through direct binding or through tyrosine phosphorylation of scaffolding adaptors, which can then bind and thereby activate PI3K (**Figure 2A**). PI3K phosphorylates phosphatidylinositol-4,5-bisphosphate (PIP2) to generate phosphatidylinositol-3,4,5-trisphosphate (PIP3), in a reaction that can be reversed by the PIP3 phosphatase PTEN. AKT can then activate its downstream targets like mTOR, eventually leading to cell proliferation (**Figure 2A**). It was shown that EGFR endocytosis and degradation are accelerated in Parkin-knockout cells from mouse brain, and EGFR signaling via the PI3K/Akt pathway is reduced (69). Fallon et al. propose that Parkin delays EGFR internalization and degradation, thereby promoting PI3K/Akt signaling (69). Therefore, by decreasing the efficiency of EGFR-mediated Akt signaling in neurons, the loss of Parkin leads to neuronal degeneration (69). In post-mortem brains of idiopathic PD patients, protein levels of EGF and EGFR were shown to be decreased in the prefrontal cortex and the striatum (70). Mutations in *EGFR* are commonly occurring in GBM (71). These mutations result in EGFR gene amplification and

intrinsic alterations of the EGFR structure (71). Brennan et al. showed that gene amplification and mutation of EGFR results in enhanced EGFR activation and is found in about 60% of GBM (72). The most common EGFR mutation in GBM is EGFRvIII, which is caused by the deletion of exon 2–7 leading to constitutively activated EGFR (71, 73, 74). It was shown that EGFR is overexpressed in most of primary GBM and some of the secondary GBM and that EGFR overexpression is associated with more aggressive GBM (75).

PTEN/PI3K/Akt Signaling in PD and GBM

In PD, PTEN/PI3K/Akt signaling is down-regulated and therefore causes decreased pro-survival signaling (76). In GBM, PTEN/PI3K/Akt signaling is upregulated (77–79). PTEN negatively regulates PI3K (**Figure 2A**), thereby inhibiting PI3K/Akt mediated proliferation and cell survival. In PD patient-derived post mortem brains, Sekar et al. found an increase in PTEN levels (80). Absence of PTEN protected dopaminergic neurons in PTEN knockout mice from neuronal death after neurotoxin treatment (81). In another mouse model, depletion of PTEN attenuated the loss of tyrosine hydroxylase-positive (dopaminergic) cells after neurotoxin treatment (82). An increase in PTEN in PD results in decreased pro-survival signaling leading to increased neuronal cell death. In line, it was shown that the ratio of phospho-Akt/total-Akt decreases in dopaminergic neurons indicating a decrease in activation of the pro-survival signaling mediated by Akt upon phosphorylation (83). Overall, an impaired PTEN/PI3K/Akt signaling in PD leading to neuronal cell death can be due to mutations in PD-associated genes regulating Akt signaling [e.g., DJ-1 (84), (**Figure 2A**)], excessive Akt dephosphorylation, inhibition of Akt activation or oxidative stress (85). In GBM, PTEN/PI3K/Akt signaling is upregulated due to EGFR overexpression or loss of PTEN (78). Mutations or homozygous deletions of PTEN were shown in 36% of the GBM cases that were studied by McLendon et al. and 86% of the GBM harbored at least one genetic event in the receptor tyrosine kinase PI3K pathway (86). High level of phosphorylated Akt was shown to correlate with a poor prognosis for patients with GBM (87). Mutations in the phosphatidylinositol-4,5-bisphosphcxate 3-kinase catalytic subunit alpha (PIK3CA), which is one subunit of PI3K, were shown to induce gliomagenesis (77).

The PD-Associated Oncogene DJ-1 and Regulation of Cell Proliferation in PD and GBM

The protein DJ-1 was shown to be inversely regulated in PD and GBM. (**Figure 2A**). Homozygous mutations in *PARK7* (DJ-1) resulting in loss of protein lead to PD (88). DJ-1 expression was shown to be increased in GBM (38, 89, 90). Wang et al. found that high DJ-1 and high β-catenin expression in GBM were significantly associated with high grade and poor prognosis in glioma patients, suggesting DJ-1 levels in GBM as a strong independent prognostic factor (89). DJ-1 also accelerates transformation of tumor cells by c-Myc activating the Erk pathway (91). Hinkle et al. found that GBM tumor tissue expressed DJ-1 protein at significant levels, and

typically in a cytoplasmic, non-nuclear manner. They found that immunostaining intensity of DJ-1 varied directly with strong nuclear p53 expression and inversely with EGFR amplification (38). In addition to the fact that DJ-1 negatively regulates pro-apoptotic p53 (**Figure 2A**) (92), and EGFR signaling is crucial for gliomagenesis (72), these observations suggest that DJ-1 might be involved in tumorigenesis of GBM (38). Toda et al. found that in a serial transplantation study, DJ-1 knockdown resulted in a prolonged survival of mice in secondary transplantation (39). DJ-1 is known to counteract ROS, among others via Nrf2 stabilization leading to the expression of endogenous antioxidant synthesis and ROS-eliminating enzymes like glutathione (**Figure 2A**) (93, 94). It was shown that a reduction in DJ-1 protein is associated with reduced Nrf2 transcriptional activity and that in PD patients, Nrf2 activation is associated with dysregulated downstream gene expression (93, 95). In contrast, it was found that Nrf2 overexpression accelerates proliferation and oncogenic transformation of glioma cells and that GBM patients have reduced overall survival when Nrf2 levels are upregulated (**Figure 2A**) (96).

Immune-Signaling

The innate immune system obtains various functions in health and disease. It represents the first line of defense against infection and it is involved in many different processes like tissue repair, wound healing and the clearance of apoptotic cells and cellular debris. An excessive or non-resolving activation of the innate immune system can result in systemic or local inflammatory complications and cause or contribute to the development of neurodegeneration and cancer. In the brain, the innate immune cells are represented by microglia, which regulate brain development, brain maturation, and homeostasis. An impairment of functional microglia through abnormal activation or decreased functionality can occur during aging and during neurodegeneration and the resulting inflammation was shown to be involved in neurodegenerative diseases and cancer (97).

Hypoxia and HIF-1α in PD and GBM

It is well known that hypoxia-inducible factor-1α (HIF-1α) plays an important role in gliomagenesis due to its angiogenesis-promoting effects (98). While HIF-1α is upregulated in GBM, it was shown that HIF-1α is impaired in PD (**Figure 2B**) (99, 100).

Treatment with MPTP, a prodrug to the neurotoxin MPP+, which causes Parkinsonism symptoms by destroying the dopaminergic neurons, was shown to inhibit HIF-1α accumulation in mice and in dopaminergic cell lines (99). Moreover, Milosevic et al. found that a conditional knock-down of HIF-1α in mice resulted in a 40% decrease in expression of tyrosine hydroxylase, a known marker for dopaminergic neurons, in the *substantia nigra* of mice (101). In healthy individuals, HIF-1α mediates protection of dopaminergic neurons by regulation of iron homeostasis, improved defense against oxidative stress by upregulation in response to reactive oxygen species (ROS) (**Figure 2B**) and mitochondrial dysfunction (100). PD is characterized by an accumulation of iron in dopaminergic neurons of the *substantia nigra* (102). Free cytosolic iron can lead to

oxidative stress and trigger α-synuclein aggregation (102). HIF-1α influences iron homeostasis by expression of its target genes ferroportin and heme oxygenase in the *substantia nigra* which are known to be involved in the attenuation of iron accumulation (100). This way, HIF-1α can counteract iron accumulation (**Figure 2B**). However, in PD, downregulation of HIF-1α can lead to a dysregulation in iron homeostasis eventually leading to iron accumulation (**Figure 2B**). In turn, iron accumulation decreases HIF-1α activity, because iron is a necessary cofactor for prolyl hydroxylases that inactivate HIF-1α via subsequent ubiquitinylation through von Hippel-Lindau factor (VHL) (**Figure 2B**) (102, 103). HIF-1α target genes Erythropoietin (EPO) and vascular endothelial growth factor (VEGF) (**Figure 2B**) have been shown to contribute to the protection of neurons from PD pathogenesis (100). EPO was shown to be neuroprotective against dopaminergic neurotoxins (104). In rat explants of the ventral mesencephalon, VEGF treatment was shown to be mitogenic for endothelial cells, astrocytes, and could promote growth and survival of neurons and specifically dopaminergic neurons (105). There are accumulating data which suggest that the activation of HIF-1α can exert neuroprotective effects through the induction of intrinsic adaptive mechanisms in neuronal and non-neuronal cells (106). Lee et al. showed that stabilization of HIF-1α leads to the upregulation of several proteins involved in iron efflux and mitochondrial integrity and bioenergetics, cell components that are compromised in PD. This is why Lee's data emphasize the concept that the pharmacological induction of HIF-1α could have neuroprotective effects in PD cells and mice models, with a beneficial impact on dopamine synthesis, iron homeostasis, antioxidant defenses and mitochondrial dysfunction (107).

In contrast to these observations in PD, in GBM, HIF-1α levels are increased (**Figure 2B**) (108). Liu et al. found that HIF-1α expression was associated with high grade glioma and the overall survival of glioma patients, which indicates that HIF-1α could predict prognosis and provide clinical insights into the therapeutic strategy for GBM patients (109). The lack of oxygen in the GBM microenvironment results from inappropriate neovascularization, irregular blood flow, and excessive consumption of oxygen from the uncontrolled proliferating GBM cells (110). The hypoxia in the GBM tumor induces the expression of genes involved in tumor cell growth and angiogenesis like the signal transducer and activator of transcription 3 (STAT3), which triggers the synthesis of HIF-1α that subsequently induces activation of T-regulatory cells (Tregs) and the production of VEGF (111). Tregs are important modulators of the immune response, and VEGF has known immunosuppressive effects. Moreover, the hypoxic microenvironment causes the transformation of CNS macrophages into tumor-associated macrophages (TAMs), which are capable of adopting immunosuppressive and tumor-supportive phenotypes. Via the STAT3 pathway, this transformation triggers TAMs to enhance angiogenesis and tumor cell invasion (26, 112). Furthermore, HIFs are critical for the upregulation of glycolysis (**Figure 2B**) (113). Hypoxia is also a known regulator of many other innate immunological functions like cell migration, apoptosis, phagocytosis of pathogens,

antigen presentation and production of cytokines, chemokines, and angiogenic and antimicrobial factors (113). In summary, HIF is an important factor in the regulation of the tumor microenvironment due to its central role in promoting proangiogenic and invasive properties. Since HIF activation results in angiogenesis and the emerging vasculature is often abnormal, this leads to a vicious cycle that causes further hypoxia and HIF upregulation in GBM (98).

Interleukins and Immune Escape

In PD, increased cytokine levels in response to cellular stress can lead to neuronal cell death whereas in GBM, cytokines like interleukins IL-1β, IL-6, and IL-8 released by the tumor cells, inhibit the immune response and allow the tumor cells to escape the eradication by the immune system (**Figure 2B**).

IL-6 was found to be increased in the nigrostriatal region and in the cerebrospinal fluid of patients with PD (114). Further, Hofmann et al. found that patients with more severe PD had higher IL-6 levels compared to patients with a milder phenotype (114). In addition, a study from Chen et al. found that patients with PD had elevated levels of transforming growth factor-beta 1 (TGF-β1), IL-6, and IL-1β in cerebrospinal fluid compared to controls (115). In line, it is described that, in autopsy brains of PD, the number of activated microglia, which were among others TNF- α, and IL-6-positive, increased in the *substantia nigra* and putamen during the progress of PD (116). The activated microglia in PD was observed in various brain regions like the nigro-striatal region, the hippocampus and the cerebral cortex. The levels of IL-6 and TNF- α mRNAs increased in the hippocampus of PD patients (116). It is postulated that cytokines (IL-1β, TNF-α, IL-6) from activated microglia (117) in the *substantia nigra* and putamen may be initially neuroprotective, but may later turn to be neurotoxic during PD pathogenesis (116).

In contrast to PD, in GBM, the cells can profit from the cytoprotective effects of specific cytokines like IL-1β, IL-6, and IL-8 leading to increased robustness regarding cellular stress (118). As already mentioned, GBM arises from glial cells with surrounding brain parenchyma that contains CNS cells like astrocytes, neurons and microglia, as well as a distinctive extracellular matrix composition. GBM induces a tumor microenvironment characterized by immunosuppressive cytokines secreted by tumor cells, microglia and tumor macrophages. IL-6, IL-10, and TGF-β, and prostaglandin-E collectively inhibit both the innate and adaptive immune systems leading among others to the suppression of natural killer cell activity, T-cell activation and proliferation and induction of T-cell apoptosis (119). IL-1β is a known master pro-inflammatory cytokine that triggers various malignant processes driving oncogenic events such as proliferation and invasiveness (118, 120). Elevated levels of IL-1β were observed in many different GBM cell lines (121) and in human GBM tumor specimens (122). IL-6 was shown to be overexpressed in GBM clinical samples and cell lines and IL-6 gene expression seems to correlate with the aggressiveness of the tumor (123). It was shown that IL-6 is secreted by GBM cells and sustains the cell proliferation by activation of STAT3 pro-survival pathway (124). IL-6 is produced by GBM cells in response to external stimuli or intrinsic factors, for example oncogenic mutations (118). IL-1β and TNF-α induce stabilization of IL-6 mRNA and increase IL-6 biosynthesis (125). Like IL-6, IL-8 is highly expressed and secreted from GBM cell lines, tumor stem cells and human specimens (118). It was shown that the expression of the constitutively active mutant EGFRvIII is associated with significantly higher expression of IL-8 induced by nuclear factor kappa B (NF-κB) (**Figure 2B**) in human GBM specimens and GBM cell lines (126). In a similar manner as the regulation of IL-6, IL-8 expression can be enhanced by TNF-α, IL-1β or macrophage infiltration (127). Thus, elevated levels of one cytokine like TNF-α for example can lead to an increase in other cytokines. These findings of elevated cytokines and their associated roles in GBM underline the importance of specific cytokines for immune escape mechanisms and tumor proliferation and invasiveness observed in GBM pathogenesis.

Toll-Like Receptors in PD and GBM

Toll-like-receptors (TLRs) are receptors that recognize distinct molecular patterns like lipopolysaccharides, single and double stranded RNAs, hemagglutinin, viral proteins etc. (128), and allow an appropriate immune response to be initiated. The TLR family consists of 10 members (TLR1-10) in humans with different expression profiles and ligands (129). TLR2 is essential for the recognition of peptidoglycans and lipoproteins, whereas TLR4 recognizes bacterial lipopolysaccharide (LPS) (130). TLR2 and TLR4 are both the most important TLRs with regard to innate immune response as they are both implicated in the recognition of endogenous ligands involved in the inflammatory response regardless of the source of infection (131). This is why the implication of TLR2 and TLR4 in PD and GBM will be discussed in the following.

TLR2 and TLR4 are frequently upregulated in PD and downregulated in GBM allowing the tumor cells to escape clearance by the innate immune system. TLR2 and TLR4 were shown to be upregulated in many α-synuclein-overexpressing or toxin-induced animal models (132–135), and accumulating evidence from human studies further implicates these receptors in the pathogenesis of PD (136). Clinical studies revealed that TLR2 expression is increased in PD (137). It was shown that microglial TLR2 is increased in the *substantia nigra* and the hippocampus in the early stages of PD, but not during the late stages (138), while another study found that TLR2 is increased in the striatum of advanced PD patients (135).

In contrast, GBM cancer stem cells downregulate TLR4 to evade immune suppression (139). Alvarado et al. showed that in GBM, cancer stem cells have low TLR4 expression which enables cell survival by avoiding inhibitory innate immune signaling (e.g., clearance by dendritic cells, cytotoxic T cells, and natural killer cells) that aims to suppress self-renewal of the GBM stem cells (140). This is why TLR agonists that trigger antitumoral immune signaling are being discussed as therapy for GBM (141).

Mitochondria and Metabolism

Mitochondria and cellular metabolism are closely linked. Mitochondria host many enzymatic reactions of cellular metabolism like the tricarboxylic acid (TCA) cycle and oxidative

phosphorylation (OXPHOS) which generate ATP from pyruvate in the presence of oxygen (**Figure 2C**). In age-related disease, like PD and GBM, damaged mitochondria lead to impaired cellular metabolism (142).

Cellular Metabolism in PD and GBM

The human brain, even though constituting only 2% of the total body weight, uses ~20% of the body's total oxygen consumption and 60% of our daily glucose intake (143). Furthermore, the brain needs a constant supply of glucose since it lacks fuel stores and cannot store glycogen. This is why cellular changes in glucose metabolism can have high impact on brain cell homeostasis, proliferation and viability.

It was shown that glycolysis and mitochondrial function like respiration are decreased in individuals with PD (**Figure 2C**) (144–146). In GBM, increased glycolytic activity results from certain oncogenic alterations like c-Myc amplification, PTEN deletion or mutations in p53 (**Figure 2C**) (147, 148).

While mitochondrial dysfunction in PD can cause increased generation of ROS and subsequent oxidative damage (**Figure 2C**), it can also result in failing neuronal compensation of their insufficient ATP generation (149). Activation of glycolysis in neurons leads to excessive oxidative stress and apoptosis, suggesting that neurons are predominantly restricted to OXPHOS (150). In line, Hall et al. showed that the majority of ATP used by neurons is produced by OXPHOS (151). Powers et al. found that overexpression of α-synuclein in N27 dopaminergic cells resulted in an impairment in glycolysis, a reduction in glycolytic capacity and mitochondrial respiration (152). This is why an increase in glycolysis as counteract mechanism to neuronal energy failure induced by mitochondrial dysfunction in PD eventually leads to neuronal cell death (153–155). Neurons also metabolize glucose via the pentose phosphate pathway (PPP) to maintain their antioxidant status (156). It was shown that inhibition of the PPP in neuronal cell models causes cell death (157). In rodents, PPP inhibition caused dopaminergic cell death causing motor deficits that resemble Parkinsonism (158). Using postmortem human brain tissue, Dunn et al. characterized glucose metabolism via the PPP in early sporadic PD and controls and observed a down-regulation of PPP enzymes in patients compared to controls (156). This observation suggests that the impairment of the PPP is an early event in sporadic PD (156).

In the absence of oxygen, pyruvate can be metabolized into lactate, a process known as glucose fermentation or anaerobic glycolysis. Rapidly proliferating cells, such as cancer cells, also have the ability to ferment glucose into lactate, even in the presence of abundant oxygen; this process is called aerobic glycolysis. It has been observed already decades ago, that cancer cells, even in aerobic conditions, tend to favor metabolism via glycolysis rather than OXPHOS, which is preferred by most other cells. This phenomenon is called the Warburg effect (56, 159). This is why, in contrast to PD neurons, GBM cells ferment glucose into lactate, even in the presence of abundant oxygen (**Figure 2B**). Even though ATP production is less efficient in aerobic glycolysis when compared to ATP production via complete oxidative metabolism of glucose, it

is being hypothesized that GBM cells use aerobic glycolysis to generate precursors for anabolism to grow and are able to generate enough ATP to sustain their cellular function (160). By modulating glycolysis and altering mitochondrial metabolism, GBM cells generate biomass, namely nucleotides, lipids, proteins, and NADPH by using glycolytic/TCA intermediates (160). Knockdown of glycolytic genes strongly inhibits GBM growth further emphasizing that glycolytic enzymes are essential for GBM growth (148). GBM cells also generate large amounts of lactate for several pro-tumor growth functions (161). Li et al. found that EGFR activation in GBM cells promotes the translocation of phosphoglycerate kinase (PGK1) into mitochondria (162, 163). In the mitochondria, PGK1 phosphorylates and activates pyruvate dehydrogenase kinase that phosphorylates and thereby inhibits pyruvate dehydrogenase and thus mitochondrial pyruvate consumption which eventually leads to enhanced lactate production (162, 163). In addition to the aerobic glycolysis, GBM cells also utilize TCA and OXPHOS (160).

The differential expression of metabolic genes in neurons and astrocytes might explain the differences in glycolysis and OXPHOS rates. For example, neurons lack 6-phosphofructo-2-kinase/fructose-2,6-bisphosphatase-3 (PFKFB3) since it is continuously degraded by the ubiquitin-proteasome pathway. PFKFB3 regulates the biogenesis and degradation of fructose-2,6-bisphosphate, a known glycolytic activator. In contrast, in astrocytes, PFKFB3 is activated by adenosine monophosphate-activated protein kinase (AMPK) and promotes glycolysis (149). In line, it was shown that the expression of PFKFB3 is higher in mouse astrocytes than in murine neurons due to proteasomal degradation in the neurons (164). In neurons, the activation of PFKFB3 results in enhanced glycolysis but eventually leads to cell death since neurons lose their ability to generate glutathione, an essential antioxidant involved in the management of oxidative stress. This means that unlike astrocytes, neurons use glucose to maintain their antioxidant status and not for bioenergetic purposes (164). These findings might help to explain why PD neurons fail to increase their glycolysis rates and why increased glycolysis leads to sustained cell proliferation in astrocyte-originating GBM cells.

EPIDEMIOLOGY OF PD AND CANCER

Epidemiological evidence suggests that patients with PD have a reduced incidence of primary CNS tumors (165, 166). In contrast, there are a few epidemiological studies that show a positive association of PD with benign and malignant brain tumors, but not specifically with GBM (167–169). However, the problem with these studies is that they do not distinguish between the types of brain cancer, e.g., meningioma or astrocytoma. The described increased risk of all types of brain cancers in PD might be caused by diagnostic misclassification and detection bias. Increased incidence of meningioma in PD patients for example might result from the fact that the symptoms can be wrongly diagnosed as a sign of PD, if the intracranial tumor leads for example to a compression of the basal ganglia resulting in PD

Introduction - Manuscript I

Mencke et al.   Bidirectional Relation PD and GBM

symptoms (170–173). Moreover, a positive association of brain tumors and PD can be caused by detection bias as brain tumors can be diagnosed during the clinical work-up for PD (174). Since patients diagnosed with parkinsonism are more likely to have a Magnetic Resonance Imaging at the time of diagnosis, this may explain a higher risk of detecting silent brain tumors (173, 175). The close temporal association between diagnosis of PD and the incidence of brain tumors further leads to the suggestion that brain tumors might be misdiagnosed as PD or *vice versa* (176). Specifically, for GBM, as it is lethal, it is difficult to study PD in individuals who survived GBM. This is why future studies should focus on evaluating the risk of GBM in PD patients.

Interestingly, there is an increased risk of melanoma in PD patients compared to controls (177–179). In 1985, Dr. Rampen reported a 55-year-old male with PD who developed a local recurrence of a primary melanoma and multiple primary melanomas 4 years after primary excision and 4 months after starting levodopa (180). An increased risk of malignant melanoma in PD patients has been confirmed since in many studies (8, 176, 181, 182). Several hypotheses could account for this association. Since levodopa is a metabolite in the biosynthesis of dopamine and melanin which involves the enzyme tyrosinase, and increased tyrosinase activity is found in melanoma, it was initially hypothesized that levodopa could enhance and stimulate growth on any residual melanoma tissue (183). However, recent studies have refuted a causal association for several reasons (178, 184). In particular, the observation that the risk of melanoma is increased in PD patients before diagnosis argues against an effect of levodopa. Additional explanations may be the existence of shared genetic or environmental factors, or the common embryonic origin of melanocytes and neurons from neural crest cells (178, 185). In addition, mechanistic links caused by common mutations or other alterations in a number of genes or proteins in PD and melanoma could explain the co-occurrence of PD and melanoma (184). Common mechanisms that are dysregulated in PD and melanoma are for example cellular detoxification, melanin biosynthesis or oxidative stress response (184).

Future studies should investigate underlying mechanisms of decreased risk of some cancers and increased risk of other cancers like melanoma in PD patients.

CONCLUSION

PD and GBM are two highly complex disease entities characterized by multiple cellular changes. Similar mutations within the same gene, for example Parkin (25), can have inverse effects, depending on whether they are germline or somatic mutations and depending on the type of cell in which they occur: a dividing cell in GBM or a post-mitotic neuron in PD. One could hypothesize that neurons are primarily unaffected in GBM due to their postmitotic state. On the contrary, somatic mutations causing tumorigenesis can spread through proliferative astrocytes.

Another inverse association of PD and GBM that requires future causal investigation is the time frame of the pathophysiology of both diseases. While PD is a chronic, generally slowly progressing neurodegenerative disease characterized by gradual neuronal loss, GBM is a rapidly progressing disease with rapid proliferation of glial cells in a much shorter time frame. Possible explanations for these observations are that in PD, the neuronal loss can be compensated for a long time whereas the aggressiveness of GBM due to highly infiltrative growing and metastasizing cells that also display a vast cell heterogeneity leads to a rapid disease progression.

In this review, we showed that there are common pathogenic mechanisms involved in PD and GBM including inversely deregulated pro-survival and immune signaling, mitochondrial dysfunction and metabolic alterations. There is an inverse regulation for p53, EGF(R), PTEN/PI3K/Akt, DJ-1, HIF-1α in PD and GBM. Due to the complexity of both PD and GBM etiology and pathogenesis, future studies need to unveil so far unknown mechanisms of both diseases that will help to better understand and to compare both diseases and to explain why common inverse dysregulated cellular pathways can lead to two such different diseases. Eventually, a deeper understanding of the pathological mechanisms underlying PD and GBM will guide the identification of possibly shared drug targets that need to be modulated inversely for causative treatment of both diseases.

AUTHOR CONTRIBUTIONS

PM wrote the review. ZH, IB, AE, P-ES and RK advised, structured, and reviewed. All authors contributed to the article and approved the submitted version.

FUNDING

REFERENCES

1. Devine MJ, Plun-Favreau H, Wood NW. Parkinson's disease and cancer: two wars, one front. *Nat Rev Cancer*. (2011) 11:812–23. doi: 10.1038/nrc3150
2. Driver JA. Understanding the link between cancer and neurodegeneration. *J Geriatr Oncol*. (2012) 3:58–67. doi: 10.1016/j.jgo.2011.11.007
3. Tallaksen CME, Müller U. Cancer and neurodegeneration: time to move beyond Janus? *Neurology*. (2017) 88:1106–7. doi: 10.1212/WNL.0000000000003727
4. Plun-Favreau H, Lewis PA, Hardy J, Martins LM, Wood NW. Cancer and neurodegeneration: between the devil and the deep blue sea. *PLoS Genet*. (2010) 6:1–8. doi: 10.1371/journal.pgen.1001257

Introduction - Manuscript I

Mencke et al.   Bidirectional Relation PD and GBM

5. Gao X, Ning Y. Cancer and Parkinson's disease: the odd couple. *Drugs Today*. (2011) 47:215–22. doi: 10.1358/dot.2011.47.3.1519657

6. Ibáñez K, Boullosa C, Tabarés-Seisdedos R, Baudot A, Valencia A. Molecular evidence for the inverse comorbidity between central nervous system disorders and cancers detected by transcriptomic meta-analyses. *PLoS Genet*. (2014) 10:1–7. doi: 10.1371/journal.pgen.1004173

7. Klus P, Cirillo D, Botta Orfila T, Gaetano Tartaglia G. Neurodegeneration and cancer: where the disorder prevails. *Sci Rep*. (2015) 5:1–7. doi: 10.1038/srep15390

8. D'Amelio M, Ragonese P, Sconzo G, Aridon P, Savettieri G. Parkinson's disease and cancer: insights for pathogenesis from epidemiology. *Ann N Y Acad Sci*. (2009) 1155:324–34. doi: 10.1111/j.1749-6632.2008.03681.x

9. Garcia-Ratés S, Greenfield S. Cancer and neurodegeneration: two sides, same coin? *Oncotarget*. (2017) 8:22307–8. doi: 10.18632/oncotarget.16190

10. Li Z, Zheng Z, Ruan J, Li Z, Tzeng CM. Chronic inflammation links cancer and Parkinson's disease. *Front Aging Neurosci*. (2016) 8:1–7. doi: 10.3389/fnagi.2016.00126

11. Ganguli M. Cancer and dementia. *Alzheimer Dis Assoc Disord*. (2015) 29:177–82. doi: 10.1097/WAD.0000000000000086

12. Noyce AJ, Bandres-Ciga S, Kim J, Heilbron K, Kia D, Hemani G, et al. The Parkinson's Disease Mendelian randomization research portal. *Mov Disord*. (2019) 34:1864–72. doi: 10.1002/mds.27873

13. Antony PMA, Diederich NJ, Krüger R, Balling R. The hallmarks of Parkinson's disease. *FEBS J*. (2013) 280:5981–93. doi: 10.1111/febs.12335

14. Tysnes OB, Storstein A. Epidemiology of Parkinson's disease. *J Neural Transm*. (2017) 124:901–5. doi: 10.1007/s00702-017-1686-y

15. Kawashima M, Suzuki SO, Doh-Ura K, Iwaki T. A-synuclein is expressed in a variety of brain tumors showing neuronal differentiation. *Acta Neuropathol*. (2000) 99:154–60. doi: 10.1007/PL00007419

16. Tanji K, Imaizumi T, Yoshida H, Mori F, Yoshimoto M, Satoh K, et al. Expression of α-synuclein in a human glioma cell line and its up-regulation by interleukin-1β. *Neuroreport*. (2001) 12:1909–12. doi: 10.1097/00001756-200107030-00028

17. Stefanova N, Emgård M, Klimaschewski L, Wenning GK, Reindl M. Ultrastructure of α-synuclein-positive aggregations in U373 astrocytoma and rat primary glial cells. *Neurosci Lett*. (2002) 323:37–40. doi: 10.1016/S0304-3940(02)00117-9

18. Klegeris A, Giasson BI, Zhang H, Maguire J, Pelech S, McGeer PL. Alpha-synuclein and its disease-causing mutants induce ICAM-1 and IL-6 in human astrocytes and astrocytoma cells. *FASEB J*. (2006) 20:2000–8. doi: 10.1096/fj.06-6183com

19. Tousi NS, Buck DJ, Curtis JT, Davis RL. α-Synuclein potentiates interleukin-1β-induced CXCL10 expression in human A172 astrocytoma cells. *Neurosci Lett*. (2012) 507:133–6. doi: 10.1016/j.neulet.2011.12.001

20. Duan J, Ying Z, Su Y, Lin F, Deng Y. α-Synuclein binds to cytoplasmic vesicles in U251 glioblastoma cells. *Neurosci Lett*. (2017) 642:148–52. doi: 10.1016/j.neulet.2017.01.067

21. Sánchez-Valle J, Tejero H, Ibáñez K, Portero JL, Krallinger M, Al-Shahrour F, et al. A molecular hypothesis to explain direct and inverse co-morbidities between Alzheimer's Disease, glioblastoma and lung cancer. *Sci Rep*. (2017) 7:1–12. doi: 10.1038/s41598-017-04400-6

22. Song YC, Lu GX, Zhang HW, Zhong XM, Cong XL, Xue SB, et al. Proteogenomic characterization and integrative analysis of glioblastoma multiforme. *Oncotarget*. (2017) 8:97304–12. doi: 10.18632/oncotarget.21937

23. Wipfler K, Cornish AS, Guda C. Comparative molecular characterization of typical and exceptional responders in glioblastoma. *Oncotarget*. (2018) 9:28421–33. doi: 10.18632/oncotarget.25420

24. Ge Y, Xu K. Alpha-synuclein contributes to malignant progression of human meningioma via the Akt/mTOR pathway. *Cancer Cell Int*. (2016) 16:1–7. doi: 10.1186/s12935-016-0361-y

25. Veeriah S, Taylor BS, Fang F, Yilmaz E, Vivanco I, Janakiraman M, et al. Somatic mutations of the Parkinson's disease–associated gene PARK2 in glioblastoma and other human malignancies. *Nat Genet*. (2010) 23:1–7. doi: 10.1038/ng.491

26. Lin EY, Li JF, Gnatovskiy L, Deng Y, Zhu L, Grzesik DA, et al. Macrophages regulate the angiogenic switch in a mouse model of breast cancer. *Cancer Res*. (2006) 66:11238–46. doi: 10.1158/0008-5472.CAN-06-1278

27. Yeo CWS, Ng FSL, Chai C, Tan JMM, Koh GRH, Chong YK, et al. Parkin pathway activation mitigates glioma cell proliferation and predicts patient survival. *Cancer Res*. (2012) 72:2543–53. doi: 10.1158/0008-5472.CAN-11-3060

28. Viotti J, Duplan E, Caillava C, Condat J, Goiran T, Giordano C, et al. Glioma tumor grade correlates with parkin depletion in mutant p53-linked tumors and results from loss of function of p53 transcriptional activity. *Oncogene*. (2014) 33:1764–75. doi: 10.1038/onc.2013.124

29. Feng DD, Cai W, Chen X. The associations between Parkinson's disease and cancer: the plot thickens. *Transl Neurodegener*. (2015) 4:20. doi: 10.1186/s40035-015-0043-z

30. Maugeri G, D'Amico AG, Magro G, Salvatorelli L, Barbagall O, Saccone S, et al. Expression profile of parkin isoforms in human gliomas. *Int J Oncol*. (2015) 47:1282–92. doi: 10.3892/ijo.2015.3105

31. Liu K, Li F, Han H, Chen Y, Mao Z, Luo J, et al. Parkin regulates the activity of pyruvate kinase M2. *J Biol Chem*. (2016) 291:10307–17. doi: 10.1074/jbc.M115.703066

32. Scott TL, Wicker CA, Suganya R, Dhar B, Pittman T, Horbinski C, et al. Polyubiquitination of apurinic/apyrimidinic endonuclease 1 by Parkin. *Mol Carcinog*. (2017) 56:325–36. doi: 10.1002/mc.22495

33. Yao ZQ, Zhang X, Zhen Y, He XY, Zhao S, Li XF, et al. A novel small-molecule activator of Sirtuin-1 induces autophagic cell death/mitophagy as a potential therapeutic strategy in glioblastoma article. *Cell Death Dis*. (2018) 9:767. doi: 10.1038/s41419-018-0799-z

34. Sanchez-Diaz PC, Chang JC, Moses ES, Dao T, Chen Y, Hung JY. Ubiquitin carboxyl-Terminal esterase L1 (UCHL1) is associated with stem-like cancer cell functions in pediatric high-grade glioma. *PLoS ONE*. (2017) 12:1–19. doi: 10.1371/journal.pone.0176879

35. Zhong J, Zhao M, Ma Y, Luo Q, Liu J, Wang J, et al. UCHL1 acts as a colorectal cancer oncogene via activation of the β-catenin/TCF pathway through its deubiquitinating activity. *Int J Mol Med*. (2012) 30:430–6. doi: 10.3892/ijmm.2012.1012

36. Agnihotri S, Golbourn B, Huang X, Remke M, Younger S, Cairns RA, et al. PINK1 is a negative regulator of growth and the warburg effect in glioblastoma. *Cancer Res*. (2016) 76:4708–19. doi: 10.1158/0008-5472.CAN-15-3079

37. Lee KS, Wu Z, Song Y, Mitra SS, Feroze AH, Cheshier SH, et al. Roles of PINK1, mTORC2, and mitochondria in preserving brain tumor-forming stem cells in a noncanonical Notch signaling pathway. *Genes Dev*. (2013) 27:2642–7. doi: 10.1101/gad.225169.113

38. Hinkle DA, Mullett SJ, Gabris BE, Hamilton RL. DJ-1 expression in glioblastomas shows positive correlation with p53 expression and negative correlation with epidermal growth factor receptor amplification. *Neuropathology*. (2011) 31:29–37. doi: 10.1111/j.1440-1789.2010.01124.x

39. Toda Y, Yoshimura R, Itahara M, Imai Y, Yamada K, Uno T, et al. DJ-1 contributes to self-renewal of stem cells in the U87-MG glioblastoma cell line. *Anticancer Res*. (2019) 39:5983–90. doi: 10.21873/anticanres.13803

40. Jin S, Dai Y, Li C, Fang X, Han H, Wang D. MicroRNA-544 inhibits glioma proliferation, invasion and migration but induces cell apoptosis by targeting PARK7. *Am J Transl Res*. (2016) 8:1826–37.

41. Haapasalo J, Nordfors K, Granberg KJ, Kivioja T, Nykter M, Haapasalo H, et al. NRF2, DJ1 AND SNRX1 and their prognostic impact in astrocytic gliomas. *Histol Histophatol*. (2018) 33:791–801. doi: 10.14670/HH-11-973

42. Zhao B, Shen C, Zheng Z, Wang X, Zhao W, Chen X, et al. Peiminine Inhibits glioblastoma in vitro and in vivo through cell cycle arrest and autophagic flux blocking. *Cell Physiol Biochem*. (2018) 51:1566–83. doi: 10.1159/000495646

43. Agalliu I, San Luciano M, Mirelman A, Giladi N, Waro B, et al. Higher frequency of certain cancers in LRRK2 G2019S mutation carriers with Parkinson disease a pooled analysis. *JAMA Neurol*. (2015) 72:58–65. doi: 10.1001/jamaneurol.2014.1973

44. Nord H, Hartmann C, Andersson R, Menzel U, Pfeifer S, Piotrowski A, et al. Characterization of novel and complex genomic aberrations in glioblastoma using a 32K BAC array. *Neuro Oncol*. (2009) 11:803–18. doi: 10.1215/15228517-2009-013

45. Wang Z, Liu P, Inuzuka H, Wei W. Roles of F-box proteins in cancer NIH Public Access. *Nat Rev Cancer*. (2014) 14:233–47. doi: 10.1038/nrc3700

46. Teixeira FR, Randle SJ, Patel SP, Mevissen TET, Zenkeviciute G, Koide T, et al. Gsk3β and Tomm20 are substrates of the SCFFbxo7/PARK15 ubiquitin ligase associated with Parkinson's disease. *Biochem J.* (2016) 473:3563–80. doi: 10.1042/BCJ20160387

47. Inamdar N, Arulmozhi D, Tandon A, Bodhankar S. Parkinsons Disease: genetics and beyond. *Curr Neuropharmacol.* (2007) 5:99–113. doi: 10.2174/157015907780866893

48. Senkevich K, Gan-Or Z. Autophagy lysosomal pathway dysfunction in Parkinson's disease; evidence from human genetics. *Parkinsonism Relat Disord.* (2019) 73:60–71. doi: 10.1016/j.parkreldis.2019.11.015

49. Larsen SB, Hanss Z, Krüger R. The genetic architecture of mitochondrial dysfunction in Parkinson's disease. *Cell Tissue Res.* (2018) 373:21–37. doi: 10.1007/s00441-017-2768-8

50. Lee J, Giordano S, Zhang J. Autophagy, mitochondria and oxidative stress: cross-talk and redox signalling. *Biochem J.* (2012) 441:523–40. doi: 10.1042/BJ20111451

51. Shiba-Fukushima K, Imai Y, Yoshida S, Ishihama Y, Kanao T, Sato S, et al. PINK1-mediated phosphorylation of the Parkin ubiquitin-like domain primes mitochondrial translocation of Parkin and regulates mitophagy. *Sci Rep.* (2012) 2:1–8. doi: 10.1038/srep01002

52. Stefanis L. α-Synuclein in Parkinson's disease. *Cold Spring Harb Perspect Med.* (2012) 2:1–23. doi: 10.1101/cshperspect.a009399

53. Jiang Y, Uhrbom L. On the origin of glioma. *Ups J Med Sci.* (2012) 117:113–21. doi: 10.3109/03009734.2012.658976

54. Silantyev AS, Falzone L, Libra M, Gurina OI, Kardashova KS, Nikolouzakis TK, et al. Current and future trends on diagnosis and prognosis of glioblastoma: from molecular biology to proteomics. *Cells.* (2019) 8:863. doi: 10.3390/cells8080863

55. Davis ME. Glioblastoma: overview of disease and treatment. *Clin J Oncol Nurs.* (2016) 20:1–8. doi: 10.1188/16.CJON.S1.2-8

56. Warburg O. Injuring of respiration the origin of cancer cells. *Science.* (1956) 123:309–14. doi: 10.1126/science.123.3191.309

57. Libby CJ, Tran AN, Scott SE, Griguer C, Anita B. The pro-tumorigenic effects of metabolic alterations in glioblastoma including brain tumor initiating cells. (2019) 1869:175–88. doi: 10.1016/j.bbcan.2018.01.004

58. Szybinska A, Lesniak W. P53 dysfunction in neurodegenerative diseases - The cause or effect of pathological changes? *Aging Dis.* (2017) 8:506–18. doi: 10.14336/AD.2016.1120

59. Zhu H, Wang H, Huang Q, Liu Q, Guo Y, Lu J, et al. Transcriptional repression of p53 by PAX3 contributes to gliomagenesis and differentiation of glioma stem cells. *Front Mol Neurosci.* (2018) 11:187. doi: 10.3389/fnmol.2018.00187

60. Houck AL, Seddighi S, Driver JA. Review of overlapping biology and its implications. *Curr Aging Sci.* (2019) 11:77–89. doi: 10.2174/1874609811666180223154436

61. Vousden KH, Prives C. Blinded by the light: the growing complexity of p53. *Cell.* (2009) 137:413–31. doi: 10.1016/j.cell.2009.04.037

62. Mogi M, Kondo T, Mizuno Y, Nagatsu T. p53 protein, interferon-γ, and NF-κB levels are elevated in the parkinsonian brain. *Neurosci Lett.* (2007) 414:94–7. doi: 10.1016/j.neulet.2006.12.003

63. Duplan E, Giordano C, Checler F, Alves Da Costa C. Direct α-synuclein promoter transactivation by the tumor suppressor p53. *Mol Neurodegener.* (2016) 11:1–9. doi: 10.1186/s13024-016-0079-2

64. Kato I, Maita H, Takahashi-Niki K, Saito Y, Noguchi N, Iguchi-Ariga SMM, et al. Oxidized DJ-1 inhibits p53 by sequestering p53 from promoters in a DNA-binding affinity-dependent manner. *Mol Cell Biol.* (2013) 33:340–59. doi: 10.1128/MCB.01350-12

65. Zhang Y, Dube C, Gibert M, Cruickshanks N, Wang B, Coughlan M, et al. The p53 pathway in glioblastoma. *Cancers.* (2018) 10:297. doi: 10.3390/cancers10090297

66. Djuzenova CS, Fiedler V, Memmel S, Katzer A, Hartmann S, Krohne G, et al. Actin cytoskeleton organization, cell surface modification and invasion rate of 5 glioblastoma cell lines differing in PTEN and p53 status. *Exp Cell Res.* (2015) 330:346–57. doi: 10.1016/j.yexcr.2014.08.013

67. Zheng H, Ying H, Yan H, Kimmelman AC, Hiller DJ, Chen AJ, et al. P53 and Pten control neural and glioma stem/progenitor cell renewal and differentiation. *Nature.* (2008) 455:1129–33. doi: 10.1038/nature07443

68. Marte BM, Downward J. PKB/Akt: connecting phosphoinositide 3-kinase to cell survival and beyond. *Trends Biochem Sci.* (1997) 22:355–8. doi: 10.1016/S0968-0004(97)01097-9

69. Fallon L, Bélanger CML, Corera AT, Kontogiannea M, Regan-Klapisz E, Moreau F, et al. A regulated interaction with the UIM protein Eps15 implicates parkin in EGF receptor trafficking and PI(3)K-Akt signalling. *Nat Cell Biol.* (2006) 8:834–42. doi: 10.1038/ncb1441

70. Iwakura Y, Piao YS, Mizuno M, Takei N, Kakita A, Takahashi H, et al. Influences of dopaminergic lesion on epidermal growth factor-ErbB signals in Parkinson's disease and its model: neurotrophic implication in nigrostriatal neurons. *J Neurochem.* (2005) 93:974–83. doi: 10.1111/j.1471-4159.2005.03073.x

71. Taylor TE, Furnari FB, Cavenee WK. Targeting EGFR for treatment of glioblastoma: molecular basis to overcome resistance. *Curr Cancer Drug Targets.* (2012) 12:197–209. doi: 10.2174/156800912799277557

72. Brennan CW, Verhaak RGW, McKenna A, Campos B, Noushmehr H, Salama SR, et al. The somatic genomic landscape of glioblastoma. *Cell.* (2014) 157:753. doi: 10.1016/j.cell.2014.04.004

73. Chistiakov DA, Chekhonin IV, Chekhonin VP. The EGFR variant III mutant as a target for immunotherapy of glioblastoma multiforme. *Eur J Pharmacol.* (2017) 810:70–82. doi: 10.1016/j.ejphar.2017.05.064

74. Gao Y, Vallentgoed WR, French PJ. Finding the right way to target EGFR in glioblastomas; Lessons from lung adenocarcinomas. *Cancers.* (2018) 10:489. doi: 10.3390/cancers10120489

75. Huang PH, Xu AM, White FM. Networks in glioma. *Sci Signal.* (2009) 2:1–13. doi: 10.1126/scisignal.287re6

76. Timmons S, Coakley MF, Moloney AM, O'Neill C. Akt signal transduction dysfunction in Parkinson's disease. *Neurosci Lett.* (2009) 467:30–5. doi: 10.1016/j.neulet.2009.09.055

77. Cheng CK, Fan QW, Weiss WA. PI3K signaling in glioma – animal models and therapeutic challenges. *Bone.* (2008) 23:1–7. doi: 10.1111/j.1750-3639.2008.00233.x

78. Li X, Wu C, Chen N, Gu H, Yen A, Cao L, et al. PI3K/Akt/mTOR signaling pathway and targeted therapy for glioblastoma. *Oncotarget.* (2016) 7:33440–50. doi: 10.18632/oncotarget.7961

79. Langhans J, Schneele L, Trenkler N, Von Bandemer H, Nonnenmacher L, Karpel-Massler G, et al. The effects of PI3K-mediated signalling on glioblastoma cell behaviour. *Oncogenesis.* (2017) 6:1–8. doi: 10.1038/s41389-017-0004-8

80. Sekar S, Taghibiglou C. Elevated nuclear phosphatase and tensin homolog (PTEN) and altered insulin signaling in substantia nigral region of patients with Parkinson's disease. *Neurosci Lett.* (2018) 666:139–43. doi: 10.1016/j.neulet.2017.12.049

81. Diaz-Ruiz O, Zapata A, Shan L, Zhang Y, Tomac AC, Malik N, et al. Selective deletion of PTEN in dopamine neurons leads to trophic effects and adaptation of striatal medium spiny projecting neurons. *Brain Pathol.* (2009) 4:e7027. doi: 10.1371/journal.pone.0007027

82. Domanskyi A, Geißler C, Vinnikov IA, Alter H, Schober A, Vogt MA, et al. Pten ablation in adult dopaminergic neurons is neuroprotective in Parkinson's disease models. *FASEB J.* (2011) 25:2898–910. doi: 10.1096/fj.11-181958

83. Malagelada C, Zong HJ, Greene LA. RTP801 is induced in Parkinson's disease and mediates neuron death by inhibiting Akt phosphorylation/activation. *J Neurosci.* (2008) 28:14363–71. doi: 10.1523/JNEUROSCI.3928-08.2008

84. Kim RH, Peters M, Jang Y, Shi W, Pintilie M, Fletcher GC, et al. DJ-1, a novel regulator of the tumor suppressor PTEN. *Cancer Cell.* (2005) 7:263–73. doi: 10.1016/j.ccr.2005.02.010

85. Greene LA, Levy O, Malagelada C. Akt as a victim, villain and potential hero in Parkinson's disease pathophysiology and treatment. *Cell Mol Neurobiol.* (2011) 31:969–78. doi: 10.1007/s10571-011-9671-8

86. McLendon R, Friedman A, Bigner D, Van Meir EG, Brat DJ, Mastrogianakis GM, et al. Comprehensive genomic characterization defines human glioblastoma genes and core pathways. *Nature.* (2008) 455:1061–8. doi: 10.1038/nature07385

87. Majewska E, Szeliga M. AKT/GSK3β signaling in glioblastoma. *Neurochem Res.* (2017) 42:918–24. doi: 10.1007/s11064-016-2044-4

88. Bonifati V, Rizzu P, Van Baren MJ, Schaap O, Breedveld GJ, Krieger E, et al. Mutations in the DJ-1 gene associated with autosomal recessive early-onset parkinsonism. *Science (80-.).* (2003) 299:256–9. doi: 10.1126/science.1077209

89. Wang C, Fang M, Zhang M, Li W, Guan H, Sun Y, et al. The positive correlation between DJ-1 and β-catenin expression shows prognostic value for patients with glioma. *Neuropathology.* (2013) 33:628–36. doi: 10.1111/neup.12041

90. Ariga H. Common mechanisms of onset of cancer and neurodegenerative diseases. *Biol Pharm Bull.* (2015) 38:795–808. doi: 10.1248/bpb.b15-00125

91. Kim YC, Kitaura H, Iguchi-Ariga SMM, Ariga H. DJ-1, an oncogene and causative gene for familial Parkinson's disease, is essential for SV40 transformation in mouse fibroblasts through up-regulation of c-Myc. *FEBS Lett.* (2010) 584:3891–5. doi: 10.1016/j.febslet.2010.08.010

92. Fan J, Ren H, Jia N, Fei E, Zhou T, Jiang P, et al. DJ-1 decreases Bax expression through repressing p53 transcriptional activity. *J Biol Chem.* (2008) 283:4022–30. doi: 10.1074/jbc.M707176200

93. Todorovic M, Wood SA, Mellick GD. Nrf2: a modulator of Parkinson's disease? *J Neural Transm.* (2016) 123:611–9. doi: 10.1007/s00702-016-1563-0

94. Vomund S, Schäfer A, Parnham MJ, Brüne B, Von Knethen A. Nrf2, the master regulator of anti-oxidative responses. *Int J Mol Sci.* (2017) 18:1–19. doi: 10.3390/ijms18122772

95. Liu C, Chen Y, Kochevar IE, Jurkunas UV. Decreased DJ-1 leads to impaired Nrf2-regulated antioxidant defense and increased UV-A–induced apoptosis in corneal endothelial cells. *Investig Ophthalmol Vis Sci.* (2014) 55:5551–60. doi: 10.1167/iovs.14-14580

96. Fan Z, Wirth A-K, Chen D, Wruck CJ, Rauh M, Buchfelder M, et al. Nrf2-Keap1 pathway promotes cell proliferation and diminishes ferroptosis. *Oncogenesis.* (2017) 6:e371. doi: 10.1038/oncsis.2017.65

97. Labzin LI, Heneka MT, Latz E. Innate immunity and neurodegeneration. *Annu Rev Med.* (2018) 69:437–49. doi: 10.1146/annurev-med-050715-104343

98. Kaur B, Khwaja FW, Severson EA, Matheny SL, Brat DJ, Van Meir EG. Hypoxia and the hypoxia-inducible-factor pathway in glioma growth and angiogenesis. *Neuro Oncol.* (2005) 7:134–53. doi: 10.1215/S1152851704001115

99. Agani FH, Pichiule P, Chavez JC, LaManna JC. The role of mitochondria in the regulation of hypoxia-inducible factor 1 expression during hypoxia. *J Biol Chem.* (2000) 275:35863–7. doi: 10.1074/jbc.M005643200

100. Zhang Z, Yan J, Chang Y, Yan SS, Shi H. Hypoxia inducible factor-1 as a target for neurodegenerative diseases. *Curr Med Chem.* (2011) 18:4335–43. doi: 10.2174/092986711797200426

101. Milosevic J, Maisel M, Wegner F, Leuchtenberger J, Wenger RH, Gerlach M, et al. Lack of hypoxia-inducible factor-1α impairs midbrain neural precursor cells involving vascular endothelial growth factor signaling. *J Neurosci.* (2007) 27:412–21. doi: 10.1523/JNEUROSCI.2482-06.2007

102. Zecca L, Youdim MBH, Riederer P, Connor JR, Crichton RR. Iron, brain ageing and neurodegenerative disorders. *Nat Rev Neurosci.* (2004) 5:863–73. doi: 10.1038/nrn1537

103. Sofic E, Riederer P, Heinsen H, Beckmann H, Reynolds GP, Hebenstreit G, et al. Increased iron (II1) and total iron content in post mortem substantia nigra of parkinsonian brain. *J Neural Transm.* (1988) 4:132–43.

104. Signore AP, Weng Z, Hastings T, Van Laar AD, Liang Q, Lee YJ, et al. Erythropoietin protects against 6-hydroxydopamine-induced dopaminergic cell death. *J Neurochem.* (2006) 96:428–43. doi: 10.1111/j.1471-4159.2005.03587.x

105. Silverman WF, Krum JM, Mani N, Rosenstein JM. Vascular, glial and neuronal effects of vascular endothelial growth factor in mesencephalic explant cultures. *Neuroscience.* (1999) 90:1529–41. doi: 10.1016/S0306-4522(98)00540-5

106. Correia SC, Moreira PI. Hypoxia-inducible factor 1: a new hope to counteract neurodegeneration? *J Neurochem.* (2010) 112:1–12. doi: 10.1111/j.1471-4159.2009.06443.x

107. Lee DW, Rajagopalan S, Siddiq A, Gwiazda R, Yang L, Beal MF, et al. Inhibition of prolyl hydroxylase protects against 1-methyl-4-phenyl-1,2,3,6-tetrahydropyridine-induced neurotoxicity. Model for the potential involvement of the hypoxia-unducible factor pathway in Parkinson disease. *J Biol Chem.* (2009) 284:29065–76. doi: 10.1074/jbc.M109.000638

108. Tanaka H, Sasayama T, Tanaka K, Nakamizo S, Nishihara M, Mizukawa K, et al. MicroRNA-183 upregulates HIF-1α by targeting isocitrate dehydrogenase 2 (IDH2) in glioma cells. *J Neurooncol.* (2013) 111:273–83. doi: 10.1007/s11060-012-1027-9

109. Liu Q, Cao P. Clinical and prognostic significance of HIF-1α in glioma patients: a meta-analysis. *Int J Clin Exp Med.* (2015) 8:22073–83.

110. Razavi S-M, Lee KE, Jin BE, Aujla PS, Gholamin S, Li G. Immune evasion strategies of glioblastoma. *Front Surg.* (2016) 3:1–9. doi: 10.3389/fsurg.2016.00011

111. Wei J, Wu A, Kong LY, Wang Y, Fuller G, Fokt I, et al. Hypoxia potentiates glioma-mediated immunosuppression. *PLoS ONE.* (2011) 6:e16195. doi: 10.1371/journal.pone.0016195

112. Wang H, Jiang Z, Na M, Ge H, Tang C, Shen H, et al. PARK2 negatively regulates the metastasis and epithelial-mesenchymal transition of glioblastoma cells via ZEB1. *Oncol Lett.* (2017) 14:2933–9. doi: 10.3892/ol.2017.6488

113. Harris A, Thompson AAR, Whyte MKB, Walmsley S. HIF-mediated innate immune responses: cell signaling and therapeutic implications. *Hypoxia.* (2014) 47:47–58. doi: 10.2147/HP.S50269

114. Hofmann KW, Schuh AFS, Saute J, Townsend R, Fricke D, Leke R, et al. Interleukin-6 serum levels in patients with parkinson's disease. *Neurochem Res.* (2009) 34:1401–4. doi: 10.1007/s11064-009-9921-z

115. Chen X, Hu Y, Cao Z, Liu Q, Cheng Y. Cerebrospinal fluid inflammatory cytokine aberrations in Alzheimer's disease, Parkinson's disease and amyotrophic lateral sclerosis: a systematic review and meta-analysis. *Front Immunol.* (2018) 9:1–10. doi: 10.3389/fimmu.2018.02122

116. Sawada M, Imamura K, Nagatsu T. Role of cytokines in inflammatory process in Parkinson's disease. *J Neural Transm Suppl.* (2006) 373–81. doi: 10.1007/978-3-211-45295-0_57

117. Kim YS, Joh TH. Microglia, major player in the brain inflammation: their roles in the pathogenesis of Parkinson's disease. *Exp Mol Med.* (2006) 38:333–47. doi: 10.1038/emm.2006.40

118. Yeung YT, McDonald KL, Grewal T, Munoz L. Interleukins in glioblastoma pathophysiology: implications for therapy. *Br J Pharmacol.* (2013) 168:591–606. doi: 10.1111/bph.12008

119. Brown NF, Carter TJ, Ottaviani D, Mulholland P. Harnessing the immune system in glioblastoma. *Br J Cancer.* (2018) 119:1171–81. doi: 10.1038/s41416-018-0258-8

120. Paugh BS, Bryan L, Paugh SW, Wilczynska KM, Alvarez SM, Singh SK, et al. Interleukin-1 regulates the expression of sphingosine kinase 1 in glioblastoma cells. *J Biol Chem.* (2009) 284:3408–17. doi: 10.1074/jbc.M807170200

121. Lu T, Tian L, Han Y, Vogelbaum M, Stark GR. Dose-dependent cross-talk between the transforming growth factor-β and interleukin-1 signaling pathways. *Proc Natl Acad Sci USA.* (2007) 104:4365–70. doi: 10.1073/pnas.0700118104

122. Sharma V, Dixit D, Koul N, Mehta VS, Sen E. Ras regulates interleukin-1β-induced HIF-1α transcriptional activity in glioblastoma. *J Mol Med.* (2011) 89:123–36. doi: 10.1007/s00109-010-0683-5

123. Tchirkov A, Rolhion C, Bertrand S, Doré JF, Dubost JJ, Verrelle P. IL-6 gene amplification and expression in human glioblastomas. *Br J Cancer.* (2001) 85:518–22. doi: 10.1054/bjoc.2001.1942

124. Rahaman SO, Harbor PC, Chernova O, Barnett GH, Vogelbaum MA, Haque SJ. Inhibition of constitutively active Stat3 suppresses proliferation and induces apoptosis in glioblastoma multiforme cells. *Oncogene.* (2002) 21:8404–13. doi: 10.1038/sj.onc.1206047

125. Tanabe K, Matsushima-Nishiwaki R, Yamaguchi S, Iida H, Dohi S, Kozawa O. Mechanisms of tumor necrosis factor-α-induced interleukin-6 synthesis in glioma cells. *J Neuroinflammation.* (2010) 7:3–10. doi: 10.1186/1742-2094-7-16

126. Bonavia R, Inda M, Vandenberg S, Cheng S, Nagane M, Hadwiger P, et al. EGFRvIII promotes glioma angiogenesis and growth through the NF-κB, interleukin-8 pathway. *Bone.* (2012) 23:1–7. doi: 10.1038/onc.2011.563

127. Hong TM, Teng LJ, Shun CT, Peng MC, Tsai JC. Induced interleukin-8 expression in gliomas by tumor-associated macrophages. *J Neurooncol.* (2009) 93:289–301. doi: 10.1007/s11060-008-9786-z

128. Bauer S, Müller T, Hamm S. Pattern recognition by toll-like receptors. *Adv Exp Med Biol.* (2009) 653:15–34. doi: 10.1007/978-1-4419-0901-5_2

129. Takeda K, Akira S. Toll-like receptors. *Curr Protoc Immunol.* (2015) 2015:14.12.1–10. doi: 10.1002/0471142735.im1412s109

130. Kawasaki T, Kawai T. Toll-like receptor signaling pathways. *Front Immunol.* (2014) 5:1–8. doi: 10.3389/fimmu.2014.00461

131. Arancibia SA, Beltrán CJ, Aguirre IM, Silva P, Peralta AL, Malinarich F, et al. Toll-like receptors are key participants in innate immune responses. *Biol Res.* (2007) 40:97–112. doi: 10.4067/S0716-97602007000200001

132. Kim C, Ho DH, Suk JE, You S, Michael S, Kang J, et al. Neuron-released oligomeric α-synuclein is an endogenous agonist of TLR2 for paracrine activation of microglia. *Nat Commun.* (2013) 4:1–24. doi: 10.1038/ncomms2534

133. Noelker C, Morel L, Lescot T, Osterloh A, Alvarez-Fischer D, Breloer M, et al. Toll like receptor 4 mediates cell death in a mouse MPTP model of Parkinson disease. *Sci Rep.* (2013) 3:1–5. doi: 10.1038/srep01393

134. Watson MB, Richter F, Lee SK, Gabby L, Wu J, Masliah E, et al. Regionally-specific microglial activation in young mice overexpressing human wildtype alpha-synuclein. *Exp Neurol.* (2013) 237:318–34. doi: 10.1016/j.expneurol.2012.06.025

135. Drouin-Ouellet J, St-Amour I, Saint-Pierre M, Lamontagne-Proulx J, Kriz J, Barker RA, et al. Toll-like receptor expression in the blood and brain of patients and a mouse model of Parkinson's disease. *Int J Neuropsychopharmacol.* (2015) 18:1–11. doi: 10.1093/ijnp/pyu103

136. Kouli A, Horne CB, Williams-Gray CH. Toll-like receptors and their therapeutic potential in Parkinson's disease and α-synucleinopathies. *Brain Behav Immun.* (2019) 81:41–51. doi: 10.1016/j.bbi.2019.06.042

137. Rietdijk CD, Van Wezel RJA, Garssen J, Kraneveld AD. Neuronal toll-like receptors and neuro-immunity in Parkinson's disease, Alzheimer's disease and stroke. *Neuroimmunol Neuroinflammation.* (2016) 3:27. doi: 10.20517/2347-8659.2015.28

138. Doorn KJ, Moors T, Drukarch B, van de Berg WDJ, Lucassen PJ, van Dam AM. Microglial phenotypes and toll-like receptor 2 in the substantia nigra and hippocampus of incidental Lewy body disease cases and Parkinson's disease patients. *Acta Neuropathol Commun.* (2014) 2:1–17. doi: 10.1186/s40478-014-0090-1

139. Finocchiaro G. TLRgeting evasion of immune pathways in glioblastoma. *Cell Stem Cell.* (2017) 20:422–4. doi: 10.1016/j.stem.2017.03.018

140. Alvarado AG, Thiagarajan PS, Mulkearns-Hubert EE, Silver DJ, Hale JS, Alban TJ, et al. Glioblastoma cancer stem cells evade innate immune suppression of self-renewal through reduced TLR4 expression. *Cell Stem Cell.* (2017) 20:450–61.e4. doi: 10.1016/j.stem.2016.12.001

141. Abarca-Merlin DM, Maldonado-Bernal C, Alvarez-Arellano L, Muthuraju S. Toll-like receptors as therapeutic targets in central nervous system tumors. *Biomed Res Int.* (2019) 2019:1–9. doi: 10.1155/2019/5286358

142. Barrera G, Gentile F, Pizzimenti S, Canuto RA, Daga M, Arcaro A, et al. Mitochondrial dysfunction in cancer and neurodegenerative diseases: spotlight on fatty acid oxidation and lipoperoxidation products. *Antioxidants.* (2016) 5:1–25. doi: 10.3390/antiox5010007

143. Siegel GJ, Albers RW, Agranoff BW. (1999). Basic neurochemistry. 6th ed. In: Siegel GJ, Albers RW, Agranoff BW, editors. *Molecular, Cellular and Medical Aspects.* Available online at: https://www.ncbi.nlm.nih.gov/books/NBK20385/

144. Schapira AHV, Cooper JM, Dexter D, Clark JB, Jenner P, Marsden CD. Mitochondrial complex I deficiency in Parkinson's Disease. *J Neurochem.* (1990) 54:823–7. doi: 10.1111/j.1471-4159.1990.tb02325.x

145. Requejo-Aguilar R, Bolaños JP. Mitochondrial control of cell bioenergetics in Parkinson's disease. *Free Radic Biol Med.* (2016) 100:123–37. doi: 10.1016/j.freeradbiomed.2016.04.012

146. Hsu CC, Huang N, Lin PY, Fang SY, Tsai DC, Chen SY, et al. Risk factors for myopia progression in second-grade primary school children in Taipei: a population-based cohort study. *Br J Ophthalmol.* (2017) 101:1611–7. doi: 10.1136/bjophthalmol-2016-309299

147. Qazi MA, Vora P, Venugopal C, Sidhu SS, Moffat J, Swanton C, et al. Intratumoral heterogeneity: pathways to treatment resistance and relapse in human glioblastoma. *Ann Oncol.* (2017) 28:1448–56. doi: 10.1093/annonc/mdx169

148. Zhou W, Wahl DR. Metabolic abnormalities in glioblastoma and metabolic strategies to overcome treatment resistance. *Cancers.* (2019) 11:1231. doi: 10.3390/cancers11091231

149. Anandhan A, Jacome MS, Lei S, Hernandez-Franco P, Pappa A, Panayiotidis MI, et al. Metabolic dysfunction in Parkinson's Disease: bioenergetics, redox homeostasis and central carbon metabolism. *Brain Res Bull.* (2017) 133:12–30. doi: 10.1016/j.brainresbull.2017.03.009

150. Zheng X, Boyer L, Jin M, Mertens J, Kim Y, Ma L, et al. Metabolic reprogramming during neuronal differentiation from aerobic glycolysis to neuronal oxidative phosphorylation. *Elife.* (2016) 5:1–25. doi: 10.7554/eLife.13374

151. Hall CN, Klein-Flügge MC, Howarth C, Attwell D. Oxidative phosphorylation, not glycolysis, powers presynaptic and postsynaptic mechanisms underlying brain information processing. *J Neurosci.* (2012) 32:8940–51. doi: 10.1523/JNEUROSCI.0026-12.2012

152. Powers R, Lei S, Anandhan A, Marshall DD, Worley B, Cerny RL, et al. Metabolic investigations of the molecular mechanisms associated with Parkinson's disease. *Metabolites.* (2017) 7:22. doi: 10.3390/metabo7020022

153. Lannuzel A, Michel PP, Höglinger GU, Champy P, Jousset A, Medja F, et al. The mitochondrial complex I inhibitor annonacin is toxic to mesencephalic dopaminergic neurons by impairment of energy metabolism. *Neuroscience.* (2003) 121:287–96. doi: 10.1016/S0306-4522(03)00441-X

154. Chaudhuri AD, Kabaria S, Choi DC, Mouradian MM, Junn E. MicroRNA-7 promotes glycolysis to protect against 1-methyl-4-phenylpyridinium-induced cell death. *J Biol Chem.* (2015) 290:12425–34. doi: 10.1074/jbc.M114.625962

155. Hong CT, Chau KY, Schapira AHV. Meclizine-induced enhanced glycolysis is neuroprotective in Parkinson disease cell models. *Sci Rep.* (2016) 6:6–13. doi: 10.1038/srep25344

156. Dunn L, Allen GFG, Mamais A, Ling H, Li A, Duberley KE, et al. Dysregulation of glucose metabolism is an early event in sporadic Parkinson's disease. *Neurobiol Aging.* (2014) 35:1111–5. doi: 10.1016/j.neurobiolaging.2013.11.001

157. Filosa S, Fico A, Paglialunga F, Balestrieri M, Crooke A, Verde P, et al. Failure to increase glucose consumption through the pentose-phosphate pathway results in the death of glucose-6-phosphate dehydrogenase gene-deleted mouse embryonic stem cells subjected to oxidative stress. *Biochem J.* (2003) 370:935–43. doi: 10.1042/bj20021614

158. Herken H. Neurotoxin-induced impairment of biopterin synthesis and function: initial stage of a Parkinson-like dopamine deficiency syndrome. *Neurochem Int.* (1990) 17:223–38. doi: 10.1016/0197-0186(90)90145-J

159. Weinhouse S, Warburg O, Burk D, Schade AL. On respiratory impairment in cancer cells. *Science.* (1956) 124:270–2. doi: 10.1126/science.124.3215.267

160. Agnihotri S, Zadeh G. Metabolic reprogramming in glioblastoma: the influence of cancer metabolism on epigenetics and unanswered questions. *Neuro Oncol.* (2016) 18:160–72. doi: 10.1093/neuonc/nov125

161. Kahlon AS, Alexander M, Kahlon A, Wright J. Lactate levels with glioblastoma multiforme. *Baylor Univ Med Cent Proc.* (2016) 29:313–4. doi: 10.1080/08998280.2016.11929449

162. Li X, Jiang Y, Meisenhelder J, Yang W, Hawke DH, Xia Y, et al. Mitochondria-translocated PGK1 functions as a protein kinase to coordinate glycolysis and the TCA cycle in tumorigenesis. *Mol Cell.* (2016) 61:705–19. doi: 10.1016/j.molcel.2016.02.009

163. Li X, Zheng Y, Lu Z. PGK1 is a new member of the protein kinome. *Cell Cycle.* (2016) 15:1803–4. doi: 10.1080/15384101.2016.1179037

164. Herrero-Mendez A, Almeida A, Fernández E, Maestre C, Moncada S, Bolaños JP. The bioenergetic and antioxidant status of neurons is controlled by continuous degradation of a key glycolytic enzyme by APC/C-Cdh1. *Nat Cell Biol.* (2009) 11:747–52. doi: 10.1038/ncb1881

165. Lalonde FM, Myslobodsky M. Are dopamine antagonists a risk factor for breast cancer? An answer from Parkinson's disease. *Breast.* (2003) 12:280–2. doi: 10.1016/S0960-9776(03)00061-4

166. Diamandis P, Sacher AG, Tyers M, Dirks PB. New drugs for brain tumors? Insights from chemical probing of neural stem cells. *Med Hypotheses.* (2009) 72:683–7. doi: 10.1016/j.mehy.2008.10.034

Introduction - Manuscript I

Mencke et al.   Bidirectional Relation PD and GBM

167. Wirdefeldt K, Weibull CE, Chen H, Kamel F, Lundholm C, Fang F, et al. Parkinson's disease and cancer: a register-based family study. *Am J Epidemiol.* (2014) 179:85–94. doi: 10.1093/aje/kwt232

168. Tang CF, Lu MK, Muo CH, Tsai CH, Kao CH. Increased risk of brain tumor in patients with Parkinson's disease: a nationwide cohort study in Taiwan. *Acta Neurol Scand.* (2016) 134:148–53. doi: 10.1111/ane.12524

169. Ye R, Shen T, Jiang Y, Xu L, Si X, Zhang B. The relationship between Parkinson disease and brain tumor: a meta-analysis. *PLoS ONE.* (2016) 11:e0164388. doi: 10.1371/journal.pone.0164388

170. Adhiyaman V, Meara J. Meningioma presenting as bilateral parkinsonism. *Age Ageing.* (2003) 32:456–8. doi: 10.1093/ageing/32.4.456

171. Freeman J, Westerhuis B, Asfora W, Free T, Salem B. Meningioma mimicking Parkinson's disease: a case report and analysis. *South Dakota Med.* (2013) 66:101–3.

172. Kim J-I, Choi JK, Lee J-W, Hong JY. Intracranial Meningioma-induced Parkinsonism. *J Lifestyle Med.* (2014) 4:101–3. doi: 10.15280/jlm.2014.4.2.101

173. Fong M, Ghahreman A, Masters L, Huynh W. Large intracranial meningioma masquerading as Parkinson's disease. *J Neurol Neurosurg Psychiatry.* (2016) 87:1251. doi: 10.1136/jnnp-2015-311531

174. Olsen JH, Friis S, Frederiksen K, McLaughlin JK, Mellemkjaer L, Møller H. Atypical cancer pattern in patients with Parkinson's disease. *Br J Cancer.* (2005) 92:201–5. doi: 10.1038/sj.bjc.6602279

175. Choi KH, Choi SM, Nam TS, Lee MC. Astrocytoma in the third ventricle and hypothalamus presenting with parkinsonism. *J Korean Neurosurg Soc.* (2012) 51:144–6. doi: 10.3340/jkns.2012.51.3.144

176. Møller H, Mellemkjaer L, McLaughlin JK, Olsen JH. Occurrence of different cancers in patients with Parkinson's disease. *BMJ.* (1995) 310:1500. doi: 10.1136/bmj.310.6993.1500

177. Skibba JL, Pinckley J, Gilbert EF, Johnson RO. Multiple primary melanoma following administration of levodopa. *Arch Pathol.* (1972) 93:556.

178. Liu R, Gao X, Lu Y, Chen H. Meta-analysis of the relationship between Parkinson disease and melanoma. *Neurology.* (2011) 76:2002–9. doi: 10.1212/WNL.0b013e31821e554e

179. Catalá-López F, Suárez-Pinilla M, Suárez-Pinilla P, Valderas JM, Gómez-Beneyto M, Martinez S, et al. Inverse and direct cancer comorbidity in people with central nervous system disorders: a meta-analysis of cancer incidence in 577,013 participants of 50 observational studies. *Psychother Psychosom.* (2014) 83:89–105. doi: 10.1159/000356498

180. Rampen FHJ. Levodopa and melanoma: three cases and review of literature. *J Neurol Neurosurg Psychiatry.* (1985) 48:585–8. doi: 10.1136/jnnp.48.6.585

181. Jansson B, Jankovic J. Low cancer rates among patients with Parkinson's disease. *Ann Neurol.* (1985) 17:505–9. doi: 10.1002/ana.410170514

182. Tacik P, Currya S, Fujioka S, Strongosky A, Uitti RJ, van Gerpen JA, et al. Cancer in Parkinson's disease. *Parkinsonism Relat Disord.* (2016) 31:28–33. doi: 10.1016/j.parkreldis.2016.06.014

183. Skinner RB Jr, LeDoux MS. Dermatological disorders in Parkinson's disease. *Curr Clin Neurol.* (2012) 24:237–42. doi: 10.1007/978-1-60761-429-6_16

184. Bose A, Petsko GA, Eliezer D. Parkinson's disease and melanoma: co-occurrence and mechanisms. *J Parkinsons Dis.* (2018) 8:385–98. doi: 10.3233/JPD-171263

185. Rugbjerg K, Friis S, Lassen CF, Ritz B, Olsen JH. Malignant melanoma, breast cancer and other cancers in patients with Parkinson's disease. *Int J Cancer.* (2012) 131:1904–11. doi: 10.1002/ijc.27443

Manuscript II

The Role of DJ-1 in Cellular Metabolism and Pathophysiological Implications for Parkinson's Disease

Mencke et al. 2021

Status:

Published in Cells 07.02.2021

Preface

For the following review, I collaborated with Miss Romano, Dr. Kitami and Dr. Linster. I generated all figures and tables, drafted all paragraphs except for chapter 2.2, which was drafted by Miss Romano.

Dr. Boussaad, Dr. Kitami, Dr. Linster and Prof. Dr. Krüger helped to edit the draft and the final manuscript was reviewed and approved by all authors.

cells

MDPI

Review

The Role of DJ-1 in Cellular Metabolism and Pathophysiological Implications for Parkinson's Disease

Pauline Mencke [1,*] , **Ibrahim Boussaad** [1] , **Chiara D. Romano** [2,3] , **Toshimori Kitami** [4] , **Carole L. Linster** [3] **and Rejko Krüger** [1,5,6,*]

1   Translational Neuroscience, Luxembourg Centre for Systems Biomedicine, University of Luxembourg, 4365 Esch-sur-Alzette, Luxembourg; ibrahim.boussaad@uni.lu

2   Biospecimen Research Group, Integrated Biobank of Luxembourg, Luxembourg Institute of Health (LIH), 3531 Dudelange, Luxembourg; chiara.romano@ext.uni.lu

3   Enzymology & Metabolism, Luxembourg Centre for Systems Biomedicine, University of Luxembourg, 4365 Esch-sur-Alzette, Luxembourg; carole.linster@uni.lu

4   RIKEN Outpost Laboratory, Luxembourg Centre for Systems Biomedicine, University of Luxembourg, 4365 Esch-sur-Alzette, Luxembourg; toshimori.kitami@uni.lu

5   Parkinson Research Clinic, Centre Hospitalier de Luxembourg (CHL), 1210 Luxembourg (Belair), Luxembourg

6   Transversal Translational Medicine, Luxembourg Institute of Health (LIH), 1445 Strassen, Luxembourg

*   Correspondence: pauline.mencke@uni.lu (P.M.); rejko.krueger@uni.lu (R.K.)

Abstract: DJ-1 is a multifunctional protein associated with pathomechanisms implicated in different chronic diseases including neurodegeneration, cancer and diabetes. Several of the physiological functions of DJ-1 are not yet fully understood; however, in the last years, there has been increasing evidence for a potential role of DJ-1 in the regulation of cellular metabolism. Here, we summarize the current knowledge on specific functions of DJ-1 relevant to cellular metabolism and their role in modulating metabolic pathways. Further, we illustrate pathophysiological implications of the metabolic effects of DJ-1 in the context of neurodegeneration in Parkinson´s disease.

Keywords: DJ-1; Parkinson´s disease; metabolism

check for **updates**

1. Introduction

Despite having been originally identified as an oncogene upregulated in different types of cancer, DJ-1 has also been clearly assigned as a causative factor for neurodegeneration in rare inherited forms of Parkinson's disease (PD) [1,2]. DJ-1 is encoded by the *Park7* gene and is ubiquitously expressed. In the human brain, the DJ-1 protein is abundantly expressed in reactive astrocytes and to a lower extent in neurons [3,4]. In the mouse CNS, DJ-1 transcript and protein were shown to be expressed at similar levels in neurons, astrocytes, microglia and oligodendrocytes [5].

DJ-1 is a small protein of 189 amino acids that forms homodimers. DJ-1 belongs to a functionally diverse protein superfamily whose members are all characterized by an α/ β-flavodoxin fold [6]. Human DJ-1 displays the characteristic central β-sheet surrounded by eight α-helices (sandwiched structure) and the highly conserved cysteine (Cys) 106 residue in the "nucleophile elbow" pocket [7]. The thiolate group of Cys106 can be oxidized to sulfinate (-SO2−) and sulfonate (-SO3−) under oxidative stress conditions [8]. This oxidation shifts the isoelectric point of the protein, promoting intracellular relocation of the enzyme to the mitochondria as well as its cytoprotective function [9]. DJ-1 was shown to be involved in many processes, including regulation of apoptosis and pro-survival signaling, autophagy, inflammatory responses and protection against oxidative stress [10,11]. DJ-1 was also shown to have chaperone activity [12] and to act as a glyoxalase III, able to detoxify reactive dicarbonyl species such as glyoxal (GO) and methylglyoxal (MGO) in

a glutathione-independent way [13] (Figure 1). Recently, an additional debate emerged about a potential deglycase activity of DJ-1 [14].
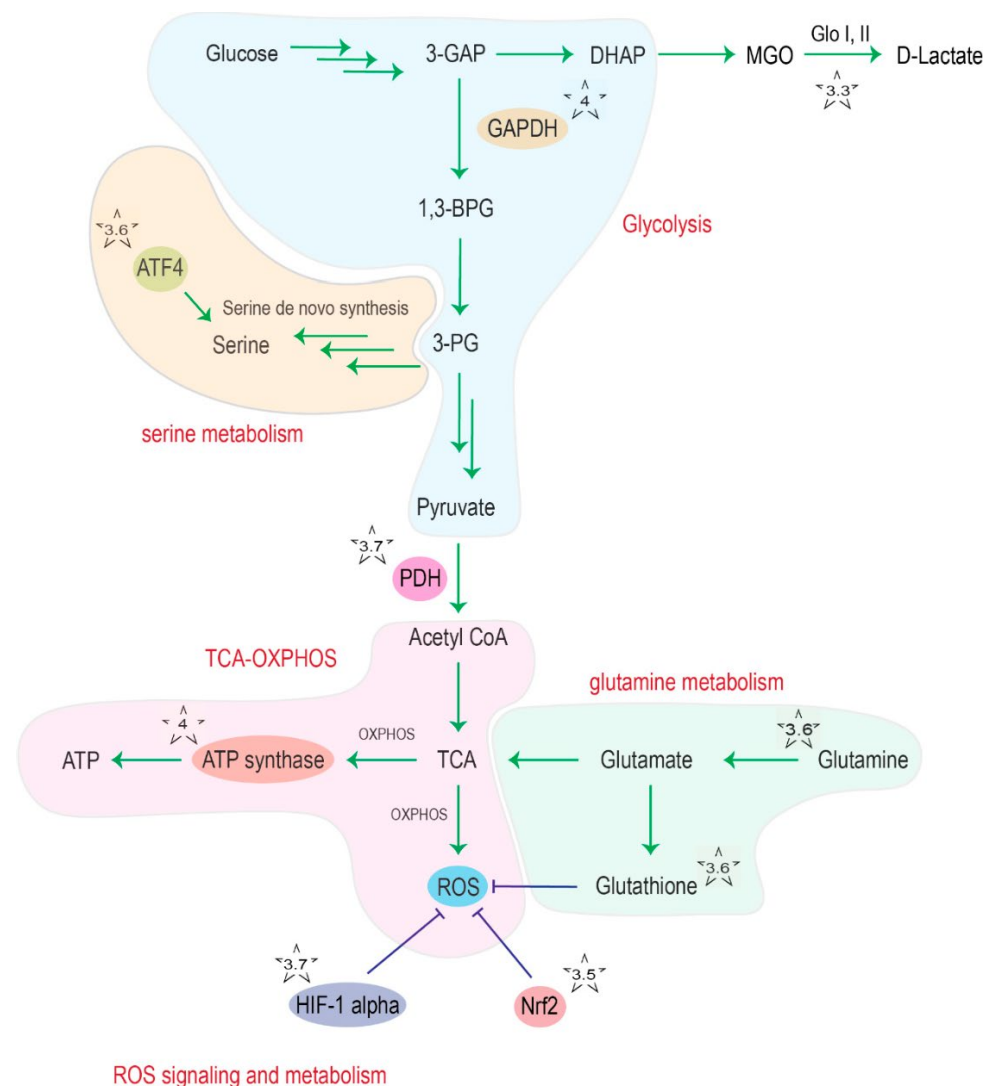
Figure 1. Overview of DJ-1 interaction points (indicated with a star) with cellular metabolism. The chapter discussing the indicated interaction points is given as number in the respective star. Abbreviations: 3-GAP: glyceraldehyde 3-phosphate; DHAP: dihydroxyacetone phosphate; MGO: methyglyoxal; Glo: glyoxalase, GAPDH; glyceraldehyde 3-phosphate dehydrogenase; 1,3-BPG: 1,3-bisphosphoglycerate; 3-PG: 3-phosphoglycerate; ATF4: activating transcription factor 4; PDH: pyruvate dehydrogenase; TCA: tricarboxylic acid cycle; OXPHOS: oxidative phosphorylation; ROS: reactive oxygen species; Nrf2: nuclear factor erythroid 2-related factor 2.

There are many studies pointing towards the effects of DJ-1 on cellular metabolism at different levels, but the underlying molecular mechanisms remain for the most part poorly understood.

Metabolic alterations are often linked to pathogenic conditions, and first links have been established for PD [15,16]. Indeed, impaired energy metabolism is associated with PD, as the inactivation of the electron transport chain complex 1 is classified as one of the hallmarks of PD [17], and the importance of metabolic dysfunction in PD has been increasingly discussed [15,16]. To what extent the loss of DJ-1 function in PD could contribute to disease pathogenesis by impairing or dysregulating energy or other parts of metabolism remains elusive.

In this review, we will summarize the current knowledge on the modulation of cellular metabolism by DJ-1 and the potential pathophysiological implications for neurodegeneration in PD. For other disease conditions associated with DJ-1 or for disease connections to broader functions of DJ-1, we refer readers to excellent reviews focusing on cancer [18], diabetes [19,20], inflammatory diseases [21] and Parkinson's disease [22].

2. DJ-1 in Parkinson's Disease

Parkinson's disease (PD) is the second most common neurodegenerative disease that affects 1–2% of the population over age 60 world-wide with increasing prevalence [23,24]. Cardinal symptoms of PD include tremor, bradykinesia, rigor and postural instability resulting from loss of dopaminergic neurons in the substantia nigra pars compacta [25]. Cellular hallmarks of PD include intraneuronal proteinaceous inclusions, Lewy bodies and neurites that contain α-synuclein as a major component [26]. Familial cases of PD account for up to 20% of all PD cases, of which approximately 5–10% have known monogenetic causes. To date, mutations in *SNCA*, *Parkin*, *PINK1, DJ-1*, *LRRK2* and *ATP13A2* are known to be causative for familial PD, but each of these monogenetic forms of PD is rather rare [24].

In 2003, Bonifati and colleagues found a large (about 14 kb) deletion and a missense mutation (Leucine166Proline, L166P) in the *Park7* gene in a Dutch and Italian family, respectively, which led to the identification of *Park7* as a causative gene for familial PD with recessive inheritance [2]. Since then, more than 20 DJ-1 mutations have been associated with early-onset PD. The impact of pathogenic single amino acid substitutions on the enzyme structure has been analyzed quite systematically [6]. The L166P mutation, for instance, affects the DJ-1 protein structure and function [27]. The lysine 166 residue is located in the center of the α-helix 7, which is located near the dimeric interface [8,28,29]. Introduction of a proline residue into a helix structure is not well tolerated as it increases the molecular rigidity, leading to a break in the helix and, predictably, C-terminal unfolding of the DJ-1 L166P variant [30]. The latter loses the dimerization property observed in the wildtype (WT) protein, forming unstable monomers that are prone to degradation [6]. The L10P and P158 mutations also disrupt the homodimerization of DJ-1 [31]. Other missense mutations, such as M26I and A104T, have less severe impact on the protein structure and do not prevent homodimerization [6]. However, both mutant proteins have been reported to be unstable, especially in the cellular environment [6,32]. Very recently, a DJ-1 mutation initially predicted to lead to a missense mutation (E64D) was shown to lead to decreased intracellular protein levels due to U1-dependent pre-mRNA mis-splicing [33]. Taken together, the information available on PD-associated DJ-1 variants so far seems to converge on the notion that a resulting loss-of-protein function explains their pathogenicity [34].

Patients with DJ-1 mutations develop early onset, slowly progressive parkinsonism, and most of them present with typical PD [35]. However, atypical forms with clinical symptoms related to other neurodegenerative diseases, i.e., amyotrophic lateral sclerosis and dementia, were described [36]. Cellular phenotypes of DJ-1 loss of function are predominantly mitochondrial dysfunction [37] and a reduced dopaminergic differentiation potential of PD patient-derived DJ-1-deficient cells [33]. These initial studies suggested that metabolic functions of DJ-1 may be important for the PD pathogenesis.

The mitochondrial phenotype in DJ-1-deficient models as well as other metabolic alterations induced by pathogenic DJ-1 mutations (summarized in Table 1) support the notion that PD pathogenesis involves an important metabolic component.

Table 1. Overview of metabolic alterations depending on DJ-1 status.

Metabolic Alteration	DJ-1 Status or Mutation	Model	Reference
Nucleotide/DNA/RNA glycation	siRNA knockdown	HeLa cells	[38]
Amino acid/protein glycation	C106S, C53S, and C46S DJ-1 mutants	-	[39]
Dicarbonyl-adduct damage	L10P, M26I, A104T, D149A, and L166P	-	[40]
Abnormal mitochondrial morphology mitochondrial/neuronal dysfunction mitochondrial/neuronal dysfunction	Loss of protein	M17 human neuroblastoma cells Mouse embryonic fibroblasts (MEFs) PD patient iPSC-derived neurons	[37] [41] [42] [43] [33]
Compromised mitochondrial uncoupling	Loss of protein	primary murine neurons	[44]
Increased ROS levels	Loss of protein	primary mouse embryonic fibroblasts brains from DJ- KO mice	[45]
Decreased PDH protein levels in DJ-1 KO compared to WT mice	Loss of protein	brain tissue from DJ-1 deficient mice	[46]
Decreased HIF1α level upon hypoxia	Loss of protein	primary cortical neurons derived from DJ-1 KO mouse embryos	[47]
Reduced serine biosynthesis	Loss of protein	LUHMES cells, a dopaminergic neuronal culture model	[48]
Decreased ATF4 transcript expression	Loss of protein	mouse embryonic fibroblasts	[49]

2.1. DJ-1 in Other Diseases

Despite its clear pathogenic role in PD, DJ-1 is also involved in diseases such as cancer [50], obesity, insulin resistance and type 2 diabetes mellitus (T2DM) [19,51,52].

In cancer, DJ-1 was found to play an important role in tumor progression of various cancer types through regulation of prosurvival signaling, for example via negative regulation of the tumor suppressor p53 [53]. DJ-1 regulates cell survival and proliferation via the extracellular signal-regulated kinase (ERK1/2) pathway and the phosphatidylinositol-3-kinase (PI3K)/Akt pathway. It counteracts apoptosis by inhibiting the activation of apoptosis signal-regulating kinase 1 (ASK1) and of the mitogen-activated protein kinase kinase kinase 1 (MEKK1/ MAP3K1) apoptotic cascades [10]. For example, in glioblastoma multiforme (GBM), DJ-1 levels were shown to be increased [54]. Hinkle and colleagues found also that immunostaining intensity of DJ-1 in GBM tissue varied directly with strong nuclear p53 expression and inversely with EGFR amplification [54]. Since DJ-1 negatively regulates pro-apoptotic p53 and EGFR signaling, these findings suggest that DJ-1 might be involved in promoting gliomagenesis.

The role of DJ-1 in glioblastoma is especially interesting as glioblastoma is thought to originate from astrocytes, which are also involved in PD pathogenesis, and increased DJ-1 expression is pathogenic for glioblastoma, but protective in models of PD [18].

In the following, we will focus on discussing the functions of DJ-1 in the modulation of cellular metabolism in the context of neurodegeneration in PD.

2.2. DJ-1 and Its Chaperone Function

Chaperone activity is essential to promote correct protein folding. Under "critical" situations, such as during oxidative stress, it becomes important to counteract protein denaturation and aggregation caused by oxidative damage. DJ-1 belongs to the DJ-1/ThiJ/PfpI superfamily and, albeit belonging to a different phylogenetic clade, shows structural similarities with another member of that superfamily, the heat shock protein Hsp31 [6,9]. The latter is a microbial protein and has been studied more extensively in the model organism *Saccharomyces cerevisiae* (i.e., budding yeast). Hsp31 is involved in the protection against reactive oxygen species (ROS), as confirmed by the *hsp31Δ* yeast strain, which is more sensitive to linoleic acid hydroperoxide and other ROS generating agents [55]. In addition to its ROS scavenging function, Hsp31 also acts as a chaperone for an array of proteins, including α-synuclein [56]. This small protein, encoded by the *SNCA* gene, exists under a native unfolded form in the cytoplasm and a more organized α-helical conformation when associated with cellular membranes [57]. Pathological conformational changes in α-synuclein lead to the formation of protein fibrils and Lewy bodies, the characteristic intraneuronal pathological inclusions in brains of PD patients [58]. The Hsp31 protein has been shown to prevent aggregation of α-synuclein in vitro and in living yeast cells expressing toxic levels of human α-synuclein [56,59]. This chaperone activity of Hsp31 was not dependent on the protein's glyoxalase activity [56].

A similar, although weaker chaperone activity against α-synuclein aggregation (in vitro, in the yeast α-synuclein model, and in murine neuroblastoma cells) has been reported for human DJ-1, and PD-causing DJ-1 mutations were shown to decrease the interaction with α-synuclein [12,56,59]. Burbulla and colleagues found that intracellular levels of soluble and insoluble α-synuclein were elevated in iPSC-derived human neurons from homozygous DJ-1 mutation carriers [60]. Kumar and colleagues reported that partially oxidized DJ-1 exposes an adhesive surface, which can sequester monomers of α-synuclein and block early stages of α-synuclein aggregation and also restrict the elongation of α-synuclein fibrils [61]. Importantly, and in line with this chaperoning function of DJ-1, patients with an autosomal recessively inherited form of juvenile PD due to homozygous loss-of-function mutations in the DJ-1 gene indeed show Lewy bodies in affected brain regions post-mortem [62].

Interestingly, Solti and colleagues found that DJ-1 itself can aggregate into β-sheet structured soluble and fibrillar aggregates in vitro under physiological conditions and accelerated when oxidized at its Cys106 residue [63]. They observed that as a result of the aggregation of DJ-1, its glyoxalase function was abolished [63]. In addition, DJ-1 aggregates were localized within Lewy bodies, neurofibrillary tangles and amyloid plaques in post-mortem brain tissue from PD and Alzheimer's patients [63]. The authors discuss that PD-associated loss of DJ-1 function in sporadic PD could be caused by its aggregation [63].

2.3. DJ-1 and Its Enzymatic Function

The reactive dicarbonyls glyoxal (GO) and methylglyoxal (MGO), which are formed in cells from various sources, including lipid peroxidation and the glycolytic triose-phosphate intermediates, respectively, can damage biomolecules via glycation. The latter are spontaneous chemical reactions between amino or thiol groups of, e.g., proteins or nucleotides and the carbonyl carbon of aldehyde and ketone groups in sugars and sugar derivatives [64]. The resulting adducts can react further to form "advanced glycation end products" (or AGEs), which accumulate over time and are considered as an inevitable component of the aging process [65]. An accumulation of AGEs can interfere with biological function and result in cellular damage [65]. Dicarbonyl damage has been associated with several diseases, including T2DM and PD [66]. The glutathione-dependent glyoxalase system is the major cellular protection mechanism against dicarbonyl damage. It converts GO and MGO to glycolic and lactic acid, respectively, through the consecutive action of glyoxalase I and glyoxalase II in the presence of catalytic amounts of reduced glutathione (GSH) [67]. An additional glutathione-independent glyoxalase activity, named glyoxalase III, has first been detected in *Escherichia coli* [68] and was subsequently identified as Hsp31 [69], a mem-

ber of the DJ-1 superfamily (already mentioned above because of its chaperone activity). Robust glyoxalase III activity has since also been detected in the yeast species *S. cerevisiae*, *Schizosaccharomyces pombe* and *Candida albicans* [70–72]. A weaker glyoxalase III activity has also been measured for human DJ-1 and its *Caenorhabditis elegans* homologs [13,72] (Figure 1). DJ-1 conferred protection against toxic effects of glyoxal treatment in mouse embryonic fibroblasts, SH-SY5Y cells and *C. elegans* worms [13]. Given the relatively weak glyoxalase activity of DJ-1, compared to the highly active and ubiquitous glyoxalase I/II system, the physiological relevance of DJ-1 for (methyl)glyoxal detoxification remains, however, questionable.

In addition to its glyoxalase function, Richarme and colleagues proposed that DJ-1 could act as a novel deglycase that repairs methylglyoxal- and glyoxal-glycated amino acids, proteins, nucleotides and nucleic acids by acting on early glycation intermediates and releasing lactate or glycolate [38,39]. Matsuda and colleagues suggested that DJ-1 protects glutathione and coenzyme A (CoA) from aldehyde attack [40]. They found that glutathione (GSH), CoA and β-alanine (a CoA precursor) are recovered from methylglyoxal-adducts by recombinant human DJ-1 purified from *E. coli*. During this process, MGO was converted to L-lactate rather than the D-lactate produced by the conventional glyoxalase I/II system. PD-associated DJ-1 mutations (L10P, M26I, A104T, D149A and L166P) were shown to impair or abolish this detoxification activity, suggesting that further dissection of the methylglyoxal-adduct hydrolase activity of DJ-1, which protects low-molecular thiols from dicarbonyl damage, may be a promising research direction to progress in our understanding of PD pathophysiology [40].

Jun and Kool recently published a comprehensive review that explains the controversial debate around the deglycase function of DJ-1, concluding that further studies are needed to clarify this potential function of DJ-1 [14]. As a central question, it remains to be determined whether DJ-1 has a direct deglycase activity or whether the observed deglycation results from removal of the small aldehydes (via the glyoxalase activity described above), which are in rapid equilibrium with the glycated adducts.

2.4. DJ-1 and Mitochondrial Function

In addition to its enzymatic functions, DJ-1 plays an important role in mitochondrial homeostasis. Mitochondria are the essential organelles for energy metabolism, as they provide the cell with ATP via the tricarboxylic acid (TCA) cycle and subsequent oxidative phosphorylation (OXPHOS) through the electron transport chain. Thus, changes in mitochondrial homeostasis can have drastic effects on the energy metabolism of the cell, especially on neurons that have a high energy consumption for maintaining synaptic activity.

It is well documented that changes in mitochondrial organellar homeostasis, as indicated for example by altered mitochondrial morphology, are associated with different in vitro and in vivo models of PD [46]. The *Drosophila melanogaster* genome encodes two DJ-1 homologs: DJ-1α and DJ-1β [47]. In *Drosophila*, the impact of loss of DJ-1 on mitochondrial quality control may involve two other important effectors well known in the context of PD: PINK1 and Parkin. It was shown that PINK1 and Parkin are both implicated in a common pathway that regulates mitochondrial dynamics and cell survival [73–75]. Yang and colleagues found that downregulation of PINK1 has deleterious effects in the fly model: flight ability is compromised by the flight muscle degeneration, and dopamine levels in the brain decrease with age. Electron microscopy analysis of tissues revealed swollen mitochondria, also in agreement with low ATP levels [76]. The overexpression of Parkin rescued loss-of-PINK1 related phenotypes, further supporting that Parkin acts downstream of PINK [76]. It is still a debate whether and how DJ-1 may integrate into this pathway, and what relation exists between PINK1, Parkin and DJ-1 in the maintenance of mitochondrial homeostasis. In *Drosophila*, there are controversial data for PINK1 knockout (KO) models concerning a selective rescue of PINK1 mutants by DJ-1 [73,76]. Even if one study places DJ-1 homologs downstream of *Drosophila* PINK1 with an expression-level dependent rescue of loss of PINK1 function, the fact that DJ-1 cannot rescue Parkin mutants

and Parkin cannot rescue loss of DJ-1 in flies indicates that DJ-1 does not act within the same pathway. Here, it has been suggested that DJ-1 acts in a pathway parallel to that of PINK1/Parkin [73].

Another modulator of mitochondrial dynamics is dynamin-like protein 1 (DLP1), or Drp1, a regulator of mitochondrial fission. It was shown that the levels of Drp1 were increased in DJ-1 mutant M17 human neuroblastoma cells [37]. The knockdown of Drp1 in DJ-1 mutant cells resulted in a rescue of the abnormal mitochondrial morphology and associated mitochondrial/neuronal dysfunction. Other studies confirmed the fragmentation phenotype, but remained controversial about the impact of modulations of Drp1, with normal total Drp1 [42,43] or decreased Mfn1 levels [41] in different models of reduced DJ-1 function. Therefore, increased fission related to loss of DJ-1 could be caused by an insufficient energy supply to maintain mitochondrial fusion processes [42] or based on an impaired ER-mitochondria communication related to altered tethering of membranes from both organelles [77]. Taken together, these controversial data suggest that DJ-1 might not regulate mitochondrial dynamics primarily via modulation of Drp1 expression, but that PD-associated loss of DJ-1 function may cause impaired mitochondrial function with impact on morphology and clearance of mitochondria based on multiple pathways [37]. PD-associated loss of DJ-1 function was found to be associated with reduced basal autophagy in mice [41,42] and M17 [43] cells, which was corroborated by an accumulation of dysfunctional mitochondria [41–43], eventually creating a vicious circle of dysfunctional mitochondria that accumulate and cause further cellular damage. Interestingly, GSH supplementation of DJ-1-deficient cells reversed both mitochondrial and autophagic alterations, which implies that DJ-1 may play an even more important role in mitochondrial function under oxidative stress and that it could influence mitochondrial dynamics and autophagy indirectly [78].

In addition to its role in the regulation of mitochondrial dynamics, DJ-1 was also shown to regulate the association of mitochondria and the endoplasmatic reticulum (ER).

Liu and colleagues found that DJ-1 localized to the mitochondria-associated membrane in vitro and in vivo. More specifically, they observed that DJ-1 physically interacts with the IP3R3-Grp75-VDAC1 complexes at the mitochondria-associated membrane and that DJ-1 is an important component of that complex. In the absence of DJ-1, the complex formation was disrupted and ER-mitochondria association was reduced. This phenotype was rescued by the expression of WT DJ-1, but not by the familial PD-associated L166P mutant [79], suggesting that impaired ER–mitochondria interaction plays a role in DJ-1-associated PD pathogenesis [79]. Overall, DJ-1 can regulate mitochondrial function via changes in mitochondrial clearance as well as through ER–mitochondria interaction.

Given the importance of DJ-1 for the maintenance of mitochondrial function, deficiency of this protein should directly impact cellular metabolism. In addition, DJ-1 acts as a scavenger of ROS, which play an important role as signaling molecules in cellular metabolism, but can also be deleterious when chronically increased.

2.5. DJ-1 and ROS Signaling

ROS signaling contributes to physiological homeostasis, but when dysregulated it contributes to disease pathogenesis via alterations in signaling cascades controlling metabolic function.

Cytosolic ROS are produced predominantly by the NADPH oxidase (NOX) family enzymes. ROS produced by NOX enzymes induce the expression of hypoxia inducible factor 1α (HIF1α), which activates the expression of glucose transporter 1 (GLUT1) and the activity of hexokinase, thereby upregulating glycolysis during hypoxia [80]. Mitochondrial ROS are mainly produced by the electron transport chain complexes, and they can also stabilize HIF1α and regulate cell proliferation [81]. DJ-1 deficiency, which is associated with increased ROS levels [45], disturbs these hypoxia response pathways. Parsanejad and colleagues have shown that loss of DJ-1 resulted in decreased HIF1α levels upon hypoxia in primary cortical neurons [82].

DJ-1 can regulate ROS levels via nuclear factor erythroid 2–related factor 2 (Nrf2), a transcription factor that activates genes involved in oxidative stress response as well as in NADPH and ATP production [48]. Clements and colleagues have shown that DJ-1 induces the dissociation of Nrf2 from its inhibitor Keap1 (Kelch-like ECH-associated protein 1), which leads to nuclear translocation of Nrf2 and binding to antioxidant response elements (AREs) in MEF cells [48]. By inducing Nrf2 activation, DJ-1 protects neurons against oxidative stress [48].

However, in another study involving primary cortical neurons, Nrf2 could still be activated in DJ-1 deficient mice, suggesting that DJ-1 is not required for Nrf2 activation at least in this cell type [49].

Structurally, the Cys106 of DJ-1 is preferentially oxidized in cells exposed to oxidative stress [8,83] and is generally known to be the key residue involved in DJ-1 antioxidative function [84]. This is why DJ-1 is also referred to as an "oxidative stress sensor" within cells whose stable Cys106-SO2- modification induces the mitochondrial relocalization of DJ-1. The latter leads to the protection from oxidative stress-induced cellular damage [9,85], one of many mechanisms through which DJ-1 exerts its neuroprotective function [83]. Importantly, the oxidation status of DJ-1 Cys106 seems to be biphasic. Cys106 resides in a pocket, and the transition from oxidized Cys106-SO_2^- to over oxidized Cys106-(e.g., SO_3^-) can change the local conformation of the protein leading to destabilized dysfunctional DJ-1 [53]. Therefore, it can be envisaged that the composition of DJ-1 complexes under acute or mild oxidative stress will be different from the one that can be found under conditions that are chronically and excessively oxidizing, thus changing the physiological response of the cell, for example, from pro-survival to apoptotic [53]. Piston and colleagues found that the levels of total DJ-1 and of DJ-1 oxidized at Cys106 were decreased in the cortex of idiopathic PD brains when compared to age-matched control tissue. Moreover, DJ-1 formed high molecular weight complexes in the human brain, which was dependent on the oxidation state of Cys106 [86]. Piston and colleagues also found that proteins involved in RNA transcription/translation seemed to be associated with the complexes of DJ-1, and the composition of the complexes was affected by the oxidation status of DJ-1. Interestingly, these transcripts were associated with the catecholamine system, including dopamine metabolism [87].

2.6. DJ-1 and Serine/Glutathione/Glutamine Metabolism

Meiser and colleagues used stable isotope-assisted metabolic profiling to investigate the effect of a functional loss of DJ-1 in LUHMES cells, a human dopaminergic neuronal culture model, and found that DJ-1-deficient neurons exhibit decreased glutamine uptake and reduced serine biosynthesis (Figure 1). Both glutamine and serine are required to generate L-glutamyl-L-cysteine, an important precursor of the antioxidant molecule GSH. Serine is converted into cysteine via the transsulfuration pathway, and glutamine is converted into glutamate, and they together form L-glutamyl-L-cysteine via glutamate cysteine ligase. Downregulation of these pathways, as a result of loss of DJ-1, leads to an impaired antioxidant response [88]. In line with the decreased serine biosynthesis in DJ-1-deficient cells, loss of DJ-1 in MEFs decreased protein and transcript levels of ATF4 [89], a transcription factor that activates serine biosynthesis genes including PSPH, PHGDH and PSAT1 [90] (Figure 1).

Meiser and colleagues also reported an increased sensitivity to H2O2-induced oxidative stress, resulting in a 30% decrease in reduced GSH levels and higher ratio of oxidized (GSSG) to reduced GSH in DJ-1 KO mice [88]. The observed that a decrease in GSH levels and a decrease in enzyme levels of the GSH homeostasis pathways are caused by the loss of DJ-1 and result in insufficient ROS quenching in DJ-1-deficient neurons [88].

Zhou and colleagues found that overexpression of DJ-1 in the N27 rat dopaminergic cell line and in primary dopaminergic neurons protected these cells from death induced by H2O2 and 6-hydroxydopamine [91]. They found that DJ-1 prevents cell death by increasing the level of glutamate cysteine ligase, a rate-limiting enzyme for GSH biosynthesis.

The cytoprotective effect of DJ-1 was absent when GSH synthesis was blocked, but the protection could be restored by adding exogenous GSH.

These data indicate that DJ-1 protects dopaminergic neurons from oxidative stress-induced cell death by upregulating GSH synthesis [91] (Figure 1).

In another study, the effect of oxidative stress on GSH metabolism and DJ-1 protein was investigated. Downregulation of glutaredoxin (GRX), but not GSH depletion, resulted in a decrease in DJ-1 protein, translocation of Daxx (a death-associated protein) from the nucleus and subsequent cell death. Daxx translocation and cytotoxicity was prevented by overexpression of DJ-1. Protease inhibitors prevented the decrease in DJ-1 level. Residual DJ-1 was present in a reduced state, which implies that when DJ-1 was oxidized, it was degraded through proteolysis. Thus, the loss of DJ-1 occurring through its oxidative modification and subsequent proteolysis may contribute to PD pathogenesis [92].

In vivo, Lopert and colleagues found that brains from DJ-1 KO mice had an increase in mitochondrial respiration-dependent H_2O_2 consumption when compared to control mice [93], indicating that DJ-1 KO mice had a higher capacity to eliminate H_2O_2 compared to WT control. However, DJ-1 KO mice showed an increase in oxidized GSSG to reduced GSH ratio and a decrease in mitochondrial glutathione reductase activity, suggesting that other factors may be responsible for increased H_2O_2 consumption. The authors instead found an increase in mitochondrial thioredoxin 2 (TRX2) activity and mitochondrial glutaredoxin activity in DJ-1 KO brain compared to WT controls. Therefore, the observed increase in the enzymatic activities of mitochondrial TRX2 and GRX could be causal for the observed increased H_2O_2 consumption in mitochondria of brains from DJ-1 KO mice, and this might be an adaptive response to chronic DJ-1 deficiency [93].

2.7. DJ-1 and the Regulation of Glycolysis and the TCA Cycle

There is increasing evidence for a direct involvement of DJ-1 in cellular energy metabolism via effects on glycolysis and the TCA cycle. Here, we will describe this involvement of DJ-1 starting from glycolysis, onto TCA cycle and OXPHOS, and finally to signaling and transcriptional regulation of metabolism.

Piston and colleagues analyzed DJ-1 WT high molecular weight complexes from dopaminergic SH-SY5Y cells and identified that glyceraldehyde 3-phosphate dehydrogenase (GAPDH) forms a complex with DJ-1 [86] (Figure 1). GAPDH is a glycolytic enzyme that converts glyceraldehyde 3-phosphate into 1,3-bisphosphoglycerate. Importantly, knockdown of DJ-1 or expression of the PD-associated DJ-1 variant L166P resulted in the absence of high molecular weight DJ-1 complexes [86]. It is not known what the consequences of the interaction of DJ-1 and GAPDH are, but it suggests a possible modulation of the glycolytic pathway by DJ-1 via regulation of GAPDH.

Ozawa and colleagues performed a 2D gel electrophoresis-based proteomic analysis of brain tissue from DJ-1 deficient mice and found a significant change in protein expression of pathways related to energy production including glycolysis, creatine pathway, mitochondrial TCA cycle, and ROS signaling pathway [94]. According to their analysis, spots of proteins such as PDH were decreased in DJ-1 KO compared to WT mice (Figure 1). PDH is a key enzyme in the regulation of metabolism as it connects glycolysis and the TCA cycle and determines whether pyruvate is converted into acetyl-CoA or reduced into lactate. Consistent with a decrease in PDH protein level, the authors found a decrease in mitochondrial ATP production rate in DJ-1 KO SH-SY5Y cells, although a compensatory increase in lactate production was not detected.

DJ-1 was also shown to control PDH activity in CD4 regulatory T cells (Tregs). DJ-1 binds to PDH-E1 beta (PDHB), which leads to the inhibition of the phosphorylation of PDH-E1 alpha (PDHA), thereby promoting PDH activity and OXPHOS [95] (Figure 1).

DJ-1 depletion caused impaired Treg proliferation and cellular maintenance in older mice [95]. DJ-1 was also shown to interact with PDHB in HEK 293, SH-SY5Y and in the mouse brain using immunoprecipitation and mass spectrometry of the mitochondrial

protein interactome [96]. However, the effect of this direct protein–protein interaction on the activity of the PDH enzyme still needs to be investigated in neuronal cells.

As mentioned earlier, DJ-1 was found in different subcellular compartments, and it is claimed that the localization of DJ-1 determines its function. Cali and colleagues used HeLa cells to analyze whether DJ-1 metabolic function depends on its localization and activity within the mitochondria. This study revealed that a small DJ-1 fraction is located within the mitochondrial matrix [97] and that it consistently increases upon nutrient depletion. Targeting of DJ-1 to the mitochondrial matrix enhanced mitochondrial and cytosolic ATP levels. Interestingly, overexpression of DJ-1 pathogenic mutants (C106T, M26I and L166P) did not enhance ATP levels, and these mutants were unable to translocate into the mitochondrial matrix upon nutrient depletion, suggesting that DJ-1 localization is also critical for regulating cellular metabolism [98].

It was shown by Chen and colleagues that DJ-1 binds directly to the F1FO ATP synthase β-subunit in HEK293T cells. The interaction of DJ-1 with the β-subunit increased the efficiency of ATP production [99]. Guzman and colleagues found that DJ-1 deficiency in murine neurons resulted in decreased mRNA levels of the uncoupling proteins Ucp5 and Ucp4 and compromised mitochondrial uncoupling in ex vivo brain slices of DJ-1 KO mice [100]. These data provide additional support for an important role of DJ-1 in the modulation of mitochondrial energy production.

Weinert and colleagues describe an interaction between DJ-1 and signaling molecule 14-3-3β that regulates the localization of DJ-1 in a hypoxia-dependent manner, either to the cytosol or to mitochondria [101]. In HEK293T cells, the authors found that DJ-1 is preferentially located in the cytosol by forming a complex with 14-3-3β. Upon cellular stress, including hypoxia or dissipation of mitochondrial membrane potential, DJ-1 dissociates from 14-3-3β and enters mitochondria. In primary neurons, however, DJ-1 was already found to be abundant in mitochondria, suggesting that different cell types have different baseline levels of mitochondrial DJ-1 relative to cytosolic DJ-1 [48]. Furthermore, it was shown that DJ-1 knockdown decreased and 14-3-3β knockdown increased mitochondrial membrane potential in HEK293T cells, suggesting that DJ-1 localization may regulate the energetic potential of mitochondria [101].

Another important molecular interaction concerning metabolic control involves DJ-1 and the Von Hippel Lindau (VHL) protein. VHL ubiquitinates HIF-1α in normoxia, leading to HIF-1α degradation, thus preventing hypoxic response. DJ-1 was shown to bind VHL in SH-SY5Y cells and to suppress VHL ubiquitin ligase activity, thereby blocking VHL-mediated degradation of HIF-1α [82]. Under hypoxia, DJ-1 KO resulted in lower HIF-1α level and showed increased sensitivity to oxidative stress induced by MPP+ in cortical neurons [82]. Increased sensitivity to MPP+ was rescued by HIF-1α overexpression, suggesting that DJ-1 is important for activating the HIF-1α-dependent oxidative stress response.

However, HIF-1α activation is also known to reprogram cellular metabolism by upregulating glycolytic gene expression and by inhibiting pyruvate entry into the TCA cycle, thus mediating a shift from OXPHOS to glycolysis and attenuating ROS production in cells [44]. Mechanistically, HIF-1α activates pyruvate dehydrogenase kinase 1 (PDK1), leading to phosphorylation and inhibition of PDH [102]. Therefore, the role of DJ-1 in regulating metabolic flux through PDH may change depending on the status of HIF-1α activation. Under normoxia or low oxidative stress, a direct interaction between DJ-1 and PDH or mitochondrial localization may upregulate mitochondrial ATP production, while under hypoxia or increased oxidative stress, DJ-1 may block flux through PDH by stabilizing HIF-1α and activating PDK1.

3. DJ-1 and Pathophysiological Implications of Altered Metabolism in PD

The importance of metabolism in the pathogenesis of neurodegenerative diseases such as PD is reflected by an increasing number of studies discussing the effect of the nutrition of PD patients [103,104] and that metabolic syndrome can contribute to the pathophysiology of PD [105]. Berry and colleagues found for example that large neutral amino acid levels in

the plasma of PD patients were more stable and that the motor performance was superior for patients who had a balanced (5:1) carbohydrate:protein diet compared to patients with unbalanced diets [103], indicating a general role of nutrition and the metabolism in PD pathogenesis. Regarding the involvement of DJ-1 in the regulation of cellular metabolism in the context of PD, there is only little known so far.

In the following, we will present different hypotheses for such a role on the basis of observations made in DJ-1 deficient cells, animal models and in clinical studies.

GO and MGO are byproducts of lipid peroxidation and glycolysis [106] that, if not quenched, lead to cellular damage via protein and DNA glycation. The two main enzymes responsible for the detoxification of GO and MGO are glyoxalase I and II [106]. DJ-1 as glyoxalase III may contribute to this process [13], especially under conditions where GSH availability is limited (glyoxalase III, as opposed to the glyoxalase I/II system, is GSH-independent) (Section 2.3). A novel deglycase activity has more recently been proposed for DJ-1 [39,107] that repairs glycation damage induced on proteins and DNA by glyoxal and methylglyoxal. Loss of DJ-1 was shown to increase the levels of glycated DNA and DNA strand breaks [38]. However, the proposed deglycase activity of DJ-1 is not yet commonly accepted, as conflicting observations have been reported [108,109]. If confirmed, it would imply, however, that lack of functional DJ-1 could lead to reduced protection from glycation, increased DNA and protein damage and, hence, premature cellular aging via accumulation of advanced glycation end products (AGEs) [38]. A recent clinical study has shown that PD patients have higher plasma levels of carboxymethyllysine, one of the AGEs, compared to healthy controls, suggesting that the roles of AGEs and deglycase function of DJ-1 in PD pathogenesis need to be further studied [110].

A more direct involvement of DJ-1 in the regulation of metabolism was defined by its physical interaction with PDH (Section 2.7), as already mentioned [95]. The consequence of decreased PDH activity in DJ-1-deficient cells is a decreased conversion of pyruvate into acetyl-CoA, which is the main gateway to fuel the TCA cycle [95]. Neurons are metabolically very demanding cells as they need large amounts of ATP to meet their functional requirements, i.e., maintenance of synaptic transmission. Neurons rely on energy production via the TCA cycle and OXPHOS and are incapable of relying solely on glycolysis [111]. Therefore, TCA-OXPHOS impairment due to decreased PDH activity would predictably lead to insufficient ATP production and force neurons to increase their glycolytic flux. Eventually, this could contribute to neuronal cell death. Clinical trials involving a high-energy substrate for ATP, creatine, which bypasses TCA and OXPHOS, have shown that creatine does not improve the clinical outcome of patients with PD [112]. Although it is possible that a sufficient amount of creatine did not reach the brain of the patients, other strategies for restoring energy flux may need to be discovered. In addition, a compensatory increase in glycolytic flux under DJ-1 deficiency could accelerate accumulation of methylglyoxal. Therefore, the effect of DJ-1 on PDH activity could contribute to PD pathogenesis also via AGEs.

DJ-1 also interacts with GAPDH (Section 2.7), although the biological significance and functional consequences of the interaction are unknown. However, the product of GAPDH (1,3-bisphosphoglycerate) is a precursor of 3-phosphoglycerate, which is needed for serine de novo synthesis. As loss of DJ-1 results in decreased serine biosynthesis [88] (Section 2.6), the absence of DJ-1 GAPDH complex in DJ-1-deficient cells could result in decreased 1,3-bisphosphoglycerate synthesis and eventually less 3-phosphoglycerate required for the serine de novo synthesis. Impaired serine biosynthesis was found in PD patient-derived cells [113]. In addition, levels of D-serine in the cerebrospinal fluid of PD patients were lower compared to healthy controls, suggesting that serine metabolism is also important for PD pathogenesis [114].

Interestingly, Gelfin and colleagues found that the treatment of PD patients with D-serine could alleviate behavioral and motor symptoms of the patients [115]. In more detail, D-serine was found to regulate N-methyl-D-aspartate subtype of glutamate receptor (NMDAR) mediated neurotransmission, resulting in an improvement in extrapyramidal

symptoms and abnormal involuntary movements, further supporting the importance of serine metabolism in the pathogenesis of PD [115].

In addition to an impairment of serine biosynthesis, glutamine flux was shown to be reduced in the absence of DJ-1, and as glutamine is essential for glutathione synthesis, DJ-1 deficiency impairs the latter on two different levels resulting in an increased sensitivity to oxidative stress [88]. One regulator of oxidative stress that was mentioned earlier to be activated under certain conditions by DJ-1 is the transcription factor Nrf2. In addition to its role in oxidative stress, Nrf2 is increasingly discussed to play a role in mitochondrial bioenergetics and the regulation of expression of metabolic enzymes [116]. Esteras and colleagues discussed pharmacological activation of Nrf2 aiming to restore mitochondrial and metabolic function for the treatment of PD [116]. Nrf2 activation via, for example, Keap1-targeting compounds leads to an increase in substrates that can be used by the TCA cycle and enhances the mitochondrial membrane potential and ATP production [116]. These effects of Nrf2 activation could increase neuronal viability due to their high energy demand in combination with their low glycolytic capacity, suggesting that Nrf2-activating drugs could be of relevance for the treatment of PD [116].

Reduced scavenging of ROS via GSH can have a direct effect on the TCA cycle and OXPHOS as both are regulated by ROS [117]. ROS were shown to stimulate glucose uptake [118]. Under a normal range, ROS stimulate glucose uptake with a beneficial effect on metabolism [117]. However, when ROS levels increase chronically, a vicious cycle of ROS-stimulated glucose uptake and glucose-stimulated ROS production via increased TCA-OXPHOS can be triggered. To counteract this cycle, ROS levels need to be decreased via the DJ-1-mediated pathways or via a decrease in glucose uptake, which will decrease carbon flux into the TCA cycle and depolarize mitochondrial membrane potential if the ATP demand remains high [119]. In addition, chronically high ROS levels in DJ-1 deficiency can eventually lead to mitochondrial dysfunction and apoptosis. In line with these hypotheses, a recent study has shown that DJ-1 deficiency results in decreased mitochondrial membrane potential and decreased ATP production [45]. However, as a decrease in OXPHOS can also be caused by altered TCA flux, these studies are insufficient to capture the entire metabolic status of DJ-1 deficiency.

Clinically, high levels of urate, an antioxidant, in the serum and cerebrospinal fluid of PD patients is associated with slower progression of PD [120,121]. However, randomized clinical trials involving antioxidant vitamin E (tocopherol) have not shown improvement of PD symptoms [122], although more prolonged treatment, once levodopa treatment starts, appeared to slow motor decline [123]. In addition, clinical trials involving mitochondria-targeted antioxidant MitoQ [124] and antioxidant and OXPHOS cofactor CoQ10 [125] have not shown clinical benefit, suggesting that oxidative stress alone may not fully explain the PD pathogenesis.

On a final note, it could be that DJ-1 affects neuronal metabolism in part indirectly via astrocytes. Astrocytes are the major route for brain glucose uptake during periods of strong synaptic activity, indicating that astrocytic glucose uptake is of key importance to neurons [119]. Astrocytes also provide neurons with lactate and glutamine, which are converted into pyruvate and glutamate, respectively, and used in the TCA cycle [118,119]. The loss of DJ-1 in astrocytes could influence neuronal metabolism and viability.

As an outlook, future studies need to define the molecular underpinnings of the role of DJ-1 deficiency in neurodegeneration in PD, and they should include astrocytic, neuronal and co-culture models for metabolic investigations. In addition, there are no studies that investigate the TCA cycle flux in DJ-1-deficient PD cellular or animal models, and the use of experimental tools such as metabolic flux analysis will also shed more light on metabolic effects of DJ-1. Lastly, there is a lack of studies using PD-patient derived cellular models for metabolic studies in the context of DJ-1 deficiency. All of these new tools, when applied to DJ-1 biology, will further clarify the role of DJ-1 in cellular metabolism and their implications in PD pathogenesis.

References

1. Ariga, H. Common mechanisms of onset of cancer and neurodegenerative diseases. *Biol. Pharm. Bull.* **2015**, *38*, 795–808. [CrossRef]
2. Bonifati, V.; Rizzu, P.; Squitieri, F.; Krieger, E.; Vanacore, N.; van Swieten, J.C.; Brice, A.; van Duijn, C.M.; Oostra, B.; Meco, G.; et al. DJ-1 (PARK7), a novel gene for autosomal recessive, early onset parkinsonism. *Neurol. Sci.* **2003**, *24*, 159–160. [CrossRef]
3. Bandopadhyay, R.; Kingsbury, A.E.; Cookson, M.R.; Reid, A.R.; Evans, I.M.; Hope, A.D.; Pittman, A.M.; Lashley, T.; Canet-Aviles, R.; Miller, D.W.; et al. The expression of DJ-1 (PARK7) in normal human CNS and idiopathic Parkinson's disease. *Brain* **2004**, *127*, 420–430. [CrossRef]
4. Rizzu, P.; Hinkle, D.A.; Zhukareva, V.; Bonifati, V.; Severijnen, L.A.; Martinez, D.; Ravid, R.; Kamphorst, W.; Eberwine, J.H.; Lee, V.M.Y.; et al. DJ-1 Colocalizes with Tau Inclusions: A Link between Parkinsonism and Dementia. *Ann. Neurol.* **2004**, *55*, 113–118. [CrossRef]
5. Bader, V.; Zhu, X.R.; Lübbert, H.; Stichel, C.C. Expression of DJ-1 in the adult mouse CNS. *Brain Res.* **2005**, *1041*, 102–111. [CrossRef] [PubMed]
6. Smith, N.; Wilson, M.A. Structural biology of the DJ-1 superfamily. *Adv. Exp. Med. Biol.* **2017**, *1037*, 5–24.
7. Wilson, M.A.; Collins, J.L.; Hod, Y.; Ringe, D.; Petsko, G.A. The 1.1-Å Resolution Crystal Structure of DJ-1, the Protein Mutated in Autosomal Recessive Early Onset Parkinson's Disease. 2003. Available online: www.rcsb.org (accessed on 24 December 2020).
8. Wilson, M.A. The role of cysteine oxidation in DJ-1 function and dysfunction. *Antioxidants Redox Signal.* **2011**, *15*, 111–122. [CrossRef] [PubMed]
9. Canet-Avilés, R.M.; Wilson, M.A.; Miller, D.W.; Ahmad, R.; McLendon, C.; Bandyopadhyay, S.; Baptista, M.J.; Ringe, D.; Petsko, G.A.; Cookson, M.R. The Parkinson's disease DJ-1 is neuroprotective due to cysteine-sulfinic acid-driven mitochondrial localization. *Proc. Natl. Acad. Sci. USA* **2004**, *101*, 9103–9108. [CrossRef]
10. Oh, S.E.; Mouradian, M.M. Regulation of Signal Transduction by DJ-1. In *DJ-1/PARK7 Protein*; Advances in Experimental Medicine and Biology; Springer: Singapore, 2017; Volume 1037, pp. 97–131. ISBN 9789811065835.
11. Waak, J.; Weber, S.S.; Waldenmaier, A.; Görner, K.; Alunni-Fabbroni, M.; Schell, H.; Vogt-Weisenhorn, D.; Pham, T.T.; Reumers, V.; Baekelandt, V.; et al. Regulation of astrocyte inflammatory responses by the Parkinson's disease-associated gene DJ-1. *FASEB J.* **2009**, *23*, 2478–2489. [CrossRef]
12. Shendelman, S.; Jonason, A.; Martinat, C.; Leete, T.; Abeliovich, A. DJ-1 Is a redox-dependent molecular chaperone that inhibits α-synuclein aggregate formation. *PLoS Biol.* **2004**, *2*, e362. [CrossRef] [PubMed]
13. Lee, J.Y.; Song, J.; Kwon, K.; Jang, S.; Kim, C.; Baek, K.; Kim, J.; Park, C. Human DJ-1 and its homologs are novel glyoxalases. *Hum. Mol. Genet.* **2012**, *21*, 3215–3225. [CrossRef] [PubMed]
14. Jun, Y.W.; Kool, E.T. Small Substrate or Large? Debate Over the Mechanism of Glycation Adduct Repair by DJ-1. *Cell Chem. Biol.* **2020**, *27*, 1117–1123. [CrossRef] [PubMed]
15. Anandhan, A.; Jacome, M.S.; Lei, S.; Hernandez-Franco, P.; Pappa, A.; Panayiotidis, M.I.; Powers, R.; Franco, R. Metabolic Dysfunction in Parkinson's Disease: Bioenergetics, Redox Homeostasis and Central Carbon Metabolism. *Brain Res. Bull.* **2017**, *133*, 12–30. [CrossRef] [PubMed]
16. Powers, R.; Lei, S.; Anandhan, A.; Marshall, D.D.; Worley, B.; Cerny, R.L.; Dodds, E.D.; Huang, Y.; Panayiotidis, M.I.; Pappa, A.; et al. Metabolic investigations of the molecular mechanisms associated with Parkinson's disease. *Metabolites* **2017**, *7*, 22. [CrossRef]
17. Schapira, A.H.V.; Cooper, J.M.; Dexter, D.; Clark, J.B.; Jenner, P.; Marsden, C.D. Mitochondrial Complex I Deficiency in Parkinson's Disease. *J. Neurochem.* **1990**, *54*, 823–827. [CrossRef]
18. Mencke, P.; Hanss, Z.; Boussaad, I.; Sugier, P.E.; Elbaz, A.; Krüger, R. Bidirectional Relation Between Parkinson's Disease and Glioblastoma Multiforme. *Front. Neurol.* **2020**, *11*, 1–14. [CrossRef]
19. Jain, D.; Jain, R.; Eberhard, D.; Eglinger, J.; Bugliani, M.; Piemonti, L.; Marchetti, P.; Lammert, E. Age-and diet-dependent requirement of DJ-1 for glucose homeostasis in mice with implications for human type 2 diabetes. *J. Mol. Cell Biol.* **2012**, *4*, 221–230. [CrossRef] [PubMed]

20. Eberhard, D.; Lammert, E. The role of the antioxidant protein DJ-1 in type 2 diabetes mellitus. *Adv. Exp. Med. Biol.* **2017**, *1037*, 173–186. [PubMed]

21. Zhang, L.; Wang, J.; Wang, J.; Yang, B.; He, Q.; Weng, Q. Role of DJ-1 in Immune and Inflammatory Diseases. *Front. Immunol.* **2020**, *11*, 1–10. [CrossRef]

22. Lev, N.; Roncevich, D.; Ickowicz, D.; Melamed, E.; Offen, D. Role of DJ-1 in Parkinson ' s Disease. *Mol. Neurosci.* **2006**, *29*, 215–225. [CrossRef]

23. Mhyre, T.R.; Nw, R.; Boyd, J.T.; Hall, G.; Room, C. Parkinson's Disease. In *Protein Aggregation and Fibrillogenesis in Cerebral and Systemic Amyloid Disease*; Springer: Dordrecht, The Netherlands, 2012; Volume 65, ISBN 978-94-007-5415-7.

24. Tysnes, O.B.; Storstein, A. Epidemiology of Parkinson's disease. *J. Neural Transm.* **2017**, *124*, 901–905. [CrossRef]

25. Bereczki, D. The description of all four cardinal signs of Parkinson's disease in a Hungarian medical text published in 1690. *Park. Relat. Disord.* **2010**, *16*, 290–293. [CrossRef]

26. Inamdar, N.; Arulmozhi, D.; Tandon, A.; Bodhankar, S. Parkinsons Disease: Genetics and Beyond. *Curr. Neuropharmacol.* **2007**, *5*, 99–113. [CrossRef]

27. Olzmann, J.A.; Brown, K.; Wilkinson, K.D.; Rees, H.D.; Huai, Q.; Ke, H.; Levey, A.I.; Li, L.; Chin, L.S. Familial Parkinson's Disease-associated L166P Mutation Disrupts DJ-1 Protein Folding and Function. *J. Biol. Chem.* **2004**, *279*, 8506–8515. [CrossRef]

28. Honbou, K.; Suzuki, N.N.; Horiuchi, M.; Niki, T.; Taira, T.; Ariga, H.; Inagaki, F. The crystal structure of DJ-1, a protein related to male fertility and Parkinson's disease. *J. Biol. Chem.* **2003**, *278*, 31380–31384. [CrossRef] [PubMed]

29. Tao, X.; Tong, L. Crystal structure of human DJ-1, a protein associated with early onset Parkinson's disease. *J. Biol. Chem.* **2003**, *278*, 31372–31379. [CrossRef] [PubMed]

30. Moore, D.J.; Zhang, L.; Dawson, T.M.; Dawson, V.L. A missense mutation (L166P) in DJ-1, linked to familial Parkinson's disease, confers reduced protein stability and impairs homo-oligomerization. *J. Neurochem.* **2003**, *87*, 1558–1567. [CrossRef]

31. Repici, M.; Straatman, K.R.; Balduccio, N.; Enguita, F.J.; Outeiro, T.F.; Giorgini, F. Parkinson's disease-associated mutations in DJ-1 modulate its dimerization in living cells. *J. Mol. Med.* **2013**, *91*, 599–611. [CrossRef] [PubMed]

32. Milkovic, N.M.; Catazaro, J.; Lin, J.; Halouska, S.; Kizziah, J.L.; Basiaga, S.; Cerny, R.L.; Powers, R.; Wilson, M.A. Transient sampling of aggregation-prone conformations causes pathogenic instability of a parkinsonian mutant of DJ-1 at physiological temperature. *Protein Sci.* **2015**, *24*, 1671–1685. [CrossRef] [PubMed]

33. Boussaad, I.; Obermaier, C.D.; Hanss, Z.; Bobbili, D.R.; Bolognin, S.; Glaab, E.; Wolynska, K.; Weisschuh, N.; De Conti, L.; May, C.; et al. A patient-based model of RNA mis-splicing uncovers treatment targets in Parkinson's disease. *Sci. Transl. Med.* **2020**, 1–12.

34. Hauser, D.N.; Primiani, C.T.; Cookson, M.R. The Effects of Variants in the Parkin, PINK1, and DJ-1 Genes along with Evidence for their Pathogenicity. *Curr. Protein Pept. Sci.* **2016**, *18*, 702–714. [CrossRef] [PubMed]

35. Bonifati, V.; Rizzu, P.; Van Baren, M.J.; Schaap, O.; Breedveld, G.J.; Krieger, E.; Dekker, M.C.J.; Squitieri, F.; Ibanez, P.; Joosse, M.; et al. Mutations in the DJ-1 gene associated with autosomal recessive early-onset parkinsonism. *Science* **2003**, *299*, 256–259. [CrossRef] [PubMed]

36. Annesi, G.; Savettieri, G.; Pugliese, P.; D'Amelio, M.; Tarantino, P.; Ragonese, P.; La Bella, V.; Piccoli, T.; Civitelli, D.; Annesi, F.; et al. DJ-1 mutations and parkinsonism-dementia-amyotrophic lateral sclerosis complex. *Ann. Neurol.* **2005**, *58*, 803–807. [CrossRef] [PubMed]

37. Wang, X.; Petrie, T.G.; Liu, Y.; Liu, J.; Fujioka, H.; Zhu, X. Parkinson's disease-associated DJ-1 mutations impair mitochondrial dynamics and cause mitochondrial dysfunction. *J. Neurochem.* **2012**, *121*, 830–839. [CrossRef]

38. Richarme, G.; Liu, C.; Mihoub, M.; Abdallah, J.; Leger, T.; Joly, N.; Liebart, J.C.; Jurkunas, U.V.; Nadal, M.; Bouloc, P.; et al. Guanine glycation repair by DJ-1/ Park7 and its bacterial homologs. *Science* **2017**, *357*, 208–211. [CrossRef]

39. Richarme, G.; Mihoub, M.; Dairou, J.; Chi Bui, L.; Leger, T.; Lamouri, A. Parkinsonism-associated protein DJ-1/park7 is a major protein deglycase that repairs methylglyoxal- and glyoxal-glycated cysteine, arginine, and lysine residues. *J. Biol. Chem.* **2015**, *290*, 1885–1897. [CrossRef]

40. Matsuda, N.; Kimura, M.; Queliconi, B.B.; Kojima, W.; Mishima, M.; Takagi, K.; Koyano, F.; Yamano, K.; Mizushima, T.; Ito, Y.; et al. Parkinson's disease-related DJ-1 functions in thiol quality control against aldehyde attack in vitro. *Sci. Rep.* **2017**, *7*, 1–15. [CrossRef]

41. Irrcher, I.; Aleyasin, H.; Seifert, E.L.; Hewitt, S.J.; Chhabra, S.; Phillips, M.; Lutz, A.K.; Rousseaux, M.W.C.; Bevilacqua, L.; Jahani-Asl, A.; et al. Loss of the Parkinson's disease-linked gene DJ-1 perturbs mitochondrial dynamics. *Hum. Mol. Genet.* **2010**, *19*, 3734–3746. [CrossRef] [PubMed]

42. Krebiehl, G.; Ruckerbauer, S.; Burbulla, L.F.; Kieper, N.; Maurer, B.; Waak, J.; Wolburg, H.; Gizatullina, Z.; Gellerich, F.N.; Woitalla, D.; et al. Reduced basal autophagy and impaired mitochondrial dynamics due to loss of Parkinson's disease-associated protein DJ-1. *PLoS ONE* **2010**, *5*, e9367. [CrossRef] [PubMed]

43. Thomas, K.J.; McCoy, M.K.; Blackinton, J.; Beilina, A.; van der Brug, M.; Sandebring, A.; Miller, D.; Maric, D.; Cedazo-Minguez, A.; Cookson, M.R. DJ-1 acts in parallel to the PINK1/parkin pathway to control mitochondrial function and autophagy. *Hum. Mol. Genet.* **2011**, *20*, 40–50. [CrossRef] [PubMed]

44. Lin, T.-Y.; Cantley, L.C.; DeNicola, G.M. NRF2 Rewires Cellular Metabolism to Support the Antioxidant Response. *Master Regul. Oxidative Stress Transcr. Factor Nrf2* **2016**, 1–28.

45. Giaime, E.; Yamaguchi, H.; Gautier, C.A.; Kitada, T.; Shen, J. Loss of DJ-1 does not affect mitochondrial respiration but increases ROS production and mitochondrial permeability transition pore opening. *PLoS ONE* **2012**, *7*, e40501. [CrossRef] [PubMed]

46. Park, J.S.; Davis, R.L.; Sue, C.M. Mitochondrial Dysfunction in Parkinson's Disease: New Mechanistic Insights and Therapeutic Perspectives. *Curr. Neurol. Neurosci. Rep.* **2018**, *18*, 1–11. [CrossRef] [PubMed]

47. Meulener, M.; Whitworth, A.J.; Armstrong-Gold, C.E.; Rizzu, P.; Heutink, P.; Wes, P.D.; Pallanck, L.J.; Bonini, N.M. Drosophila DJ-1 mutants are selectively sensitive to environmental toxins associated with Parkinson's disease. *Curr. Biol.* **2005**, *15*, 1572–1577. [CrossRef]

48. Dolgacheva, L.P.; Berezhnov, A.V.; Fedotova, E.I.; Zinchenko, V.P.; Abramov, A.Y. Role of DJ-1 in the mechanism of pathogenesis of Parkinson's disease. *J. Bioenerg. Biomembr.* **2019**, *51*, 175–188. [CrossRef]

49. Gan, L.; Johnson, D.A.; Johnson, J.A. Keap1-Nrf2 activation in the presence and absence of DJ-1. *Eur. J. Neurosci.* **2010**, *31*, 967–977. [CrossRef]

50. Zhou, J.; Liu, H.; Zhang, L.; Liu, X.; Zhang, C.; Wang, Y.; He, Q.; Zhang, Y.; Li, Y.; Chen, Q.; et al. DJ-1 promotes colorectal cancer progression through activating PLAGL2/Wnt/BMP4 axis. *Cell Death Dis.* **2018**, *9*, 1–12. [CrossRef]

51. De Lazzari, F.; Bisaglia, M. DJ-1 as a deglycating enzyme: A unique function to explain a multifaceted protein? *Neural Regen. Res.* **2017**, *12*, 1797–1798.

52. Santiago, J.A.; Potashkin, J.A. Shared dysregulated pathways lead to Parkinson's disease and diabetes. *Trends Mol. Med.* **2013**, *19*, 176–186. [CrossRef]

53. Cao, J.; Lou, S.; Ying, M.; Yang, B. DJ-1 as a human oncogene and potential therapeutic target. *Biochem. Pharmacol.* **2015**, *93*, 241–250. [CrossRef]

54. Hinkle, D.A.; Mullett, S.J.; Gabris, B.E.; Hamilton, R.L. DJ-1 expression in glioblastomas shows positive correlation with p53 expression and negative correlation with epidermal growth factor receptor amplification. *Neuropathology* **2011**, *31*, 29–37. [CrossRef]

55. Skoneczna, A.; Miciałkiewicz, A.; Skoneczny, M. Saccharomyces cerevisiae Hsp31p, a stress response protein conferring protection against reactive oxygen species. *Free Radic. Biol. Med.* **2007**, *42*, 1409–1420. [CrossRef]

56. Tsai, C.J.; Aslam, K.; Drendel, H.M.; Asiago, J.M.; Goode, K.M.; Paul, L.N.; Rochet, J.C.; Hazbun, T.R. Hsp31 is a stress response chaperone that intervenes in the protein misfolding process. *J. Biol. Chem.* **2015**, *290*, 24816–24834. [CrossRef]

57. Guerrero, E.; Vasudevaraju, P.; Hegde, M.L.; Britton, G.B.; Rao, K.S. Recent advances in α-synuclein functions, advanced glycation, and toxicity: Implications for Parkinson's disease. *Mol. Neurobiol.* **2013**, *47*, 525–536. [CrossRef] [PubMed]

58. Spillantini, M.G.; Schmidt, M.L.; Lee, V.M.Y.; Trojanowski, J.Q.; Jakes, R.; Goedert, M. α-synuclein in Lewy bodies. *Nature* **1997**, *388*, 839–840. [CrossRef]

59. Zondler, L.; Miller-Fleming, L.; Repici, M.; Gonçalves, S.; Tenreiro, S.; Rosado-Ramos, R.; Betzer, C.; Straatman, K.R.; Jensen, P.H.; Giorgini, F.; et al. DJ-1 interactions with α-synuclein attenuate aggregation and cellular toxicity in models of Parkinson's disease. *Cit. Cell Death Dis.* **2014**, *5*, e1350. [CrossRef]

60. Burbulla, L.F.; Song, P.; Mazzulli, J.R.; Zampese, E.; Wong, Y.C.; Jeon, S.; Santos, D.P.; Blanz, J.; Obermaier, C.D.; Strojny, C.; et al. Dopamine oxidation mediates mitochondrial and lysosomal dysfunction in Parkinson's disease. *Science* **2017**, *357*, 1255–1261. [CrossRef] [PubMed]

61. Kumar, R.; Kumar, S.; Hanpude, P.; Singh, A.K.; Johari, T.; Majumder, S.; Maiti, T.K. Partially oxidized DJ-1 inhibits α-synuclein nucleation and remodels mature α-synuclein fibrils in vitro. *Commun. Biol.* **2019**, *2*, 1–14. [CrossRef] [PubMed]

62. Taipa, R.; Pereira, C.; Reis, I.; Alonso, I.; Bastos-Lima, A.; Melo-Pires, M.; Magalhães, M. DJ-1 linked parkinsonism (PARK7) is associated with Lewy body pathology. *Brain* **2016**, *139*, 1680–1687. [CrossRef] [PubMed]

63. Solti, K.; Kuan, W.L.; Fórizs, B.; Kustos, G.; Mihály, J.; Varga, Z.; Herberth, B.; Moravcsik, É.; Kiss, R.; Kárpáti, M.; et al. DJ-1 can form β-sheet structured aggregates that co-localize with pathological amyloid deposits. *Neurobiol. Dis.* **2020**, *134*, 104629. [CrossRef]

64. Maillard, L.C.; Maillard, L.C.; Maillard, L.; Maillard, L. Action des acides aminés sur les sucres: Formation des mélanoïdines par voie méthodique. *C. R. Acad. Sci. (Paris)* **1912**, *154*, 66–68.

65. Chaudhuri, J.; Bains, Y.; Guha, S.; Kahn, A.; Hall, D.; Bose, N.; Gugliucci, A.; Kapahi, P. The Role of Advanced Glycation End Products in Aging and Metabolic Diseases: Bridging Association and Causality. *Cell Metab.* **2018**, *28*, 337–352. [CrossRef] [PubMed]

66. Thornalley, P.J. Protein and nucleotide damage by glyoxal and methylglyoxal in physiological systems—Role in ageing and disease. *Drug Metab. Drug Interact.* **2009**, *23*, 1–19. [CrossRef] [PubMed]

67. Thornalley, P.J. The glyoxalase system: New developments towards functional characterization of a metabolic pathway fundamental to biological life. *Biochem. J.* **1990**, *269*, 1–11. [CrossRef]

68. Misra, K.; Banerjee, A.B.; Ray, S.; Raytt, M. Glyoxalase III from Escherichia coli: A single novel enzyme for the conversion of methylglyoxal into D-lactate without reduced glutathione. *Biochem. J.* **2000**, *1003*, 999–1003. [CrossRef]

69. Subedi, K.P.; Choi, D.; Kim, I.; Min, B.; Park, C. Hsp31 of Escherichia coli K-12 is glyoxalase III. *Mol. Microbiol.* **2011**, *81*, 926–936. [CrossRef]

70. Bankapalli, K.; Saladi, S.D.; Awadia, S.S.; Goswami, A.V.; Samaddar, M.; D'Silva, P. Robust Glyoxalase activity of Hsp31, a ThiJ/DJ-1/PfpI Family Member Protein, Is Critical for Oxidative Stress Resistance in Saccharomyces cerevisiae. *J. Biol. Chem.* **2015**, *290*, 26491–26507. [CrossRef]

71. Zhao, Q.; Su, Y.; Wang, Z.; Chen, C.; Wu, T.; Huang, Y. Identification of glutathione (GSH)-independent glyoxalase III from Schizosaccharomyces pombe. *BMC Evol. Biol.* **2014**, *14*, 1–18. [CrossRef]

72. Hasim, S.; Hussin, N.A.; Alomar, F.; Bidasee, K.R.; Nickerson, K.W.; Wilson, M.A. A glutathione-independent glyoxalase of the DJ-1 superfamily plays an important role in managing metabolically generated methylglyoxal in candida albicans. *J. Biol. Chem.* **2014**, *289*, 1662–1674. [CrossRef]

73. Hao, L.Y.; Giasson, B.I.; Bonini, N.M. DJ-1 is critical for mitochondrial function and rescues PINK1 loss of function. *Proc. Natl. Acad. Sci. USA* **2010**, *107*, 9747–9752. [CrossRef] [PubMed]

74. Narendra, D.; Tanaka, A.; Suen, D.F.; Youle, R.J. Parkin is recruited selectively to impaired mitochondria and promotes their autophagy. *J. Cell Biol.* **2008**, *183*, 795–803. [CrossRef]

75. Narendra, D.P.; Jin, S.M.; Tanaka, A.; Suen, D.F.; Gautier, C.A.; Shen, J.; Cookson, M.R.; Youle, R.J. PINK1 is selectively stabilized on impaired mitochondria to activate Parkin. *PLoS Biol.* **2010**, *8*, e1000298. [CrossRef]

76. Yang, Y.; Gehrke, S.; Imai, Y.; Huang, Z.; Ouyang, Y.; Wang, J.W.; Yang, L.; Beal, M.F.; Vogel, H.; Lu, B. Mitochondrial pathology and muscle and dopaminergic neuron degeneration caused by inactivation of Drosophila Pink1 is rescued by Parkin. *Proc. Natl. Acad. Sci. USA* **2006**, *103*, 10793–10798. [CrossRef] [PubMed]

77. Ottolini, D.; Calì, T.; Negro, A.; Brini, M. The Parkinson disease-related protein DJ-1 counteracts mitochondrial impairment induced by the tumour suppressor protein p53 by enhancing endoplasmic reticulum-mitochondria tethering. *Hum. Mol. Genet.* **2013**, *22*, 2152–2168. [CrossRef] [PubMed]

78. McCoy, M.K.; Cookson, M.R. DJ-1 regulation of mitochondrial function and autophagy through oxidative stress. *Autophagy* **2011**, *7*, 531–532. [CrossRef]

79. Liu, Y.; Ma, X.; Fujioka, H.; Liu, J.; Chen, S.; Zhu, X. DJ-1 regulates the integrity and function of ER-mitochondria association through interaction with IP3R3-Grp75-VDAC1. *Proc. Natl. Acad. Sci. USA* **2019**, *116*, 25322–25328. [CrossRef]

80. Paik, J.Y.; Jung, K.H.; Lee, J.H.; Park, J.W.; Lee, K.H. Reactive oxygen species-driven HIF1α triggers accelerated glycolysis in endothelial cells exposed to low oxygen tension. *Nucl. Med. Biol.* **2017**, *45*, 8–14. [CrossRef] [PubMed]

81. Forrester, S.J.; Kikuchi, D.S.; Hernandes, M.S.; Xu, Q.; Griendling, K.K. Reactive Oxygen Species in Metabolic and Inflammatory Signaling. *Circ. Res.* **2018**, *122*, 877–902. [CrossRef]

82. Parsanejad, M.; Zhang, Y.; Qu, D.; Irrcher, I.; Rousseaux, M.W.C.; Aleyasin, H.; Kamkar, F.; Callaghan, S.; Slack, R.S.; Mak, T.W.; et al. Regulation of the VHL/HIF-1 pathway by DJ-1. *J. Neurosci.* **2014**, *34*, 8043–8050. [CrossRef] [PubMed]

83. Ariga, H.; Takahashi-Niki, K.; Kato, I.; Maita, H.; Niki, T.; Iguchi-Ariga, S.M.M. Neuroprotective function of dj-1 in Parkinson's disease. *Oxid. Med. Cell. Longev.* **2013**, *2013*, 683920. [CrossRef] [PubMed]

84. Saito, Y. Oxidized DJ1 as a possible biomarker of Parkinson's disease. *J. Clin. Biochem. Nutr.* **2013**, *54*, 31–38.

85. Junn, E.; Jang, W.H.; Zhao, X.; Jeong, B.S.; Mouradian, M.M. Mitochondrial localization of DJ-1 leads to enhanced neuroprotection. *J. Neurosci. Res.* **2009**, *87*, 123–129. [CrossRef]

86. Piston, D.; Alvarez-Erviti, L.; Bansal, V.; Gargano, D.; Yao, Z.; Szabadkai, G.; Odell, M.; Rhyan Puno, M.; Björkblom, B.; Maple-Grødem, J.; et al. Corrigendum: DJ-1 is a redox sensitive adapter protein for high molecular weight complexes involved in regulation of catecholamine homeostasis. *Hum. Mol. Genet.* **2017**, *26*, 4028–4041. [CrossRef]

87. Piston, D.; Gegg, M.E. The role of DJ-1 complexes and catecholamine metabolism: Relevance for familial and idiopathic Parkinson's disease. *Neural Regen. Res.* **2018**, *13*, 815–816.

88. Meiser, J.; Delcambre, S.; Wegner, A.; Jäger, C.; Ghelfi, J.; d'Herouel, A.F.; Dong, X.; Weindl, D.; Stautner, C.; Nonnenmacher, Y.; et al. Loss of DJ-impairs antioxidant response by altered glutamine and serine metabolism. *Neurobiol. Dis.* **2016**, *89*, 112–125. [CrossRef] [PubMed]

89. Yang, J.; Kim, K.S.; Iyirhiaro, G.O.; Marcogliese, P.C.; Callaghan, S.M.; Qu, D.; Kim, W.J.; Slack, R.S.; Park, D.S. DJ-1 modulates the unfolded protein response and cell death via upregulation of ATF4 following ER stress. *Cell Death Dis.* **2019**, *10*, 1–17. [CrossRef] [PubMed]

90. Selvarajah, B.; Azuelos, I.; Platé, M.; Guillotin, D.; Forty, E.J.; Contento, G.; Woodcock, H.V.; Redding, M.; Taylor, A.; Brunori, G.; et al. MTORC1 amplifies the ATF4-dependent de novo serine-glycine pathway to supply glycine during TGF-1-induced collagen biosynthesis. *Sci. Signal.* **2019**, *12*, eaav3048. [CrossRef]

91. Zhou, W.; Freed, C.R. DJ-1 up-regulates glutathione synthesis during oxidative stress and inhibits A53T α-synuclein toxicity. *J. Biol. Chem.* **2005**, *280*, 43150–43158. [CrossRef]

92. Saeed, U.; Ray, A.; Valli, R.K.; Kumar, A.M.R.; Ravindranath, V. DJ-1 Loss by glutaredoxin but not glutathione depletion triggers daxx translocation and cell death. *Antioxidants Redox Signal.* **2010**, *13*, 127–144. [CrossRef]

93. Lopert, P.; Patel, M. Brain mitochondria from DJ-1 knockout mice show increased respiration-dependent hydrogen peroxide consumption. *Redox Biol.* **2014**, *2*, 667–672. [CrossRef]

94. Ozawa, K.; Tsumoto, H.; Miura, Y.; Yamaguchi, J.; Iguchi-Ariga, S.M.M.; Sakuma, T.; Yamamoto, T.; Uchiyama, Y. DJ-1 is indispensable for the S-nitrosylation of Parkin, which maintains function of mitochondria. *Sci. Rep.* **2020**, *10*, 1–11. [CrossRef]

95. Danileviciute, E.; Zeng, N.; Capelle, C.; Paczia, N.; Kurniawan, H.; Gillespie, M.A.; Coowar, D.; Maria, D.; Weisenhorn, V.; Grusdat, M.; et al. PARK7/DJ-1 promotes pyruvate dehydrogenase activity and maintains Treg homeostasis. *bioRxiv* **2019**, 4–6. [CrossRef]

96. Malty, R.H.; Aoki, H.; Kumar, A.; Phanse, S.; Amin, S.; Zhang, Q.; Minic, Z.; Goebels, F.; Musso, G.; Wu, Z.; et al. A Map of Human Mitochondrial Protein Interactions Linked to Neurodegeneration Reveals New Mechanisms of Redox Homeostasis and NF-κB Signaling. *Cell Syst.* **2017**, *5*, 564–577. [CrossRef] [PubMed]

97. Zhang, L.; Shimoji, M.; Thomas, B.; Moore, D.J.; Yu, S.W.; Marupudi, N.I.; Torp, R.; Torgner, I.A.; Ottersen, O.P.; Dawson, T.M.; et al. Mitochondrial localization of the Parkinson's disease related protein DJ-1: Implications for pathogenesis. *Hum. Mol. Genet.* **2005**, *14*, 2063–2073. [CrossRef] [PubMed]

98. Calì, T.; Ottolini, D.; Soriano, M.E.; Brini, M. A new split-GFP-based probe reveals DJ-1 translocation into the mitochondrial matrix to sustain ATP synthesis upon nutrient deprivation. *Hum. Mol. Genet.* **2015**, *24*, 1045–1060. [CrossRef]

99. Chen, R.; Park, H.A.; Mnatsakanyan, N.; Niu, Y.; Licznerski, P.; Wu, J.; Miranda, P.; Graham, M.; Tang, J.; Boon, A.J.W.; et al. Parkinson's disease protein DJ-1 regulates ATP synthase protein components to increase neuronal process outgrowth. *Cell Death Dis.* **2019**, *10*, 1–12. [CrossRef] [PubMed]

100. Guzman, J.N.; Sanchez-Padilla, J.; Wokosin, D.; Kondapalli, J.; Ilijic, E.; Schumacker, P.T.; Surmeier, D.J. Oxidant stress evoked by pacemaking in dopaminergic neurons is attenuated by DJ-1. *Nature* **2010**, *468*, 696–700. [CrossRef]

101. Weinert, M.; Millet, A.; Jonas, E.A.; Alavian, K.N. The mitochondrial metabolic function of DJ-1 is modulated by 14-3-3b. *FASEB J.* **2019**, *33*, 8925–8934. [CrossRef]

102. Kim, J.W.; Tchernyshyov, I.; Semenza, G.L.; Dang, C.V. HIF-1-mediated expression of pyruvate dehydrogenase kinase: A metabolic switch required for cellular adaptation to hypoxia. *Cell Metab.* **2006**, *3*, 177–185. [CrossRef]

103. Berry, E.M.; Growdon, J.H.; Wurtman, J.J.; Caballero, B.; Wurtman, R.J. A balanced carbohydrate: Protein diet in the management of Parkinson's disease. *Neurology* **1991**, *41*, 1295. [CrossRef]

104. VanItallie, T.B.; Nonas, C.; Di Rocco, A.; Boyar, K.; Hyams, K.; Heymsfield, S.B. Treatment of Parkinson disease with diet-induced hyperketonemia: A feasibility study. *Neurology* **2005**, *64*, 728–730. [CrossRef] [PubMed]

105. Zhang, P.; Tian, B. Metabolic syndrome: An important risk factor for Parkinson's disease. *Oxid. Med. Cell. Longev.* **2014**, *2014*, 729194. [CrossRef]

106. Allaman, I.; Bélanger, M.; Magistretti, P.J. Methylglyoxal, the dark side of glycolysis. *Front. Neurosci.* **2015**, *9*, 1–12. [CrossRef] [PubMed]

107. Richarme, G.; Abdallah, J.; Mathas, N.; Gautier, V.; Dairou, J. Further characterization of the Maillard deglycase DJ-1 and its prokaryotic homologs, deglycase 1/Hsp31, deglycase 2/YhbO, and deglycase 3/YajL. *Biochem. Biophys. Res. Commun.* **2018**, *503*, 703–709. [CrossRef]

108. Pfaff, D.H.; Fleming, T.; Nawroth, P.; Teleman, A.A. Evidence Against a Role for the Parkinsonism-associated Protein DJ-1 in Methylglyoxal Detoxification. *J. Biol. Chem.* **2017**, *292*, 685–690. [CrossRef]

109. Andreeva, A.; Bekkhozhin, Z.; Omertassova, N.; Baizhumanov, T.; Yeltay, G.; Akhmetali, M.; Toibazar, D.; Utepbergenov, D. The apparent deglycase activity of DJ-1 results from the conversion of free methylglyoxal present in fast equilibrium with hemithioacetals and hemiaminals. *J. Biol. Chem.* **2019**, *294*, 18863–18872. [CrossRef] [PubMed]

110. Sharma, A.; Weber, D.; Raupbach, J.; Dakal, T.C.; Fließbach, K.; Ramirez, A.; Grune, T.; Wüllner, U. Advanced glycation end products and protein carbonyl levels in plasma reveal sex-specific differences in Parkinson's and Alzheimer's disease. *Redox Biol.* **2020**, *34*, 101546. [CrossRef]

111. Zheng, X.; Boyer, L.; Jin, M.; Mertens, J.; Kim, Y.; Ma, L.; Ma, L.; Hamm, M.; Gage, F.H.; Hunter, T. Metabolic reprogramming during neuronal differentiation from aerobic glycolysis to neuronal oxidative phosphorylation. *Elife* **2016**, *5*, 1–25. [CrossRef] [PubMed]

112. Kieburtz, K.; Tilley, B.C.; Elm, J.J.; Babcock, D.; Hauser, R.; Ross, G.W.; Augustine, A.H.; Augustine, E.U.; Aminoff, M.J.; Bodis-Wollner, I.G.; et al. Effect of creatine monohydrate on clinical progression in patients with parkinson disease: A randomized clinical trial. *JAMA J. Am. Med. Assoc.* **2015**, *313*, 584–593. [CrossRef] [PubMed]

113. Nickels, S.L.; Walter, J.; Bolognin, S.; Gérard, D.; Jaeger, C.; Qing, X.; Tisserand, J.; Jarazo, J.; Hemmer, K.; Harms, A.; et al. Impaired serine metabolism complements LRRK2-G2019S pathogenicity in PD patients. *Park. Relat. Disord.* **2019**, *67*, 48–55. [CrossRef]

114. Nuzzo, T.; Punzo, D.; Devoto, P.; Rosini, E.; Paciotti, S.; Sacchi, S.; Li, Q.; Thiolat, M.L.; Véga, C.; Carella, M.; et al. The levels of the NMDA receptor co-agonist D-serine are reduced in the substantia nigra of MPTP-lesioned macaques and in the cerebrospinal fluid of Parkinson's disease patients. *Sci. Rep.* **2019**, *9*, 1–15. [CrossRef]

115. Gelfin, E.; Kaufman, Y.; Korn-Lubetzki, I.; Bloch, B.; Kremer, I.; Javitt, D.C.; Heresco-Levy, U. D-serine adjuvant treatment alleviates behavioural and motor symptoms in Parkinson's disease. *Int. J. Neuropsychopharmacol.* **2012**, *15*, 543–549. [CrossRef] [PubMed]

116. Esteras, N.; Dinkova-Kostova, A.T.; Abramov, A.Y. Nrf2 activation in the treatment of neurodegenerative diseases: A focus on its role in mitochondrial bioenergetics and function. *Biol. Chem.* **2016**, *397*, 383–400. [CrossRef] [PubMed]

117. Mailloux, R.J.; Jin, X.; Willmore, W.G. Redox regulation of mitochondrial function with emphasis on cysteine oxidation reactions. *Redox Biol.* **2014**, *2*, 123–139. [CrossRef]

118. Prasad, R.K.; Ismail-Beigi, F. Mechanism of stimulation of glucose transport by H2O2: Role of phospholipase C. *Arch. Biochem. Biophys.* **1999**, *362*, 113–122. [CrossRef]

119. Liemburg-Apers, D.C.; Willems, P.H.G.M.; Koopman, W.J.H.; Grefte, S. Interactions between mitochondrial reactive oxygen species and cellular glucose metabolism. *Arch. Toxicol.* **2015**, *89*, 1209–1226. [CrossRef] [PubMed]

120. Ascherio, A.; LeWitt, P.A.; Xu, K.; Eberly, S.; Watts, A.; Matson, W.R.; Marras, C.; Kieburtz, K.; Rudolph, A.; Bogdanov, M.B.; et al. Urate as a predictor of the rate of clinical decline in Parkinson disease. *Arch. Neurol.* **2009**, *66*, 1460–1468. [CrossRef] [PubMed]

121. Schwarzschild, M.A.; Schwid, S.R.; Marek, K.; Watts, A.; Lang, A.E.; Oakes, D.; Shoulson, I.; Ascherio, A.; Hyson, C.; Gorbold, E.; et al. Serum urate as a predictor of clinical and radiographic progression in Parkinson disease. *Arch. Neurol.* **2008**, *65*, 716–723. [CrossRef] [PubMed]

122. Shoulsen, I.; Fann, S.; Oakes, D.; Kieburtz, K. Effects-of-Tocopherol-and-Deprenyl-on-the-Progression-of-Disabil-1993. *N. Engl. J. Med.* **1993**, *328*, 176–183.

123. Shoulson, I.; Oakes, D.; Fahn, S.; Lang, A.; William Langston, J.; LeWitt, P.; Warren Olanow, C.; Penney, J.B.; Tanner, C.; Kieburtz, K.; et al. Impact of sustained deprenyl (selegiline) in levodopa-treated Parkinson's disease: A randomized placebo-controlled extension of the Deprenyl and Tocopherol Antioxidative Therapy of Parkinsonism trial. *Ann. Neurol.* **2002**, *51*, 604–612. [CrossRef]

124. Snow, B.J.; Rolfe, F.L.; Lockhart, M.M.; Frampton, C.M.; O'Sullivan, J.D.; Fung, V.; Smith, R.A.J.; Murphy, M.P.; Taylor, K.M. A double-blind, placebo-controlled study to assess the mitochondria- targeted antioxidant MitoQ as a disease-modifying therapy in Parkinson's disease. *Mov. Disord.* **2010**, *25*, 1670–1674. [CrossRef] [PubMed]

125. Flint Beal, M.; Oakes, D.; Shoulson, I.; Henchcliffe, C.; Galpern, W.R.; Haas, R.; Juncos, J.L.; Nutt, J.G.; Voss, T.S.; Ravina, B.; et al. A randomized clinical trial of high-dosage coenzyme Q10 in early parkinson disease no evidence of benefit. *JAMA Neurol.* **2014**, *75*, 543–552.

Motivation and Aims

Cancer and neurodegeneration show two disease mechanisms that lie on the opposite ends of a spectrum; one is characterized by increased cell proliferation and the other due to premature cell death. In the last years, there has been increasing evidence that links these two processes. Epidemiologic studies have shown that people with a neurodegenerative disorder have a reduced incidence for many different cancer types, but an increased risk for other cancers[9].

It was shown by several epidemiological studies that there is an inverse correlation for gene expression of disease linked proteins in PD and cancer genes that are down regulated in PD can be up regulated in cancer and vice versa[1,11]. So far, the association of PD and cancer was mainly focusing on the most common cancer types like lung, colorectal or prostate cancer Despite that, PD associated genes (e.g. *PARK2*, *PARK7*) can also be involved in rather rare cancer types like Glioblastoma. In fact, high expression of PD associated genes plays an important role in tumor proliferation and migration of glioma cells due to their influence on cell cycle and apoptosis[6].

This is why we studied inverse modulatory effects of DJ-1 downregulation in GBM cells and DJ-1 upregulation in PD cells to investigate the role of this protein in both diseases and further shed light on the effect of differential levels of DJ-1 in PD and GBM. Parallels and differences in phenotypes like altered energy metabolism in PD-patient-derived astrocytes and GBM cells were assessed to identify underlying molecular mechanisms that are inversely correlated.

The aims for the study include:

- Generation and characterization of PD patient-derived iPSC
- Generation of isogenic control
- Generation of iPSC-derived astrocytes
- Phenotyping of PD patient-derived astrocytes
- Generation of DJ-1 overexpression astrocytes and DJ-1 knockdown in GBM cell lines
- Phenotypic comparison of DJ-1 overexpression astrocytes and DJ-1 knockdown in GBM cells

Manuscript III

Generation and characterization of a genetic Parkinson's disease-patient-derived iPSC line DJ-1-delP (LCSBi008-A)

Mencke et al. 2022

Status:

Published in Stem Cell Research 26.04.2022

Preface

Since 2006, the discovery of the generation of induced pluripotent stem cells by Yamanaka and Takahashi has significantly contributed to the improvement of modeling human diseases *in vitro* and has helped to accelerate drug discovery and development[12]. Here, we describe the generation and characterization of a human induced pluripotent stem cell line-derived from fibroblasts of a PD patient with a DJ-1 mutation.

I contributed to the following manuscript by conducting the stem cell culture, immunocytochemistry stainings, PCRs and Western Blots. Co-authors provided the fibroblasts for the generation of the stem cells and helped with reprogramming. I generated all figures and wrote the paper, which was reviewed by all co-authors prior to submission.

	Contents lists available at ScienceDirect
	Stem Cell Research
	journal homepage: www.elsevier.com/locate/scr
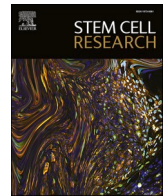
Lab Resource: Single Cell Line

Generation and characterization of a genetic Parkinson's disease-patient derived iPSC line DJ-1-delP (LCSBi008-A)

Pauline Mencke [a], Ibrahim Boussaad [a], Gizem Önal [d], Anneke J.A. Kievit [e], Agnita J.W. Boon [f], Wim Mandemakers [e], Vincenzo Bonifati [e], Rejko Krüger [a,b,c,*]

[a] Translational Neuroscience, Luxembourg Centre for Systems Biomedicine (LCSB), University of Luxembourg, Luxembourg
[b] Parkinson Research Clinic, Centre Hospitalier de Luxembourg (CHL), Luxembourg
[c] Transversal Translational Medicine, Luxembourg Institute of Health (LIH), Luxembourg
[d] Department of Physiology, Anatomy and Genetics, University of Oxford, Parks Road, Oxford OX1 3QX, United Kingdom
[e] Erasmus MC, University Medical Center Rotterdam, Dept. Clinical Genetics, Rotterdam the Netherlands
[f] Erasmus MC, University Medical Center Rotterdam, Dept. Neurology, Rotterdam the Netherlands

A B S T R A C T

Here, we describe an induced pluripotent stem cell (iPSC) line that was derived from fibroblasts obtained from a monogenic Parkinson's disease (PD) patient. The disease was caused by a c.634-636delGCC mutation in the *PARK7* gene leading to p.158P deletion in the protein DJ-1. iPSCs were generated via electroporation using three episomal plasmids encoding human *Oct3/4, Sox2, Klf4, Lin28, L-Myc* combined with a short hairpin RNA for p53. The presence of the c.471_473delGCC mutation in exon 7 of *PARK7* was confirmed by Sanger sequencing. The iPSCs express pluripotency markers, are capable of *in vitro* differentiation into the three germ layers and obtain karyotypic integrity.

1. Resource table

Unique stem cell line identifier	LCSBi008-A
Alternative name(s) of stem cell line	DJ-1-delP delP
Institution	Luxembourg Centre for Systems Biomedicine (LCSB)
Contact information of distributor	Dr. Wim Mandemakers, w.mandemakers@erasmusmc.nl
Type of cell line	Induced pluripotent stem cell line (iPSC)
Origin	Human
Additional origin info	Age: 66 Sex: male Ethnicity: Caucasian
Cell Source	fibroblasts
Clonality	Clonal
Method of reprogramming	electroporation using three episomal plasmids encoding human Oct3/4 (pCXLE-hOCT3/4 (Addgene #27076)), Sox2 and Klf4 (pCXLE-hSK ((Addgene #27078)), Lin28, L-Myc (pCXLE-hUL (Addgene #27080)) combined with a short hairpin RNA for p53
Genetic Modification	Yes
Type of Modification	Autosomal recessive mutation
Associated disease	Parkinson's disease
Gene/locus	*PARK7*
Method of modification	N/A

(continued on next column)

(continued)

Name of transgene or resistance	N/A
Inducible/constitutive system	N/A
Date archived/stock date	03. Sep. 2018
Cell line repository/bank	https://hpscreg.eu/cell-line/LCSBi008-A
Ethical approval	Medical Ethical Committee, Erasmus MC Rotterdam, The Netherlands; MEC-2012-001/NL38860.078.11 The cell line can be obtained by third parties using appropriate MTA

2. Resource utility

Parkinson s disease (PD) is the second most common neurodegenerative disease affecting 1–2% of the population that is over 60 years old with its main symptoms being tremor, rigidity and bradykinesia (Tysnes and Storstein, 2017). Most PD cases are sporadic, however, mutations in PD-associated genes (*PARK* genes) can lead to genetic PD (Klein and Westenberger, 2012). The p.158Pdel mutation in the *PARK7* gene encoding the protein DJ-1 leads to autosomal recessively inherited early onset PD (Ramsey and Giasson, 2010). By generating PD-patient iPSC-derived neuronal cell models, the iPSC line will be used to investigate

---

* Corresponding author.
E-mail address: rejko.krueger@uni.lu (R. Krüger).

Table 1
Characterization and validation.

Classification	Test	Result	Data
Morphology	Photography	Normal staining/ expression of pluripotency markers: Oct3/4, Nanog, Sox2	Fig. 1 panel A
Phenotype	Qualitative analysis: Immunocytochemistry		Fig. 1 panel D
	Quantitative analysis: RT-qPCR	Transcripts for antigen & cell surface markers	Fig. 1 panel C
Genotype	Karyotype (G-banding) and resolution	46XY, Resolution 450–500	Fig. 1 panel B
Identity	Array-based karyotyping	performed	File available with author
Mutation analysis (IF APPLICABLE)	Sequencing	homozygous c.634-636delGCC	File available with author
			Fig. 1 panel F
	Southern Blot OR WGS	N/A	N/A
Microbiology and virology	Mycoplasma	Mycoplasma testing by luminescence Negative	Supplementary Fig. 1 B
Differentiation potential	Directed differentiation	Proof of three germ layer formation	Fig. 1 panel E
Donor screening (OPTIONAL)	HIV 1 + 2, Hepatitis B, Hepatitis C	negative	Supplementary file 1
Genotype additional info (OPTIONAL)	Blood group genotyping	N/A	N/A
	HLA tissue typing	N/A	N/A

underlying pathological mechanisms of genetic PD that are caused by the loss of DJ-1 protein due to the p.158Pdel mutation.

3. Resource details

Dermal fibroblasts from a male PD patient (age at biopsy, 66 years) harbouring an autosomal recessive homozygous c.471_473delGCC mutation in *PARK7* were obtained. To generate the presented iPSC line, fibroblasts were reprogrammed by electroporation using three episomal plasmids encoding human *Oct3/4, Sox2, Klf4, Lin28, L-Myc* combined with a short hairpin RNA for p53. The cell line was called DJ-1-delP (see Table 1). We obtained three iPSC clones of the line (data shown only for clone 1) showing the typical morphology of iPSC colonies (Fig. 1 A). The cell line shows a structurally and numerically normal karyotype (46, XY) (Fig. 1 B). qPCR results for fibroblasts, control iPSC GM23338 (Larsen et al. 2020) and DJ-1-delP iPSC in triplicates confirmed that the cells also express Nanog, Oct3/4 and DMNT3B mRNA (Fig. 1 C). The DJ-1-delP iPSC express the stemness marker proteins Sox2, Oct3/4 and Nanog, as validated by immunocytochemistry (Fig. 1 D). DJ-1-delP iPSC are capable of differentiating into the three germ layers mesoderm, ectoderm and endoderm (Fig. 1 E), as shown by *in vitro* differentiation follwed by immunofluorescence staining for the germ layer marker Brachyury and Pax3 (mesoderm), Otx2 and Sox1 (ectoderm) and Sox17 and FOXA2 (endoderm) (Fig. 1 E). PCR followed by agarose gel electrophoresis confirmed that the episomal plasmids disappeared at passage 19 (supplementary Fig. 1A).

The c.471_473delGCC mutation in the *PARK7* gene leading to the deletion of proline 158 of the encoded DJ-1 protein was confirmed by Sanger sequencing in the fibroblasts and the iPSC (Fig. 1 F). The mutation results in stable DJ-1 mRNA (Fig. 1 G), but protein instability of the DJ-1 homodimer leading to a severe loss of DJ-1 protein (Fig. 1 H) (Ramsey and Giasson, 2010).

4. Materials and methods

Fibroblasts derived from the skin biopsy were cultured in Dulbecco's Modified Eagle Medium (DMEM) supplemented with 10% fetal bovine serum (FBS), 2 mM L-glutamine and 1% penicillin and streptomycin (Pen/Strep). The fibroblasts were reprogrammed into iPSC via electroporation using three episomal plasmids encoding human Oct3/4 (pCXLE-hOCT3/4 (Addgene #27076)), Sox2 and Klf4 (pCXLE-hSK ((Addgene #27078)), Lin28, L-Myc (pCXLE-hUL (Addgene #27080)) combined with a short hairpin RNA for p53. Once colonies had formed, these colonies were picked and plated on a Matrigel™ (Corning)-coated plate. Freshly prepared E8 medium (DMEM F-12 + HEPES, Life Technologies; 1% Pen/Strep, Life Technologies; 1% Insulin-Transferrin-Selenium, Life Technologies; 2 µg/L TGFβ1, Peprotech; 10 µg/L FGF2, Peprotech; 64 mg/L ascorbic acid 2 PM, Sigma-Aldrich; 100 ng/mL Heparin, Sigma-Aldrich; 10% mTesR, StemCell Technologies) was changed each day. The iPSCs were then passaged using EDTA (Life Technologies) once a week at a 1:5 ratio. Fibroblasts and iPSC were cultured at 37 °C under 5% CO2.

5. Mutation analysis

Genomic DNA was purified from fibroblasts passage 9 and iPSC passage 19 using the QIA Blood and Tissue kit (Qiagen). Using the primers listed in Table 2, the exon 7 of the *PARK7* gene was amplified with KOD Hot Start DNA Polymerase (Merck; Annealing temperature 54.8 °C, 40 cycles) on a TProfessional Basic Gradient Thermocycler (Biometra). Sanger sequencing was performed at Eurofins Genomics Germany GmbH.

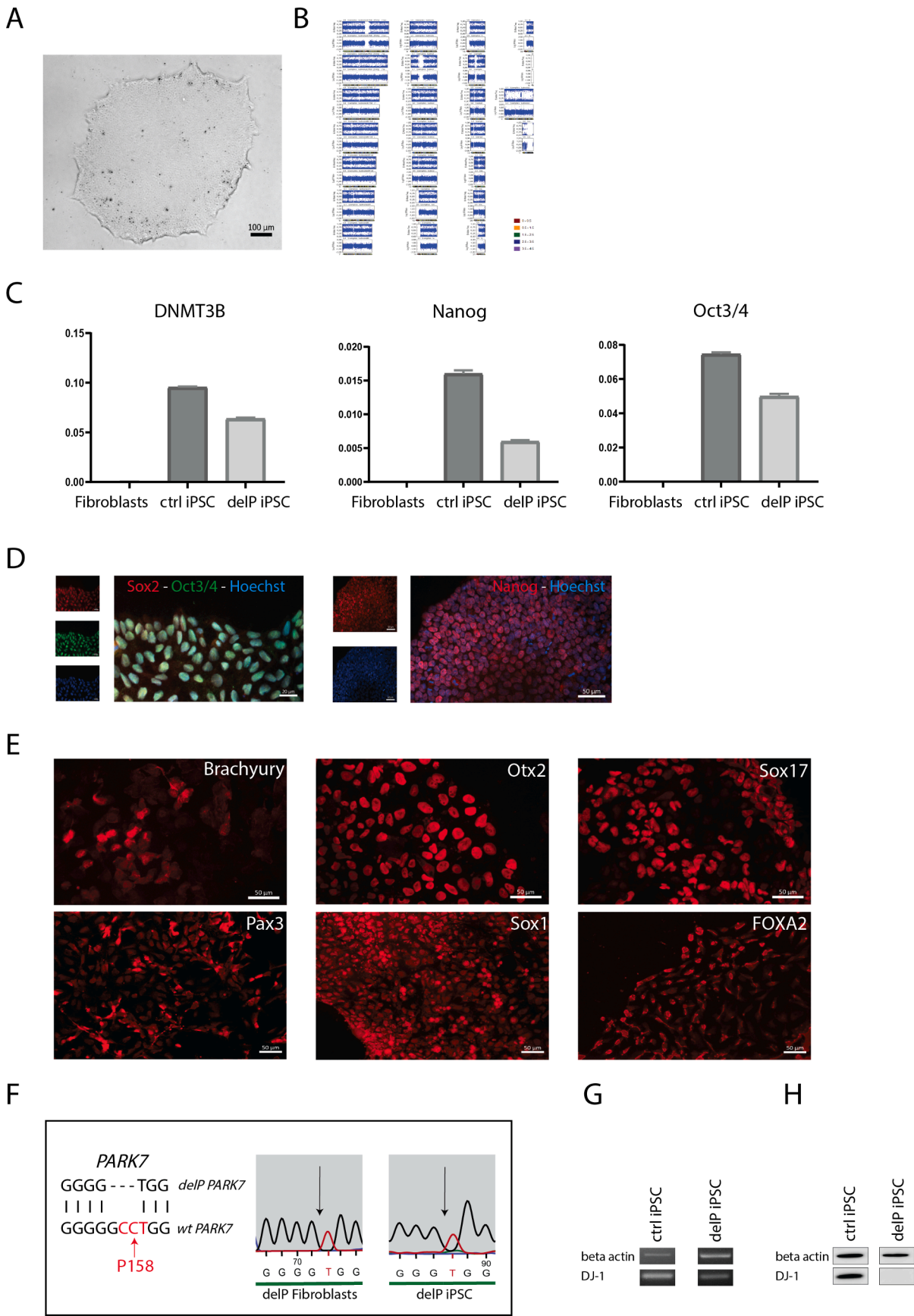### 6. RNA and protein status analysis by PCR and Western blotting

RNA and protein levels of *PARK7*/DJ-1 were evaluated by PCR and Western blotting at passage 12 using the primers and antibodies listed in Table 2 following standard protocols.

7. RT-qPCR

Total RNA was extracted from DJ-1-delP fibroblasts passage 16, control iPSC passage 24 and DJ-1-delP iPSCs passage 9 using the RNeasy Mini Kit (Qiagen). Transcriptor High Fidelity cDNA Synthesis Kit (Roche) was used to synthesize cDNA. Quantification of pluripotency markers by multiplex qPCR was performed using the LightCycler® 480 Probes Master kit (Roche) and hydrolysis probes detecting NANOG-FAM (Hs02387400_g1, Thermo Fisher Scientific), OCT4-FAM (Hs00999632_g1, Thermo Fisher Scientific) and DNMT3B (Hs00171876_m1, Thermo Fisher Scientific). ACTB (Hs03023880_g1, Thermo Fisher Scientific) was used as a housekeeping gene. cDNA from DJ-1-delP fibroblasts was used as a negative control.

8. Immunofluorescence staining

Expression of stemness markers was analysed via immunocytochemistry. iPSCs were plated on Matrigel-coated coverslips and were fixed at passage 26 with 4% paraformaldehyde in PBS for 15 min. Cells were permeabilized and blocked for 1 h in PBS supplemented with 0.4% Triton-X 100 (Carl Roth), 10% goat serum (Vector Labs) and 2% bovine serum albumin (Sigma-Aldrich). Primary antibodies (Table 2) in antibody buffer (0.1% Triton-X, 1% goat serum and 0.2% bovine serum albumin in PBS) were added for overnight incubation at 4 °C. Cells were washed three times with PBS, incubated for 2 h at room temperature with secondary antibodies in antibody buffer. Nuclei were stained with Hoechst. Images were acquired using a Zeiss spinning disk confocal microscope (Carl Zeiss Microimaging GmbH).

P. Mencke et al.

A

B

C

DNMT3B

Nanog

Oct3/4

D

Sox2 - Oct3/4 - Hoechst

Nanog - Hoechst

E

Brachyury

Otx2

Sox17

Pax3

Sox1

FOXA2

F

PARK7

GGGG - - - TGG   *delP PARK7*
| | | | | | |
GGGGGCCTGG   *wt PARK7*

P158

delP Fibroblasts   delP iPSC

G

ctrl iPSC   delP iPSC

beta actin
DJ-1

H

ctrl iPSC   delP iPSC

beta actin
DJ-1

(caption on next page)

3

Fig. 1. A: Brightfield image of DJ-1-delP iPSC colony. iPSC show the typical iPSC morphology. B: The karyotype of DJ-1-delP iPSC has no abnormalities. C: Gene expression analysis of pluripotency markers by qPCR shows the expression of DNMT3B, Nanog and Oct3/4 in control and DJ-1-delP iPSC and no expression of the markers in control fibroblasts. D: Expression of stemness markers by immunocytochemistry. DJ-1-delP iPSCs express the stemness marker Sox2, Oct3/4 and Nanog. E: DJ-1-delP iPSCs are able to differentiate into the three germ layers, as assessed by three germ layer differentiation and subsequent immunocytochemistry analysis of the markers for Brachyury and Pax3 (mesoderm), Otx2 and Sox1 (ectoderm) and Sox17 and FOXA2 (endoderm). F: The c.471_473delGCC mutation in the PARK7 gene leading to the deletion of proline 158 of the encoded DJ-1 protein was confirmed by Sanger sequencing in the DJ-1-delP fibroblasts and iPSC. G: DJ-1-delP iPSC have normal DJ-1 mRNA levels, as assessed by RT-PCR. H: The mutation in the DJ-1-delP iPSC leads to loss of DJ-1 protein, as seen by Western blotting.

9. In vitro differentiation

The ability of the iPSC to differentiate into the three germ layers was tested at passage 18 using the manufacturer's differentiation protocol of the Human Pluripotent Stem Cell Functional Identification Kit (R&D Systems). Expression of the mesodermal markers Brachyury and Pax3, the ectodermal markers Otx2 and Sox1 and the endodermal markers Sox17 and FOXA2 was confirmed after differentiation by immunocytochemistry. Images were acquired using a Zeiss spinning disk confocal microscope (Carl Zeiss Microimaging GmBH).

10. Karyotyping and identity analysis

Molecular karyotyping and identity analysis of fibroblasts passage 9 and iPSC passage 6 was performed at Life&Brain GmbH (Bonn) using the HumanOmni2.5 Exome-8 DNA Analysis BeadChip. This method does not detect translocations or inversions, alterations in chromosome structure, mosaicism or polyploidy.

11. Mycoplasma test

iPSCs were tested for Mycoplasma contamination at passage 9 by

Table 2
Reagents details.

Antibodies used for immunocytochemistry/flow-cytometry			
	Antibody	Dilution	Company Cat # and RRID
Pluripotency Markers	Goat anti SOX2 (Y-17)	1:250	Santa Cruz, Cat #: sc-17320; RRID: AB_2286684
Pluripotency Markers	Mouse anti Oct3/4	1:1000	Santa Cruz, Cat #: sc-5279; RRID: AB_628051
Pluripotency Markers	Rabbit anti Nanog	1:1000	Abcam, Cat #: ab21624; RRID: AB_446437
Pluripotency Markers	Mouse anti Pax3	1:1000	DSHB AB_528426
Pluripotency Markers	Goat anti Sox1	1:1000	R & D Systems, Cat #: AF3369, RRID: AB_2239879
Pluripotency Markers	Mouse anti FOXA2	1:1000	Santa Cruz, Cat #: sc-101060, RRID: AB_1124660
DJ-1	Rabbit anti DJ-1 (D29E5)XP	1:1500	cell signaling, Cat #: 5933; RRID: AB_11179085
β-Actin	mouse anti β-Actin (8H10D10)	1:20.000	cell signaling, Cat #: 3700S; RRID: AB_2242334
Secondary antibody	Alexa Fluor 488 Goat anti Mouse IgG (H + L)	1:1000	Invitrogen, Cat #: A11029; RRID: AB_138404
Secondary antibody	Alexa Fluor 568 Goat anti Mouse IgG (H + L)	1:1000	Invitrogen, Cat #: A-11031, RRID: AB_144696
Secondary antibody	Alexa Fluor 568 Goat anti Rabbit IgG (H + L)	1:1000	Invitrogen, Cat #: A11036; RRID: AB_143011
Secondary antibody	Alexa Fluor 568 Donkey anti Goat IgG (H + L)	1:1000	Invitrogen, Cat #: A-11057, RRID: AB_142581
Secondary antibody	Alexa Fluor 647 Donkey anti Goat IgG (H + L)	1:1000	Invitrogen, Cat #: A-21447, RRID: AB_2535864
Secondary antibody	Goat anti Rabbit IgG (H + L) Secondary Antibody, HRP, 0.5 mg GTXRB IgG F AB'2 HRP X ADS	1:5000	Invitrogen, Cat #: A24537; RRID AB_2536005
Secondary antibody	Goat anti Mouse IgG (H + L) Secondary Antibody, HRP 0.5 mg GTXMU IgG F AB'2 HRP X ADS	1:10.000	Invitrogen, Cat #: A24524; RRID AB_2535993

Primers		
	Target	Forward/Reverse primer (5′-3′)
Targeted mutation analysis	*PARK7* gene, exon 7 1815 bp	CTGAAGGAGCAAGGAACTGGA GGAATGCTGGGTGCTATTACCT
Sequencing	*PARK7* gene, exon 7, locus of DJ-1 mutation in DJ-1-delP line 213 bp	GCCCATTAGGATGTCACCTTT GCAGTTCGCTGCTCTAGTCTT
RNA status	*PARK7*, whole transcript 595 bp Beta actin 140 bp	atatatggccATGGCTTCCAAAAGAGC ccccccagatctCTAGTCTTTAAGAACAAG CTGGAACGGTGAAGGTGACA AAGGGACTTCCTGTAACAATGCA
Plasmid specific primers (PCR)	*OriP*	TCGGGGGTGTTAGAGACAAC TTCCACGAGGGTAGTGAACC
Plasmid specific primers (PCR)	*EBNA1*	ATCGTCAAAGCTGCACACAG CCCAGGAGTCCCAGTAGTCA

using a colorimetric mycoplasma detection kit (PlasmoTest™, Invivogen).

Declaration of Competing Interest

The authors declare that they have no known competing financial interests or personal relationships that could have appeared to influence the work reported in this paper.

Appendix A. Supplementary data

Supplementary data to this article can be found online at https://doi.org/10.1016/j.scr.2022.102792.

References

Klein, C., Westenberger, A., 2012. Genetics of Parkinson's disease. Cold Spring Harb. Perspect. Med. 663–697 https://doi.org/10.1016/B978-044452809-4/50169-1.

Larsen, S.B., et al., 2020. Induced pluripotent stem cell line (LCSBi001-A) derived from a patient with Parkinson's disease carrying the p. D620N mutation in VPS35. Stem Cell Res. 45, 101776.

Ramsey, C.P., Giasson, B.I., 2010. L10p and P158DEL DJ-1 mutations cause protein instability, aggregation, and dimerization impairments. J. Neurosci. Res. 88, 3111–3124. https://doi.org/10.1002/jnr.22477.

Tysnes, O.B., Storstein, A., 2017. Epidemiology of Parkinson's disease. J. Neural Transm. 124, 901–905. https://doi.org/10.1007/s00702-017-1686-y.

Manuscript IV

Generation of isogenic control DJ-1-delP GC13 for the genetic Parkinson's disease-patient-derived iPSC line DJ-1-delP (LCSBi008-A-1)

Mencke et al. 2022

Status:

Published in Stem Cell Research 17.05.2022

Preface

As mentioned above, the generation of stem cell-derived models has revolutionized ways how to investigate monogenic, complex and epigenetic diseases and has improved drug discovery approaches[13]. However, it is important to include good controls for patient-derived stem cell models. Before gene editing tools were available, age and gender matched controls were used to study disease phenotypes of patient-derived stem cells. However, these controls are not ideal as the genetic background is different from the patient, so the solely effect of a disease associated mutation on the cellular phenotype cannot be assessed. In 2012, Emmanuelle Charpentier and Jennifer Doudna published the components of the Clustered Regularly Interspaced Short Palindromic Repeats (CRISPR) – Cas 9 system and showed that the system could be used to cut specific sites in genomic DNA[14]. The advent of this technology allowed for the correction of for example disease causing mutations in patient-derived stem cells, thereby generating so called isogenic controls, which are essential for cellular phenotyping. In 2019, Jarazo and colleagues published a protocol for gene editing of stem cells to generate isogenic controls[15]. Using this protocol, I generated an isogenic control for the previously mentioned DelP line.

I contributed to the following manuscript by performing the CRISPR Cas 9 gene editing. I obtained advice during the gene editing process from Dr. Hanss and Dr. Jarazo.
Dr. Glaab generated the 3D protein structure model. Characterization of successfully edited stem cells was performed with help of co-authors.
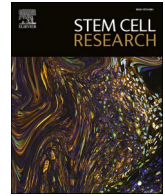
Lab Resource: Genetically-Modified Single Cell Line

Generation of isogenic control DJ-1-delP GC13 for the genetic Parkinson's disease-patient derived iPSC line DJ-1-delP (LCSBi008-A-1)

Pauline Mencke [a], Zoé Hanss [a], Javier Jarazo [b], François Massart [a], Arkadiusz Rybicki [a], Elizabet Petkovski [c], Enrico Glaab [d], Ibrahim Boussaad [a], Vincenzo Bonifati [e], Jens Christian Schwamborn [b], Wim Mandemakers [e], Rejko Krüger [a,f,g,*]

[a] Translational Neuroscience, Luxembourg Centre for Systems Biomedicine, University of Luxembourg, Luxembourg
[b] Developmental & Cellular Biology Group, Luxembourg Centre for Systems Biomedicine, University of Luxembourg, Luxembourg
[c] Forensic Genetics, Dept. Legal Medicine, Laboratoire national de santé, Luxembourg
[d] Biomedical Data Science Group, Luxembourg Centre for Systems Biomedicine, University of Luxembourg, Luxembourg
[e] Erasmus MC, University Medical Center Rotterdam, Dept. Clinical Genetics, Rotterdam The Netherlands
[f] Parkinson Research Clinic, Centre Hospitalier de Luxembourg (CHL), Luxembourg
[g] Transversal Translational Medicine, Luxembourg Institute of Health (LIH), Luxembourg

A B S T R A C T

We describe the generation of an isogenic control cell line DJ-1-delP GC13 from an induced pluripotent stem cell (iPSC) line DJ-1-delP LCSBi008-A that was derived from fibroblasts obtained from a Parkinson's disease (PD) patient. Using CRISPR/Cas9 technology, we corrected the disease causing c.471_473delGCC homozygous mutation in the *PARK7* gene leading to p.158P deletion in the encoded protein DJ-1. The generated isogenic pair will be used for phenotypic analysis of PD-patient derived neurons and astrocytes.

1. Resource table

Unique stem cell line identifier	LCSBi001-A-1
Alternative name(s) of stem cell line	DJ-1-delP GC13 delP GC13
Institution	Luxembourg Centre for Systems Biomedicine (LCSB)
Contact information of the reported cell line distributor	Dr. Wim Mandemakers, w. mandemakers@erasmusmc.nl
Type of cell line	Induced pluripotent stem cell line (iPSC)
Origin	Human
Additional origin info (applicable for human ESC or iPSC)	Age at biopsy, 66 years Sex: male Ethnicity: Caucasian
Cell Source	fibroblasts
Method of reprogramming	electroporation using three episomal plasmids Oct3/4 (pCXLE-hOCT3/4 (Addgene #27076)), *Sox2* and *Klf4* (pCXLE-hSK ((Addgene #27078)), Lin28, L-Myc combined with a short hairpin RNA for p53
Clonality	Clonal

(continued on next column)

(continued)

Unique stem cell line identifier	LCSBi001-A-1
Evidence of the reprogramming transgene loss (including genomic copy if applicable)	RT-/q-PCR, ICC, western blotting, etc. If piggyBac: evidence of excision/lack of insertion, PCR
Cell culture system used	Cells were grown on Geltrex or Matrigel
Type of Genetic Modification	Correction of mutation
Associated disease	Parkinson's disease
Gene/locus	*PARK7*
Method of modification/site-specific nuclease used	CRISPR/Cas9
Site-specific nuclease (SSN) delivery method	Plasmid transfection
All genetic material introduced into the cells	HDR donor vector
Analysis of the nuclease-targeted allele status	Sequencing of the targeted allele
Method of the off-target nuclease activity surveillance	*in silico* tool IDT CRISPR-Cas9 guide RNA design checker was used to identify off-targets, double-stranded breaks that may occur in the genome
Name of transgene	N/A puromycin

(continued on next page)

---

* Corresponding author.
  E-mail address: rejko.krueger@uni.lu (R. Krüger).

(*continued*)

Unique stem cell line identifier	LCSBi001-A-1
Eukaryotic selective agent resistance (including inducible/ gene expressing cell-specific)	
Inducible/constitutive system details	N/A
Date archived/stock date	22.09.2020
Cell line repository/bank	IBBL Luxembourg https://hpscreg.eu/us er/cellline/edit/LCSBi008-A-1
Ethical/GMO work approvals	Medical Ethical Committee, Erasmus MC Rotterdam, The Netherlands; MEC-2012-001/NL38860.078.11
Addgene/public access repository recombinant DNA sources' disclaimers (if applicable)	HDR donor plasmid was synthesized by GeneArt®, sequence is available as suppl. File pX330 plasmid sequence available as suppl. file

2. Resource utility

The p.158Pdel mutation in the *PARK7* gene encoding the protein DJ-1 leads to autosomal recessive early onset PD. By generating an isogenic control for the PD-patient derived iPSC line DJ-1-delP (Mencke et al., 2022), the obtained isogenic pair of DJ-1-delP and DJ-1-delP GC13 will be used to investigate underlying pathological mechanisms of genetic PD that are caused by the loss of DJ-1 protein due to the p.158Pdel mutation (Mencke et al., 2022).

3. Resource details

To generate the presented iPSC line, iPSC of the parental patient line DJ-1-delP (Mencke et al., 2022) were used. Using an established protocol for CRISPR/Cas9 fluorescent guided biallelic HDR targeting selection with PiggyBac system removal for gene editing (Jarazo et al., 2019), the mutation was homozygously corrected.

The generated isogenic control line shows the typical morphology of iPSC colonies (Fig. 1A). The cell line has a structurally and numerically normal karyotype (46, XY) after correction of the mutation (Fig. 1B). qPCR results for fibroblasts, control iPSC GM23338 (Larsen et al., 2020), DJ-1-delP and the newly generated DJ-1-delP GC13 iPSC in triplicates confirmed that the isogenic line express *Nanog*, Oct3/4 (*POU5F1*) and *DMNT3B* mRNA in the same range as the parental line (Fig. 1C). The DJ-1-delP GC13 iPSC express the stemness marker *Sox2*, Oct3/4 and *Nanog*, as validated by immunocytochemistry (Fig. 1D). DJ-1-delP GC13 iPSC are capable of differentiating into the 3 germ layers mesoderm, endoderm and ectoderm (Fig. 1E), as shown by immunofluorescence staining for the germ layer marker Brachyury (mesoderm), *Otx2* (endoderm) and *Sox17* (ectoderm) (Fig. 1E).

The c.471_473delGCC mutation in the exon 7 of the *PARK7* gene leading to the deletion of proline 158 of the encoded DJ-1 protein (Fig. 1F) is expected to impair homodimerization of the DJ-1 monomers as the proline residues lie in the contact site of the two monomers (Fig. 1G).

The mutation does not affect the mRNA level of DJ-1 (Fig. 1I), but leads to loss of DJ-1 protein due to protein instability followed by degradation (Fig. 1J) (Ramsey and Giasson, 2010). The successful gene correction was confirmed by Sanger sequencing (Fig. 1H) and rescues the levels of DJ-1 protein (Fig. 1J) (Table 1).

4. Materials and methods

iPSC were cultured in freshly prepared E8 medium (DMEM F-12 + HEPES, Life Technologies; 1% Pen/Strep, Life Technologies; 1% Insulin-Transferrin-Selenium, Life Technologies; 2 µg/L TGFβ1, Peprotech; 10 µg/L FGF2, Peprotech; 64 mg/L ascorbic acid 2 PM, Sigma-Aldrich; 100 ng/mL Heparin, Sigma-Aldrich; 10% mTesR, StemCell Technologies). The medium was changed each day. The iPSC were passaged using EDTA (Life Technologies) once a week at a 1:5 ratio. iPSC were cultured at 37 °C under 5% CO2.

5. Gene editing

To correct the mutation, we followed the steps described in the protocol for CRISPR/Cas9 fluorescent guided biallelic HDR targeting selection with PiggyBac system removal for gene editing (Jarazo et al., 2019). The donor plasmid (homology arms spanning the EGFP and the puromycin resistance) was synthesized by GeneArt®. The gRNA was designed using the broadinstitute gRNA design tool (sequence see Table 2, predicted off-targets see suppl. file 1). Nucleofection of the donor plasmid and the Cas9 plasmid was performed in DJ-1-delP iPSC at passage 18 using the Amaxa™ P3 Primary Cell 4D-Nucleofector™ X Kit L (24 RCT) and the Lonza Nucleofector™ (H9 program). Screening of the EGFP + colonies was performed using a Yokogawa CellVoyager CV7000 microscope. Green colonies were picked and analysed for random events and successful integration of EGFP (suppl. Fig. 1A and B, primers in Table 2). Non random EGFP integrated colonies were expanded and sorted to obtain 100% EGFP + cells with BD FASC Aria II, and sent for sequencing using primers spanning the region of the mutation (suppl. Fig. 1C, primers in Table 2). DJ-1-delP clone 13 showed the correction of the mutation (suppl. Fig. 1C, primers in Table 2). After the excision of the EGFP, cells were analysed for absence of integration of the donor plasmid and pX330 and sent for sequencing again (suppl. Fig. 1D + E, primers in Table 2).

6. Mutation analysis

Genomic DNA was purified from fibroblasts and iPSC using the QIA Blood and Tissue kit (Qiagen). Using the primers listed in Table 2, the exon 7 of the *PARK7* gene was amplified by PCR and Sanger sequenced at Eurofins Genomics Germany GmbBH.
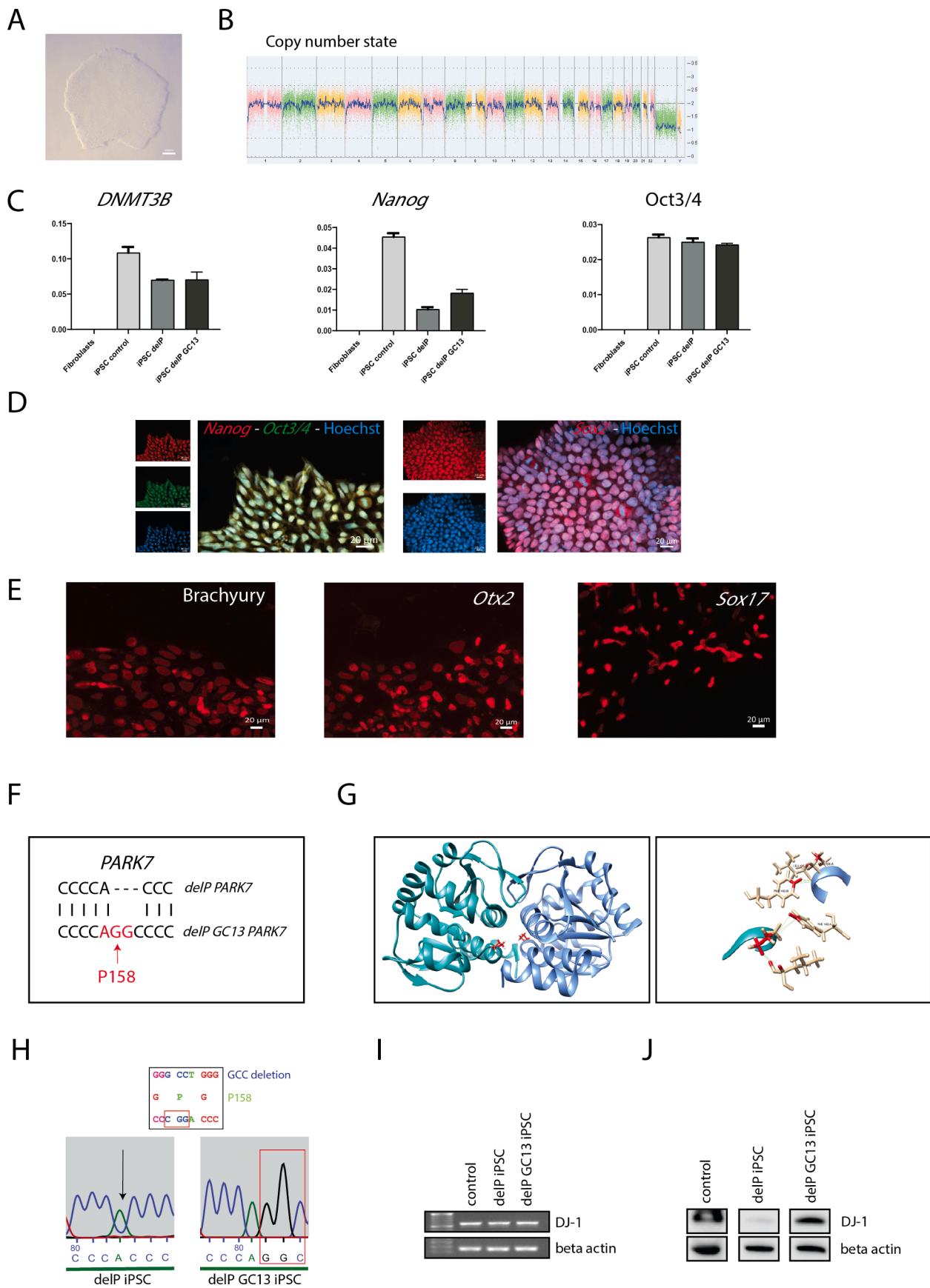
6.1. RT-qPCR

Total RNA was extracted from native fibroblasts passage 16, control iPSC passage 24, DJ-1-delP iPSC passage 9 and DJ-1-delP GC13 iPSC passage 40 using the RNeasy Mini Kit (Qiagen). Transcriptor High Fidelity cDNA Synthesis Kit (Roche) was used to synthesize cDNA. Quantification of pluripotency markers by multiplex qPCR was performed using the LightCycler® 480 Probes Master kit (Roche) and hydrolysis probes (Table 2). cDNA from DJ-1-delP fibroblasts passage 16 was used as a negative control.

7. RNA and protein status analysis by PCR and Western blotting

RNA and protein levels of *PARK7*/DJ-1 were evaluated by PCR and Western blotting using the primers and antibodies listed in Table 2 following our standard protocols (Boussaad et al., 2020).

A

B

Copy number state

C

DNMT3B   *Nanog*   Oct3/4

D

Nanog - *Oct3/4* - Hoechst   *Sox2* - Hoechst

E

Brachyury   *Otx2*   *Sox17*

F

PARK7

CCCCA - - - CCC   *delP PARK7*
| | | | | | | |
CCCC**AGG**CCCC   *delP GC13 PARK7*

P158

G

H

GGG CCT GGG   GCC deletion
G   **P**   **G**   P158
CCC C GGA CCC

delP iPSC   delP GC13 iPSC

I

DJ-1
beta actin

J

DJ-1
beta actin

(caption on next page)

3

Fig. 1. A: Brightfield image of DJ-1-delP GC13 iPSC colony. iPSC show the typical iPSC morphology. B: The karyotype of DJ-1-delP GC13 iPSC has no abnormalities. C: Gene expression analysis of pluripotency markers by qPCR shows the expression of *DNMT3B*, *Nanog* and Oct3/4 in control and DJ-1-delP GC13 iPSC and no expression of the markers in control fibroblasts. D: Expression of stemness markers by immunocytochemistry. DJ-1-delP GC13 iPSC express the stemness marker *Sox2*, Oct3/4 and *Nanog*. E: DJ-1-delP GC13 iPSC are able to differentiate into the three germ layers, as assessed by three germ layer differentiation and subsequent immunocytochemistry analysis of the markers for Brachyury (mesoderm), *Otx2* (endoderm) and *Sox17* (ectoderm). F: Graphical scheme of the location of the c.471_473delGCC mutation in the *PARK7* gene. The mutation leads to the deletion of proline 158. G: 3D protein structure model of the DJ-1 protein dimer (PDB: 1UCF). One subunit of the dimer is highlighted in blue and one in green, the proline 158 residues in these subunits are marked in red (left). The residues are located in the contact site of the two DJ-1 monomers (left) and contribute to dimer interactions via van-der-Waals contacts (right, visualized using the software UCSF Chimera). The loss of proline 158 is therefore expected to impair homodimerization of the DJ-1 protein leading to subsequent proteasomal degradation. H: The mutation in the DJ-1-delP line and the correction of the mutation in the isogenic counterpart DJ-1-delP GC13 was confirmed by Sanger sequencing. I: DJ-1-delP and DJ-1-delP GC13 iPSC have normal DJ-1 mRNA levels, as assessed by RT-PCR. J: The mutation in the DJ-1-delP iPSC leads to loss of DJ-1 protein, as seen by Western blotting. (For interpretation of the references to colour in this figure legend, the reader is referred to the web version of this article.)

Table 1
Characterization and validation.

Classification (optional *italicized*)	**Test**	**Result**	**Data**
Morphology	Photography	typical primed pluripotent human stem cell morphology	Fig. 1 panel A
Pluripotency status evidence for the described cell line	Qualitative analysis *(Immunocytochemistry)*	staining/expression of pluripotency markers: Oct3/4, *Nanog*, *Sox2*	Fig. 1 panel D
	Quantitative analysis *(RT-qPCR)*	expression of pluripotency markers: *DNMT3B*, *Nanog*, Oct3/4	Fig. 1 panel C
Karyotype	Karyotype	46XY,	Fig. 1 panel B
		Resolution 450–500 bhps	
Genotyping for the desired genomic alteration/allelic status of the gene of interest	PCR across the edited site	PCR + sequencing, Confirmation of the homozygous correction of the mutation	Suppl. Fig. 1
	Transgene-specific PCR	N/A	N/A
Verification of the absence of random plasmid integration events	PCR	Random integration of donor plasmid in edited cell line not detected Integration of CRISPR/Cas9 (modified pX330) plasmid in edited cell line not detected	Suppl. Fig. 1
Parental and modified cell line genetic identity evidence	STR analysis	DNA Profiling	Submitted in the archive with journal
Mutagenesis / genetic modification outcome analysis	Sequencing (genomic DNA PCR)	Confirmation of the homozygous correction of the mutation	Fig. 1 panel H
	PCR-based analyses	Detection of correctly-targeted and randomly-integrated selectable targeting construct status	Suppl. Figure 1
	Western blotting	Demonstration of protein rescue in gene corrected line	Fig. 1 panel J
Off-target nuclease analysis-	*in silico* analysis of off-targets	*in silico* tool IDT CRISPR-Cas9 guide RNA design checker was used to identify off-targets, double-stranded breaks that may occur in the genome	Suppl. File 1
Specific pathogen-free status	Mycoplasma	Mycoplasma testing by luminescence. Negative	Suppl. Fig. 1
Multilineage differentiation potential	Directed differentiation	Demonstration of ability to differentiate into derivatives of all 3 germ layers	Fig. 1 panel E
Donor screening (OPTIONAL)	HIV 1 + 2 Hepatitis B, Hepatitis C	*N/A*	
Genotype - additional histocompatibility info (OPTIONAL)	Blood group genotyping HLA tissue typing	*N/A* *N/A*	

7.1. Immunofluorescence staining

Expression of stemness markers was analysed via immunocytochemistry. iPSC were fixed at passage 36 with 4% paraformaldehyde in PBS for 15 min and stained according to a standard immunofluorescence protocol using antibodies against *Sox2*, Oct3/4 and *Nanog* (Table 2). Nuclei were stained with Hoechst. Images were acquired using a Zeiss spinning disk confocal microscope (Carl Zeiss Microimaging GmbBH).

7.2. In vitro differentiation

The ability of the iPSC passage 36 to differentiate into the three germ layers was tested using the manufacturer's differentiation protocol of the Human Pluripotent Stem Cell Functional Identification Kit (R&D

Systems). Expression of the germ layer marker was confirmed after differentiation by immunocytochemistry (antibodies in Table 2). Images were acquired using a Zeiss spinning disk confocal microscope (Carl Zeiss Microimaging GmbH).

7.3. Karyotyping and identity analysis

Molecular karyotyping of iPSC passage 35 was performed at Thermo Fisher using the KaryoStat™ Assay. STR analysis of iPSC DJ-1-delP passage 26 and iPSC DJ-1-delP GC13 passage 40 was perfomed at the Laboratoire national de santé (LNS) Luxembourg.

Table 2
Reagents details.

Antibodies and stains used for immunocytochemistry/flow-cytometry			
	Antibody	Dilution	Company Cat # and RRID
Pluripotency Markers	Goat anti *Sox2* (Y-17)	1:250	Santa Cruz, Cat #: sc-17320; RRID: AB_2286684
Pluripotency Markers	Mouse anti Oct3/4	1:1000	Santa Cruz, Cat #: sc-5279; RRID: AB_628051
Pluripotency Markers	Rabbit anti *Nanog*	1:1000	Abcam, Cat #: ab21624; RRID: AB_446437
DJ-1	Rabbit anti DJ-1 (D29E5)XP	1:1500	cell signaling, Cat #: 5933; PRRID: AB_11179085
β-Actin	mouse anti β-Actin (8H10D10)	1:20.000	cell signaling, Cat #: 3700S; RRID: AB_2242334
Secondary antibody	Alexa Fluor 488 Goat anti Mouse IgG (H + L)	1:1000	Invitrogen, Cat #: A11029; RRID: AB_138404
Secondary antibody	Alexa Fluor 568 Goat anti Rabbit IgG (H + L)	1:1000	Invitrogen, Cat #: A11036; RRID: AB_143011
Secondary antibody	Alexa Fluor 647 Donkey anti Goat IgG (H + L)	1:1000	Invitrogen, Cat #: A-21447, RRID: AB_2535864
Secondary antibody	Goat anti Rabbit IgG (H + L) Secondary Antibody, HRP, 0.5 mg GTXRB IgG F AB'2 HRP X ADS	1:5000	Invitrogen, Cat #: A24537; RRID AB_2536005
Secondary antibody	Goat anti Mouse IgG (H + L) Secondary Antibody, HRP 0.5 mg GTXMU IgG F AB'2 HRP X ADS	1:10.000	Invitrogen, Cat #: A24524; RRID AB_2535993

Site-specific nuclease	
Cas9	Cas9
Delivery method	Nucleofection
Selection/enrichment strategy	Puromycin

Primers and Oligonucleotides used in this study

	Target	Forward/Reverse primer (5′-3′)
Pluripotency Markers (qPCR)	*NANOG*-FAM OCT4-FAM *DNMT3B*	*NANOG*-FAM (Hs02387400_g1, Thermo Fisher Scientific) OCT4-FAM (Hs00999632_g1, Thermo Fisher Scientific) *DNMT3B* (Hs00171876_m1, Thermo Fisher Scientific)
House-Keeping Genes (qPCR)	*ACTB*	*ACTB* (Hs03023880_g1, Thermo Fisher Scientific) was used as a housekeeping gene
Genotyping (desired allele/transgene presence detection)	PCR specific for the targeted allele	Representative PCR gel (+/-) Fig. 1 I *PARK7* fw 5́-ACGAATTCGAATGGCTTCCAAAAGAGCTCTGGT-3́ *PARK7* rev 5́-AGCGGCCGCCTAGTCTTTAAGAACAAGTGGAGCC-3́ Beta actin fw 5́-AAACTGGAACGGTGAAGGTG-3́ Beta actin rev 5́-AGAGAAGTGGGGTGGCTTTT-3́
Targeted mutation analysis/sequencing	Sequencing data from both alleles	Sanger sequencing chromatograms Fig. 1 H No integration PCR primer (for detection of homozygous/heterozygous gene editing and for sequencing after removal of the cassette) 5́-CAATGCTGCGAGGGCAGTAA-3́ 5́-CTCTTTTCCCTTCCCCAGGTA-3́ Sequencing primer 5́-GCCCATTAGGATGTCACCTTT-3́ 5́-GCAGTTCGCTGCTCTAGTCTT-3́
Potential random integration-detecting PCRs	plasmid backbone, vector/homology arm end PCRs	Suppl. Figure 1 Left homology arm (LHA) primer #246 5́-CAATGCTGCGAGGGCAGTAA-3́ #861 5́-AGATGTCCTAAATGCACAGCG-3́ Right homology arm (RHA) primer #43 5́-CGATATACAGACCGATAAAACACATGC-3́ #247 5́-CTCTTTTCCCTTCCCCAGGTA-3́ Cas9 primer 5́-AGGAAATCGGCAAGGCTACC-3́ 5́-TTCGCCGTTTGTCTCGATCA-3́ Random left primer #1321 5́-AGATGTCCTAAATGCACAGCG-3́ #861 5́-GCTGCCTATCAGAAGGTGGTG-3́ Random right primer #43 5́-CGATATACAGACCGATAAAACACATGC-3́

Table 2 (*continued*)

Site-specific nuclease		
Cas9	Cas9	
gRNA sequence	*PARK7*	#1752 5́-GCAGCCACTGGTAACAGGAT-3́ 5́-CTGATTCTTACAAGCCGGGG-3́
Genomic target sequence(s)	*PARK7*	gRNA context sequence 5́-CGGCCTGATTCTTACAAGCCGGGGTGGGAC-3́ PAM: TGG
e.g. Top off-target mutagenesis predicted site sequencing (for CRISPR/Cas9 and TALENs) primers		Gene: *PARK7* Location: 1.0.878 Length:878 nt [Positional Info] XM_008975660.3 position: 527 *in silico* tool IDT CRISPR-Cas9 guide RNA design checker was used to identify off-targets, double-stranded breaks Suppl. File 1
ODNs/plasmids/RNA templates used as templates for HDR-mediated site-directed mutagenesis. Backbone modifications in utilized ODNS have to be noted using standard nomenclature.	N/A	

Declaration of Competing Interest

The authors declare that they have no known competing financial interests or personal relationships that could have appeared to influence the work reported in this paper.

Appendix A. Supplementary data

Supplementary data to this article can be found online at https://doi.org/10.1016/j.scr.2022.102815.

References

Boussaad, I., Obermaier, C.D., Hanss, Z., Bobbili, D.R., Bolognin, S., Glaab, E., Wołyńska, K., Weisschuh, N., De Conti, L., May, C., Giesert, F., Grossmann, D., Lambert, A., Kirchen, S., Biryukov, M., Burbulla, L.F., Massart, F., Bohler, J., Cruciani, G., Schmid, B., Kurz-Drexler, A., May, P., Duga, S., Klein, C., Schwamborn, J.C., Marcus, K., Woitalla, D., Vogt Weisenhorn, D.M., Wurst, W., Baralle, M., Krainc, D., Gasser, T., Wissinger, B., Krüger, R., 2020. A patient-based model of RNA mis-splicing uncovers treatment targets in Parkinson's disease. Sci. Transl. Med. 12 (560).

Jarazo, J., Qing, X., Schwamborn, J.C., 2019. Guidelines for fluorescent guided biallelic HDR targeting selection with PiggyBac system removal for gene editing. Front. Genet. 10, 1–12.

Larsen, S.B., et al., 2020. Induced pluripotent stem cell line (LCSBi001-A) derived from a patient with Parkinson's disease carrying the p. D620N mutation in VPS35. Stem Cell Res. 45, 101776.

Mencke, P., Boussaad, I., Önal, G., Kievit, A.J.A., Boon, A.J.W., Mandemakers, W., Bonifati, V., Krüger, R., 2022. Generation and characterization of a genetic Parkinson's disease-patient derived iPSC line DJ-1-delP (LCSBi008-A). Stem Cell Res. 62, 102792.

Ramsey, C.P., Giasson, B.I., 2010. L10p and P158DEL DJ-1 mutations cause protein instability, aggregation, and dimerization impairments. J. Neurosci. Res. 88, 3111–3124.

Manuscript V

Regulation of metabolism and immune response via DJ-1 defines human astrocytic cell fate in Parkinson's disease and Glioblastoma

Mencke et al.

Status:

The manuscript is about to be submitted to *Cell metabolism*

Preface

As explained in the introduction, epidemiologic studies have shown that people with a neurodegenerative disease have a reduced incidence for many different cancer types, but an increased risk for other cancers. In addition, an inverse correlation for the expression of Parkinson´s disease (PD)- and cancer-associated genes was described. *PARK7*, encoding DJ-1, was initially identified as an oncogene, but loss of DJ-1 causes early-onset PD. However, it remains elusive how differential DJ-1 levels contribute to opposite cell fates in cancer and PD.

In the following manuscript I studied differential effects of DJ-1 protein levels in patient-derived cellular models of PD and glioblastoma (GBM) cell lines.

I contributed to the manuscript by conducting astrocyte and GBM cell experiments with help of François Massart. Brain section stainings, microglia differentiation and RNA sequencing analysis were performed with collaborations. Metabolite extractions for mass spectrometry were conducted by me, measurements were run in collaboration with a mass spectrometry facility, and data analysis was performed again by me using a computational pipeline, which I established during my PhD.

Regulation of metabolism and immune response via DJ-1 defines human astrocytic cell fate in Parkinson's disease and Glioblastoma

Pauline Mencke[1], Jochen Ohnmacht[1], Félicia Jeannelle[2,3], Adrien J Ries[1], Mónica Miranda de la Maza[2,4], Mathilde Ullrich[1], François Massart[1], Patrycja Mulica[5], Katja Badanjak[5], Zoé Hanss[1], Arkadiusz Rybicki[6,7], Paul Antony[1], Sylvie Delcambre[5], Giuseppe Arena[1], Gérald Cruciani[6,7], Javier Jarazo[8,9], Floriane Gavotto[4], Christian Jäger[4], Anouk Ewen[11,12], Maria Pires Pacheco[13], Dirk Brenner[12], Jens Schwamborn[8,9], Thomas Sauter[13], Lasse Sinkkonen[13], Gunnar Dittmar[14], Ricardo Taipa[15], David Bouvier[2,3,4], Johannes Meiser[16], Anne Grünewald[5,17], Vincenzo Bonifati[18], Michael Platten[19,20,21], Rejko Krüger[1,22,23] and Ibrahim Boussaad[1]

Author affiliations:

1 Translational Neuroscience, Luxembourg Centre for Systems Biomedicine, University of Luxembourg, Luxembourg

2 Luxembourg Center of Neuropathology (LCNP), Dudelange, Luxembourg

3 Laboratoire national de santé (LNS), National Center of Pathology (NCP), Dudelange, Luxembourg

4 Luxembourg Centre for Systems Biomedicine (LCSB), University of Luxembourg, Belval, Luxembourg

5 Molecular & Functional Neurobiology, Luxembourg Centre for Systems Biomedicine, University of Luxembourg, Luxembourg

6 Disease Modelling and Screening Platform (DMSP), Luxembourg Centre for Systems Biomedicine (LCSB), University of Luxembourg, Esch-sur-Alzette, Luxembourg

7 Disease Modelling and Screening Platform (DMSP), Luxembourg Luxembourg Institute of Health (LIH), Luxembourg, Luxembourg

8 Developmental and Cellular Biology, Luxembourg Centre for Systems Biomedicine University of Luxembourg

9 OrganoTherapeutics SARL, 6A, avenue des Hauts-Fourneaux, L-4365 Esch-sur-Alzette, Luxembourg

10 Department of Infection and Immunity, Experimental and Molecular Immunology, Luxembourg Institute of Health, Esch-sur-Alzette, L-4354, Luxembourg

11 Immunology and Genetics, Luxembourg Centre for Systems Biomedicine, University of Luxembourg, 7, Avenue des Hauts Fourneaux, Esch-sur-Alzette, Luxembourg

12 Department of Infection and Immunity, Experimental and Molecular Immunology, Luxembourg Institute of Health, Esch-sur-Alzette, L-4354, Luxembourg

13 Department of Life Sciences and Medicine, University of Luxembourg, Belvaux, Luxembourg

14 Proteomics of cellular signalling, Luxembourg Institute of Health, Strassen, Luxembourg

15 Portuguese Brain Bank, Neuropathology Unit, Centro Hospitalar Universitário do Porto, Portugal

16 Cancer Metabolism Group, Department of Cancer Research, Luxembourg Institute of Health (LIH), Luxembourg

17 Institute of Neurogenetics, University of Lübeck, Lübeck, Germany

18 Department of Clinical Genetics, Erasmus Medical Center, Rotterdam, The Netherlands

19 DKTK (German Cancer Consortium) Clinical Cooperation Unit (CCU) Neuroimmunology and Brain Tumor Immunology, German Cancer Research Center (DKFZ), Heidelberg, Germany

20 Department of Neurology, Medical Faculty Mannheim, MCTN, University of Heidelberg, Mannheim, Germany

21 DKFZ-Hector Cancer Institute at the University Hospital Mannheim, Mannheim, Germany

22 Centre Hospitalier de Luxembourg (CHL), Luxembourg

23 Transversal Translational Medicine, Luxembourg Institute of Health (LIH), Luxembourg

Correspondence to: Rejko Krüger

Full address: Translational Neuroscience, Luxembourg Centre for Systems Biomedicine, University of Luxembourg, Luxembourg, 7 Av. des Hauts-Fourneaux, 4362 Esch-sur-Alzette

E-mail: rejko.krueger@uni.lu; rejko.krueger@lih.lu

Summary

An inverse correlation for the expression of Parkinson´s disease (PD)- and cancer-associated genes has been previously reported. *PARK7*, encoding DJ-1, was initially identified as an oncogene, but loss of DJ-1 causes early-onset PD. However, it remains elusive how differential DJ-1 levels contribute to opposite cell fates in cancer and PD. Here, we demonstrate specific and differential effects of DJ-1 protein levels in patient-derived cellular models of PD and glioblastoma (GBM) cell lines. Loss of DJ-1 protein in human astrocytes led to impairment of energy metabolism and cell growth associated with an increased immune response upon IL-1β stimulation. In contrast, elevated DJ-1 levels in DJ-1 overexpressing astrocytes and GBM cell lines had the opposite effect. We show that decreased glutathione (GSH) synthesis and therefore increased reactive oxygen species (ROS) levels underl, the observed cellular phenotypes, which could be rescued by supplementation with glutathione precursors. Thus, the mechanism by which DJ-1 modulates these phenotypes is the same in both diseases.

Graphical Abstract
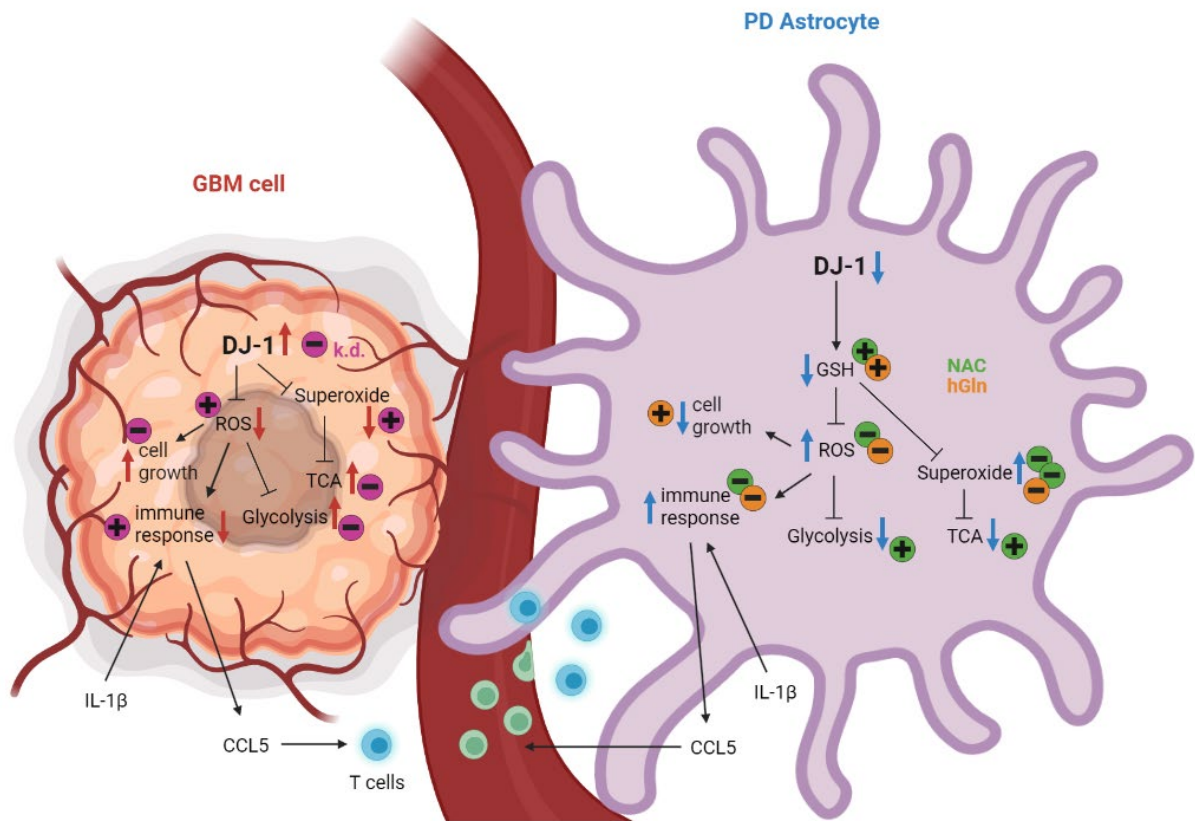
Modulation of GSH synthesis by DJ-1 regulates ROS levels and subsequently cell growth, the immune response and metabolism. DJ-1 deficiency associated phenotypes can be rescued by antioxidant treatment by restoring GSH levels.

Keywords:

Parkinson´s disease, glioblastoma, astrocytes, DJ-1, metabolism, immune response

Introduction

Epidemiologic studies have shown that there is an inverse correlation for gene expression of Parkinson´s disease (PD) and cancer associated genes. Genes that are downregulated in PD are upregulated in cancer and vice versa. Here, PD-associated genes (e.g. *PARK2*, *PARK7*) are involved in rather rare cancer types like Glioblastoma (GBM)[1]. In fact, high expression of *PARK7*, encoding the protein DJ-1, is associated with high grade and poor prognosis in glioma patients due to its influence on cell cycle and apoptosis[2]. The origin of GBM is still unsolved and over the last years emerging evidence indicated astrocytes as cells of origin for GBM[3,4]. Astrocytes are the most abundant glial subtype in the brain and are critical for the normal functioning of the brain. Recently, there has been increasing evidence for an important role of astrocytes in the pathogenesis of PD[5]. Under physiological conditions, one of the main functions of astrocytes is to metabolically support the surrounding neurons. Astrocytes have many different neuroprotective functions like releasing neurotrophic factors, producing antioxidants like glutathione (GSH), and disposing of neuronal waste products[6]. Since neurons are highly energy demanding cells[7], it is crucial that astrocytes support their metabolism by providing them with glutamine, which can be converted into glutamate and fueled into the neuronal tricarboxylic acid cycle (TCA)[8]. Astrocytes also release stored glycogen, which can be converted into lactate that can be transported to the surrounding neurons and used to fuel their metabolism[8].

Astrocytes are also involved in inflammatory response or promote immunosuppression and tissue repair. It was shown that pro-inflammatory cytokines like interleukin 1 beta (IL-1β) as well as interferon gamma (IFNG), tumor necrosis factor (TNF), and interleukin 6 (IL-6), reduce the astrocytic glycogen storage and lactate transport[9]. Importantly, many key factors and intracellular signaling pathways were identified during the last years that mediate astrocyte behavior during neuroinflammation[10].

In pathological conditions like PD, astrocytes produce inflammatory cytokines[11]. In fact, astrogliosis is a common pathological feature in PD[12,13]. In addition, impaired astrocytes contribute to PD-linked pathological mechanisms like oxidative stress, neuroinflammation, and mitochondrial impairment[6]. Therefore, targeting astrocytic dysfunction to repair their neuroprotective ability may represent a therapeutic approach to prevent progressive neurodegeneration in PD.

The *PARK7* gene was initially described as an oncogene as it was isolated in the course of screening for c-Myc-binding proteins in 1997[14]. In 2003, a large deletion and missense mutation in *PARK7* was identified in Italian and Dutch PD patients, leading to the discovery of *PARK7* as a causative gene for familial PD with recessive inheritance[15]. DJ-1 is localized in the cytoplasm, nucleus and mitochondria[16]. In the human brain, DJ-1 displays much higher expression levels in astrocytes than neurons[17]. In PD patient-brains, it was shown that DJ-1 is increased in reactive astrocytes[18]. Several studies in mice showed that DJ-1 overexpression in astrocytes resulted in protection from parkinsonism due to rotenone-induced neuronal cell death and that DJ-1 knockdown or knockout impaired the neuroprotective capacity of astrocytes and decreased neuronal survival[19]. These observations indicate an important role of DJ-1 for astrocytic function and astrocyte-mediated neuronal protection. There is increasing evidence for a direct involvement of DJ-1 in cellular energy metabolism via effects on glycolysis and the TCA cycle[20]. So far, it is not known how DJ-1 affects astrocytic and neuronal metabolism in PD. Astrocytes are the major route for brain glucose uptake during periods of strong synaptic activity, indicating that astrocytic glucose uptake is of key importance to neurons[21]. The loss of DJ-1 in astrocytes could therefore also influence neuronal metabolism and viability. On the other hand, overexpression of DJ-1 could enhance brain metabolism and enable increased cell proliferation.

In this study we analyzed the effects of DJ-1 deficiency or overexpression in human induced pluripotent stem cell (iPSC) derived astrocytes and GBM cell lines. We show that metabolic activity, cell growth and

immune response upon IL-1β stimulation in both cell types is dependent on DJ-1 levels which modulate these phenotypes via regulation of glutathione and ROS levels.

Results

Astrogliosis in DJ-1 PD patient brain

In 2016, Taipa and colleagues described a case of a homozygous DJ-1-mutant patient (p.L172Q mutation) with early-onset parkinsonism with first symptoms at the age of 22. The mutation in the *PARK7* gene causes DJ-1 protein loss and the patient brain showed diffuse Lewy body and astrogliosis[22]. To further analyze astrogliosis in this patient, we obtained sections from the cortex (of the patient, male, 49 years old, and a gender-matched control, male, 47 years old). We found that the patient brain showed a higher abundance of the activated astrocyte marker GFAP when compared to the control, which was accompanied by enlarged cell bodies and processes, known indicators for astrocyte activation[23] (Figure 1A). In addition, astrocytes in the patient brain displayed reduced intensity of staining for the astrocyte marker aldolase c (Aldoc), a glycolytic enzyme (Figure 1B), implying that the patient astrocytes shift from a metabolically active to a reactive state (more GFAP staining). In addition, the microglial marker Allograft inflammatory factor 1 (Iba1) showed an increased staining in the cortex of the DJ-1 patient when compared to the control, indicating increased neuroinflammation in the patient (Figure 1C, Suppl. file 1).

Increased immune response in DJ-1 deficient astrocytes

To further investigate the effect of DJ-1 deficiency in PD astrocytes, we derived astrocytes from induced pluripotent stem cells (iPSCs) carrying two different PD-associated DJ-1 mutations. We used isogenic pairs with two different homozygous DJ-1 mutations - P158Δ in-frame deletion (DelP) and DelP gene-corrected (GC), and c.192G>C (C4 mut) and C4, respectively[24–26]. Sixty days-old astrocytes were used for all experiments. The cells showed an astrocytic morphology and the majority stained positive for canonical astrocyte markers like GFAP, S100b, Vimentin, EAAT2, NFIA, ID3, and EZRIN. No neuronal contamination was observed, as assessed by markers for TUJ1 and MAP2 (Suppl. Fig. 1). Expression of typical markers of astrocyte precursors is shown in supplementary figures (Suppl. Fig. 2-3). Gene expression of all cell lines was assessed using next generation RNA sequencing (Suppl. Fig. 4 and methods). Differential expression analysis showed downregulation of 146 genes and upregulation of 56 genes in C4 mut astrocytes compared to isogenic control C4 astrocytes using a with log2-fold change cut-off of $\pm$ 1 with an adjusted p value < 0.05 (Suppl. Fig. 5A and B). Ingenuity pathway analysis (IPA)[27] on the differentially expressed genes[27] considering $-\log$(p-value) > 2 identified that the highest ranked upregulated pathway in DJ-1-deficient astrocytes was neuroinflammation (z-score = 0.632) (Suppl. Fig. 5C). The graphical summary of this IPA core analysis illustrates the relation of upregulated Interleukin 1 beta (IL-1β) and interferon gamma (IFNG) signaling, immune signaling involved in T cell cytotoxicity and cancer immunotherapy, and apoptosis (Figure 2A and B). Therefore, we first validated the increased immune response in DJ-1-deficient astrocytes, which showed increased gene expression of *C-C Motif Chemokine Ligand 5 (CCL5)*, also known as RANTES, upon stimulation with IL-1β for 2 to 12 hours, and for 24 and 48 hours when compared to isogenic controls (Suppl. Fig. 6A). A similar phenotype was observed in DJ-1-deficient microglia (Suppl. Fig. 6B). The increased gene expression levels of *CCL5* in DJ-1-deficient astrocytes resulted in increased secretion of CCL5 protein into the medium (Figure 2C). Concordantly with the increased cytokine expression and release, DJ-1-deficient astrocytes attracted more CD4+ and CD8+ human T cells, as assessed by T cell migration assay, and CCL5 secretion was also increased during the assay after 48 hours upon stimulation with IL-1β (Figure 2D). The migration towards DJ-1-deficient astrocytes was even increased upon knockdown of DJ-1 in control T cells (60% knockdown, see Suppl. Fig. 7), a scenario that is closer to the situation of a PD patient with homozygous DJ-1 mutations in which the T cells are also DJ-1-deficient. Additionally, DJ-1 deficiency also significantly decreased astrocytic proliferation (Figure 2F).

DJ-1 deficiency in astrocytes causes impaired metabolic carbon contribution and GSH levels

Based on the observed decrease in cell growth, we next investigated whether DJ-1-deficient astrocytes might have an impairment in energy metabolism. We analyzed glucose and glutamine metabolism in more detail by performing glucose and glutamine tracing. DJ-1-deficient astrocytes took up less glucose and released less lactic acid (Figure 3A)[8]. In line with reduced glucose uptake, glucose carbon contribution to the TCA was decreased (Figure 3B). However, the glycolytic carbon contribution towards 3PG and lactate was unaffected, as seen by analyzing the production of pyruvate from 3PG (by calculating the ratio of M3 pyruvate over M3 3PG) and the ratio of M3 lactate over M3 pyruvate (Figure 3C). Pyruvate entry into the TCA was reduced as assessed via the analysis of the production of M2 citrate from M3 pyruvate (Figure 3D). Consequently, the TCA cycling was reduced due to decreased production of M4 citrate from M2 citrate (Figure 3E). Labelling of glutamate was decreased indicating a deficiency of the cell to provide glutamate and eventually glutamine via glucose metabolism (Figure 3B). Glutamate is used by the cell for the synthesis of glutathione (GSH), the most important molecule in cellular oxidative stress response, and like lactic acid, glutamine is released by astrocytes to metabolically support neurons[8]. The reduced metabolic carbon contribution seen in deficient astrocytes by metabolic tracing was functionally confirmed by measurements of the extracellular acidification rate (ECAR) (Figure 3F) and the oxygen consumption rate (OCR) (Figure 3G), which revealed decreased glycolysis and oxidative phosphorylation (OXPHOS) compared to controls (Figure 3F and G). The decreased contribution of glucose to the TCA and glutamate production raised the question about the ability of the cell to compensate via the use of glutamine. Glutamine tracing revealed that glutamine uptake was significantly increased in DJ-1 -deficient astrocytes, and that over 95% of the glutamine detected in all cell lines was taken up from the medium (over 95% carbon contribution, Figure 3H). Yet, glutamine carbon contribution to all TCA cycle metabolites was decreased in DJ-1-deficient astrocytes compared to isogenic controls (Figure 3H). Interestingly, DJ-1 deficient astrocytes used more glutamine for fueling into the TCA, as seen by the increased ratio of M5 alpha-ketoglutarate over M5 glutamate (Figure 3I). However, increased alpha-ketoglutarate labeling did not translate into increased succinate labeling, as the production of succinate from alpha-ketoglutarate was significantly decreased (Figure 3J). Glutamine carbon contribution of the subsequent TCA cycle metabolites and the cycling of the TCA were therefore also significantly reduced in DJ-1 deficient astrocytes Figure 3K). This means that the increased glutamine carbon contribution to alpha-ketoglutarate is not channeled towards the TCA cycle to compensate for lower glycolytic contribution. Glutamine can also be used for GSH synthesis, which is known to be decreased in DJ-1-deficient cells[28]. Indeed, GSH and oxidized glutathione (GSSG) labeling was increased compared to isogenic controls (Figure 3K and 3L). However, despite increased use of glutamine for GSH production, total GSH levels were decreased and GSSG levels still increased in DJ-1-deficient astrocytes when compared to isogenic controls, as assessed by luminescence-based quantification (Figure 3M). As more glutamine from the medium was used by DJ-1-deficient astrocytes to synthesize GSH, we next analyzed whether doubling the amount of glutamine in the medium could rescue GSH levels. Upon high glutamine supplementation (4 mM), GSH levels in the DJ-1-deficient astrocytes reached wildtype levels (Figure 3K). GSSG levels remained increased in DJ-1-deficient astrocytes when compared to the isogenic counterparts, indicating that the increased GSH levels upon glutamine supplementation are being used to diminish increased ROS levels (Figure 3M). GSSG/GSH ratio was significantly decreased upon glutamine supplementation (Figure 3M), which indicates a decrease in oxidative stress upon glutamine supplementation in DJ-1-deficient cells, but not in the isogenic controls.

Increased glutamine supply reduces ROS levels and rescues immune phenotype and growth impairment of DJ-1 deficient astrocytes

DJ-1 is a known ROS scavenger[28–31] and loss of DJ-1 protein was shown to increase ROS in mouse primary astrocyte cultures[32–36]. Consistent with these findings, DJ-1-deficient human astrocytes had elevated levels of cellular ROS, RNS and superoxide, which are predominantly produced as by-products of mitochondrial respiration (Figure 4A). The observed increase in GSSG levels in DJ-1 deficient cells (Figure 3K) indicate failure in oxidative stress response. We saw that glutamine uptake was increased in DJ-1-deficient astrocytes to produce GSH (Figure 3K). Thus, we further assessed whether increasing the amount of glutamine could also rescue the increased ROS levels. ROS levels were significantly reduced by high glutamine treatment in all cell lines, but not as efficiently as when treated with the positive control N-Acetyl-Cysteine (NAC) (Figure 4B and C). ROS are important signaling molecules involved in immune signaling[37]. Therefore, we analyzed whether high glutamine or NAC supplementation in the astrocyte cultures could rescue immune related phenotypes. Both treatments reduced cytokine release (Figure 4D) and T cell migration (Figure 4E). Furthermore, doubling the amount of glutamine in the astrocyte medium rescued astrocyte cell growth of DJ-1-deficient astrocytes compared to isogenic controls (Figure 4F). The dependency on glutamine uptake can also be seen in cell survival rates. In baseline conditions, early apoptosis was significantly increased in DJ-1 deficient astrocytes compared to isogenic controls. Additional glutamine starvation for 4 hours further led to a significant increase of apoptosis in DJ-1-deficient astrocytes, which was not observed in isogenic controls (Figure 4G).

Metabolic and growth impairment are reversed in DJ-1 overexpressing astrocytes and GBM cell lines

Our observation that DJ-1 deficiency negatively modulates astrocyte metabolism and growth while increasing immune response led us to hypothesize that these mechanisms might be inversely regulated in GBM cases due to increased DJ-1 levels in GBM. Therefore, we generated DJ-1-overexpressing iPSC-derived astrocytes as an oncogenic model to study the influence of elevated DJ-1 levels in astrocytes. Lentiviral overexpression was established in the iPSC line C4 to keep the same genetic background as the isogenic pair used to model PD (Suppl. Fig. 8 and 9). To study the role of DJ-1 in GBM, we used three different GBM cell lines, namely U251, U87 and LN229. All three lines displayed upregulated DJ-1 protein levels when compared to C4 astrocytes (Suppl. Fig. 10A).

Gene expression of DJ-1-overexpressing and C4 astrocytes was profiled using RNA sequencing (Suppl. Fig. 4). Differential expression analysis revealed that 323 genes were downregulated and 225 upregulated in DJ-1-overexpressing astrocytes compared to isogenic control C4 with log2-fold change of -1 and padj of 0.05 (Suppl. Fig. 11). IPA gene expression analysis showed an upregulation of pathways involved in cell cycle control, cell growth, and especially pathways associated with proliferation of tumor cells (Figure 5A and B) compared to C4 astrocytes. Thus, we again analyzed the growth behavior of the cells. Concordantly, C4 DJ-1 overexpression astrocytes showed increased cell growth compared to C4 control astrocytes (Figure 5B). On the other hand, cell growth was reduced upon DJ-1 knockdown in the GBM cells (Figure 5C), which could be rescued by doubling the amount of glutamine in the medium (Figure 5D).

DJ-1 overexpression in astrocytes caused reduced ROS levels, which were further reduced by high glutamine and NAC supplementation (Figure 5E). The overexpression decreased CCL5 secretion (Figure 5F) but did not affect T cell migration (Figure 5G). On the other hand, the knockdown of DJ-1 in the GBM cells increased ROS levels (Figure 5H and I) and led to increased CCL5 secretion (Figure 5J) and consequently T cell migration (Figure 5K). Taken all together, overexpression of DJ-1 in astrocytes lead to opposite cellular phenotypes than observed in DJ-1-deficient astrocytes. However, glutamine carbon contribution to the TCA (Figure 5L and M) and to GSH production (Figure 5N) was decreased in DJ-1 overexpression astrocytes compared to wildtype astrocytes. This suggests that low ROS levels and a sufficient metabolic activity make the cells less dependent on glutamine. In that case an increased carbon contribution of glucose to the TCA cycle should be seen.

Indeed, when analyzing glucose metabolism using labeled glucose, DJ-1 overexpression in astrocytes increased the carbon contribution from glucose to the TCA cycle (Figure 6A). Expectedly, we saw that knockdown of DJ-1 in the three different GBM cell lines reduced the carbon contribution from glucose to the TCA cycle and the reduction correlated with the knockdown efficiency of the three different shRNAs on protein levels in the GBM lines (Figure 6A and B). This suggests a dependency of the metabolic activity on DJ-1 levels in both cell types. Importantly, glutamate is known to be crucial for cancer cell metabolism[38,39] . The contribution of glucose to its labeling was significantly increased in the oncogenic model, and DJ-1 knockdown in the GBM cells significantly reduced the carbon contribution of glucose to glutamate. Analysis of OXPHOS activity by OCR measurements revealed that the increased contribution from glycolysis in DJ-1 overexpressing astrocytes did not lead to an increase in mitochondrial respiration (Figure 6C). However, DJ-1 knockdown in GBM cells significantly decreased OXPHOS suggesting that increased DJ-1 levels are not sufficient to increase mitochondrial respiration but are essential to maintain an increased metabolic activity.

NAC supplementation rescues TCA cycle carbon contribution deficits in DJ-1 deficient astrocytes and high glutamine supplementation increases TCA cycling and GSH synthesis from glutamine

To understand whether the observed phenotypes of increased immune response and impaired cellular metabolism were caused by decreased GSH levels and subsequently increased ROS in the absence of DJ-1, we then analyzed glucose and glutamine metabolism in the patient-derived isogenic astrocytes by LC-MS tracing after treating the cells with NAC as a positive control or doubling the amount of glutamine in the medium. NAC supplementation rescued the glucose carbon contribution to all TCA intermediates (Figure 7C). The increased TCA carbon contribution was not only due to increased carbon contribution of glucose to pyruvate but also due to increased pyruvate entry into the TCA cycle (Figure 7B). Consequently, glucose carbon contribution to glutamate was brought back to wildtype levels (Figure 7C). In contrast, high glutamine did not rescue glucose carbon contribution to TCA cycle intermediates (Figure 7C) nor pyruvate entry into the TCA cycle (Figure 7B). Glutamine tracing under the same conditions revealed that 99% of the intracellularly detected glutamine in both cell lines and all conditions was taken up from the medium (Figure 7C). NAC treatment rescued the TCA cycle intermediate labeling (Figure 7C) to wildtype levels. Increased glutamine carbon contribution to alpha-ketoglutarate in DJ-1 deficient astrocytes was reduced by NAC (Figure 7D)by restoring the ability of the cells to convert alpha-ketoglutarate to succinate(Figure 7E). In contrast to this, supplying the cells with 4 mM glutamine did not rescue the glutamine carbon contribution to the TCA cycle intermediates (Figure 7C). Increased fueling of glutamine into the TCA until alpha ketoglutarate remained also increased in the presence of 4 mM glutamine (Figure 7D). The analysis of the ratio of M4 succinate over M5 alpha-ketoglutarate showed that the additionally provided glutamine did not enable the cells to use it efficiently for the TCA and to compensate for the reduced glucose carbon contribution to the TCA (Figure 7E). However, and confirming the results from earlier experiments (Figure 3L-N), the increase of glutamine concentration led to an increased carbon contribution from glutamine to GSH (Figure 7E, M5 GSH) compared to wildtype cells and to the same cells in basal conditions or treated with NAC. NAC supplementation significantly decreased carbon contribution from glutamine to GSSG, but high glutamine did not affect GSSG labeling (Figure 7F). This suggests that additionally supplied glutamine is used for oxidative stress response, but that the protective effect is not as strong as with NAC treatment that caused a stronger reduction of ROS levels, especially of superoxide (Figure 5A and B) and hence, was able to not only rescue the growth and immune phenotypes, but also the TCA cycle insufficiency.

Discussion

Astrocytes play an important role in the pathogenesis of PD, and GBM is claimed to be originating from astrocytes[3,40]. Thus, we analyzed the role of DJ-1 downregulation in PD, and DJ-1 upregulation in GBM to shed light on the opposite disease-related phenotypes of PD and GBM associated with diverging DJ-1 levels.

In human cortex of a PD patient with a DJ-1 mutation, we found increased astrogliosis[22], which supports an activated immune mechanism involving astrocytes in the neurodegenerative process. Increased astrogliosis in PD midbrain was observed in previous studies of human midbrain of patients with idiopathic PD[13], and neuroinflammation is increasingly recognized to play a critical role in the pathology of PD[41]. Our observation in human astrocytes deficient of DJ-1 was supported by next generation RNA sequencing showing an upregulation of proinflammatory pathways, which was subsequently validated by increased cytokine expression and release upon stimulation. It was previously shown that IL-1β and IL-6 are elevated in the brains from idiopathic PD patients[42]. A recent publication showed an increased cytokine release in human astrocytes derived from a PD patient carrying a G2019S mutation in LRRK2[43]. It was shown that astrocytes and microglia from DJ-1-deficient mice showed increased inducible NO synthase (iNOS) levels[44], which indicates that dysfunctional astrocytes may act as source for neuroinflammation. Kahle and colleagues also demonstrated higher astrocyte reactivity by showing increased cytokine release in astrocytes from DJ-1$^{-/-}$ mice upon lipopolysaccharide (LPS) stimulation compared to controls[32]. Furthermore, astrocytes from DJ-1$^{-/-}$ mice produced more nitric oxide (NO), which was mediated by ROS signaling leading to activation of iNOS[32]. Additional evidence for a primary pathological role of DJ-1$^{-/-}$ astrocytes in neurodegeneration came from Kahle´s *in vitro* study. Neurotoxicity upon LPS treatment was only observed, when either wt or DJ-1$^{-/-}$ neurons were co-cultured with DJ-1$^{-/-}$ astrocytes, but not with wt astrocytes[32]. Interestingly, also in the *in vivo* situation of DJ-1 knockout mice no other neurodegeneration was observed as these animals displayed no nigral or striatal loss of dopaminergic neurons and only mild non-motor symptoms[45], which may indicate that astrocytic pathology did not yet translate into neurodegeneration. Taken together, this strengthens the hypothesis that dysfunctional astrocytes significantly contribute to the pathogenesis of neurodegeneration and precedes neuronal loss *in vivo*. Consistent with an astrocytic activation, we found significantly decreased GSH levels and increased ROS in DJ-1-deficient human astrocytes compared to isogenic controls. ROS are known to regulate the immune response[37,46,47]. In fact, it was shown that mitochondrial ROS can induce proinflammatory cytokine production[48]. A recent study suggests that transiently increased CCL5 expression in mice brains after mild traumatic brain injury (TBI) is a coping mechanism to reduce elevated ROS levels caused by the injury via glutathione peroxidase-1 (GPX1) activation[49]. However, in contrast to the situation after TBI, ROS levels in DJ-1-deficient cells are chronically elevated. In the case of astrocytes, this leads to an increased CCL5 release, which over time can contribute to neuroinflammation[50]. These results are again indicating an important role of astrocytes as direct key players in causing neurodegeneration by maintaining a chronic inflammatory reaction. It was shown that infiltration of CD4+ lymphocytes into the brain contributes to neurodegeneration in a PD mouse model[51]. Here, we assessed the functional relevance of the increased ROS levels and cytokine release in DJ-1-deficient astrocytes and found increased T cell migration towards DJ-1-deficient astrocytes. Previously, it was shown that T cells from DJ-1 KO mice had elevated ROS levels[52], pointing to the importance of evaluating the effect of lack of DJ-1 in T cells from DJ-1 patients. It is also known that ROS can activate T cells[53]. We observed an even increased T cell migration towards DJ-1-deficient astrocytes after knockdown of DJ-1 in T cells, further implying a contribution to neuroinflammation observed in PD patients with loss of function mutations in the DJ-1 gene.

On the other hand, CCL5 secretion upon stimulation by all three GBM cell lines was lower than in wildtype astrocytes and increased significantly upon DJ-1 knockdown. The knockdown also led to a significant

increase in T cell migration towards GBM cells suggesting that elevated DJ-1 levels in GBM might contribute to immune evasion of the tumor. GBM is known for its high metabolic activity[54] and its immunosuppressive microenvironment that causes T cell dysfunction and therefore impaired T cell migration[55]. These immune evasion mechanisms are decreasing the effectiveness of immune therapy options. Increasing the infiltration of the tumor microenvironment with T lymphocytes is crucial for an improved tumor therapy. The observed increased glycolysis and TCA cycle activity are also connected to T cell exhaustion, as GBM cells deprive the tumor microenvironment from glucose that could be used by infiltrating T cells, which depend on glycolysis[56]. Therapeutic targeting of DJ-1-mediated regulation of cytokine secretion and metabolic modulation could help to decrease tumor growth and immune suppression, which in turn enables effective T cell infiltration, and eventually a better anti-tumor response. On the other hand, for PD, restoring metabolic activity and decreasing cytokine release could counteract neuroinflammation.

Since the T cell migration was reduced upon NAC and glutamine supplementation, we investigated the energy metabolism in DJ-1-deficient astrocytes, which was reduced, as seen by decreased glycolysis, OXPHOS and TCA cycle carbon contribution. ROS are known to reduce the activity of the TCA cycle[57], which is why the increased ROS levels in the DJ-1-deficient astrocytes might have caused the observed reduced TCA cycle carbon contribution, especially as the phenotype was rescued by NAC. In addition, we saw an increased glutamine fueling into the TCA until alpha-ketoglutarate in DJ-1 deficient astrocytes, which did not translate into increased glutamine carbon contribution to subsequent TCA cycle intermediates. This effect was associated with an impairment in the conversion of alpha-ketoglutarate to succinate. Thus, we observed an inability to use glutaminolysis for energy supply in the absence of DJ-1.

GSH synthesis from glutamine was increased leading to the conclusion that DJ-1-deficient astrocytes use glutamine for GSH synthesis. Nonetheless, despite increased GSH synthesis, DJ-1-deficient astrocytes had decreased total GSH and increased GSSG levels, which indicates that the increased production from glutamine did not translate into higher total GSH and GSSG levels. The increased GSSG levels are again in line with the increased ROS, which the cells cannot cope with. Taken together, we found a vicious cycle of reduced GSH levels causing increased ROS levels leading to decreased TCA carbon contribution, which in turn leads to reduced production of the GSH precursor glutamine. In consequence, DJ-1-deficient astrocytes showed decreased cell growth, an increased immune response and increased cell death. All eventually leading to a reduced support of neuronal homeostasis by astrocytes. In fact, it has been shown that impairment of DJ-1 in primary mouse astrocytes negatively affects primary neurons following an oxidative insult[19,58,59].

In contrast to the observations in DJ-1-deficient astrocytes, DJ-1 overexpression had the inverse effect as it resulted in increased cell growth, metabolic activity and reduced ROS compared to wildtype astrocytes. Ingenuity pathway analysis revealed an upregulation of cancer-associated pathways involved in cell proliferation and cell cycle regulation, which again confirms DJ-1 overexpression in astrocytes as oncogenic model. In rat astrocytes, DJ-1 overexpression could protect against rotenone-induced neurotoxicity[60]. Overexpression of DJ-1 in mouse astrocytes was shown to be protective against rotenone-induced mitochondrial dysfunction and ROS generation of co-cultured neurons[19]. Our results and these studies highlight the relevance of DJ-1 in astrocytes and their impact on surrounding neurons, again emphasizing the importance of astrocyte dysfunction in the pathogenesis of PD. Concordant with the results in the astrocytes, knockdown of DJ-1 in the GBM cell lines also decreased GBM cell growth and metabolism, increased ROS and the immune response.

Thus, the mechanism by which DJ-1 modulates these pathways seems to be the same in both diseases, as the knockdown of DJ-1 in the GBM cells had the same effect as loss of DJ-1 in PD patient-derived

astrocytes. The opposite phenotypic observations in our models of PD and GBM can therefore be attributed to initially inverse DJ-1 levels.

In summary, we showed here, for the first time, that the two diseases share molecular pathophysiological features, which is supported by epidemiological evidence that individuals affected by a neurodegenerative disease may have a decreased risk of certain cancer types[61]. We have shown that PD and GBM cellular phenotypes are correlating with the levels of the disease associated protein DJ-1. Future large-scale studies will help to modulate these pathways in order to pave the way towards an improved therapy of these yet incurable conditions.

PM conducted the main experiments and drafted the manuscript, FJ and MMDLM performed brain section stainings, MU performed ICC experiments, FM supported main experiments, PKM and KB provided microglia, AJR helped with Seahorse, AR and GC performed qPCR experiments, PA and JJ helped with image analysis, SD, GD, FG and CJ helped with metabolomics, GA provided lentiviral constructs, AE established GSH assay, MP and JO performed RNAseq analysis, AL helped with Co-IP Mass spec, RT provided DJ-1 brain sections, DB and MM helped with brain section stainings, TS and LS helped with RNAseq, ZH supervised, JCS, JM, AG, MP, IB and RK advised, supervised and PM, IB and RK conceived the study and wrote the manuscript.

Acknowledgements

Competing interests

The authors report no competing interests.

References

1. Hinkle, D. A., Mullett, S. J., Gabris, B. E. & Hamilton, R. L. DJ-1 expression in glioblastomas shows positive correlation with p53 expression and negative correlation with epidermal growth factor receptor amplification. *Neuropathology* **31**, 29–37 (2011).

2. Wang, C. *et al.* The positive correlation between DJ-1 and β-catenin expression shows prognostic value for patients with glioma. *Neuropathology* **33**, 628–636 (2013).

3. Goffart, N., Kroonen, J. & Rogister, B. Glioblastoma-initiating cells: Relationship with neural stem cells and the micro-environment. *Cancers (Basel).* **5**, 1049–1071 (2013).

4. Jiang, Y. & Uhrbom, L. On the origin of glioma. *Ups. J. Med. Sci.* **117**, 113–121 (2012).

5. Booth, H. D. E., Hirst, W. D. & Wade-Martins, R. The Role of Astrocyte Dysfunction in Parkinson's Disease Pathogenesis. *Trends Neurosci.* **40**, 358–370 (2017).

6. Miyazaki, I. & Asanuma, M. Neuron-Astrocyte Interactions in Parkinson's Disease. (2020) doi:10.3390/cells9122623.

7. Vergara, R. C. *et al.* The Energy Homeostasis Principle: Neuronal Energy Regulation Drives Local Network Dynamics Generating Behavior. *Front. Comput. Neurosci.* **13**, 1–18 (2019).

8. Turner, D. A. & Adamson, D. C. Neuronal-astrocyte metabolic interactions: Understanding the transition into abnormal astrocytoma metabolism. *J. Neuropathol. Exp. Neurol.* **70**, 167–176 (2011).

9. Klein, A. S. and R. S. Astrocytes: Initiators of and Responders to Inflammation. *Glia Heal. Dis.* (2019) doi:10.5772/intechopen.89760.

10. Colombo, E. & Farina, C. Astrocytes: Key Regulators of Neuroinflammation. *Trends Immunol.* **37**, 608–620 (2016).

11. Kam, T. I., Hinkle, J. T., Dawson, T. M. & Dawson, V. L. Microglia and astrocyte dysfunction in parkinson's disease. *Neurobiol. Dis.* **144**, 105028 (2020).

12. Wang, B. *et al.* Effect of DJ-1 overexpression on the proliferation, apoptosis, invasion and migration of laryngeal squamous cell carcinoma SNU-46 cells through PI3K/AKT/mTOR. *Oncol. Rep.* **32**, 1108–1116 (2014).

13. Smajic, S. *et al.* Single-cell sequencing of human midbrain reveals glial activation and a Parkinson-specific neuronal state. *Brain* **145**, 964–978 (2022).

14. Ariga, H. Common mechanisms of onset of cancer and neurodegenerative diseases. *Biol. Pharm. Bull.* **38**, 795–808 (2015).

15. Bonifati, V. *et al.* Mutations in the DJ-1 gene associated with autosomal recessive early-onset parkinsonism. *Science (80-.).* **299**, 256–259 (2003).

16. Canet-Avilés, R. M. *et al.* The Parkinson's disease DJ-1 is neuroprotective due to cysteine-sulfinic acid-driven mitochondrial localization. *Proc. Natl. Acad. Sci. U. S. A.* **101**, 9103–9108 (2004).

17. Bandopadhyay, R. *et al.* The expression of DJ-1 (PARK7) in normal human CNS and idiopathic Parkinson's disease. *Brain* **127**, 420–430 (2004).

18. Rizzu, P. *et al.* DJ-1 Colocalizes with Tau Inclusions: A Link between Parkinsonism and Dementia. *Ann. Neurol.* **55**, 113–118 (2004).

19. Mullett, S. J., Di Maio, R., Greenamyre, J. T. & Hinkle, D. A. DJ-1 Expression Modulates Astrocyte-

Mediated Protection Against Neuronal Oxidative Stress. *J. Mol. Neurosci.* **49**, 507–511 (2013).

20. Mencke, P. *et al.* The Role of DJ-1 in Cellular Metabolism and Pathophysiological Implications for Parkinson's Disease. *Cells* **10**, 1–18 (2021).

21. Bélanger, M., Allaman, I. & Magistretti, P. J. Brain energy metabolism: Focus on Astrocyte-neuron metabolic cooperation. *Cell Metab.* **14**, 724–738 (2011).

22. Taipa, R. *et al.* DJ-1 linked parkinsonism (PARK7) is associated with Lewy body pathology. *Brain* **139**, 1680–1687 (2016).

23. Wilhelmsson, U. *et al.* Redefining the concept of reactive astrocytes as cells that remain within their unique domains upon reaction to injury. *Proc. Natl. Acad. Sci. U. S. A.* **103**, 17513–17518 (2006).

24. Boussaad, I. *et al.* A patient-based model of RNA mis-splicing uncovers treatment targets in Parkinson's disease. *Sci. Transl. Med.* **12**, (2020).

25. Mencke, P. *et al.* Generation and characterization of a genetic Parkinson's disease-patient derived iPSC line DJ-1-delP (LCSBi008-A). *Stem Cell Res.* **62**, 1–5 (2022).

26. Mencke, P. *et al.* Generation of isogenic control DJ-1-delP GC13 for the genetic Parkinson's disease-patient derived iPSC line DJ-1-delP (LCSBi008-A-1). *Stem Cell Res.* **62**, 102815 (2022).

27. Qiagen, C. version: 60467501 (release date: 2020-11-19). IPA.

28. Meiser, J. *et al.* Loss of DJ-impairs antioxidant response by altered glutamine and serine metabolism. *Neurobiol. Dis.* **89**, 112–125 (2016).

29. Zhang, L. *et al.* Role of DJ-1 in Immune and Inflammatory Diseases. *Front. Immunol.* **11**, 1–10 (2020).

30. Eltoweissy, M., Dihazi, G. H., Müller, G. A., Asif, A. R. & Dihazi, H. Protein DJ-1 and its anti-oxidative stress function play an important role in renal cell mediated response to profibrotic agents. *Mol. Biosyst.* **12**, 1842–1859 (2016).

31. Xu, X. M. & Møller, S. G. ROS removal by DJ-1: Arabidopsis as a new model to understand Parkinson disease. *Plant Signal. Behav.* **5**, 1034–1036 (2010).

32. Waak, J. *et al.* Regulation of astrocyte inflammatory responses by the Parkinson's disease-associated gene DJ-1. *FASEB J.* **23**, 2478–2489 (2009).

33. Clements, C. M., McNally, R. S., Conti, B. J., Mak, T. W. & Ting, J. P. Y. DJ-1, a cancer- and Parkinson's disease-associated protein, stabilizes the antioxidant transcriptional master regulator Nrf2. *Proc. Natl. Acad. Sci. U. S. A.* **103**, 15091–15096 (2006).

34. Ariga, H. *et al.* Neuroprotective function of dj-1 in Parkinson's disease. *Oxid. Med. Cell. Longev.* **2013**, (2013).

35. Irrcher, I. *et al.* Loss of the Parkinson's disease-linked gene DJ-1 perturbs mitochondrial dynamics. *Hum. Mol. Genet.* **19**, 3734–3746 (2010).

36. Krebiehl, G. *et al.* Reduced basal autophagy and impaired mitochondrial dynamics due to loss of Parkinson's disease-associated protein DJ-1. *PLoS One* **5**, (2010).

37. Tavassolifar, M. J., Vodjgani, M., Salehi, Z. & Izad, M. The Influence of Reactive Oxygen Species in the Immune System and Pathogenesis of Multiple Sclerosis. *Autoimmune Dis.* **2020**, (2020).

38. Moreira Franco, Y. E. *et al.* Glutaminolysis dynamics during astrocytoma progression correlates

with tumor aggressiveness. *Cancer Metab.* **9**, 1–15 (2021).

39. Obara-Michlewska, M. & Szeliga, M. Targeting glutamine addiction in meningioma. *Neuro. Oncol.* **24**, 569–570 (2020).

40. Zong, H., Verhaak, R. G. W. & Canolk, P. The cellular origin for malignant glioma and prospects for clinical advancements. *Expert Rev. Mol. Diagn.* **12**, 383–394 (2012).

41. Salemi, M. *et al.* Examples of Inverse Comorbidity between Cancer and Neurodegenerative Diseases: A Possible Role for Noncoding RNA. *Cells* **11**, 1930 (2022).

42. Mogi, M. Interleukin-lfl, interleukin-6, epidermal growth factor and transforming growth factor- are elevated in the brain from parkinsonian patients. **180**, 147–150 (1994).

43. Sonninen, T. M. *et al.* Metabolic alterations in Parkinson's disease astrocytes. *Sci. Rep.* **10**, (2020).

44. Kim, J. hyeon *et al.* DJ-1 facilitates the interaction between STAT1 and its phosphatase, SHP-1, in brain microglia and astrocytes: A novel anti-inflammatory function of DJ-1. *Neurobiol. Dis.* **60**, 1–10 (2013).

45. Floss, T., Angelis, D., Kahle, P. J. & Wurst, W. DJ-1-deficient mice show less TH-positive neurons in the ventral tegmental area and exhibit non-motoric. 305–317 (2010) doi:10.1111/j.1601-183X.2009.00559.x.

46. Chen, X., Song, M., Zhang, B. & Zhang, Y. Reactive Oxygen Species Regulate T Cell Immune Response in the Tumor Microenvironment. *Oxid. Med. Cell. Longev.* **2016**, 11–16 (2016).

47. Yang, Z., Min, Z. & Yu, B. Reactive oxygen species and immune regulation. *Int. Rev. Immunol.* **39**, 292–298 (2020).

48. Naik, E. & Dixit, V. M. Mitochondrial reactive oxygen species drive proinflammatory cytokine production. *J. Exp. Med.* **208**, 417–420 (2011).

49. Ho, M., Yen, C., Hsieh, T., Kao, T. & Chiu, J. Redox Biology CCL5 via GPX1 activation protects hippocampal memory function after mild traumatic brain injury. *Redox Biol.* **46**, 102067 (2021).

50. Pittaluga, A. CCL5-glutamate cross-talk in astrocyte-neuron communication in multiple sclerosis. *Front. Immunol.* **8**, 1–13 (2017).

51. Brochard, V. *et al.* Infiltration of CD4+ lymphocytes into the brain contributes to neurodegeneration in a mouse model of Parkinson disease. *J. Clin. Invest.* **119**, 182–192 (2009).

52. Singh, Y. *et al.* Differential effect of DJ-1 / PARK7 on development of natural and induced regulatory T cells. *Nat. Publ. Gr.* 1–14 doi:10.1038/srep17723.

53. Belikov, A. V., Schraven, B. & Simeoni, L. T cells and reactive oxygen species. *J. Biomed. Sci.* **22**, 1–11 (2015).

54. Stanke, K. M., Wilson, C. & Kidambi, S. High Expression of Glycolytic Genes in Clinical Glioblastoma Patients Correlates With Lower Survival. *Front. Mol. Biosci.* **8**, 1–12 (2021).

55. Wang, H. *et al.* Different T-cell subsets in glioblastoma multiforme and targeted immunotherapy. *Cancer Lett.* **496**, 134–143 (2021).

56. Mohan, A. A. *et al.* Targeting Immunometabolism in Glioblastoma. *Front. Oncol.* **11**, 1–16 (2021).

57. Simon, M. C. Coming up for air: HIF-1 and mitochondrial oxygen consumption. *Cell Metab.* **3**, 148–150 (2006).

58. Mullett, S. J. & Hinkle, D. A. DJ-1 deficiency in astrocytes selectively enhances mitochondrial Complex i inhibitor-induced neurotoxicity. *J. Neurochem.* **117**, 375–387 (2011).

59. Mullett, S. J. & Hinkle, D. A. DJ-1 knock-down in astrocytes impairs astrocyte-mediated neuroprotection against rotenone. *Neurobiol. Dis.* **33**, 28–36 (2009).

60. De Miranda, B. R. *et al.* Astrocyte-specific DJ-1 overexpression protects against rotenone-induced neurotoxicity in a rat model of Parkinson's disease. *Neurobiol. Dis.* **115**, 101–114 (2018).

61. Plun-Favreau, H., Lewis, P. A., Hardy, J., Martins, L. M. & Wood, N. W. Cancer and neurodegeneration: Between the devil and the deep blue sea. *PLoS Genet.* **6**, 1–8 (2010).

62. Haenseler, W. *et al.* A Highly Efficient Human Pluripotent Stem Cell Microglia Model Displays a Neuronal-Co-culture-Specific Expression Profile and Inflammatory Response. *Stem Cell Reports* **8**, 1727–1742 (2017).

63. van Wilgenburg, B., Browne, C., Vowles, J. & Cowley, S. A. Efficient, Long Term Production of Monocyte-Derived Macrophages from Human Pluripotent Stem Cells under Partly-Defined and Fully-Defined Conditions. *PLoS One* **8**, (2013).

64. Badanjak, K. *et al.* iPSC-Derived Microglia as a Model to Study Inflammation in Idiopathic Parkinson's Disease. *Front. Cell Dev. Biol.* **9**, 1–11 (2021).

65. Palm, T. *et al.* Rapid and robust generation of long-term self-renewing human neural stem cells with the ability to generate mature astroglia. *Sci. Rep.* **5**, 1–16 (2015).

66. Köster, J. *et al.* Sustainable data analysis with Snakemake. *F1000Research* **10**, (2021).

67. Andrews, S. FastQC: A Quality Control Tool for High Throughput Sequence Data [Online]. Available online at: http://www.bioinformatics.babraham.ac.uk/projects/fastqc/ (2010).

68. Schubert, M., Lindgreen, S. & Orlando, L. AdapterRemoval v2: Rapid adapter trimming, identification, and read merging. *BMC Res. Notes* **9**, 1–7 (2016).

69. Dobin, A. *et al.* STAR: Ultrafast universal RNA-seq aligner. *Bioinformatics* **29**, 15–21 (2013).

70. Liao, Y., Smyth, G. K. & Shi, W. The R package Rsubread is easier, faster, cheaper and better for alignment and quantification of RNA sequencing reads. *Nucleic Acids Res.* **47**, (2019).

71. Love, M. I., Huber, W. & Anders, S. Moderated estimation of fold change and dispersion for RNA-seq data with DESeq2. *Genome Biol.* **15**, 1–21 (2014).

72. Zhu, A., Ibrahim, J. G. & Love, M. I. Heavy-Tailed prior distributions for sequence count data: Removing the noise and preserving large differences. *Bioinformatics* **35**, 2084–2092 (2019).

73. Elliott, A. C., Hynan, L. S., Reisch, J. S. & Smith, J. P. Preparing data for analysis using Microsoft Excel. *J. Investig. Med.* **54**, 334–341 (2006).
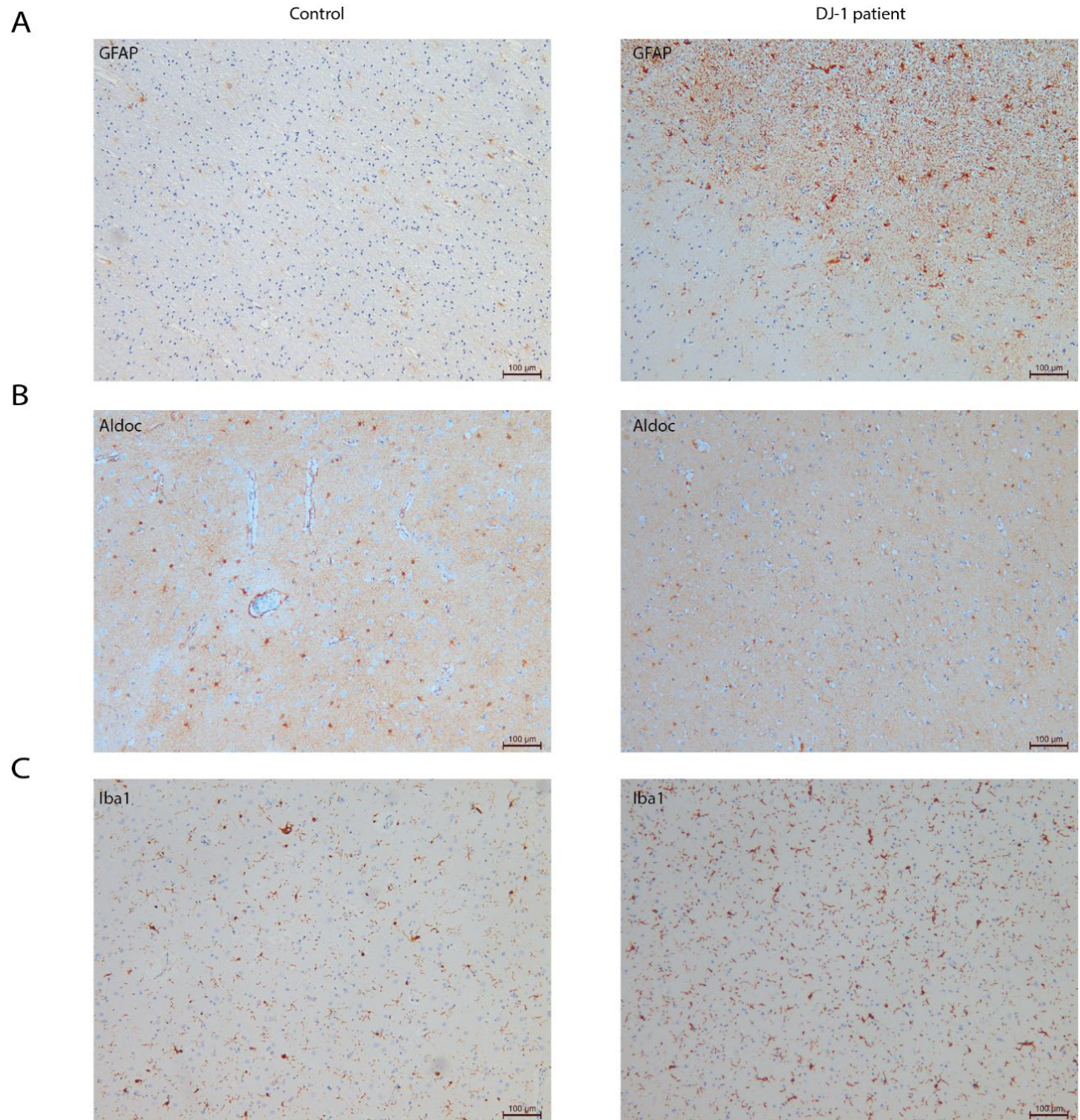
Figure 1: Astrogliosis in DJ-1 patient brain

1A-C: Cortex section of a healthy donor (control) and the PD patient (DJ-1 patient) stained for **A:** the activated astrocyte marker GFAP. **B:** the astrocyte marker aldolase c (Aldoc). **C:** the microglial marker Allograft inflammatory factor 1 (Iba1).

A

B

C

CCL5 secretion after 48h

- C4 untreated
- C4 IL1b
- C4 mut untreated
- C4 mut IL1b
- DelP GC untreated
- DelP GC IL1b
- DelP untreated
- DelP IL1b

D

CD4+ T cells

CD8+ T cells

- C4 + wt T cells
- C4 + kd T cells
- C4 mut + wt T cells
- C4 mut + kd T cells
- DelP GC + wt T cells
- DelP GC + kd T cells
- DelP + wt T cells
- DelP + kd T cells

CCL5 secretion after 48h

E

Astrocyte growth

- C4
- C4 mut

Astrocyte growth

- DelP GC
- DelP
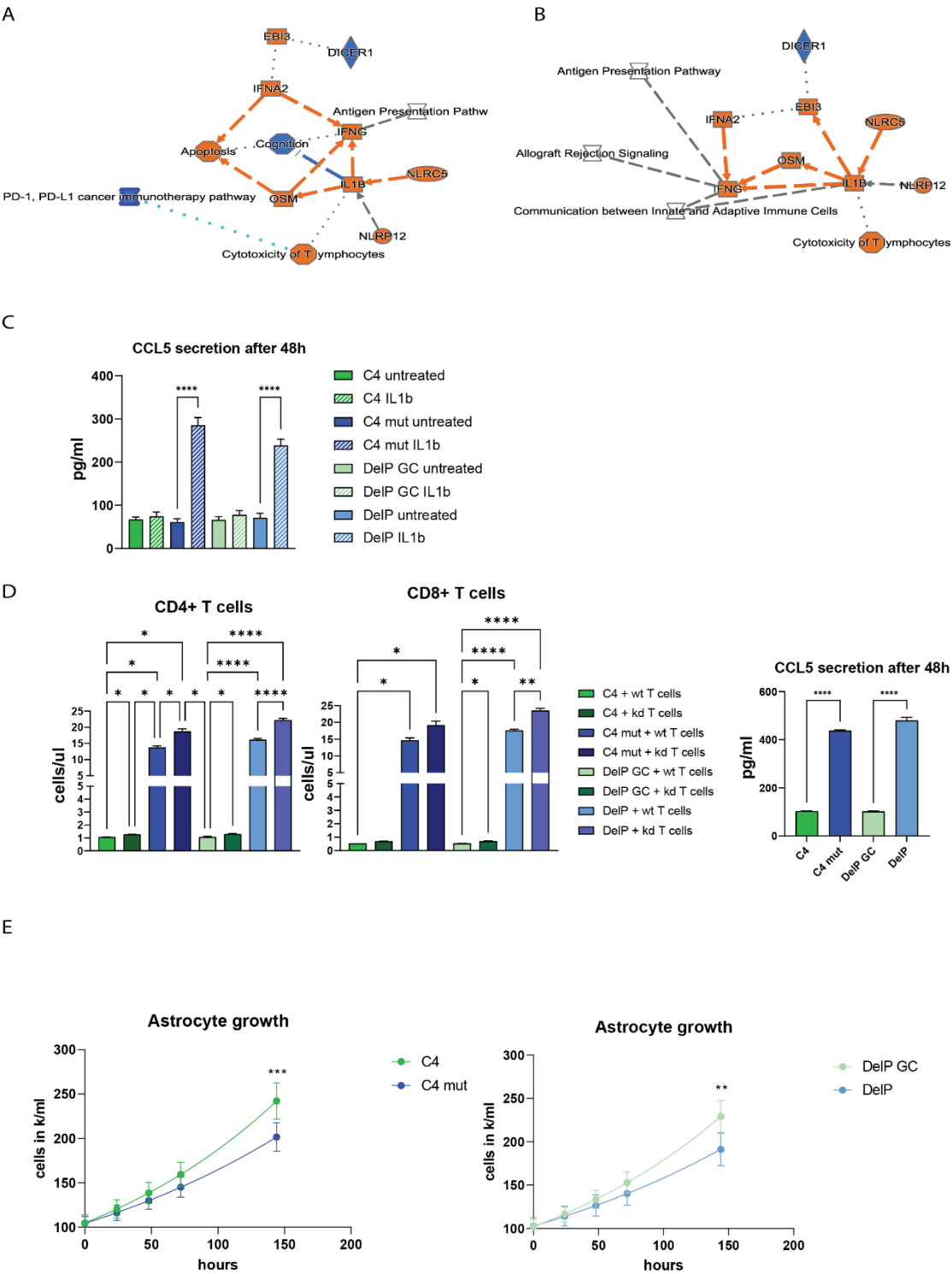
Figure 2: Increased immune response in DJ-1-deficient astrocytes

A and B: Ingenuity pathway analysis. N=3. Relaxed cut offs were chosen due to little number of differentially expressed genes cutoff -0.5-0.5 log2foldchange p adj. 0.1. **C:** CCL5 secretion. N=3. Error bars show SEM. One-way ANOVA was used with Tukey´s multiple comparisons. **D:** T cell migration towards astrocytes and CCL5 secretion measured in this assays. N=3. Error bars show SEM. One-way ANOVA was used with Tukey´s multiple comparisons. **E:** Astrocyte growth (N=3) with SEM error bars. Non-linear fit was calculated (Exponential Malthusian growth) and 2-way ANOVA for each time point with Tukey´s multiple comparisons. Significance is indicated for the last time point. **D-F:** p <0.0001 = ****, p <0.001 = ***, p <0.01 = **, p <0.05 = *.
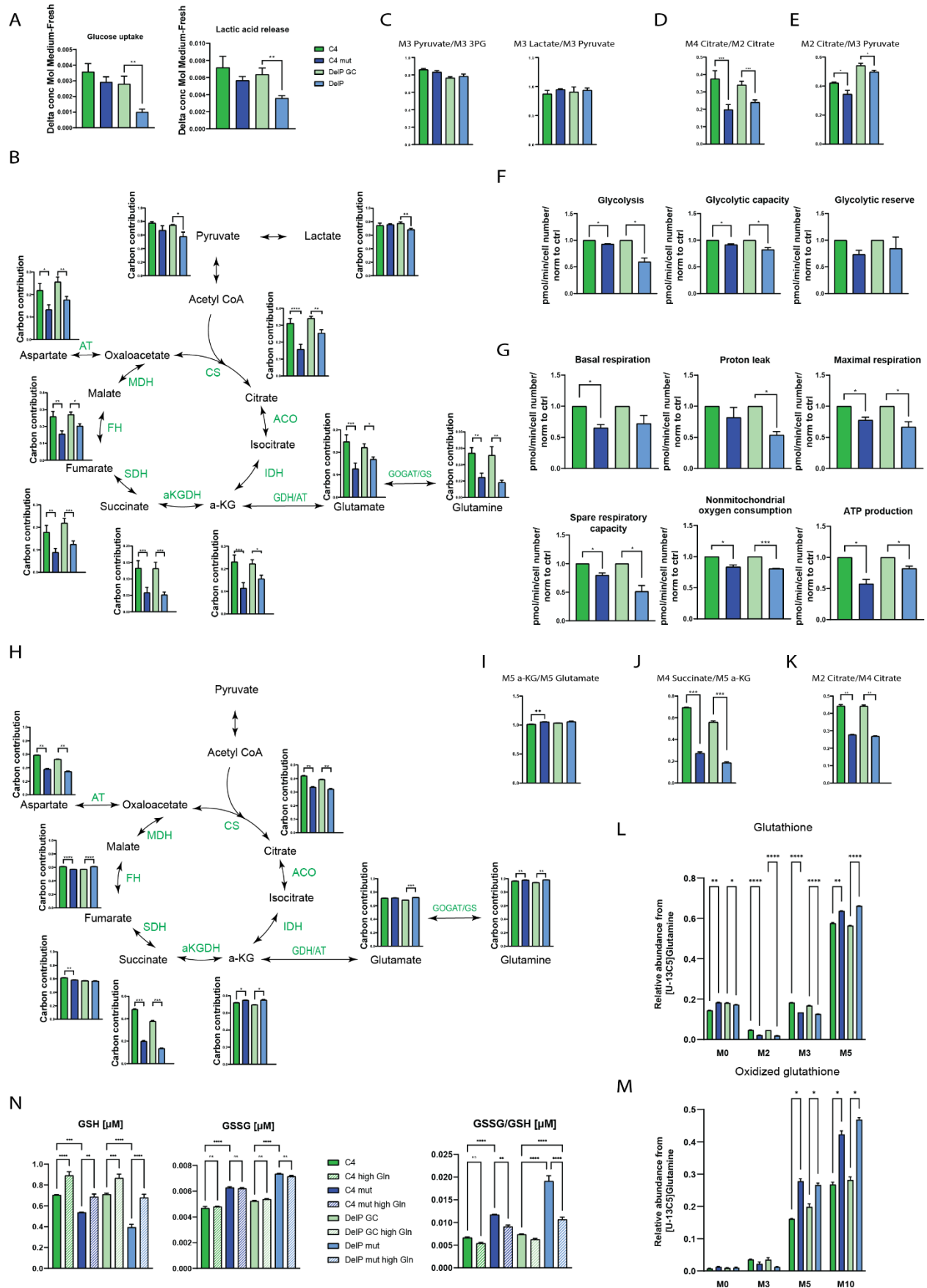
Figure 3: DJ-1 deficiency in astrocytes causes impaired metabolic carbon contribution and GSH levels

A: Analysis of uptakes and release rates from the medium by GC-MS. N=3-5. Error bars show SEM. Two-tailed paired T test was used. **B:** Analysis of glucose metabolism using [U-13C6]Glucose tracing. N=3-5. ^{13}C incorporation in metabolites was analyzed by GC-MS, resulting in heavier metabolites (M1+x), whereas no ^{13}C incorporation corresponds to M0. The graphs show the carbon contribution for each metabolite (calculation see methods part). Error bars show SEM. Two-tailed paired T test was used. **C-E:** Ratios: The higher the ratio, the more production of the respective metabolite from its precursor. Error bars show SEM. Two-tailed paired T test was used. N=3-5. **F-G:** Extracellular flux analysis using Seahorse. N=3-5. Error bars show SEM. Two-tailed paired T test was used. **H-M:** [U-13C5]Glutamine tracing. N=3. Error bars show SEM. Paired T test was used, for GSH and GSSG 2-way ANOVA with Turkey´s multiple comparisons. **N:** GSH and GSSG measurement in cell lysates. N=3. Error bars show SEM. ANOVA was used. **A-N:** p <0.0001 = ****, p <0.001 = ***, p <0.01 = **, p <0.05 = *.
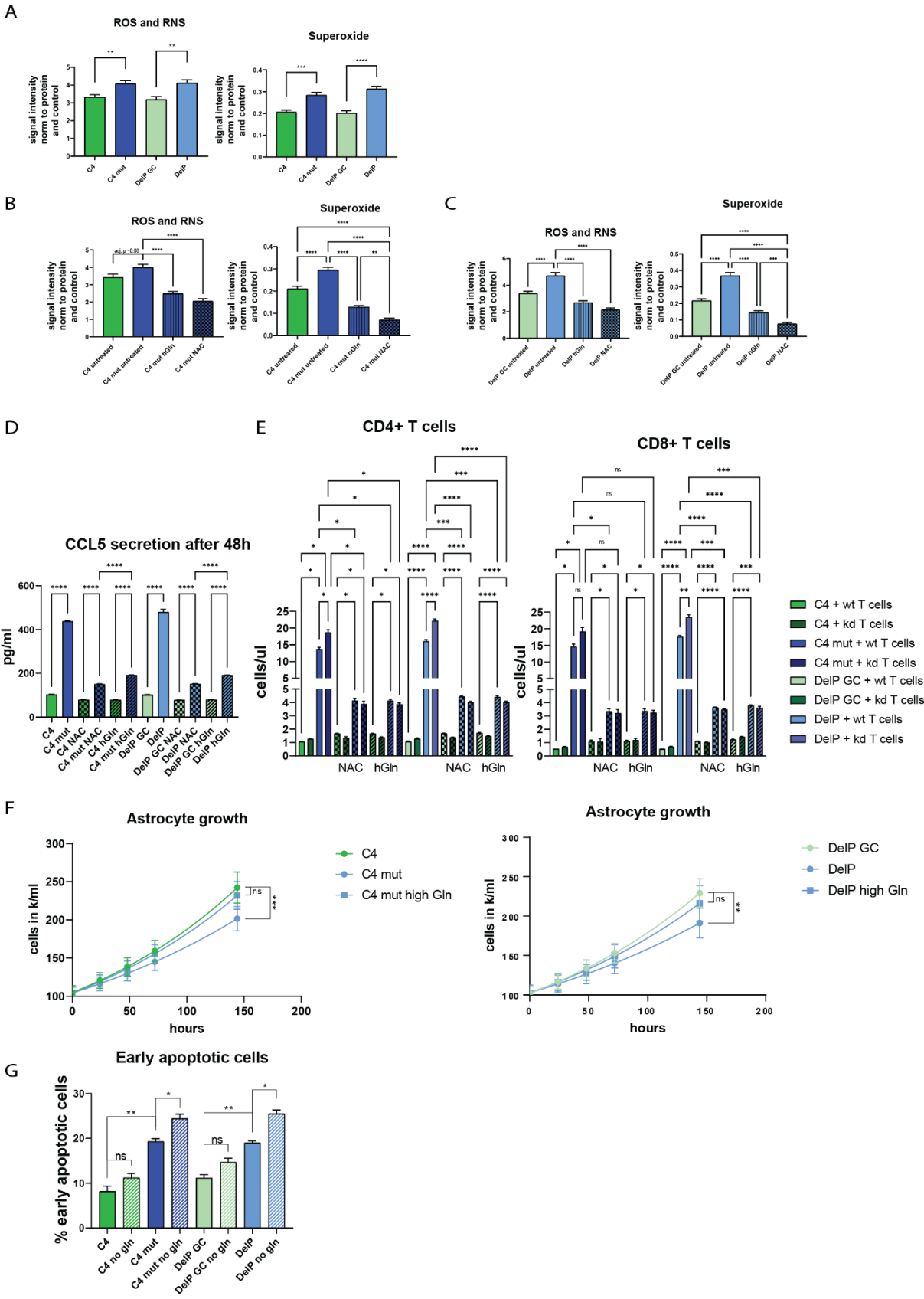
Figure 4: Increased glutamine supply reduces ROS levels and rescues cellular phenotypes

A: Cellular ROS/RNS (left) and superoxide (right) levels in astrocytes. N=3. Error bars show SEM. Two-tailed paired T test was used. **B-C:** Cellular ROS/RNS (left) and superoxide (right) levels in astrocytes upon high glutamine or NAC supplementation. N=3. Error bars show SEM. One-way ANOVA with Šídák's multiple comparisons test was used. **D:** CCL5 secretion upon high glutamine or NAC supplementation. Error bars show SEM. One-way ANOVA was used with Tukey´s multiple comparisons. **E:** T cell migration towards astrocytes. N=3 (3 different blood donors with 3 independent astrocyte differentiations). Error bars show SEM. One-way ANOVA was used with Tukey´s multiple comparisons. **F:** Astrocyte growth (N=3) with SEM error bars. Non-linear fit was calculated (Exponential Malthusian growth) and 2-way ANOVA for each time point with Tukey´s multiple comparisons. Significance is indicated for the last time point. **G:** Early apoptosis assessed by Annexin V staining. N=3. Error bars show SEM. paired T test was used. **A-G:** $p < 0.0001$ = ****, $p < 0.001$ = ***, $p < 0.01$ = **, $p < 0.05$ = *.
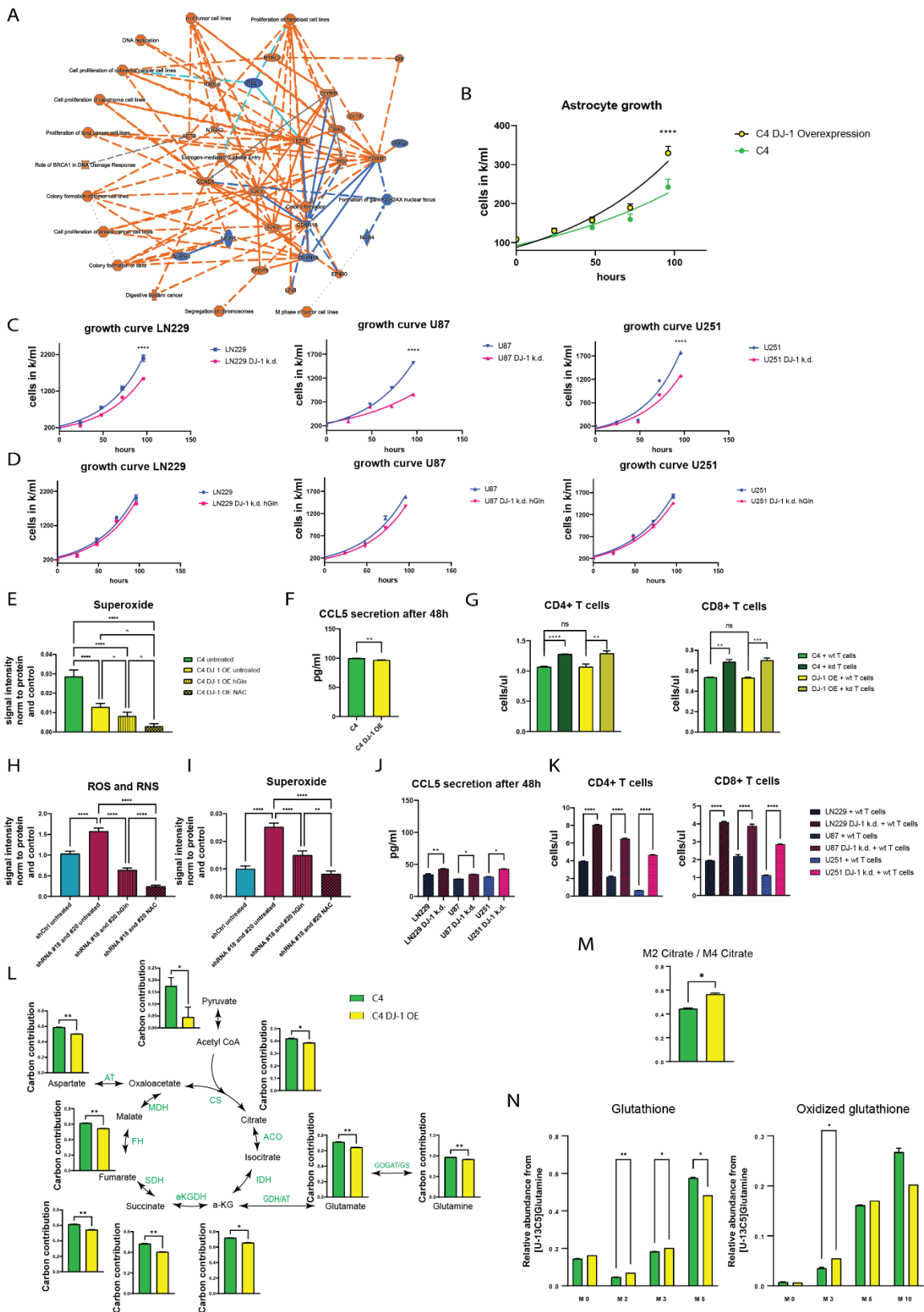
Figure 5: Growth impairment is reversed in DJ-1 overexpressing astrocytes and GBM cell lines

A: Ingenuity pathway analysis of DJ-1 overexpression astrocytes versus wildtype astrocytes. N=3. Upregulated pathways are shown in orange, downregulated ones in blue. **B:** Astrocyte cell growth with SEM error bars. N=3.Nonlinear fit was calculated with exponential (Malthusian) growth. 2-way ANOVA for each time point with Tukey´s multiple comparisons. Significance is indicated for the last time point. **C-D:** Growth curve of GBM cell lines. N=3. Nonlinear fit was calculated with exponential (Malthusian) growth. 2-way ANOVA for each time point with Tukey´s multiple comparisons. Significance is indicated for the last time point. **E:** Mitochondrial ROS level. N=3. Error bars show SEM. One-way ANOVA was used with Tukey´s multiple comparisons. **F:** CCL5 secretion of astrocytes assessed by ELISA. Error bars show SEM. Two-tailed paired T test was used. **G:** T cell migration towards astrocytes. Error bars show SEM. One-way ANOVA was used with Tukey´s multiple comparisons. **H-I:** ROS levels in GBM cells. The mean of the 3 lines is shown. Error bars show SEM. One-way ANOVA was used with Tukey´s multiple comparisons. **J:** CCL5 secretion of GBM cells assessed by ELISA. Each line is shown separately. N=1. Error bars show SEM. One-way ANOVA was used with Tukey´s multiple comparisons. **K:** T cell migration assay in GBM cell lines. Each line is shown separately. N=1. Error bars show SEM. One-way ANOVA was used with Tukey´s multiple comparisons. **L:** Glutamine LC-MS tracing in astrocytes with DJ-1 overexpression compared to wildtype astrocytes. N=3. Error bars show SEM. Two-tailed paired T test was used. **M:** Glutamine LC-MS tracing-based measurement. Ratio M2 citrate over M4 citrate. **N:** Glutamine LC-MS tracing-based measurement of GSH and GSSG. N=3. Error bars show SEM. Two-tailed paired T test was used. **B-M:** $p < 0.0001$ = ****, $p < 0.001$ = ***, $p < 0.01$ = **, $p < 0.05$ = *.
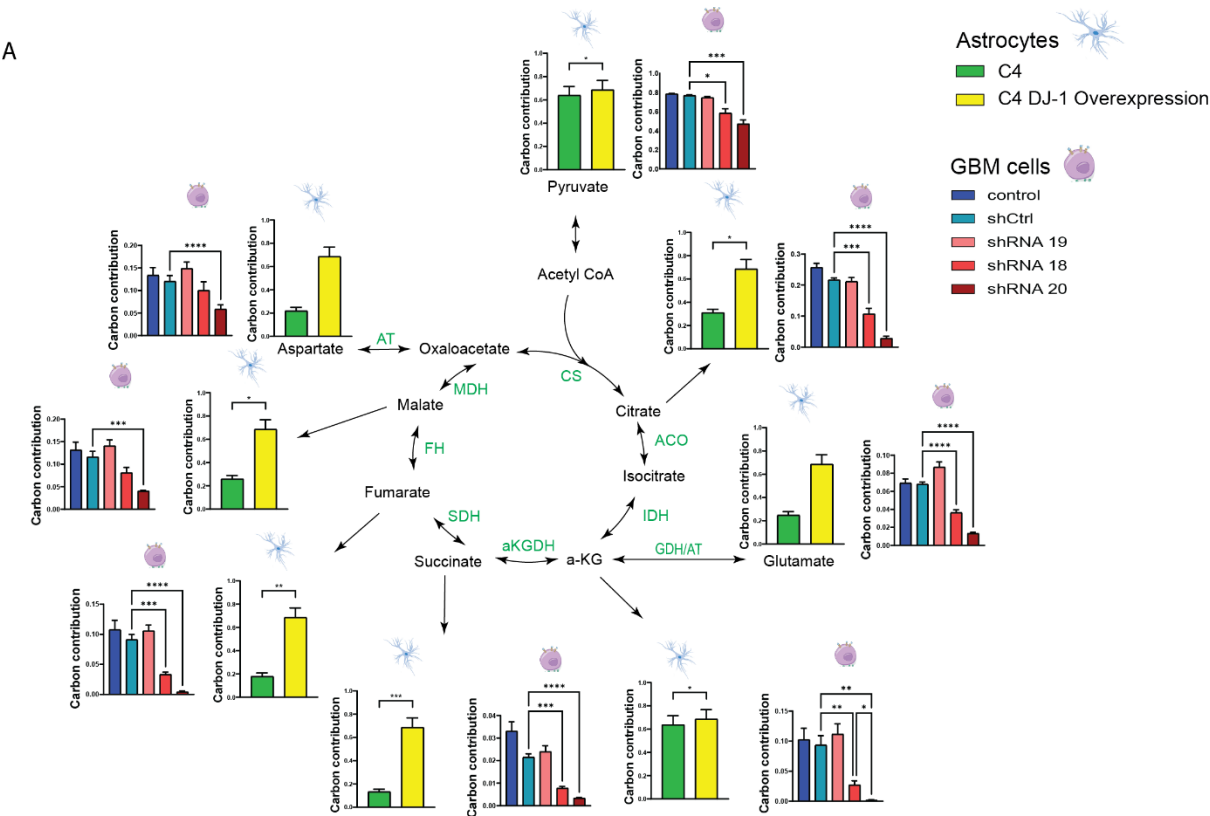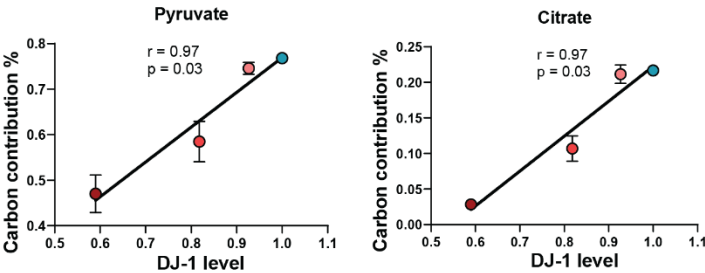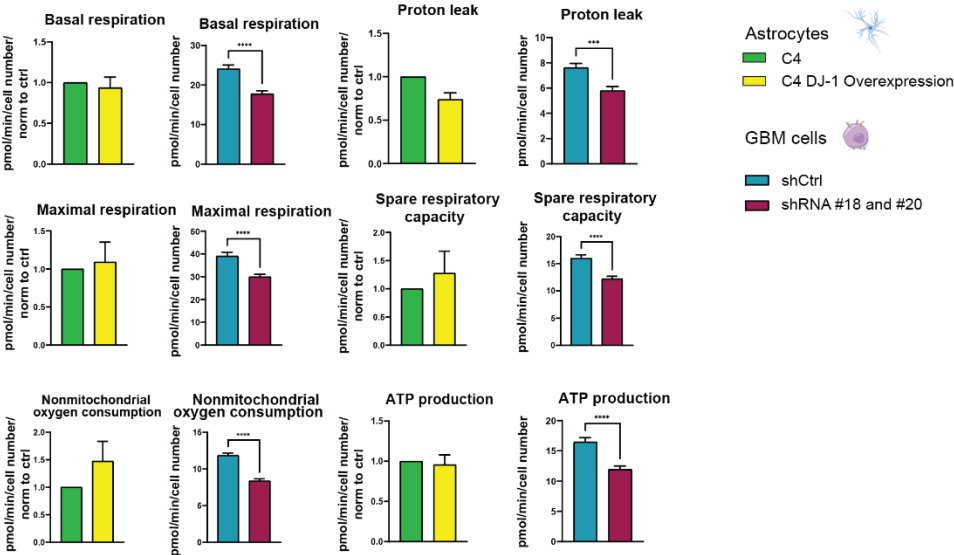
Figure 6: Metabolic impairment is reversed in DJ-1 overexpressing astrocytes and GBM cell lines

A: Analysis of glucose metabolism using [U-13C6]Glucose tracing. Error bars show SEM. One-way ANOVA was used with Tukey´s multiple comparisons. **B:** Analysis of correlation of DJ-1 protein levels and carbon contribution using simple linear regression. **C:** Extracellular flux analysis of oxygen consumption rate in astrocytes and GBM cells. Mean of the 3 different GBM cell lines is shown. Error bars show SEM. Paired T test was used. **A-C:** $p < 0.0001$ = ****, $p < 0.001$ = ***, $p < 0.01$ = **, $p < 0.05$ = *.
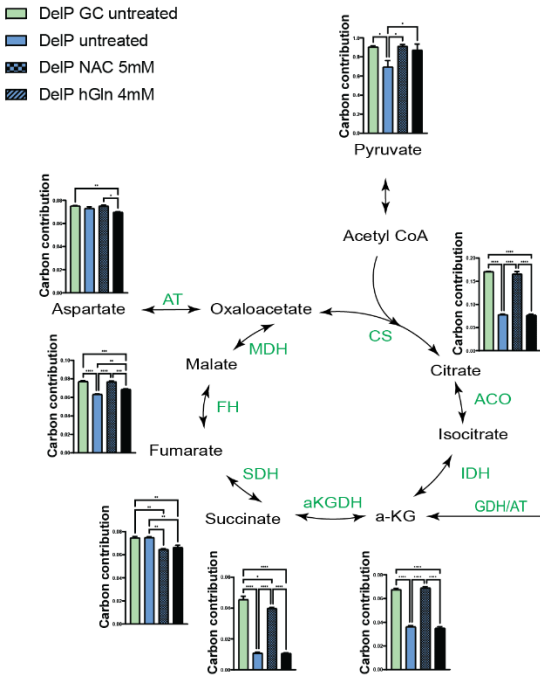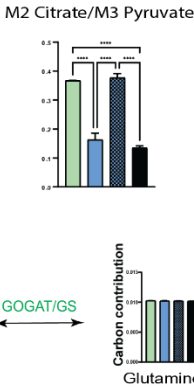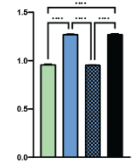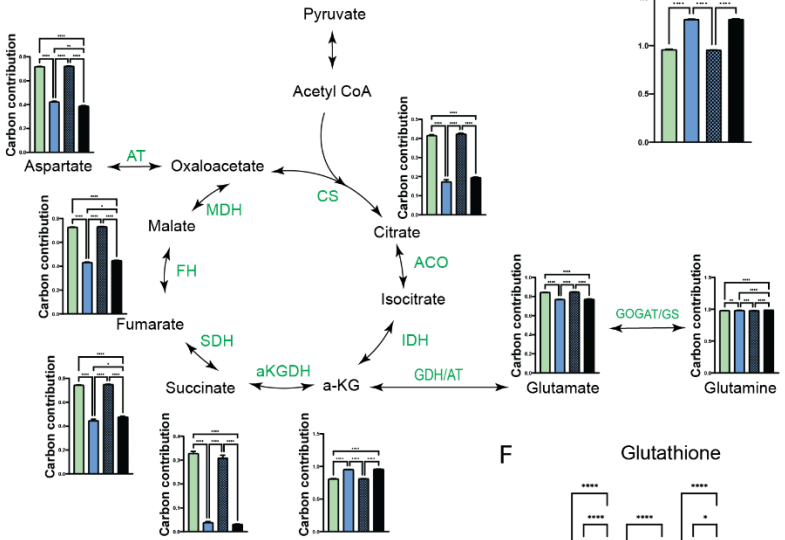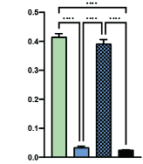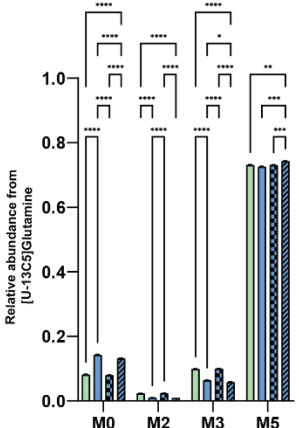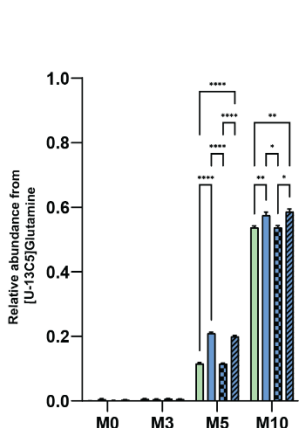
Figure 7: NAC supplementation rescues TCA cycle carbon contribution deficits in DJ-1 deficient astrocytes

A: Analysis of glucose metabolism using [U-13C6]Glucose tracing. N=3. 13C incorporation in metabolites was analyzed by GC-MS, resulting in heavier metabolites (M1+x), whereas no ^{13}C incorporation corresponds to M0. The graphs show the carbon contribution for each metabolite (calculation see methods part). Error bars show SEM. One-way ANOVA was used with Tukey´s multiple comparisons. **B:** Ratios for glucose tracing. N=3. Error bars show SEM. One-way ANOVA was used with Tukey´s multiple comparisons. **C-G:** [U-13C5]Glutamine tracing results. N=3. Error bars show SEM. One-way ANOVA was used with Tukey´s multiple comparisons. **A-F:** $p < 0.0001$ = ****, $p < 0.001$ = ***, $p < 0.01$ = **, $p < 0.05$ = *.

STAR Methods

Cell lines

We used isogenic pairs with two different homozygous DJ-1 mutations - P158Δ in-frame deletion (DelP) and DelP gene-corrected (GC), and c.192G>C (C4 mut) and C4, respectively[24–26].

Cell line	Fibroblasts for iPSC derivation were obtained from	Genetic modification
DelP	PD patient	P158Δ in-frame deletion in the *PARK7* gene
DelP GC	-	Gene corrected counterpart for DelP
C4 mut	-	Insertion of c.192G>C mutation in the *PARK7* gene of C4 control line
C4	Control person	Isogenic counterpart of C4 mut

Cell culture

iPSC

Parkinson´s disease patient-derived iPSC of the DelP mutant and the isogenic control were generated as described by Mencke et al. 2022[25,26]. The C4 and C4 mut line (WT+DJ-1 mutant) were previously described[24]. All cells (iPSC, smNPC, hNSC, astrocytes and neurons) were cultivated in wells and flasks coated with Geltrex (Gibco™ A1413302). iPSCs were cultivated with DMEM/F12 (+Hepes) (Life/Tech – 31330038) supplemented with 10 % mTESR1 (STEMCELL Technologies SARL, 5850), 1 % insulin transferrin selenin (Life/Tech – 41400045), 1 % penicillin/streptomycin (Life/Tech – 15140-163), ascorbic acid 2PM (Sigma – A8960-5G) 64μg/mL, FGF-2 (Peprotech - 100-18B) 10 ng/mL, TGF-β1 (Peprotech - 100-21) 2 ng/mL and Heparin (Sigma – H3149-25KU) 100 ng/ml.

smNPC

Differentiation of iPSC into smNPC was adopted from Reinhardt et al. 2013. On day one of differentiation, the iPSC medium was changed to iPSC medium without FGF-2 and mTESR1 plus 10 μM SB-431542 (Sigma - S4317-5mg), 1 μM dorsomorphin (Sigma – P5499-5mg), 3 μM CHIR 99021 (Axon – Axon1386) and 0.5 μM Purmorphamine (PMA) (Sigma-Aldrich – SML0868-25mg). On day 2, the medium was replaced by N2B27 medium: 50:50 DMEM/F12 w/o HEPES (Life/Tech – 21331046) and NeuroBasal medium (Life/Tech – 21103049) supplemented with 1:200 N2 supplement (Life/Tech – 17502048), 1:100 B27 supplement lacking vitamin A (Life/Tech – 12587-010), 1 % penicillin/streptomycin (Life/Tech – 15140-163) and 1 % GlutaMAX Supplement (Life/Tech – 35050-061) plus 10 μM SB-431542, 1 μM dorsomorphin, 3 μM CHIR 99021 and 0.5 μM PMA. On day five, the medium was changed to N2B27 medium supplemented with 3 μM CHIR 99021, 0.5 μM PMA and 150 μM ascorbic acid (Sigma – A8960-5 g). Upon formation of neuroepithelial structures, the neuroepithelium was picked with a pipet tip, collected in a 1.5 ml tube, dissociated by pipetting and plated into 12-well in N2B27 medium supplemented with 3 μM CHIR 99021, 0.5 μM PMA and 150 μM ascorbic acid.

Astrocytes

Astrocytes were generated from smNPC via hNSCs as described in Palm et al. 2015. 2 days prior to hNSC differentiation, 400 k smNPCs were seeded into one 6-well of a 6-well plate per line. After 2 days, the medium was changed to smNPC medium with 20 ngng/ml FGF-2 (Peprotech - 100-18B). After 4 days, the cells were split with Accutase® (Sigma A6964) and the medium was changed to hNSC medium consisting of DMEM/F12 w/o HEPES (Life/Tech – 21331046) supplemented with N2 supplement (Life/Tech – 17502048), B27 supplement with vitamin A (Life Technologies Europe BV/Thermo Fisher Scientific 17504044), GlutaMAX Supplement (Life/Tech – 35050-061), penicillin/streptomycin (Life/Tech – 15140-163), 40 ng/ml EGF (Peprotech - AF-100-15-1mg), 40 ng/ml FGF-2 (Peprotech - 100-18B) and 1.5 ng/ml hLIF (Peprotech - AF-300-05). hNSCs were split with Accutase® when reaching 70-80 % of confluence. The astrocytic differentiation medium consisted of the basic cultivation medium DMEM/F12 w/o HEPES (Life/Tech – 21331046) supplemented with 1 % penicillin/streptomycin (Life/Tech – 15140-163), 1 % GlutaMAX Supplement (Life/Tech – 35050-061) and 1 % fetal bovine serum (Life/Tech – 10270-106). 1 million hNSCs per T25 flask were plated 2 days prior to astrocyte differentiation. After 2 days, hNSC medium was changed to astrocyte medium. After 40 days, astrocytes were split to get rid of neurons that are dying during the differentiation and during the process of splitting. After 60 days, astrocytes were considered to be mature and all experiments were conducted around day 60.

Glioblastoma cell culture

GBM cell lines LN229, U87 and U251 were kindly provided by Dr. Johannes Meiser from the LIH. Cells were cultured with DMEM 1X high glucose with glutamine (Thermo) and supplemented with 10 % FBS. Knockdown of DJ-1 was done using three different shRNAs (SigmaAldrich) with different efficiencies (#18, #19#, #20). GBM lines were seeded one day prior to transduction (500 k cells per well in 6-well plates for LN229 and 750 k cells per well in 6-well plates for U87 and U251). The next day, cells were transduced for 242424 hours in the presence of polybrene 8 μg/ml. 7 days later, cells were seeded for metabolite glucose tracing (100 k cells per well in 12-well plates), Western blottingblotting (1 million cells per well in 6-well plates) and RNA collection (500 k cells per well in 12-well plates).

In addition, a stable knockdown was generated for each GBM cell line using a mix of shRNA #18 and shRNA #20. Transduction was performed as described. The puromycin selection was started 24 hours post transduction for 4 days (U87: 1.5 μg/ml, U251: 1 μg/ml, LN229: 1.5 μg/ml).

Microglia

Maintenance of iPSC lines (C4 healthy control and DJ-1 deficient C4 mut line) was done in mTeSR™ Plus medium (Stem Cell Technologies). To achieve microglia differentiation, a previously established protocol was implemented[62,63] as described briefly in Badanjak et al. 2021[64].

Midbrain dopaminergic neuronal culture

Midbrain dopaminergic neurons were differentiated as described by Reinhardt et al. 2013. Cells were split on days 2 and 5 during differentiation and then cultivated until final seeding. Neurons were used for experiments from day 21 on.

Generation of DJ-1 overexpression astrocytes

Wildtype iPSC were stably transduced with a GFP-containing DJ-1 overexpression vector. Cells were sorted with a FACS Aria sorter for GFP to obtain around 90 % GFP+ iPSC (Suppl. Figure 6A-C). iPSC were differentiated into smNPCs as described by Reinhardt and colleagues. smNPCs were sorted again for GFP to obtain 100 % GFP+ DJ-1 overexpressing cells (Suppl. Figure 6D). DJ-1 overexpression was confirmed by qPCR and Western blotting (Suppl. Figure 6E). Wildtype and DJ-1 overexpression astrocytes were differentiated into astrocytes and cultured as described by Palm and colleagues[65] (Suppl. Figure 7). Characterization of astrocytes was performed by FACS. Wildtype iPSC-derived midbrain dopaminergic neurons (differentiated according to Reinhardt and colleagues) were used as negative control.

Knockdown of DJ-1 in GBM cell lines

To assess the phenotypic effect of DJ-1 downregulation in the GBM cells, we used lentiviral constructs expressing three different shRNAs (Suppl. Fig. 10B-C). shRNA #20 had the strongest knockdown efficiency in all three lines and reduced the DJ-1 mRNA levels by around 80 % compared to shCtrl and the DJ-1 protein levels to around 50-60 % compared to shCtrl (Suppl. Fig. 10B-C).

Growth assay

Astrocytes were seeded at a density of 100.000 cells per well in 12-well plates in duplicates and GBM cells were seeded at a density of 200.000 cells per well in 6-well plates in duplicates. Cells were counted at time points 0, 24, 48, 72 and 96 hours.

Imaging

Antibodies used for imaging can be found in supplementary Table 1.

Immunocytochemistry

iPSC, smNPC and hNSC were plated onto coverslips in 24-well plates (50.000 cells per well) and fixed with 4 % PFA prior to staining. Cells were stained for the typical markers listed in Table 1 using standard immunocytochemistry techniques. Images were acquired using a Zeiss spinning disk confocal microscope. Astrocytes, neurons and microglia were plated in CellCarrier-384 ultra Microplates (Perkin Elmer 6057300) (10.000 cells per well for neurons and astrocytes, 25.000 cells per well for microglia). All cells were fixed with 4 % PFA for 15 minutes. Cells were stained for the markers listed in Table 1 using standard immunocytochemistry methods. Images were taken using a Yokogawa cell voyager microscope. 16 images were taken per well in 384-well plates. Image analysis was performed using Matlab.

Immunohistochemical staining

Sections of frontal cortex were cut at 6 µm thickness from formalin fixed, paraffin embedded blocks and mounted onto glass slides. Sections were stained automatically by using two equivalent Dako Omnis Autostainers (Dako), including hematoxylin counterstaining. According to the manufacturer's instructions, each staining was performed by using default IHC protocols from the Omnis instrument software. Once stained, the tissue sections were dehydrated by rinsing them with EtOH and coverslipped following routine procedures. Finally, they were analyzed by using a brightfield microscope.

Flow Cytometry

Characterization of astrocytes

Astrocytes and neurons were detached in single cell suspension using Accutase® and centrifuged at 300 g for 3 minutes. Cells were washed 3 times with PBS, at 700 g for 5 minutes and fixed with 4 % PFA for 15 min. Cells were washed 3 times with PBS, at 700 g for 5 minutes and split into FACS tubes for the different

stainings, before being resuspended in Saponin buffer (0.05 % Saponin/1 % BSA/PBS). Cells were incubated for 20-30 minutes at 4 °C. For unstained and isotype controls, a few µl of each cell line was mixed. After 30 minutes, cells were diluted in PBS, pelleted at 700 g for 5 minutes and resuspended in 50 µl of the primary antibody solution. Primary antibodies were prepared 1:50 in Saponin buffer (50 µl per tube). Cells were stained for GFAP, FoxA2, TH, TUJ1 and S100β or Recombinant Rabbit IgG, monoclonal [EPR25A] Isotype Control (ab172730) and Mouse IgG2a, kappa monoclonal [MG2a-53] Isotype control (ab18415). No primary antibody was added to the unstained control. Cells were incubated for 30 minutes at 4 °C. Cells were washed 3 times with diluted FACS buffer, centrifuged at 700 g for 5 minutes (FACS Buffer: PBS + 5 % BSA + 0.1 % Sodium Azide (NaN3), Diluted FACS Buffer: 1:5 dilution of FACS buffer). Cells were resuspended in secondary antibody solution (Alexa Fluor 568 Goat α-Rabbit IgG (H+L), Alexa Fluor 647 Goat α-Mouse IgG (H+L), 1:100 in PBS/10 % BSA, 50 µL per tube) and incubated for 30 minutes at 4 ºC, washed 2x with diluted FACS buffer, centrifuged at 700 g for 5 minutes, resuspend in 250 µL – 350 µL PBS and analyzed with BD LSRFortessa flow cytometry analyzer. The mean fluorescence intensity was assessed on single cells by using FlowJo LLC software.

Annexin V assay

Astrocytes were deprived from glutamine in the medium for 4 hours. After 4 hours, cells were detached with Accutase® and centrifuged at 300 g for 3 minutes. Cell pellets were resuspended in 300 µL of 1X Annexin V binding buffer (Annexin-binding buffer 5X concentrate, Thermo Fisher Scientific B.V.B.A. V13246). 100.000 cells in 100 µL were used per sample and 5 µL of Annexin V, Alexa Fluor® 568 conjugate (Life/Tech Europe BV/Thermo Fisher Scientific A13202) were added, and the samples were incubated in the dark for 15 minutes. After 15 minutes, 400 µL of 1X Annexin V binding buffer were added. For FACS analysis, 1 µL of DAPI were added per tube, and samples were analyzed with BD LSRFortessa flow cytometry analyzer. The mean fluorescence intensity was assessed on single cells by using FlowJo LLC software.

T cell migration assay

T cell medium (for 500 ml: IL2 (, Bio-Techne, 202-IL-010), CD3/CD 28 T cell activator (Stemcell, 10991), 450 ml T cell media IMDM (Gibco, 21980-032), 50 ml heat-inactivated FBS (10 %) (Gibco, 10500-064), 5 ml Pen/Strep (1 %) (Gibco, 15140-122), 5 ml non-essential amino acids (NEAA) (1 %) (Gibco, 11140-035), 0.5 ml β-mercaptoethanol (50 µM) (Gibco, 21985023)). T cell medium was adjusted to 1 % for the assay to avoid the generation of an FBS gradient that can lead to T cell migration.

Buffy coats were retrieved from different donors (each donor was treated as one biological replicate) from Red Cross Luxembourg (ethical approval proof available with author). PBMCs were isolated using SepMate™ PBMC Isolation Tubes (50 ml) and Lymphoprep™ Density Gradient Medium following standard procedures described by STEMCELL Technologies (https://www.stemcell.com/products/brands/sepmate-pbmc-isolation.html). PBMCs were frozen down until T cell isolation. PBMCs were cultivated in RPMI with 10 % FBS and 1 % penicillin/streptomycin. 11 days prior to the migration assay, PBMCs were thawed. T cells were isolated the day after using the Pan T cell isolation kit from Miltenyi following the manufacturer's instructions. Cells were characterized by FACS on the day of isolation (FACS staining for CD3, CD4, and CD8). T cells were activated on the next day prior to viral transduction using ImmunoCult™ Human CD3/CD28 T Cell Activator (Stemcell Technologies, Catalogue #10971) following the 'manufacturer's manufacturer's protocol. The next day, T cells were transduced with shCtrl and shRNA for DJ-1 #18, #19, and #20. The supernatant was removed after 24 hours and 3 days later, 200.000 astrocytes were seeded into a geltrex-coated bottom well of a 12 mm Transwell® with 3.0 µm Pore Polycarbonate Membrane Insert plate (Corning, 3402). Cells were either seeded in normal astrocyte medium or astrocyte medium supplemented with 5 mM NAC. After 2 days, astrocytes were stimulated with 10 ng/ml IL-1β in either normal astrocyte medium, astrocyte medium containing 5 mM NAC or 4 mM glutamine (double amount). The next day, T cells were activated again using ImmunoCult™ Human CD3/CD28 T Cell Activator. The day after (T cells were already 10 days in culture), inserts were placed into the stimulated astrocytes and 100.000 T cells were added in T cell medium with 1% FBS only into each insert. One well was kept without astrocytes as passive migration control and one well contained only astrocyte medium with CCL5 as positive control. Cells were incubated for 4 hours. After 4 hours, the transwell filter was removed and the T cells present in the upper chamber were saved. The astrocyte medium in the lower chamber was centrifuged to retrieve migrated T cells. The medium was saved for ELISA to analyze cytokine release after 48 hours upon IL-1β stimulation. T cells were analyzed by FACS using the antibodies listed in Supplementary Table 1 and CountBright™ Absolute Counting Beads following the manufacturer's instructions. Stopping gate was CD3.

RNA extraction, cDNA synthesis, qPCR

RNA extraction was performed using the RNeasy Kit fromfrom Qiagen according to manufacturer's instructions. RNA concentration was assessed using a NanoDrop™ spectrophotometer. Subsequent cDNA synthesis was done with the High-Capacity cDNA Reverse Transcription Kit with Rnase Inhibitor (Applied Biosystems™) following the manufacturer's instructions. qPCR was done with the hDMSPhigh-throughput platform at the LCSB using the Echo® Acoustic Liquid Handling droplet ejection system. qPCRs were run with a LightCycler® 480 machine (40 cycles per run). Standard curves for each primer were included to assess the efficiency of each primer and subsequently calculate the Pfaffl ratio.

Primer target	Reference/Sequence
PARK7	AICSXDR
ACTB	Hs03023880_g1
hACTB_F3	AAACTGGAACGGTGAAGGTG
hACTB_R3	AGAGAAGTGGGGGTGGCTTTT
GM-CSF_F	AATGTTTGACCTCCAGGAGCC
GM-CSF_R	TCTGGGTTGCACAGGAAGTTT
hIL6_ex_F65	TGAACTCCTTCTCCACAAGCG
hIL6_ex_R215	TCTGAAGAGGTGAGTGGCTGTC

RNA sequencing

RNA for RNA sequencing was extracted as described above (chapter: RNA extraction, cDNA synthesis, qPCR). RNA quality was assessed using the Agilent 2100 Bioanalyzer, RNA integrity (RIN) values were >8. Libraries were prepared using the TruSeq Stranded mRNA library prep kit and sequenced on a NextSeq2000. For GBM samples paired reads of 51 bp length were generated, for astrocyte samples single reads of 75 bp length were generated.

Data was processed using an in-house snakemake[66] workflow available as a git repository https://git-r3lab.uni.lu/aurelien.ginolhac/snakemake-rna-seq (release v0.2.3, and singularity image v0.4). Raw read quality was assessed by FastQC (v0.11.9)[67]. Adapters are removed using AdapterRemoval (v2.3.1)[68], with a minimum length of the remaining reads set to 35 bp. Reads were mapped to hg38 (GRCh38.p13) using STAR (v.2.7.4a)[69], featureCounts from the R package Rsubread (2.2.2)[70] was used to count reads. All counts >10 were used for differential gene expression analysis using the R package DESeq2 (v1.28.1)[71]. Normalization in DEseq2 was done using apeglm (v.1.10.0)[72]. All FPKM were calculated using DESeq2 package. Pathway analysis on DEGs with false discovery rate < 0.1 and a minimum $\log_2$-fold change cut-off of +/- 0.5 was performed using Ingenuity Pathway Analysis tool from Qiagen, Content version: 60467501 (release date: 2020-11-19).

Western Blotting

Cells were lysed with 200 µL lysis buffer (1 % SDS + protease inhibitor cocktail tablet Roche) per well in 6-well plates and the lysate was collected by scraping. The lysate was transferred into 1.5 ml tubes and boiled for 5 minutes at 95 °C, centrifuged briefly and stored at -80 °C. Samples were sonicated after thawing. Protein quantification was performed using the Pierce BCA assay. Invitrogen™ NuPAGE™ 4 to 12 %, Bis-Tris, 1.0 mm, Mini Protein Gels with 12-wells were used for all blots. Prior to loading, samples were diluted with loading buffer (NuPAGE™ LDS Sample Buffer (4X) with RA 10x) and boiled for 5 minutes at 95 °C. One ml of anti-oxidant for 400 ml of running buffer (NuPAGE™ MES SDS Running Buffer (20X)) were used. As ladder, PageRuler Plus Prestained Protein Ladder was used. After the run, wet transfer was performed following standard protocols (transfer buffer 1:5, 99 % Ethanol, 1X Tris glycine in

MilliQ water). The transfer was run for 75 minutes at 100 V. Ponceau red was always used after the transfer. The membrane was rinsed with TBS-T and blocked with 5 % milk in TBS-T for 1 hour prior to incubation of the primary antibody overnight at 4 °C with rotation. The next day, the membrane was washed 3 times for 10 minutes in TBS-T with shaking and incubated with the secondary antibody for 1 hour at room temperature with shaking. After 1 hour, the membrane was washed 3 times for 10 minutes in TBS-T with shaking before revealing the gel using an Odyssey® Imager after incubating the membrane for 30 seconds with ECL solution: 50 % Peroxide solution + 50 % Luminol solution.

Metabolic carbon contribution analysis using gas chromatography – mass spectrometry (GC-MS) and Liquid chromatography – mass spectrometry (LC-MS)

Metabolite extraction

Intracellular

Stable isotope-assisted metabolomics analyses were conducted using [U-13C6]Glucose or [U-13C5]Glutamine tracers. Cells were incubated with the tracing medium for 48 hours to reach an isotopic steady-state (200.000 cells per well in 12-well plates, with technical triplicates). After 48 hours, intracellular metabolite extraction was performed at 4 °C. First, the medium was collected for further extracellular metabolite analysis. For [U-13C6] Glucose labelling, measured using GC-MS, cells were washed once with 1 mL 0.9 % NaCl solution. Then, 200 µL of methanol were added (containing 5 µg/mL Tridecanoid-*D25* acid as internal standard), followed by the addition of 80 µL of MilliQ water (4 °C) (containing 1 µg/mL Pentanedioic-*D6* acid as internal standard). The plates were gently shaken for 10 minutes at 4 °C before the mixture was transferred into a new 1.5 mL-reaction tube containing 100 uL of Chloroform. The reaction tubes were shaken for 5 minutes at 4 °C and full speed in an Eppendorf Thermomixer. For phase separation, 100µL of Chloroform and 100 uL of water were added. Afterwards, the reaction tubes were vigorously vortexed for 10 seconds and centrifuged for 5 minutes at 4 °C and full speed. 125 µL of the upper polar phase were transferred into a GC vial with micro insert. The samples were evaporated in a centrifugal vacuum concentrator at -4 °C, capped and stored at -80 °C until GC-MS measurement.

For LC-MS analyses, cells were washed once with 1 mL 0.9 % NaCl solution. Then, 250 µL of an extraction fluid (4:1, Methanol/H_2O mixture) were added to each well. The following internal standards were added to the water fraction of the extraction fluid: [UL-^{13}C]Ribitol (c = 2 µg/mL), Pentanedioic-*D6* acid (c = 2 µg/mL), Tridecanoic-*D25* acid (c = 10 µg/mL), 6-Chloropurine riboside (c = 10 µg/mL), 4-Chloro-DL-phenylalanine (c = 10 µg/mL), Nε-Trifluoroacetyl-L-lysine (c = 10 µg/mL), Thionicotinamide adenine dinucleotide (c = 10 µg/mL). Then, 30 µL of MilliQ water (4 °C) were added per well and the procedure was continued like described above.

Extracellular

Medium was filtered using a Phenex Regenerated Cellulose (RC) Syringe Filters µm filter prior to freezing to remove any cells or debris. 180µL of the sample (spent medium, fresh medium and calibrants) were added to 180 µL ice-cold extraction fluid (5:1, Methanol/H_2O mixture). Two internal standards, containing [U-13C]Ribitol (c =final concentration: 50 µg/mL) and Pentanedioic-*D6* acid (final concentration: 20 µg/mL), were added to the water fraction of the extraction fluid. Then, samples were vortexed for 10 seconds and incubated for 15 minutes at 4 °C at maximum speed in an Eppendorf Thermomixer, followed by centrifugation for 5 minutes at 4 °C and full speed. 50 µL of the supernatant were transferred into a GC vial with micro insert. The samples were evaporated in a centrifugal vacuum concentrator at -4 °C, capped and stored at -80 °C until GC-MS measurement.

Metabolomics data acquisition and data analysis

Sample measurements were performed at the LCSB Metabolomics Platform using SIM-TCA, SIM-MED and LC-GlasgowMA methods.

Explanation of Metabolite tracing illustrated in supplementary Figure 14.

Intracellular

R was used to analyze the MS data. Details on all packages used can be found in the code deposited at https://gitlab.lcsb.uni.lu/TNG/papers/PD_GBM_publication. Raw data (mass isotopomer distribution for each metabolite) were loaded as excel files and formatted according to tidy data guidelines[73]. The means of the three independent replicates per biological replicate were calculated for each metabolite before calculating the mean of the biological replicates. Data were plotted in R using ggplot. Means and single values for each metabolite (isotopologue fractions) per sample were exported as .csv files and carbon contribution was calculated from isotopologue fraction for each metabolite as follows: for example for a 5 carbon molecule: $(M1*1 + M2*2 + M3*3 + M4*4 + M5*5)/5$. Final graphs were generated using GraphPad Prism. Full MIDs can be found deposited at https://gitlab.lcsb.uni.lu/TNG/papers/PD_GBM_publication and as supplementary Figures 12 and 13.

Extracellular

After loading the raw data (internal standard normalized peak areas), data were formatted according to tidy data guidelines. Outliers in standards were removed using interquartile range. To determine the concentration of each metabolite in the cell culture tracing medium and the fresh tracing medium, the calibration curve (measured in technical triplicates) was used to apply linear regression and calculate the unknown concentration for each metabolite. The concentration of each metabolite in Mol was subtracted by the concentration in Mol for each metabolite measured in the fresh tracing medium to obtain a delta corresponding to uptake and release of the respective metabolite in Mol. The means of the three independent replicates per biological replicate were calculated for each metabolite in Mol before calculating the mean of the biological replicates. Data were again plotted in R using ggplot. Means and single values for each metabolite per sample were also exported as .csv files and final graphs were generated using GraphPad Prism.

Seahorse

Oxygen consumption rate (OCR) and Extracellular Acidification Rate (ECAR) as well as the glycolytic stress test were measured in whole cells using the Seahorse Xfe96 Cell Metabolism Analyzer (Agilent). The concentrations of mitochondrial toxins and compounds used were optimized according to the manufacturer's recommendations. Final concentrations are listed in Table 2.

Table 2

Compound	Reference	Company	Molecular weight	Final concentration for assay
Oligomycin	Lot APN14317-13, ab141829	Abcam		10 µM for OCR
Oligomycin	Lot APN14317-13, ab141829	Abcam		100 µM for glycolytic stress test
FCCP	C2920-10MG	Sigma		2 µM
Rotenone	R8875-1G	Sigma	394.42	5 µM
Antimycin A	A86474	Sigma	532	5 µM
Glucose Monohydrate	6887	Carl Roth	180.156	80 mM
2-DG	D8375-5G	Sigma	164.16	500 mM

Compound aliquots were dissolved in Seahorse Base medium on the day of the experiment. To prepare the Seahorse Base medium, 990 mL of ddH2O were autoclaved and 1 vial of DMEM Basal Powder (Sigma D5030) was added, the solution was sterile filtered, and the pH was adjusted to 7.4 ± 0.05 at 37 °C (pH was checked for every experiment). Seahorse assay medium for the two different assays was prepared according to the manufacturer's instructions.

Laminin (Sigma, L2020; 25 µL aliquot) was added to 2.55 mL of PBS before 25 µL of diluted laminin were added into each well of a Seahorse Xfe96 well plate. The plate was incubated overnight at 37 °C. Astrocytes were plated in the Seahorse Xfe96 well plate 24 hours prior to measuring at a density of 80.000 cells per well. Perimeter wells were not used due to evaporation. After seeding, the plate was left at room temperature for 1 hour to prevent edge-effects. After 1 hour, all unused wells were filled with astrocyte media only and incubated overnight at 37 °C + 5 % CO_2. The cartridge was hydrated using 200 µL of XF-calibrant solution and incubated overnight at 37 °C in a non-CO_2 incubator. 100 mL of each of the prepared Seahorse assay media were aliquoted, the pH was adjusted to 7.4 ± 0.05 at 37 °C and the media were incubated in a non-CO_2 incubator overnight. The media of the cells was changed approximately 1 hour before starting the experiment by removing 60 µL of culture media (leaving 20 µL) from each well, rinsing 2x with 200 µL of Seahorse assay media and eventually adding 155 µL of assay media to each well for a final volume of 175 µL/well. The plate was then incubated in non-CO_2 incubator for at least an hour so that the cells were allowed to equilibrate to the assay media. The compounds were loaded into the cartridge on the Seahorse utility plate using the loading guide plates while the cells are incubating in the non-CO_2 incubator. After the loading of the compounds, the plate was incubated for 30 minutes in a non-CO2 incubator before the measurement was started. Normalization was performed using the CyQUANT® kit. After the Seahorse assay, the assay media was removed from the wells by inverting and blotting the surplus onto paper towels and the Seahorse cell culture plates were stored at -80 °C until the CyQUANT® assay was performed. The CyQUANT® GR stock solution in DMSO was brought to room temperature. The Seahorse cell culture plates were also equilibrated at room temperature. The 20x concentrated cell-lysis buffer stock solution (Component B) was diluted 20-fold in distilled water. For each well, 200 µL were required. The

CyQUANT® GR stock solution (Component A) was diluted 400-fold into the 1X cell-lysis buffer. 200 μL of the CyQUANT® GR dye/cell-lysis buffer were added to each well. The plates were incubated 2–5 minutes at room temperature, protected from light. The samples were transferred into a 96-well plate before measuring the sample fluorescence using a fluorescence microplate reader with filters appropriate for ~480 nm excitation and ~520 nm emission maxima.

ROS assay

5000 GBM cells and 5000 astrocytes were seeded into a CellCarrier-384 ultra Microplate (Perkin Elmer 6057300). For NAC treated cells, cells were seeded with medium containing 5 mM NAC. Two days later, the medium was changed and for the hGln condition (GlutaMAX Supplement (Life/Tech – 35050-061)), medium with hGln (4 mM for astrocytes medium, 8 mM for GBM cell medium) was added. Two days after that, cells were starved for 4 hours without FBS. To analyze ROS, the ROS-ID® Total ROS/Superoxide detection kit - ENZ-51010 was used. The assay was conducted following the manufacturer's instructions (except no pretreatment with NAC for 30 minutes was necessary as respective wells (NAC treated) had NAC for 9696 hours). After the assay, plate contents were emptied and 20 μL of RIPA buffer were added per well. The plate was stored for 30 minutes at -80 °C. After 30 minutes, the plate was retrieved from the freezer and the lysis buffer was thawed. Once the buffer was thawed, Pierce BCA was performed according to the manufacturer´s protocol (30 μL of BCA working solution per well).

GSH/GSSG measurement

Cells were seeded in a 96-well plate with different media (20k cells per well). Cells were cultivated for 48 hours. Two days later, cells were detached, counted and 3000 cells per 384-well for each condition were centrifuged. The GSH and GSSG measurement was performed using the GSH GSH/GSSG-Glo™ Assay from Promega following the manufacturer's instructions in 384-well format.

Data analysis

Each GBM cell line was treated as biological replicate so for each line, experiments were run in technical replicates and statistics were calculated using the mean of all the data. Metabolomics data were analyzed using R. Images were analyzed using the Zeiss Zen program and Yokogawa images were analyzed using Matlab and R. All original code has been deposited at https://gitlab.lcsb.uni.lu/TNG/papers/PD_GBM_publication. FACS data were analyzed using FlowJo LLC software. Final graphs were made using GraphPad Prism. All experiments have sample sizes equal to or higher than 3. Exclusion criteria were biological and technical variation. Statistical method of comparison was paired t-test for the two isogenic pairs. All error bars show the standard error of the mean.

Materials availability statement

All cell lines are available upon request. More information on use restrictions and on how to submit the request to obtain the cell lines is available at DOI: 10.17881/0m4p-ht15.

Data and code availability

The raw RNA sequencing data for this manuscript are not publicly available due to its sensitive nature. The data are available upon request. All derived data, data behind figures and supplementary material has been deposited at

https://data.mendeley.com/datasets/xv5gt4hpjd/draft?a=f39d6035-c276-4c2b-90c6-e8f21b4cffdd

under CC-BY license and it will be publicly available at DOI: 10.17632/xv5gt4hpjd.

More information on availability of data and how to submit the request to access the sensitive dataset is available at DOI: 10.17881/0m4p-ht15.

Code is deposited at https://gitlab.lcsb.uni.lu/TNG/papers/PD_GBM_publication.

Any additional information required to reanalyze the data reported in this paper is available from the lead contact upon request.

Supplementary material

Supplementary Table 1: Antibody list

| Cell type to be stained	Antibody	Species	Company	Reference	Dilution	2ndary antibody all 1:1000 for ICC, for FACS 1:100
iPSC	Anti Nanog	rabbit	abcam	ab21624	dilution 1:1000	Alexa Fluor 568 Goat α-Rabbit IgG (H+L) A11036
iPSC	Anti Oct3/4	mouse	santa cruz	sc-5279	dilution 1:1000	Alexa Fluor 647 Goat α-Mouse IgG (H+L) A21236
iPSC, smNPC	Anti SOX2 (Y-17)	goat	santa cruz	sc-17320	dilution 1:250	Alexa Fluor 647 Donkey α-Goat IgG (H+L) A21447
smNPC, hNSC	Anti Nestin	mouse	R&D Systems	MAB1259	dilution 1:1000	Alexa Fluor 647 Goat α-Mouse IgG (H+L) A21236
smNPC, hNSC	Anti Musashi	rabbit	abcam	ab21628	dilution 1:250	Alexa Fluor 568 Goat α-Rabbit IgG (H+L) A11036
hNSC	Anti SOX1	goat	R&D Systems	AF3369	dilution 1:250	Alexa Fluor 647 Donkey α-Goat IgG (H+L) A21447
Astrocytes and neurons	Anti ID3	mouse	abcam	ab236505	dilution 1:1000	Alexa Fluor 647 Goat α-Mouse IgG (H+L) A21236
Astrocytes and neurons	Anti NFIA	rabbit	abcam	ab228897	dilution 1:1000	Alexa Fluor 568 Goat α-Rabbit IgG (H+L) A11036
Astrocytes and neurons	Anti EZRIN	rabbit	abcam	ab40839	dilution 1:500	Alexa Fluor 568 Goat α-Rabbit IgG (H+L) A11036
Astrocytes and neurons	Anti S100b	rabbit	abcam	ab868	dilution 1:500	Alexa Fluor 568 Goat α-Rabbit IgG (H+L) A11036
Astrocytes and neurons	Anti EAAT2	mouse IgG2b	santa cruz	sc-365634	dilution 1:500	Alexa Fluor 647 Goat α-Mouse IgG (H+L) A21236
Astrocytes and neurons	Anti Vimentin	chicken	abcam	ab24525 9822	dilution 1:2200	Goat α-chicken 568 abcam ab175477
Astrocytes and neurons	Anti TUJ1	mouse	Biolgened	801201	dilution 1:500	Alexa Fluor 647 Goat α-Mouse IgG (H+L) A21236
Astrocytes and neurons	Anti MAP2	mouse	sigma	M4403 2ML	dilution 1:1000	Alexa Fluor 647 Goat α-Mouse IgG (H+L) A21236
Astrocytes and neurons	Anti GFAP	rabbit	Millipore	AB5804	dilution 1:500	Alexa Fluor 568 Goat α-Rabbit IgG (H+L) A11036
Astrocytes and neurons	Anti TH	rabbit	santa cruz	sc-14007	dilution 1:50	Alexa Fluor 568 Goat α-Rabbit IgG (H+L) A11036
Astrocytes and neurons	Anti HNF-3β (RY-7) [FoxA2]	mouse	santa cruz	sc-101060	dilution 1:50	Alexa Fluor 647 Goat α-Mouse IgG (H+L) A21236
Astrocytes and neurons	S100β	rabbit	abcam	ab868	dilution 1:50	Alexa Fluor 568 Goat α-Rabbit IgG (H+L) A11036
Astrocytes and neurons	Lamp1	mouse	abcam	ab2296838	dilution 1:1000	Alexa Fluor 647 Goat α-Mouse IgG (H+L) A21236
Astrocytes and neurons	Tom20 (FL-145)	rabbit	santa cruz	sc-11415	dilution 1:1000	Alexa Fluor 568 Goat α-Rabbit IgG (H+L) A11036
Microglia	Iba1	rabbit	FUJIFILM	019-19741	dilution 1:500	Alexa Fluor 647 goat α-Rabbit IgG A27040
T cells	FITC Mouse Anti-Human CD3 (clon UCHT1)	mouse	BD Pharmingen	581806	dilution 1:100	
T cells	APC Mouse Anti-Human CD4 (clon L200)	mouse	BD Pharmingen	551980	dilution 1:100	
T cells	PE Mouse Anti-Human CD8 (Clon RPA-T8)	mouse	BD Pharmingen	561949	dilution 1:100	
Astrocytes, T cells	DJ-1	rabbit				
	Beta actin	mouse				
Human brain tissue	GFAP		Sigma-HPA063513		dilution 1:800	
Human brain tissue	Aldoc		Sigma-HPA003282		dilution 1:1000	
Human brain tissue	Iba1		Wako-019-19741		dilution 1:1000	

Suppl. Figure 1
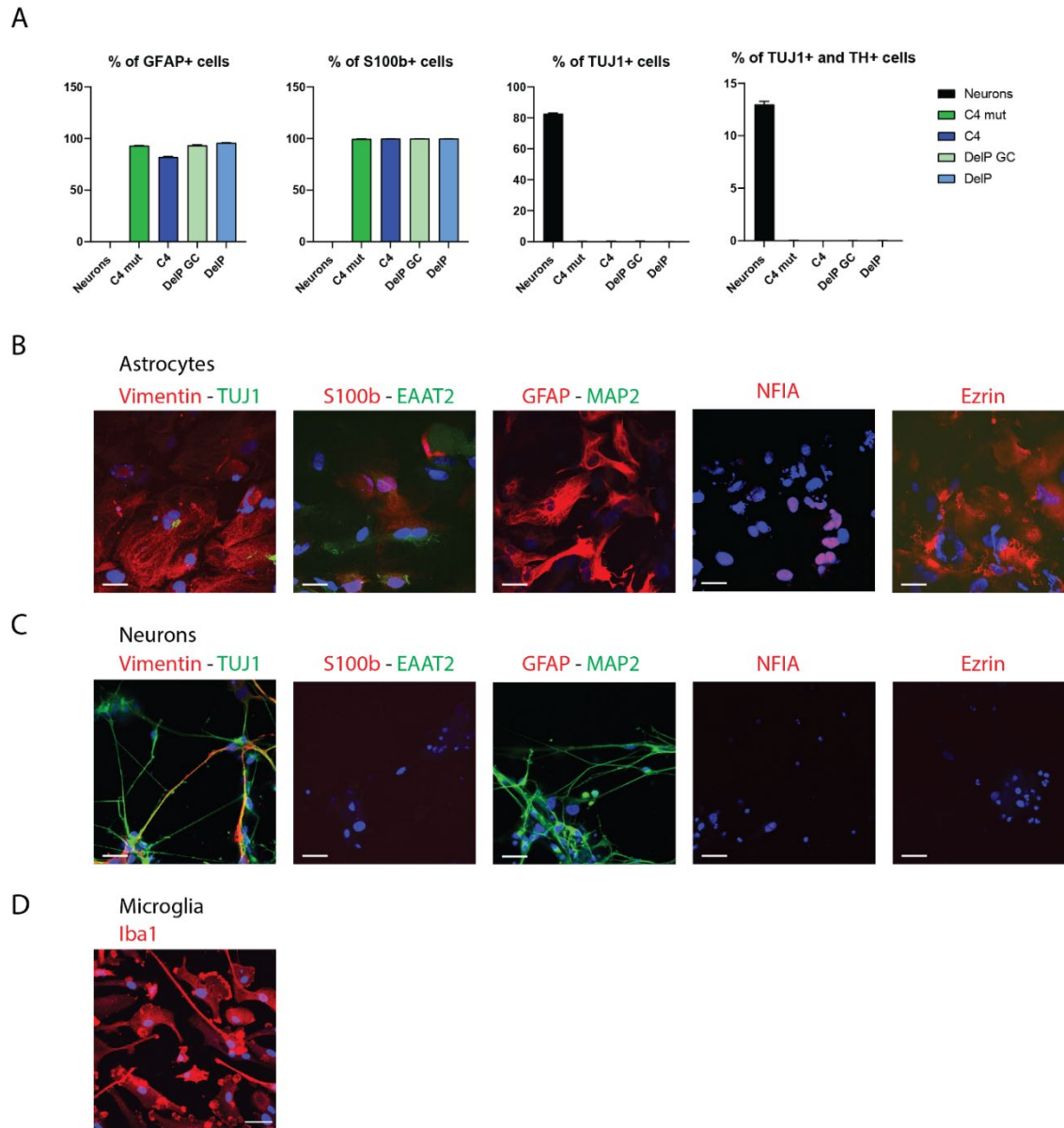
Supplementary Figure 1: A: Characterization of astrocytes by FACS. Almost all cells were GFAP and S100b positive. No neuronal contamination of astrocytic culture as assessed by TUJ1 staining. **B and C:** Characterization of astrocytes by ICC. The cells showed an astrocytic morphology and the majority stained positive for canonical astrocyte markers like GFAP, S100b, Vimentin, EAAT2, NFIA, ID3, EZRIN and no neuronal contamination as assessed by markers for TUJ1 and MAP2. **D:** Characterization of microglia by ICC. The cells showed microglia morphology and stained positive for the microglia marker Iba1.

Suppl. Figure 2
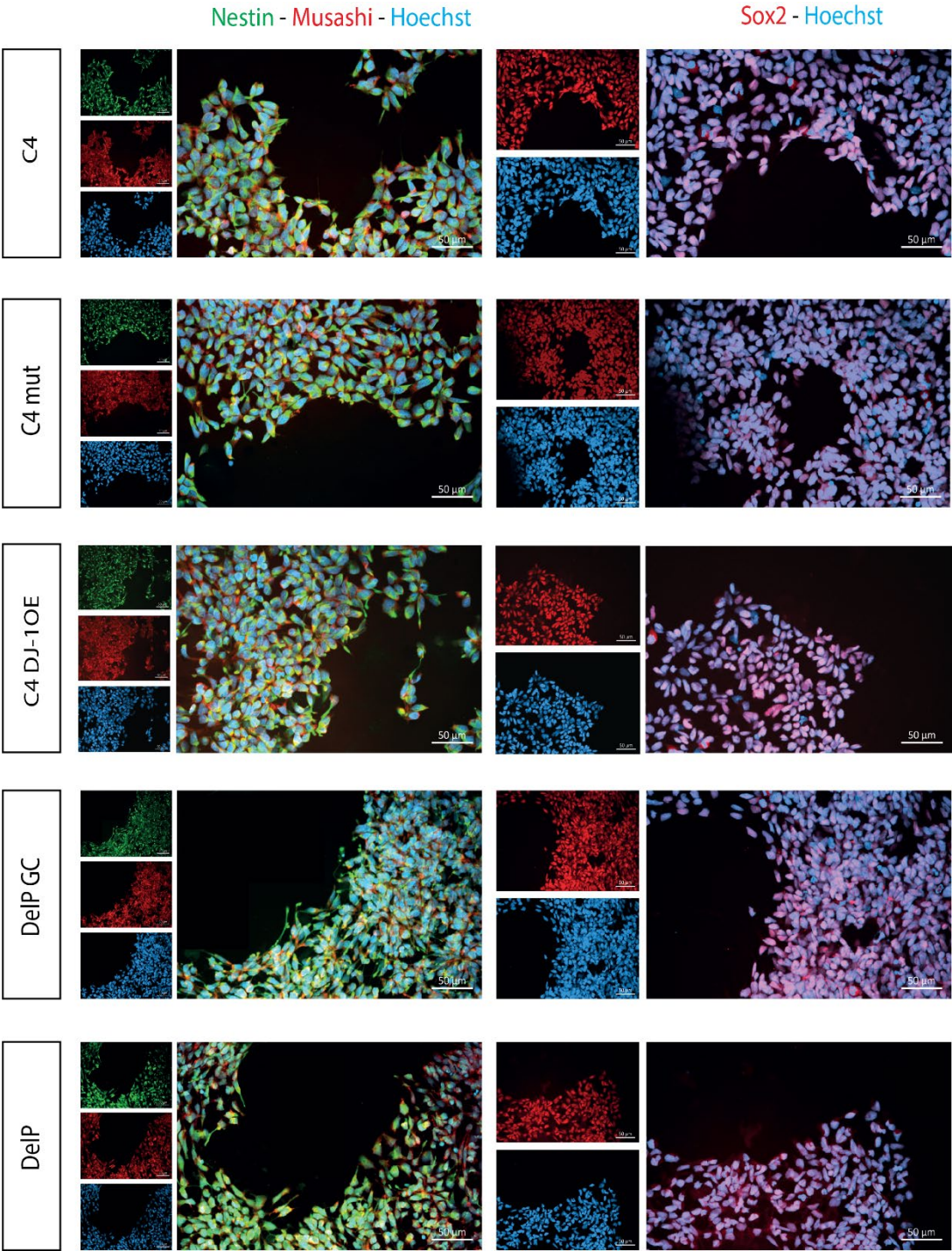
Supplementary Figure 2: Characterization of smNPCs by ICC.

Suppl. Figure 3
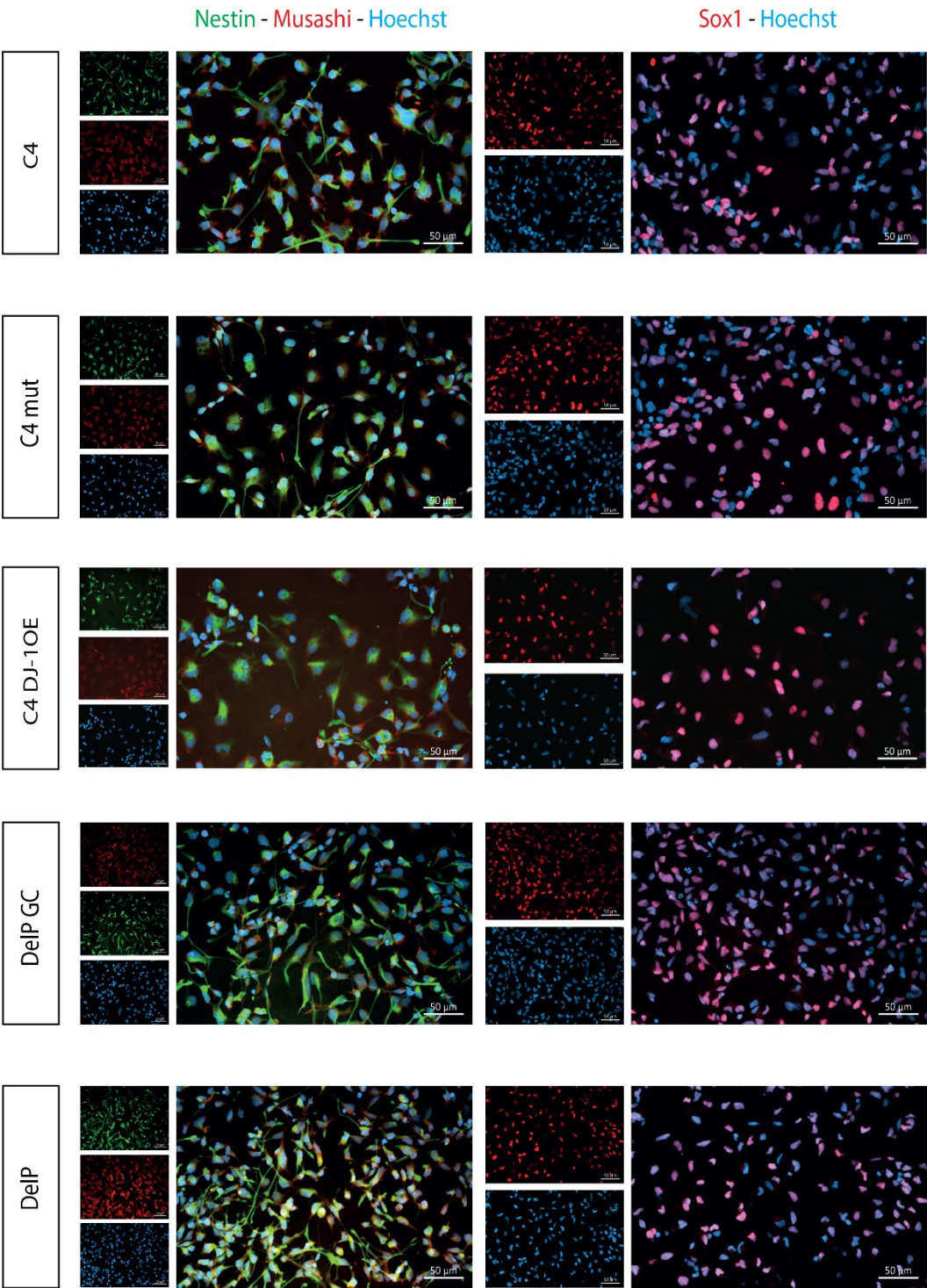
Supplementary Figure 3: Characterization of hNSCs by ICC.

Suppl. Figure 4

A
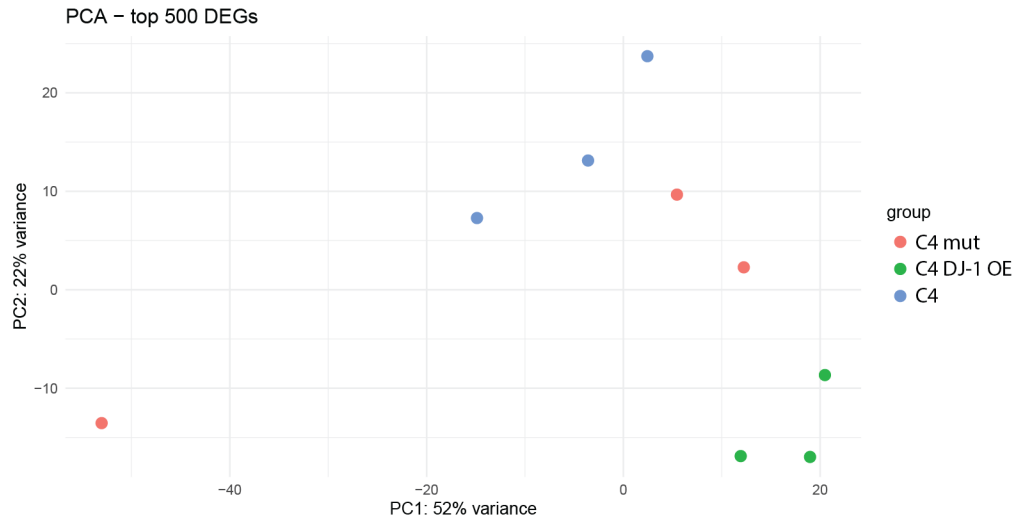
Supplementary Figure 4: RNAseq analysis of astrocytes. **A:** Principal Component Analysis (PCA) plot for RNA-seq data in each genotype based on top 500 DEGs. Three biological replicates for each cell line are represented separately.

Suppl. Figure 5

A

C4 mut vs C4

B

C4 mut vs C4

C

C4 mut vs C4 top ranked pathways
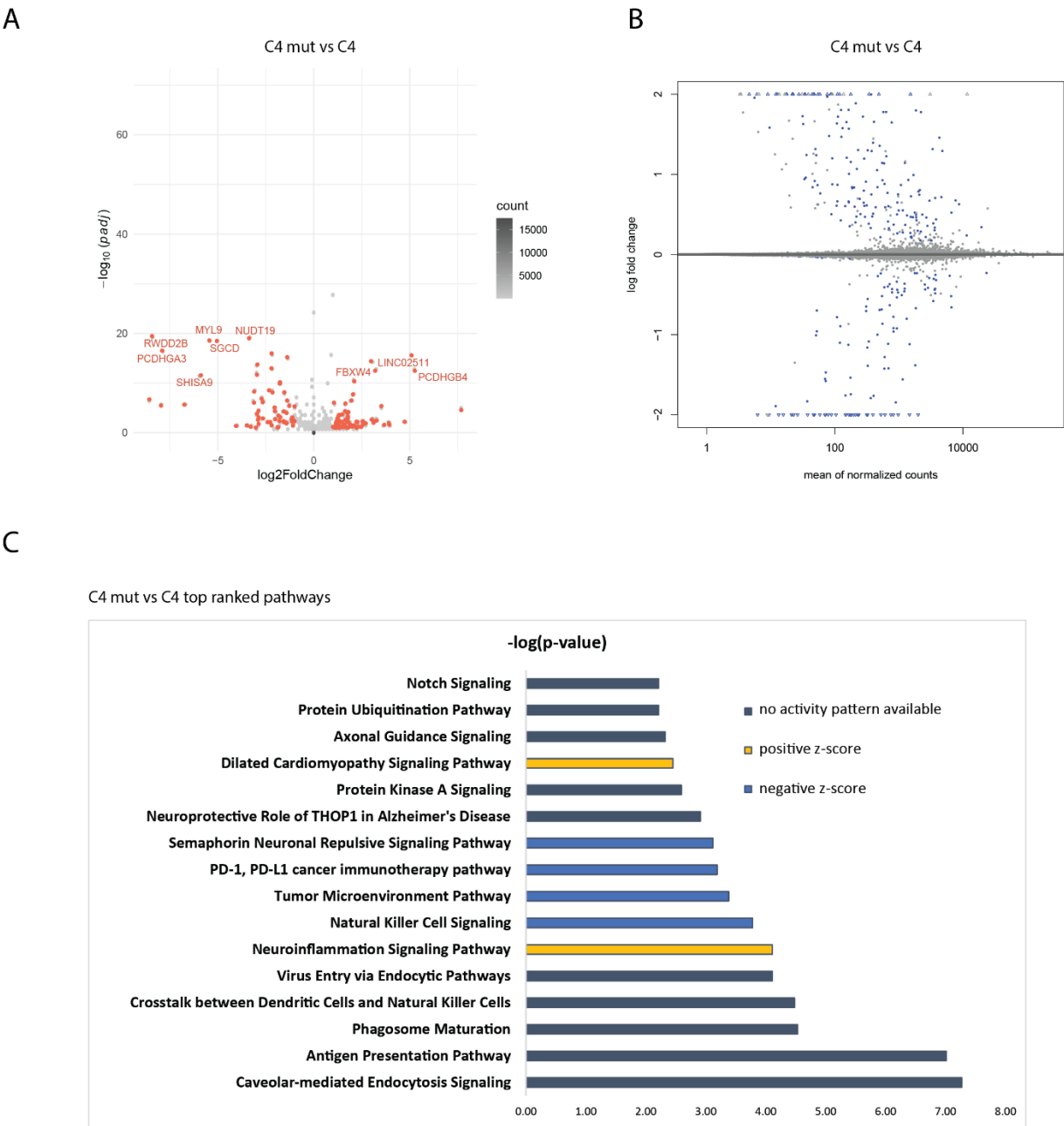
Supplementary Figure 5: RNAseq analysis of C4 mut astrocytes and C4 wildtype astrocytes. **A:** Volcano plot. Red dots highlight DEG with log2 fold change of +- - and padj < 0.05. gene names are reported for -log10(adjusted-pval) > 10 and abs(logFC) >= 3. **B:** MA-plot obtained after schrinkage of logFC by apeglm, blue dots highlight DEGs with padj < 0.05. **C:** Top ranked pathways of IPA analysis showing only −log(p-value) > 2 revealed that different pathways were enriched and that especially neuroinflammation pathways were activated (z-score >0.5).

Suppl. Figure 6

A

B
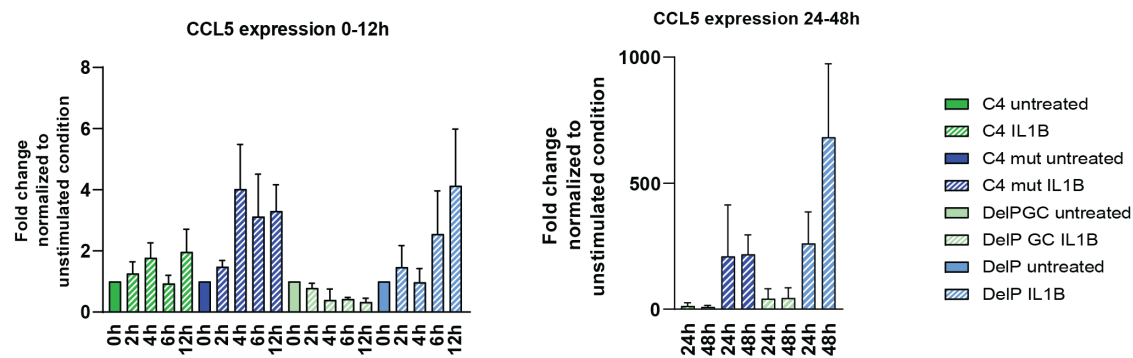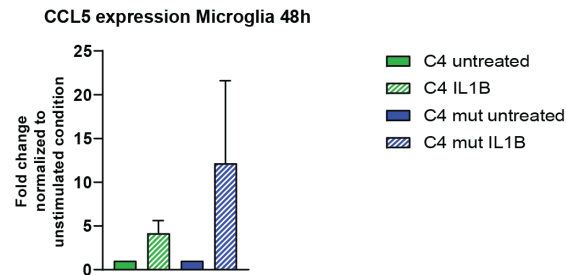
Supplementary Figure 6: CCL5 mRNA expression upon IL-1β treatment (10 ng/ml) at indicated time points. **A:** Expression levels of CCL5 mRNA in astrocytes at 0h, 2h, 4h, 6h, 12h, 24h, and 48h after IL-1β stimulation assessed by qPCR. N= 3. **B:** Expression levels of CCL5 mRNA in iPSC-derived microglia 48h after IL-1β stimulation assessed by qPCR. N= 3.

Suppl. Figure 7

A

B
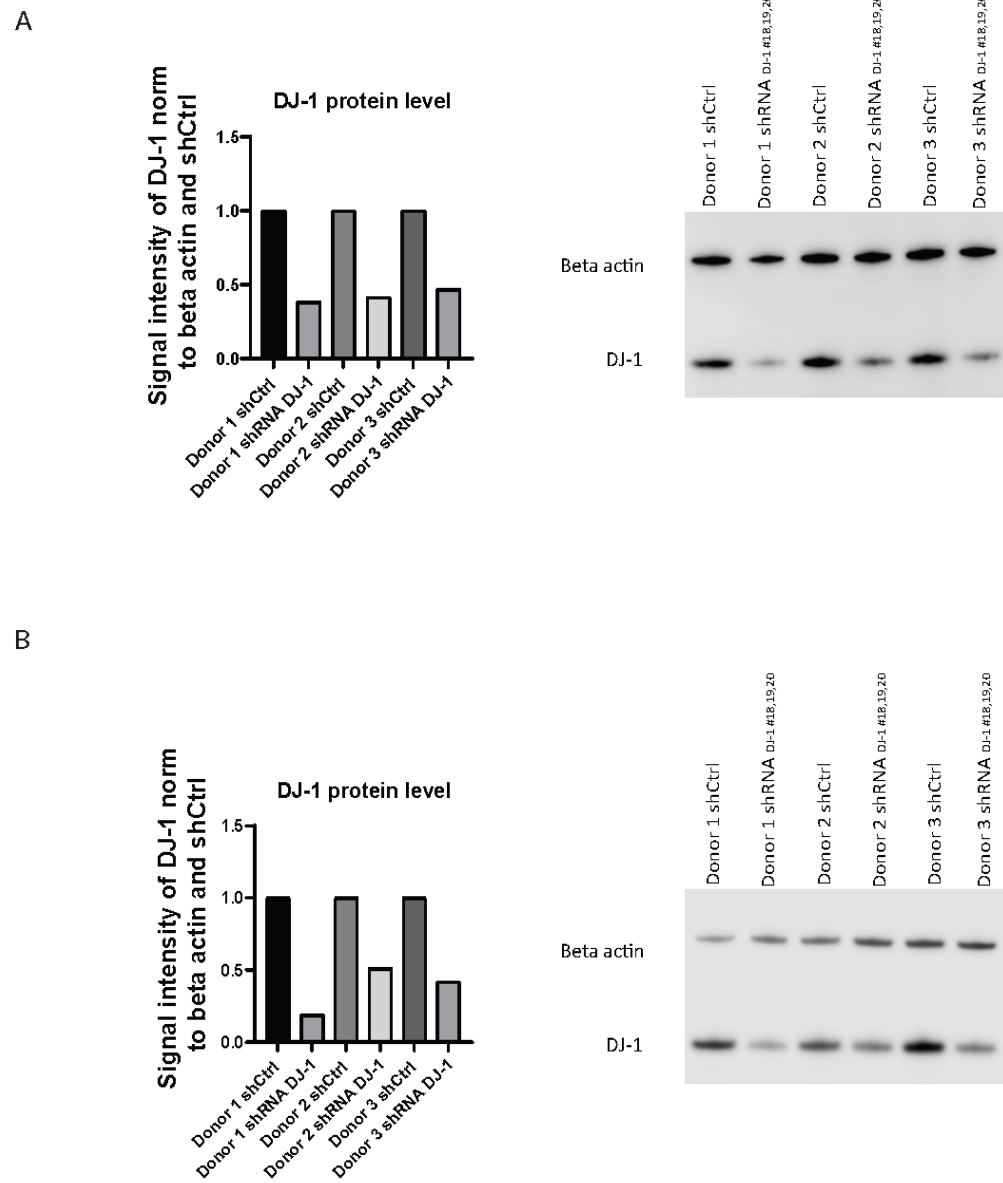
Supplementary Figure 7: A+B: DJ-1 knockdown in T cells prior to T cell migration assay using shRNAs #18 and #20 together. Each PBMC donor represents one independent biological replicate that was used for the respective different astrocyte differentiations. N=3. Panel A shows the knockdown for the T cell migration assay performed with C4 and C4 mut astrocytes, panel B for the assay with DelP GC and DelP astrocytes.

Suppl. Figure 8
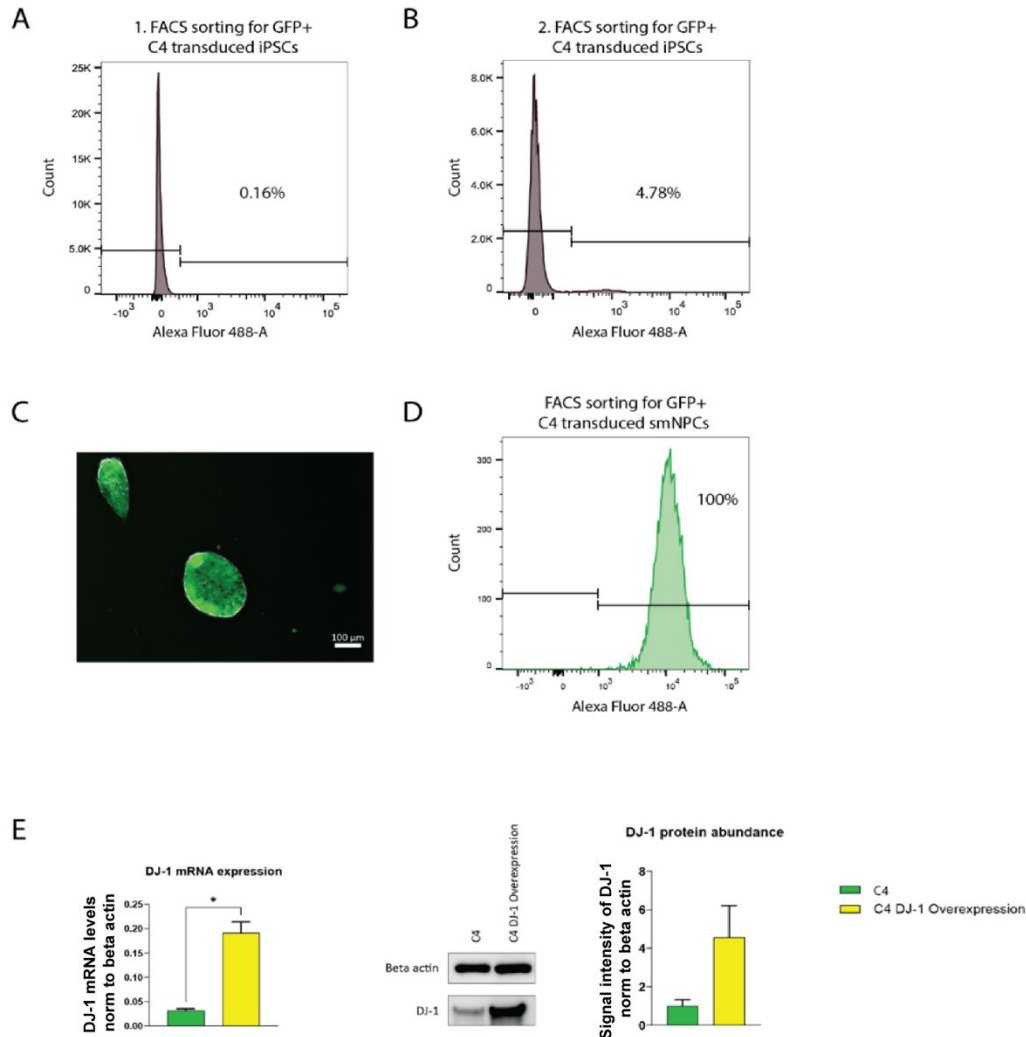
Supplementary Figure 8: A: FACS sorting for GFP+ cells of transduced C4 wildtype iPSC with GFP containing lentiviral construct for DJ-1 overexpression. For the first sort, 0.16% of the cells were GFP+. **B:** Second sort of transduced iPSC resulted in 4.78% GFP+ cells. **C:** GFP+ iPSC colonies after the second sort. **D:** GFP+ iPSCs were differentiated into smNPCs and sorted for GFP+ cells again which resulted in 100% GFP+ cells. **E:** Characterization of DJ-1 overexpression smNPCs showed increased DJ-1 mRNA and protein level.

Suppl. Figure 9

A
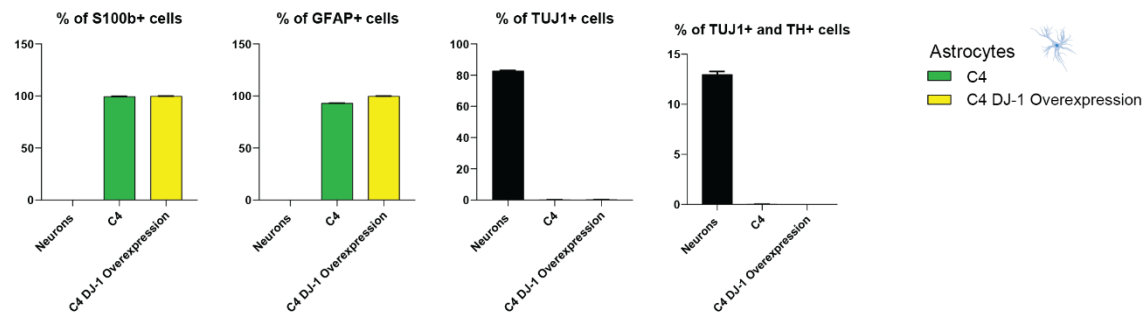
Supplementary Figure 9: A: FACS-based characterization of astrocytes showed that astrocytes express astrocyte markers GFAP and S100b, but no neuronal contamination due to absence of TUJ1 staining.

Suppl. Figure 10
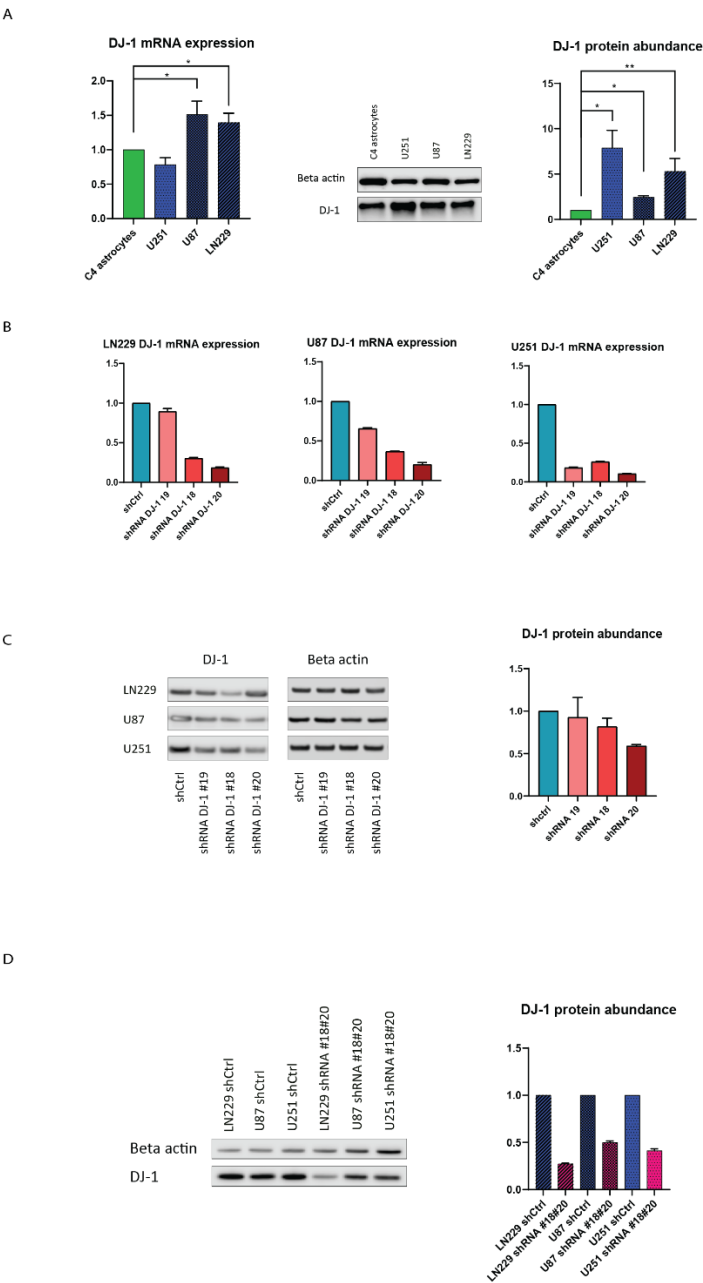
Supplementary Figure 10: A: GBM cell lines have upregulated DJ-1 mRNA and protein levels when compared to C4 astrocytes. **B:** shRNA mediated knockdown of DJ-1 reduced DJ-1 mRNA level. shRNA #20 had the strongest knockdown effect in all the lines and reduced the DJ-1 mRNA levels to around 20% compared to shCtrl. **C:** DJ-1 protein levels upon knockdown reduced to 50-60% compared to shCtrl. **D:** DJ-1 protein levels upon stable knockdown reduced to 30-50% compared to shCtrl.

Suppl. Figure 11

A

B
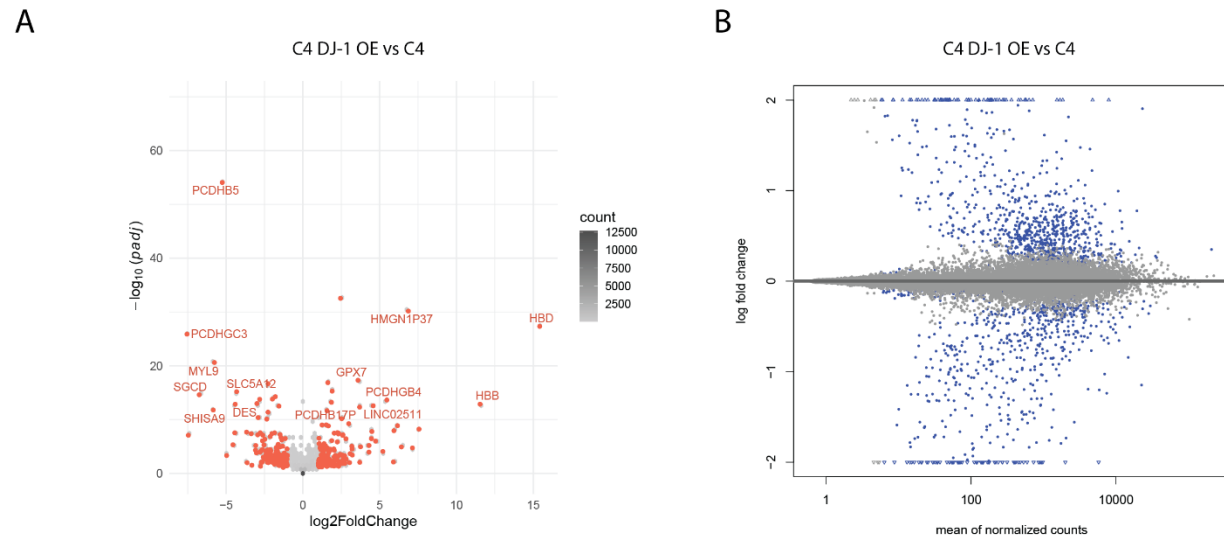
Supplementary Figure 11: RNAseq analysis of C4 DJ-1 OE astrocytes and C4 wildtype astrocytes. **A:** Volcano plot. Red dots highlight DEG with log2 fold change of +- - and padj < 0.05. gene names are reported for -log10(adjusted-pval) > 10 and abs(logFC) >= 3. **B:** MA-plot obtained after schrinkage of logFC by apeglm, blue dots highlight DEGs with padj < 0.05.
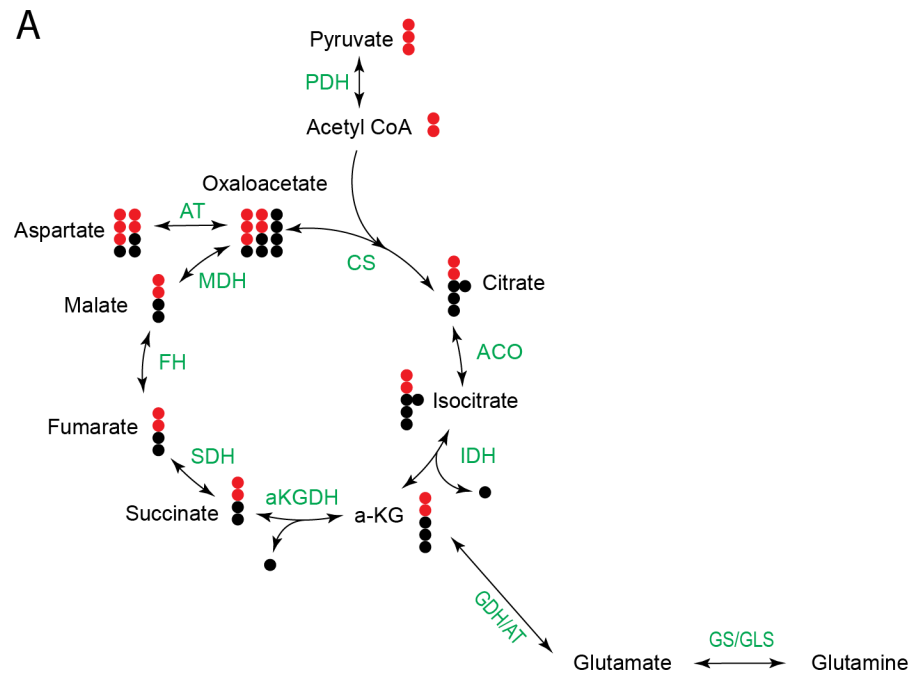
Suppl. Figure 12

A

B
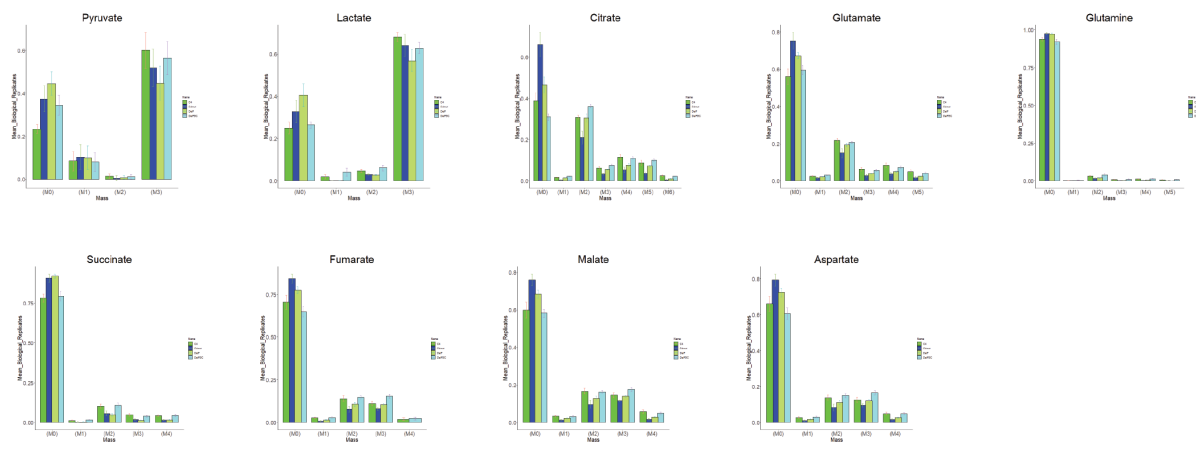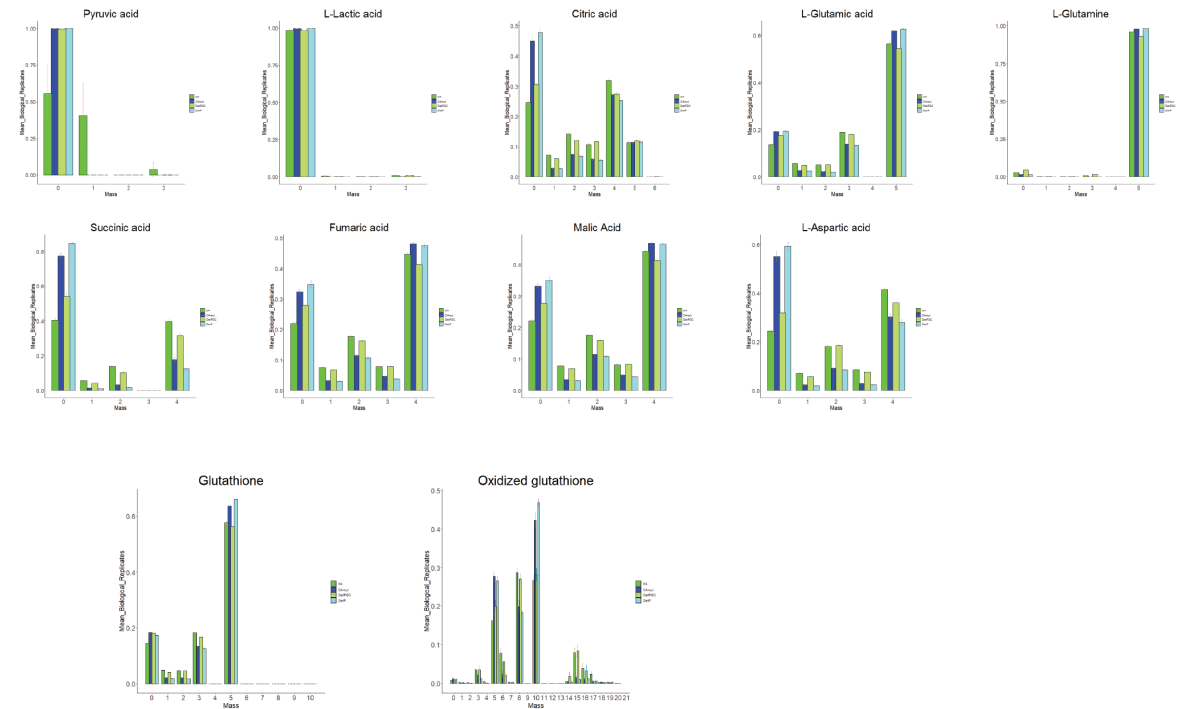
Supplementary Figure 12: A: Analysis of glucose metabolism using [U-13C6]Glucose tracing. N=3. 13C incorporation in metabolites was analyzed by GC-MS, resulting in heavier metabolites (M1+x), whereas no ^{13}C incorporation corresponds to M0. **B:** [U-13C5]Glutamine tracing results. N=3.

Suppl. Figure 13

A

Supplementary Figure 13: A: Analysis of glucose metabolism using [U-13C6]Glucose tracing. N=3. 13C incorporation in metabolites was analyzed by GC-MS, resulting in heavier metabolites (M1+x), whereas no ^{13}C incorporation corresponds to M0. **B:** [U-13C5]Glutamine tracing results. N=3.

B

Suppl. Figure 14

A
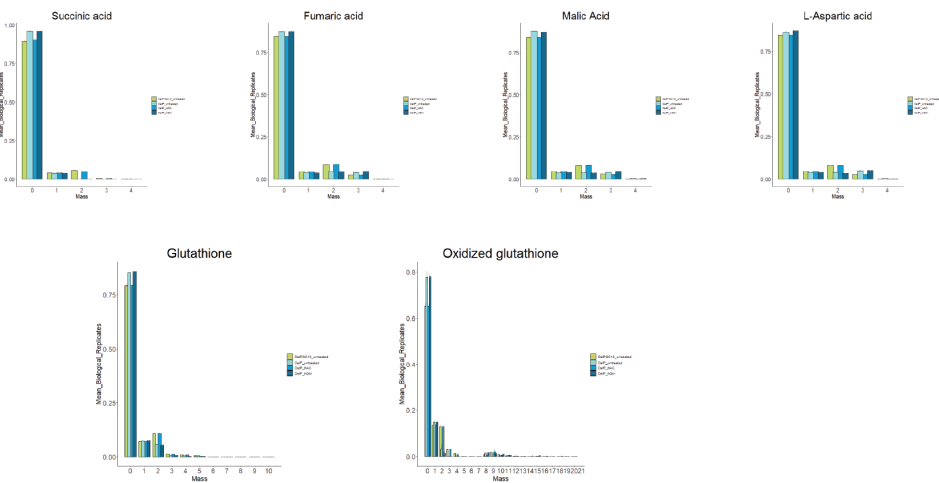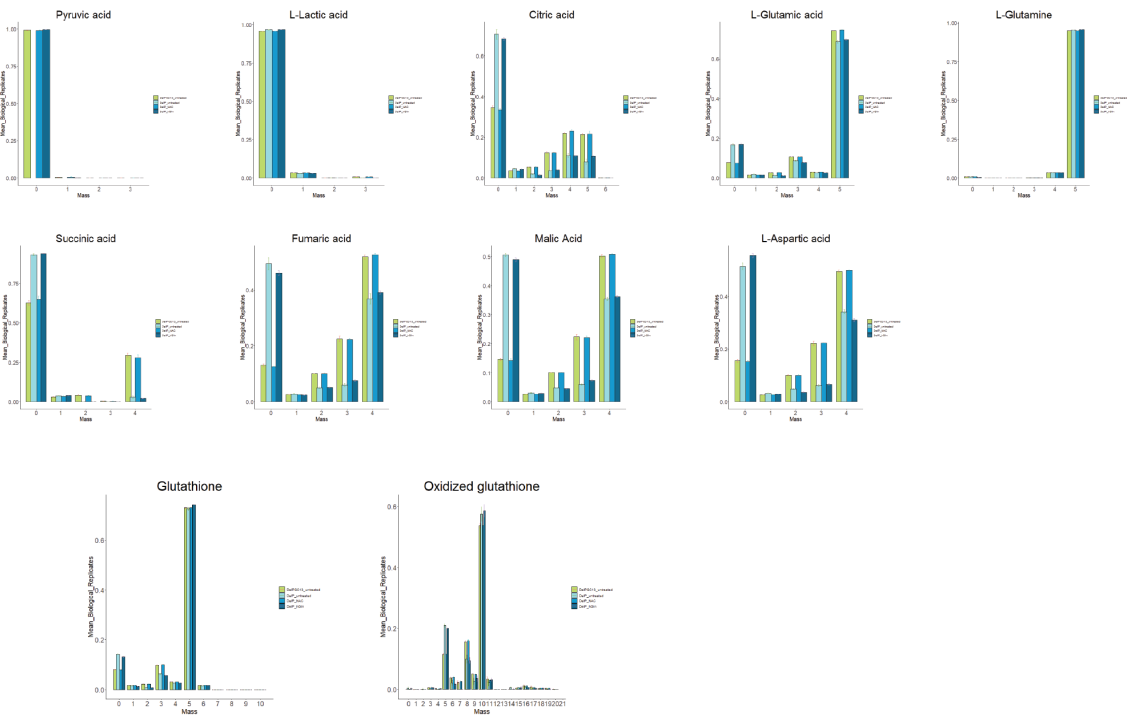
Supplementary Figure 14: A: Principle of [U-13C6]Glucose tracing. 13C (red) incorporation in metabolites is analyzed by GC-MS, resulting in heavier metabolites (M1+x), whereas no 13C incorporation corresponds to M0.

Suppl. File 1

Whole scans of immunohistochemically stained brain slides. Files can be viewed using QuPath.
A: Control brain slide stained for Aldoc
B: Control brain slide stained for GFAP
C: Control brain slide stained for Iba1
D: DJ-1 patient brain slide stained for Aldoc
E: DJ-1 patient brain slide stained for GFAP
F: DJ-1 patient brain slide stained for Iba1

Discussion

GBM and PD are characterized by pathophysiologic mechanisms that lie on the opposite ends of the spectrum of cell fate; one shows enhanced cell proliferation/survival and the other by premature cell death. As previously discussed, there has been increasing evidence that links these two disease mechanisms since epidemiological studies have shown an inverse correlation for gene expression of PD and GBM associated genes like *PARK7* (DJ-1). Loss of DJ-1 protein is causing PD and high levels of DJ-1 are associated with poor prognosis and survival of gliomas[16,17].

Thus, the aim of this doctoral thesis was to analyze the role of DJ-1 protein in PD and GBM and to identify pathways in both diseases that are regulated by DJ-1.

Astrocytes are the most populous glial subtype and are critical for brain function. So far, there are only few studies regarding the role of astrocyte function in neurodegenerative diseases like PD, but it was shown that PD associated genes are expressed in astrocytes and play important roles in astrocyte function[18]. *PARK7* is ubiquitously expressed, but especially highly expressed in astrocytes and upregulated in reactive astrocytes in patients with PD[19,20]. In addition to their emerging role in the pathogenesis of PD, astrocytes are claimed to be the origin of GBM[8], and DJ-1 was shown to be upregulated in GBM[21]. Thus, we analyzed the role of DJ-1 downregulation in PD and DJ-1 upregulation in GBM to shed light on the inverse phenotypes of PD and GBM associated with inverse DJ-1 level.

To generate PD patient-derived astrocytes, we first had to develop isogenic PD patient-derived stem cell models (Manuscript II and III) to allow the analysis of DJ-1 associated cellular phenotypes.

As mentioned in the introduction (Manuscript I and II), DJ-1 is a multifunctional protein[22]. There are many studies showing the involvement of DJ-1 in mitochondrial functioning and its ROS scavenging function, overall leading to a neuroprotective role of DJ-1[23].

However, there are only few studies analyzing the immune function and metabolic role of DJ-1. This is why we focused on the regulation of astrocytic and GBM cell metabolism and immune response by DJ-1.

Astrocytes play an important role in brain metabolism homeostasis, they have many processes (endfeet) that have contact to intraparenchymal capillaries. Via these capillaries, astrocytes can take up glucose[24]. The astrocytic endfeets can also be in contact with synapses and nerve bodies[25]. Astrocytic neurotransmitter receptors allow to sense synaptic activity[26]. Astrocytes interact with neurons via the release of gliotransmitters like ATP and D-serine, that can be used for neuronal metabolism, and neurotrophins, eicosanoids, and neuropeptides[25,27]. Astrocytic glutamine formed can be taken up by neurons and used to synthesize neurotransmitters, such as glutamate and GABA[28] (Figure 1). In addition, astrocytes release lactate that can be taken up by the neurons to fuel it into their metabolism[29] (Figure 1). Moreover, astrocytes can use glutamate removed from the synaptic cleft to fuel it into the TCA. However, in general, astrocytes mainly take up glucose from surrounding blood vessels (Figure 1) to generate energy via glycolysis[27,30] as their filopodial and lamellipodial extensions - the major part of their surface area - are too narrow for mitochondria[31].
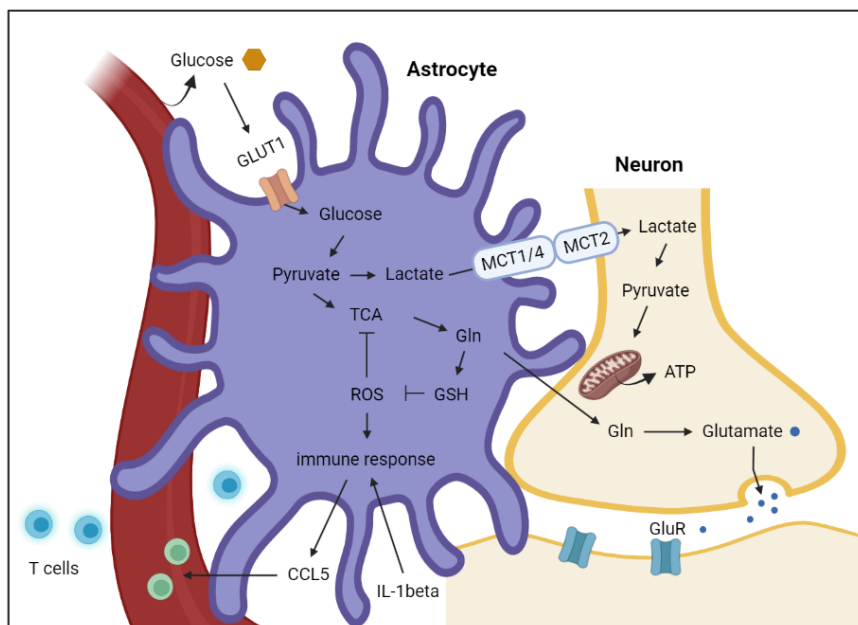
Figure 1: *Metabolic dependency of neurons and astrocytes. Astrocytes release lactate and glutamine that can be taken up by the neurons and fueled into their metabolism. As shown by our data, lactate and glutamate production are dependent on DJ-1 level. This is why DJ-1 deficiency in astrocytes impairs the neuronal metabolic support. DJ-1 also regulates the astrocytic immune response, eventually influencing T cell migration. Thus, in addition to the metabolic impairment that the neurons have due to their lack of DJ-1 in PD, the lack of astrocytic support can enhance the metabolic neuronal phenotype.*

We analyzed the influence of DJ-1 deficiency on the metabolism in PD patient iPSC-derived astrocytes and found that DJ-1 deficiency reduces glucose uptake, TCA cycle flux and OXPHOS of astrocytes. Furthermore, we saw that the glutamine contribution to the TCA cycle was reduced in DJ-1 deficient astrocytes. These results are consistent with previous findings from Meiser and colleagues who showed that DJ-1 silenced LUHMES cells showed an active TCA cycle, but also had decreased glutamine contribution to the TCA[32]. Concordantly, it was shown that PARK7 knockout (KO) and mutant astrocytes had impaired glutamate uptake due to a decreased EAAT2 protein levels[18,33].

Astrocytes are interconnected via gap junctions, which enables exchange of small molecules like ATP, glucose, neurotransmitter glutamate and glutathione (GSH) between the cells. As already mentioned, DJ-1 is an important ROS scavenger that regulates among others the synthesis of GSH[32,34]. Glutamine is an important precursor of GSH, and we found glutamine contribution to the TCA cycle to be decreased in DJ-1 deficient astrocytes. However, GSH synthesis from glutamine was increased leading to the conclusion that DJ-1 deficient astrocytes use glutamine for GSH synthesis rather than to fuel it into the TCA, which would also produce more ROS eventually via OXPHOS. Nonetheless, DJ-1 deficient astrocytes had decreased total GSH and increased oxidized GSH (GSSG) levels, which indicates that despite the increased production from glutamine, GSH levels remain lower than in isogenic counterparts. Consistently, DJ-1 knockdown was found to attenuate GSH levels in vitro and vivo[35].

The increased GSSG levels are also indicating the presence of high ROS levels in DJ-1 deficient astrocytes. Astrocytes have a loosely assembled mitochondrial respiratory chain that is associated with a higher generation of mitochondrial ROS[36]. DJ-1 knockout mice astrocytes were shown to produce more nitric oxide (NO), which was mediated by ROS signaling leading to activation of inducible NO synthase (iNOS)[37]. In another study, DJ-1 deficient mouse astrocytes and microglia had also increased iNOS[38]. Similarly, we found significantly increased ROS in DJ-1 deficient astrocytes compared to isogenic controls. It was shown that astrocytic mitochondrial ROS can modulate brain metabolism of mice[30] and ROS are known to reduce the activity of the TCA cycle[39], which is why the increased ROS levels in the DJ-1 deficient astrocytes might cause the observed reduced TCA cycle flux.

It is very well known that ROS regulate the immune response[40–42]. In fact, it was shown that mitochondrial ROS can induce proinflammatory cytokine production[43]. It is also known that ROS can activate T cells[44]. Astrocytes are also highly involved in immune signaling. The astrocytic immune response can be beneficial or harmful for tissue repair, which is dependent on the stimuli from the locus of inflammation. The immune function of astrocytes is mediated via signaling pathways - protective pathways are activated for example by TGFβ, IFNγ, STAT3, whereas among others IL17, NFκB, chemokines and VEGF trigger damaging pathways[45].

NFκB signaling has a well-known role in immune responses and inflammation and it´s signaling pathways are very complex as they are involved in many different processes[46,47]. One of many activators of NFκB signaling is interleukin 1 (IL-1) in astrocytes. Activation of the IL-1 receptor (IL-1R) leads to the activation of IκB-kinases followed by phosphorylation and degradation of several IκB isoforms. Then, NFκB translocates to the nucleus and induces the expression of proinflammatory genes[48]. One important chemokine that is activated upon IL-1β stimulation via NFκB signaling is C-C Motif Chemokine Ligand 5 (CCL5), also known as RANTES[49].

We analyzed reactive astrocyte and inflammation in the cortex of a PD patient with a DJ-1 mutation. Here, we found significant amount of astrogliosis[50], as seen by increased immunoreactivity for the reactive astrocyte marker GFAP. Increased astrogliosis in PD midbrain is in line with previous studies of human midbrain of other idiopathic and genetic PD patients[51]. Concordantly with increased GFAP expression in the PD patient brain, ingenuity pathway analysis of human DJ-1 deficient astrocytes showed upregulation of proinflammatory pathways and cells had increased cytokine expression and release.

Sonninen and colleagues have recently also shown increased cytokine release in human PD astrocytes[52]. Another study found that DJ-1 deficiency in mice delayed neuronal repair due to a decrease in the chemokine CCL2/MCP-1[53]. It has also been shown that PARK7 knockout (KO) astrocytes display alterations in inflammatory cytokine production[33,54]. DJ-1 was also shown to regulate astrocyte inflammatory response to IFN-γ by terminating the signaling cascade, which was neuroprotective; IFN-γ treatment increased neuronal toxicity in PARK7-KO brain slices when compared to wild-type samples[38]. Frøyset and colleagues found that astrocytic DJ-1 overexpression in zebrafish was neuroprotective[55]. Kahle and colleagues showed increased cytokine release in DJ-1 knockout mouse astrocytes upon lipopolysaccharide (LPS) stimulation compared to controls[37].

CCL5 was shown to regulate the migration of T lymphocytes[56]. Lymphocytes play an important role in the adaptive immune system and are produced in the bone marrow. They mature in the thymus, from which they are then being released to peripheral lymphoid organs. Here, they are primed by engaging with professional antigen presenting cells[57]. It was shown that T cells play an important role in PD pathogenesis[58]. CD3+ T cells can infiltrate the brains of PD patients and it was found that more CD4+ and CD8+ T cells were present in the substantia nigra pars compacta of patients with PD compared to controls[59].

Concordantly, we found increased T cell migration towards DJ-1 deficient astrocytes. T cell migration was even enhanced when T cells had reduced DJ-1 levels, which mimics more the PD patient situation where all cells are DJ-1 deficient.

T cell migration could be reduced in DJ-1 deficient astrocytes cultured with WT T cells and with DJ-1 knockdown T cells, by both, N-acetylcysteine (NAC) and glutamine supplementation. The fact that decreasing ROS and increasing TCA fueling/GSH precursor could rescue the enhanced immune response in DJ-1 deficient astrocytes indicates that DJ-1 level-dependent T cell migration is mediated by ROS signaling.

It was shown that reactive astrocytes enhanced their DJ-1 expression upon oxidative stress induction in rats and that DJ-1 expression is upregulated in reactive astrocytes in patients with PD[20], which indicates that astrocytic reactivity and immune response are affecting DJ-1 levels and *vice versa*[60].

In addition to its ROS scavenging functions, many studies have described DJ-1 as important regulator of cell growth and apoptosis, for example via regulation of Phosphatase And Tensin Homolog (PTEN) and p53[61,62]. Our gene expression pathway analysis showed an upregulation of apoptosis pathways in DJ-1 deficient astrocytes. Simultaneously, early apoptosis was significantly increased, and cell growth decreased in DJ-1 deficient astrocytes. Overall, we found a vicious cycle of decreased GSH levels, increased ROS, decreased energy production and therefore growth deficiency, and an increased immune response and eventually increased cell death.

Due to its influence on cell proliferation and apoptosis, DJ-1 was initially described as oncogene[63]. DJ-1 was shown to be upregulated in GBM[21]. The well-known role of DJ-1 to enhance cell proliferation, inhibit oxidative stress, regulation of metabolism and immune response can therefore be beneficial for GBM proliferation.

To study the role of DJ-1 in GBM, we performed DJ-1 knockdown in 3 different GBM cell lines (LN229, U87, U251). As GBM is claimed to be originating from astrocytes and somatic mutations in oncogenes drive tumorigenesis, we generated a DJ-1 overexpression line from wildtype (WT) iPSC to differentiate them into astrocytes and compare them to the GBM cells as an oncogenic model.

Like astrocytes, GBM tumor cells mainly rely on glycolysis[64] (Figure 2). GBM is the most malignant brain tumor with very low survival[65]. The aggressiveness of the tumor is caused by the high proliferation rate and immune escape mechanisms of the tumor cells[66]. Moreover, the tumor heterogeneity[67] and the infiltrative growth harden effective therapy[68]. Initially, GBM research was dominated by the study of enhanced glycolysis, even in the presence of oxygen (Warburg effect) regarding the analysis of tumor metabolism (Figure 2). However, in the last years, more and more studies have identified also other metabolic pathways like TCA cycle, lipid, amino acid, and nucleotide metabolism to be very relevant for tumor growth and invasion[69] (Figure 2).
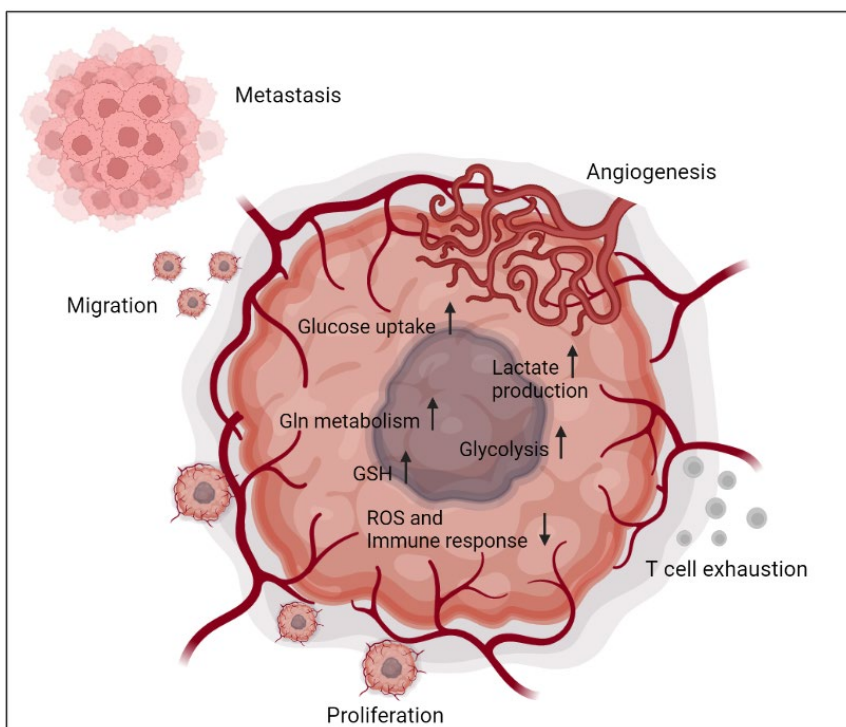
Figure 2: GBM tumor drives angiogenesis, proliferation and migration of glioma cells and glioma stem cells and T cell exhaustion via regulation of metabolism and immune pathways.

In line with these observations, *PARK7* overexpression astrocytes showed increased cell growth, metabolic activity and reduced ROS levels when compared to WT astrocytes. Ingenuity pathway analysis revealed upregulation of cancer associated pathways involved in cancer cell proliferation and cell cycle regulation, which indicates that DJ-1 overexpression in astrocytes can serve as an oncogenic model to compare it to the GBM cell lines.

The brain consumes 25% of the body's glucose. Glucose is the main energy substrate, however, other metabolites such as amino acids, fatty acids, or lactate are also used as a source of energy[70]. In fact, glutamine has also been identified to be important for GBM metabolism (Figure 2). Glutamine is the most abundant amino acid in the human body. Besides it being an excitatory neurotransmitter, it is also involved in numerous intermediary metabolic processes, especially in the synthesis of amino acids and purines and it can be fueled into the TCA cycle. It was shown that intratumoral glutamine levels were increased in GBM tissue when compared to healthy controls[71,72].

Glutamine can be derived from two sources: the main part of glutamine is coming from astrocytes that are within and surrounding the tumor and the rest is derived from the system circulation.

GBM cells are efficiently and successfully competing for the glutamine that is usually used by astrocytes by upregulating the expression of glutamine and glutamate importers. In fact, human glioma cell lines were shown to have upregulated levels of Solute Carrier Family 1 Member 5 (SLC1A5), the main glutamine importer[73]. We found that knockdown of DJ-1 in the GBM cells reduced glutamate production from glucose.

Besides the above mentioned functions, glutamine is a key substrate for the synthesis of DNA and fatty acids and a precursor of GSH, which is important to counteract oxidative stress via ROS elimination and mediate radiation and chemotherapy resistance[74]. As discussed above, ROS have been shown to play a critical role in the regulation of T cell-mediated immunity, and T cell migration/infiltration[75,76]. In addition to promoting T cell proliferation, ROS were also shown to be important in modulating the differentiation and effector functions of T cells. For example, high ROS levels were shown to be beneficial for the development of T helper cells and increased IL-4 and IL-2 production in T cells[75,77,78]. In a pathological state like during GBM pathogenesis, T cells leave the circulation and enter the brain. It was shown that T cells are the primary lymphoid

component of the GBM tumor microenvironment[64]. As explained above, GBM cells rapidly take up glucose and produce lactate[79] (Figure 2). In consequence, there is less glucose available for the T cells and therefore decreased Glucose transporter 1 (GLUT1) binding (also downregulated by cytotoxic T-lymphocyte-associated protein 4 (CTLA-4)), which eventually downregulates T cell function and motility. The high lactate production leads to internalization of lactate also by the T cells within the tumor, where it also inhibits glycolysis, eventually resulting in decreased T cell migration[80].

Once T cells traffic past the blood brain barrier and infiltrate the tumor, they will encounter the highly immunosuppressive tumor microenvironment (TME), consisting for example of regulatory T cells, tumor-associated macrophages, which works to suppress T cell function[80,81]. Regulatory T cells can trigger T cell exhaustion (Figure 2), apoptosis and inhibit the production of inflammatory cytokines, which is why GBM cells highly recruit regulatory T cells to the TME[80]. It was shown that glioma stem cell-derived pericytes also secrete CCL5, which can promote the recruitment of regulatory T cells to the TME[82].

In addition to the recruitment of regulatory T cells to suppress T cell function, stromal cells in the TME produce highly immunosuppressive cytokines, such as transforming growth factor β (TGFβ) and interleukin-10 (IL-10)[83,84], which further suppress T cell function.

We found that there is almost no T cell migration induced towards the GBM cell lines upon stimulation of the GBM cells with IL-1β. However, knockdown of DJ-1 increased T cell migration towards the tumor cells indicating that high levels of DJ-1 suppress T cell migration. DJ-1 overexpression astrocytes also showed only little T cell migration, which was increased upon DJ-1 knockdown in the T cells.

In summary, GBM cells are masters in rewiring their metabolism, signaling pathways and immune regulation to boost cell growth and enhance tumor evasion and metastasis.

Functionally relevant, it was shown that knockdown or knockout of *PARK7* in astrocytes impairs the protection of neurons in rotenone and 6-hydroxydopamine neurotoxin models of PD[85,86]. On the other hand, overexpression of WT *PARK7* increases the neuroprotective capacity of astrocytes in the rotenone model[85]. The neuroprotective effect of astrocytic DJ-1 seems to be mediated via protection against oxidative stress by reducing the amount of neuronal thiol oxidation[87]. In line with these findings for *PARK7* overexpression, but in contrast to the observations in DJ-1 deficient astrocytes, DJ-1 overexpression increased cell growth, metabolic activity and reduced ROS compared to WT astrocytes. Ingenuity

pathway analysis revealed upregulation of cancer associated pathways involved in cell proliferation and cell cycle regulation, which indicates that DJ-1 overexpression in astrocytes can serve as oncogenic model to compare it to the GBM cell lines. Consentaneous with the results in the astrocytes, knockdown of DJ-1 in the GBM cell lines also decreased cell growth and metabolism, increased ROS and the immune response.

GBM is known for its high metabolic activity[79] and its immunosuppressive microenvironment that causes T cell dysfunction and therefore impaired T cell migration[88]. These immune evasion mechanisms are decreasing the effectiveness of immune therapy options. Increasing the infiltration of the tumor microenvironment with T lymphocytes is crucial for an improved tumor therapy. The observed increased glycolysis and TCA cycle are also connected to T cell exhaustion, as GBM cells deprive the tumor microenvironment from glucose that could be used by infiltrating T cells which depend on glycolysis[89].

Since the DJ-1 knockdown aimed to normalize the DJ-1 levels in the GBM cells, the observed decreased TCA cycle flux in the GBM cells upon DJ-1 knockdown might compromise the metabolic activity of the cells so that they cannot produce as much energy as compared to GBM cells with high levels of DJ-1. As discussed above, cancer cells use glycolysis even in the presence of oxygen, rather than fuel the TCA cycle and OXPHOS. However, as stated, in the last years, an increasing number of studies have shown that the TCA cycle plays an important role in the metabolic reprogramming of the cancer cells, emphasizing the importance of our results regarding the effect of DJ-1 levels on the TCA cycle in the GBM cells.

In summary, the direction of the modulation of the pathways by DJ-1 seems to be the same in both diseases, as the knockdown of DJ-1 in the GBM cells had the same effect as loss of DJ-1 in PD patient-derived astrocytes. The inverse phenotypic observations in our models of PD and GBM are therefore attributed to initially inverse DJ-1 levels.

Conclusion and Perspectives

As a conclusion, for GBM, therapeutic targeting of DJ-1 mediated regulation of cytokine secretion and metabolic modulation could help to decrease tumor growth and immune suppressive behavior, which in turn enables effective T cell infiltration and eventually a better antitumor response and thus prognostic outcomes. On the other hand, upregulation of DJ-1 levels to WT levels as a therapeutic option for PD patients could help to restore metabolic activity and decrease neuroinflammation.

Interestingly, TCA cycle influencing mutations in isoforms 1 and 2 of isocitrate dehydrogenase (IDH1 and IDH2) were found frequently in secondary GBM, which account for 73% of clinical cases, whereas they were less seen in primary GBM (3.7%)[90]. IDH-mutant enzymes mediate the conversion of α-ketoglutarate (α-KG) to the oncometabolite D-2-Hydroxyglutarate (D-2-HG), thus draining metabolites from the TCA[91].

D-2-HG was found to be primarily derived from glutamine: glutamine is hydrolyzed by glutaminase to produce glutamate, which is converted to α-KG and eventually converted to 2-HG by mutant IDH[92]. Inhibition of glutaminase was shown to reduce glutamate and α-KG level, thereby preventing the formation of D-2-HG[92]. These results emphasize the importance of our finding of reduced glutamate labeling in the GBM cells upon DJ-1 knockdown. A reduction of DJ-1 levels in IDH mutant GBM cells could therefore not only help to reduce metabolic activity of GBM cells, but also reduce glutamate drainage for D-2-HG production[91].

IDH enzymes were also shown to play a role in neurodegeneration due to their role in cellular metabolism and redox homeostasis via the regeneration of GSH that is very well known to protect neurons from oxidative damage[93].

In PD, IDH dysregulation has been directly linked to DJ-1 as DJ-1 was shown to transcriptionally control IDH expression under oxidative stress[94]. Phenotyping of mammalian DJ-1 knockout cells with IDH1 and IDH2 constructs revealed that both paralogs were able to rescue ROS-induced cell death caused by DJ-1 loss[94].

As an outlook, future experiments could therefore for example analyze the role of DJ-1 in IDH mutant GBM lines.

Importantly, future studies should include the analysis of pathways in both DJ-1 overexpression astrocytes and GBM knockdown cell lines to shed light on the regulation of this pathway by differential DJ-1 level.

Eventually, considering phenotypic overlaps between these conditions might help to understand their mechanistic basis, and thus to define novel target-based treatment strategies for causative treatments.

Appendix

Manuscript VI

Mitochondrial and Clearance Impairment in p.D620N VPS35 Patient-derived Neurons

Hanss et al. 2021

Status:

Published in Movement Disorders 03.11.2020

Preface

I contributed to the following manuscript by performing experiments for Fig. 1A and 1B, Fig. 2E and 2F, Fig. 4B and supplementary Fig. 4A and supplementary Fig. 4B.

R E S E A R C H   A R T I C L E

Mitochondrial and Clearance Impairment in p.D620N VPS35 Patient-Derived Neurons

Zoé Hanss, PhD,[1] Simone B. Larsen, PhD,[1] Paul Antony, PhD,[1] Pauline Mencke, MSc,[1] François Massart, BSc,[1] Javier Jarazo, PhD,[1] Jens C. Schwamborn, PhD,[1] Peter A. Barbuti, PhD,[1,2,3] George D. Mellick, PhD,[4] and Rejko Krüger, MD[1,3,5*]

[1]*Luxembourg Centre for Systems Biomedicine (LCSB), University of Luxembourg, Esch-sur-Alzette, Luxembourg*
[2]*Department of Pathology and Cell Biology, Columbia University Medical Center, New York, New York, USA*
[3]*Transversal Translational Medicine, Luxembourg Institute of Health (LIH), Strassen, Luxembourg*
[4]*Griffith Institute for Drug Discovery, Griffith University, Nathan, Australia*
[5]*Parkinson Research Clinic, Centre Hospitalier de Luxembourg (CHL), Luxembourg*

ABSTRACT: Background: VPS35 is part of the retromer complex and is responsible for the trafficking and recycling of proteins implicated in autophagy and lysosomal degradation, but also takes part in the degradation of mitochondrial proteins via mitochondria-derived vesicles. The p.D620N mutation of *VPS35* causes an autosomal-dominant form of Parkinson's disease (PD), clinically representing typical PD.
Objective: Most of the studies on p.D620N VPS35 were performed on human tumor cell lines, rodent models overexpressing mutant VPS35, or in patient-derived fibroblasts. Here, based on identified target proteins, we investigated the implication of mutant VPS35 in autophagy, lysosomal degradation, and mitochondrial function in induced pluripotent stem cell-derived neurons from a patient harboring the p.D620N mutation.
Methods: We reprogrammed fibroblasts from a PD patient carrying the p.D620N mutation in the *VPS35* gene and from two healthy donors in induced pluripotent stem cells. These were subsequently differentiated into neuronal precursor cells to finally generate midbrain dopaminergic neurons.

Results: We observed a decreased autophagic flux and lysosomal mass associated with an accumulation of α-synuclein in patient-derived neurons compared to controls. Moreover, patient-derived neurons presented a mitochondrial dysfunction with decreased membrane potential, impaired mitochondrial respiration, and increased production of reactive oxygen species associated with a defect in mitochondrial quality control via mitophagy.
Conclusion: We describe for the first time the impact of the p.D620N VPS35 mutation on autophago-lysosome pathway and mitochondrial function in stem cell-derived neurons from an affected p.D620N carrier and define neuronal phenotypes for future pharmacological interventions. © 2020 The Authors. *Movement Disorders* published by Wiley Periodicals LLC on behalf of International Parkinson and Movement Disorder Society.

Key Words: VPS35; induced pluripotent stem cells; mitochondrial impairment; Parkinson's disease; α-synuclein

---

[Correction added on 28 October 2020. The copyright changed after initial online publication.]

*Correspondence to:** Dr. Rejko Krüger, LCSB, University of Luxembourg, Esch-sur-Alzette, 6 avenue du Swing, L-4367, Belvaux, Luxembourg; E-mail: rejko.krueger@uni.lu

Zoé Hanss and Simone B. Larsen contributed equally to this work.

The functional characterization of Parkinson's disease (PD)-linked mutations has enabled he identification of impaired cellular pathways underlying the neurodegeneration of dopaminergic neurons of the substantia nigra.[1] Recently, based on a growing number of genes identified in monogenic forms of PD, alterations of endosomal trafficking came into focus as a pathway linked to the disease. The p.D620N mutation in *VPS35* was identified by two independent research groups in 2011[2,3] and causes a rare autosomal-dominant form of PD, occurring in 1.3% of familial cases and 0.1% of all PD cases.[4] The clinical phenotype of patients resembles the one of typical sporadic PD patients, although variability is present in terms of age of onset.[3,5] Furthermore, *VPS35* expression has been showed to be reduced in the substantia nigra of sporadic PD patients.[6] Therefore, the study of the VPS35 pathway is of interest for a wide range of PD patients.

VPS35 is part of the retromer complex, responsible for the recycling of targeted transmembrane proteins from the early endosome back to the plasma membrane and the retrograde transport from the endosomal system towards the trans-Golgi network (TGN).[7] The retromer is composed of VPS35, VPS29, VPS26A, or VPS26B, and various sorting nexins. The pathogenic p. D620N VPS35 does not intervene with the proper formation of the retromer.[8]

The retromer transports proteins essential to lysosomal clearance, carrying them to the TGN to avoid their degradation. One of the most studied cargo proteins of the retromer is the cation-independent mannose 6-phosphate receptor (CIMPR).[9] CIMPR is an endosomal protein that transports procathepsin D from the endoplasmic reticulum (ER) to the lysosome and is essential for the maturation into the hydrolase cathepsin D. CIMPR is then recycled via the retromer. In cells with a deficiency in VPS35, either through knockdown or by expressing the p.D620N mutant protein, CIMPR is not properly recycled back to the TGN, which leads to the degradation of the receptor and the subsequent mistrafficking of cathepsin D.[10-12] The retromer also recycles key autophagy proteins: Lamp2a, implicated in chaperone-mediated autophagy, and ATG9, a protein involved in the induction of autophagy. Retromer complexes containing mutant VPS35 can no longer bind their cargo proteins and, thus, these proteins cannot escape degradation by the lysosome.[8,13] Overall, the retromer is crucial for proper trafficking of lysosomal clearance proteins, and the p.D620N mutation in VPS35 was found to be associated with dysfunctional lysosomal clearance.[12]

Several studies have identified mitochondrial impairment in rodent dopaminergic neurons expressing p. D620N VPS35. It has been reported that p.D620N VPS35 directly interacts with Drp1 (dynamin-related protein 1), a key component in mitochondria fission, leading to fragmented mitochondria and cell death.[14] Moreover, in dopaminergic neurons from mice depleted of VPS35 or expressing p.D620N VPS35, mitochondrial fragmentation was observed with reduced level of mitochondrial fusion protein Mfn2 (mitofusin 2).[15] This was related to increased mitochondrial fragmentation, with decreased mitochondrial membrane potential (MMP) and impaired respiration.[14,15] Similar results were described in patient-derived fibroblasts.[16] Overall, VPS35, by its central role in endosomal trafficking, regulates cellular and mitochondrial quality control.[17]

Most studies with VPS35 deficiency have been conducted in rodent dopaminergic neurons or *VPS35* knockdown models. Similar loss of function phenotypes were observed in cell lines overexpressing p.D620N VPS35, or in patient-derived fibroblasts of p.D620N VPS35 carriers. To date there have been no studies investigating the effect of mutant p.D620N VPS35 on cellular phenotypes related to mitochondrial function, autophago-lysosomal pathway, and α-synuclein levels in patient-derived neuronal models. Here, we reprogrammed fibroblasts from one patient carrying the p. D620N VPS35 mutation and two gender-matched controls of similar age into induced pluripotent stem cells (iPSCs). Then, we differentiated iPSCs into small molecule neuronal precursor cells (smNPC) and further into neuronal populations enriched in dopaminergic neurons.[18]

We found that iPSC-derived neurons carrying the p. D620N mutation in *VPS35* displayed severe mitochondrial dysfunction with decreased MMP, increased mitochondrial reactive oxygen species (ROS) level, and impaired respiration. Further, we found alterations in mitophagy and a decrease in overall autophagic flux that may be associated with the observed impaired lysosomal function. Moreover, these patient-derived neurons harboring the p.D620N VPS35 mutation displayed a typical accumulation of α-synuclein protein. This suggests that p.D620N VPS35 leads to a profound dysfunction of several cellular processes through its central role in trafficking of proteins.

Materials and Methods

Subjects

We included a male patient carrying the p.D620N mutation in *VPS35*, described previously by Follet et al[10] and two healthy male controls from Tübingen Biobank Control 1 and Control 2. Skin biopsies were taken from each individual aged 73, 72, and 77 years, respectively.

Ethical approval for the generation and functional characterization of patient-derived iPSCs have been provided by informed consent.

Cell Culture and Treatments

For mitochondrial morphology, membrane potential, and ROS assessment, neurons were cultivated in neuronal medium without B27 and ascorbic acid (without antioxidants supplementation) 4 hours prior to the experiment. All treatments were performed in the neuronal medium without antioxidants. To assess the mitophagic clearance capacity, the edited neurons with the Rosella construct were treated with 10 μM CCCP (carbonyl cyanide 3-chlorophenylhydrazone) (Abcam, Cambridge, UK) for 24 hours. For the autophagy experiment, neurons were treated with 100 nM Bafilomycin A1 (Enzo Life Sciences, Bruxelles, Belgium) for 24 hours. For autophagy enhancement, neurons were treated with 25 or 50 nM rapamycin (Enzo Life Sciences) for 24 hours. All experiments were repeated on three to six independent neuronal differentiations.

Live Cell Imaging and Analysis

Mitochondria were visualized using 100 nM MitoTracker Green FM (Invitrogen, Gent, Belgium) in neuronal medium without antioxidants and lysosomes with 100 nM LysoTracker Deep Red (Invitrogen) in neuronal medium with or without antioxidants. At least five Z-stack images per well were acquired using a Zeiss spinning disk confocal microscope. All the raw image datasets used in this study are deposited online in our R3 lab of the University of Luxembourg (https://webdav-r3lab.uni.lu/public/MitoNetworks/VPS35Neurons/).

To segment mitochondria, the mitochondrial channel was pre-processed with a difference of Gaussians where the foreground image was convolved with a Gaussian of size 11 and standard deviation 1 and the subtracted background image with a Gaussian of size 11 and standard deviation 3 (Mito_DoG). Only pixels above threshold 3000 in Mito_DoG and an intensity above 5000 in the raw mitochondrial channel were considered as foreground pixels. The mitochondrial mask was defined by removing connected components with less than 10 pixels. Mitochondrial morphometrics were quantified as previously described.[19] Additional data on mitochondrial network can be consulted in Zanin et al.[20]

Mitorosella Sensor, Generation of the Lines, Image Acquisition and Analysis

The generation of the lines carrying the Rosella reporter was performed as previously described.[21] Briefly, the tandem fluorescent proteins consisting of pH sensor fluorescent protein pHluorin (F64L, S65T, V193G, and H231Q) and DsRed were fused to the entire open reading frame of ATP5C1 serving as a mitochondrial targeting sequence, and placed in between the homology arms targeting the AAV1 safe harbour[22] (Addgene plasmid #22075). A double-strand break for triggering homologous recombination was performed with the px330[23] (Addgene plasmid #42230) carrying the sgRNA targeting sequence for the safe harbor as described by Mali et al.[24] SmNPC from patients (VPS35 1_2) and control individuals (Control 1) were nucleofected (P3 Primary Cell 4D-Nucleofector, V4XP-3024; Lonza, Basel, Switzerland) with both constructs and expanded before purification by fluorescence-activated cell sorting (FACS) (Aria III; Beckton Dickinson, Franklin Lakes, NJ).

Images were obtained on an Opera QEHS confocal spinning disk microscope (Perkin Elmer, Waltham, MA) with a 60× water immersion objective (NA = 1.2). pHluorin was excited with a 488 nm laser and detected on camera 1 behind a 520/35 bandpass filter, while DsRed was excited with a 561 nm laser and detected on camera 2 behind a 600/40 bandpass filter. A 568 dichroic mirror split the light towards the corresponding cameras. Both fluorescent channels were acquired simultaneously with a binning setting of 2. One plane and 15 fields per well were acquired. One pixel corresponds to 0.2152 μm. Differentiated neurons were maintained under normal incubation conditions (37°C, 5% CO_2, and 80% humidity) within the microscope in between and during the different acquisition time points.

The automated image analysis was performed through a series of pre-processing and thresholds in MATLAB (The MathWorks, Inc., Natick, MA) as previously described.[21] Briefly, a difference of Gaussian of convoluted foreground and background images was used for detecting all the events in the field. For classifying the events either as a mitochondrial or mitophagic event, a combination of green to red fluorescence ratio analysis and morphological filtering based on difference of Gaussians thresholding was used. Those presenting a mean ratio value below 0.6 were classified as mitophagic events.

Flow Cytometry

Neurons were detached with Accutase (Sigma, Bornem, Begium) and centrifuged at 300 g for 3 minutes. Batches of 200,000 cells were then incubated in the dye or in the buffer (unstained). MMP was assessed by staining the single-cell suspension with 200 nM tetramethylrhodamine ethyl ester (TMRE; Invitrogen) for 30 minutes at 37°C. To correct for mitochondrial mass, MitoTracker Green FM (Invitrogen) was used as a counterstaining. For mitochondrial ROS, the single-cell suspension was stained with 2 μM MitoSOX Red (Invitrogen) for 15 minutes at 37°C without CO_2. Cells were analyzed with the BD LSRFortessa flow cytometry analyser and the mean fluorescence intensity of each dye was assessed on at least 20,000 single cells by using FlowJo LLC software. Mean

fluorescence of the unstained cells was subtracted to account for autofluorescence.

Oxygen Consumption Rate Measurement

Oxygen consumption rate (OCR) was measured in whole cells using the Seahorse XFe96 Cell Metabolism Analyser (Agilent, Diegem, Belgium). Neurons were plated in the Seahorse XFe96 well plates 24 hours prior to measuring at a density of 80,000 cells per well. The concentrations of mitochondrial toxins used were optimized for neurons according to the manufacturer's recommendations. The final concentrations of toxin used were: oligomycin (oligo) - 2 μM; FCCP - 250 nM; antimycin A (AA), and rotenone (rot) - 5 μM. The cells of each well were lysed with radioimmuno-precipitation assay (RIPA) buffer after the experiment and the OCR of each well was corrected for protein amount.Statistics

Statistical analyses were performed with GraphPad Prism. The statistical analyses performed and the P value of each experiment can be found in the legend of the figures.
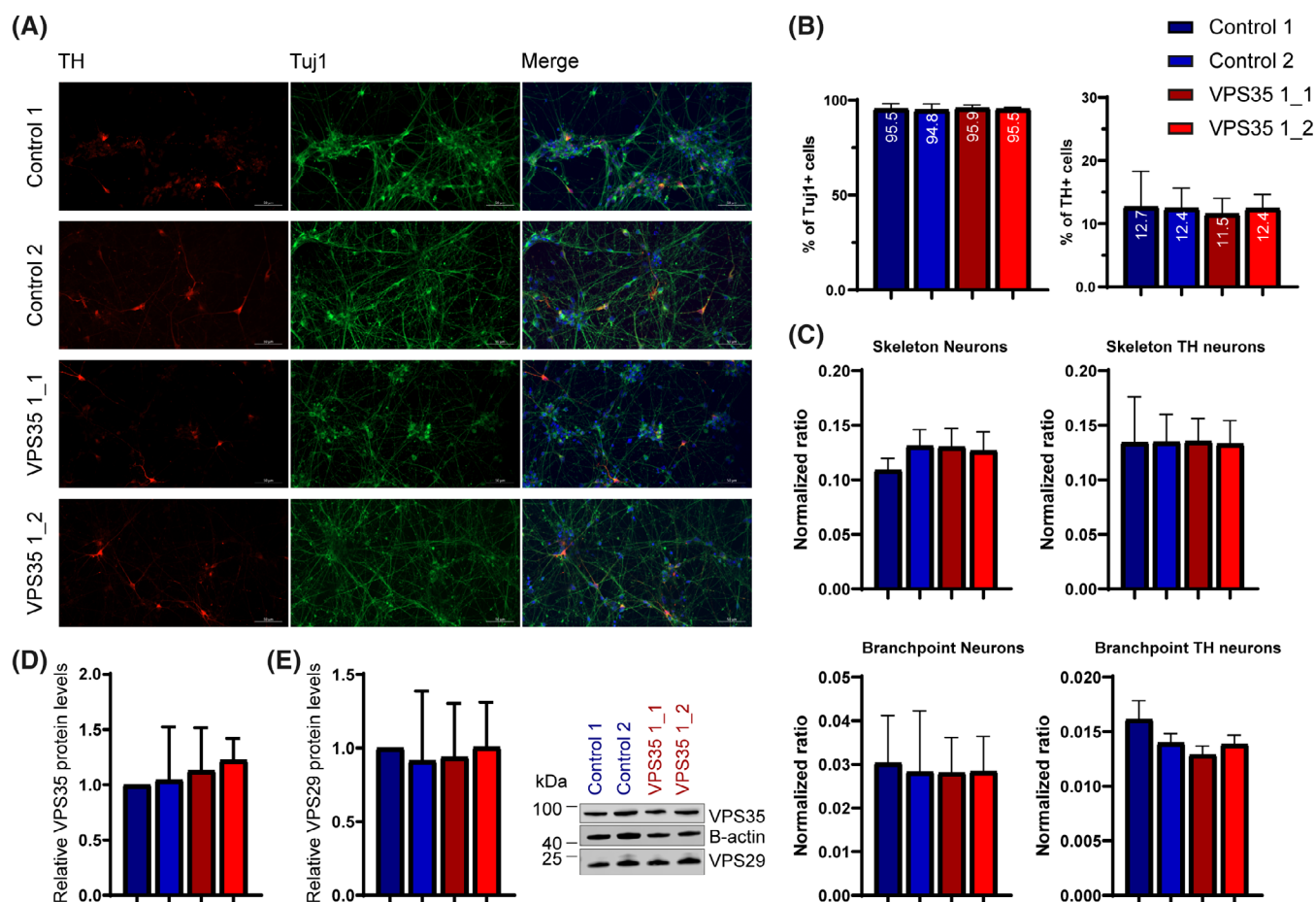
Data Availability

The authors confirm that the data supporting the findings of this study are available within the article and its supplementary material.

Results

Clinical Phenotype of p.D620N VPS35 Patient

The male patient donor case #2610 comes from a multi-incident family #445 reported previously from

FIG. 1. No difference in neuronal morphology and network nor in levels of VPS35 and VPS29 proteins between patient and control induced pluripotent stem cell (IPSC)-derived neurons. (**A**) Representative images of immunofluorescence staining show expression of tyrosine hydroxylase (TH), class III β-tubulin (Tuj1), and nuclear DAPI in IPSC-derived neurons. (**B**) Fluorescence-activated cell sorting (FACS) analysis of neuronal culture revealed no difference in terms of percentage of dopaminergic neurons (TH+) among all neurons (Tuj1+) in control- and patient-derived neuronal cultures after 30 days of maturation (n = 4). (**C**) Analysis of the neuronal network by comparison of neurite length (skeleton) and number of branchpoints shows similar complexity between control- and patient-derived neurons. Values represent pixel count of skeleton or branchpoint normalized to the pixel count of the respective neuronal mask (n = 4). (**D,E**) Western blot analysis of VPS35 (**D**), VPS29 (**E**), and β-actin (loading control) show no difference in protein levels between control (Control 1 and 2) and VPS35 D620N mutant (VPS35 clones 1_1 and 1_2) neurons under basal culture condition. Values normalized to Control 1 (n = 4–6). [Color figure can be viewed at wileyonlinelibrary.com]

the Queensland Parkinson's Project,[25] that immigrated from Western Europe. Besides the index patient, the diagnosis of PD was made in his mother and maternal grandfather but no additional family members are known to be affected. The diagnosis of PD was made by a movement disorders neurologist after a 1-year history of muscular rigidity and tremor. The PD-related motor symptoms responded well to levodopa therapy. The index patient underwent deep brain stimulation 6 years after diagnosis after experiencing motor fluctuations with good treatment response.

VPS35 and VPS29 Levels are Unchanged in p.D620N VPS35 Patient-Derived Neurons

Previous studies have reported that VPS35 protein levels did not change in cells carrying mutant VPS35.[8] The p.D620N mutation in VPS35 has been shown not to impair its binding to the other components of the retromer.[10] To investigate the levels of retromer components we differentiated iPSC from the index patient (VPS35 1_1 and 1_2)[26] and two age- and gender-matched controls (Control 1 and 2) into smNPC.[18] All iPSC and smNPC clones were fully characterized in this study (Figs. S1–S3) or elsewhere.[26] We successfully differentiated these smNPC into physiologically active neurons expressing the neuronal marker Tuj1 (tubulin β3), enriched in dopaminergic neurons expressing tyrosine hydroxylase (TH) (Figs. 1A and S4A-H).[18] No difference was observed in terms of neuronal differentiation efficiency (Figs. 1B and S4A, B) or neuronal network complexity between control- and patient-derived lines (Figs. 1C and S4D). We identified by western blotting that protein levels of both retromer components VPS35 and VPS29 were unchanged between control- and patient-derived neurons (Fig. 1D,E).

p.D620N VPS35 Patient-Derived Neurons Display Mitochondrial Dysfunction

To evaluate the mitochondrial network, we analyzed Z-stack images from two controls and two clones of patient-derived neurons stained with MitoTracker Green FM (Fig. 2A). Computational analyses revealed a decrease in mitochondrial size representative of fragmentation (Fig. 2B). Moreover, mitochondrial branching as a readout for connectivity within the mitochondrial network was impaired with a decreased average number of links (Fig. 2C) and nodes (Fig. 2D).

The identification of these morphological alterations observed in patient-derived neurons led us to assess the mitochondrial function. We measured the bioenergetic profile and found a decreased MMP in patient-derived neurons compared to controls (Fig. 2E). The reduced MMP was accompanied by an increase of intra-mitochondrial ROS compared to controls (Fig. 2F).

Subsequently, mitochondrial respiration was assessed by recording the OCR while we applied mitochondrial stressors: oligomycin, FCCP, antimycin A, and rotenone to measure different respiratory parameters (Fig. 2G). We found that neurons carrying the p.D620N VPS35 mutation displayed a reduced basal and maximal respiration, reduced spare respiratory capacity, and non-mitochondrial oxygen consumption (Fig. 2H). This was associated with a significantly reduced ATP production in patient-derived neurons compared to controls.

VPS35 D620N Patient-Derived Neurons Show an Impaired Mitochondrial Clearance

As patient neurons present morphologically and functionally altered mitochondria, we hypothesized that mitochondrial mass, biogenesis, and clearance (ie, mitophagy) might be dysregulated. We found no difference in mitochondrial mass between patient and control neurons as defined by western blotting against the mitochondrial proteins TOM20 (Fig. 3A) and VDAC1 (Fig. 3B). Moreover, protein expression levels of PGC1α (Fig. 3C), the master regulator of mitochondrial biogenesis, were unchanged in patient-derived neurons under basal conditions.

In order to study mitophagy, Control 1 and VPS35 1_2 cell lines underwent CRISPR-Cas9 gene engineering as iPSC-derived smNPC to express a mitochondrial fusion protein: ATP5C1-DsRed-pHluorin. Briefly, when mitochondria are in the cytoplasm, both fluorophores are functional. Once mitochondria are exposed to an acidic environment inside the autophagosome (mitophagic event) the green fluorescence will be quenched (Fig. 3D). To induce mitophagic events, we treated the gene-edited neurons with CCCP and acquired images from the same field of view at different time points: t = 0, 3, 8, and 24 hours. In control neurons (Fig. 3E), the number of mitochondria inside autophagosomes increased significantly after 3 hours CCCP treatment. After 8 hours and further after 24 hours of CCCP treatment, the number of mitochondria inside autophagosomes were decreasing, showing an efficient clearance. In the patient-derived neurons harbouring the p.D620N VPS35 (Fig. 3F), the number of mitochondria inside autophagosome also increased significantly after 3 hours of CCCP treatment. After 8 hours and 24 hours, the number of mitochondria inside autophagosomes failed to decrease and stayed elevated, indicating a deficient clearance (Fig. 3G). Under basal conditions (t = 0), we see no significant differences in the number of mitochondria inside autophagosomes between patient and control neurons. In addition, after 3 hours of CCCP treatment there was no difference in the number of mitochondria inside autophagosomes between patients and controls (Fig. 3G), indicating that the induction of mitophagy was not impaired in patient neurons.
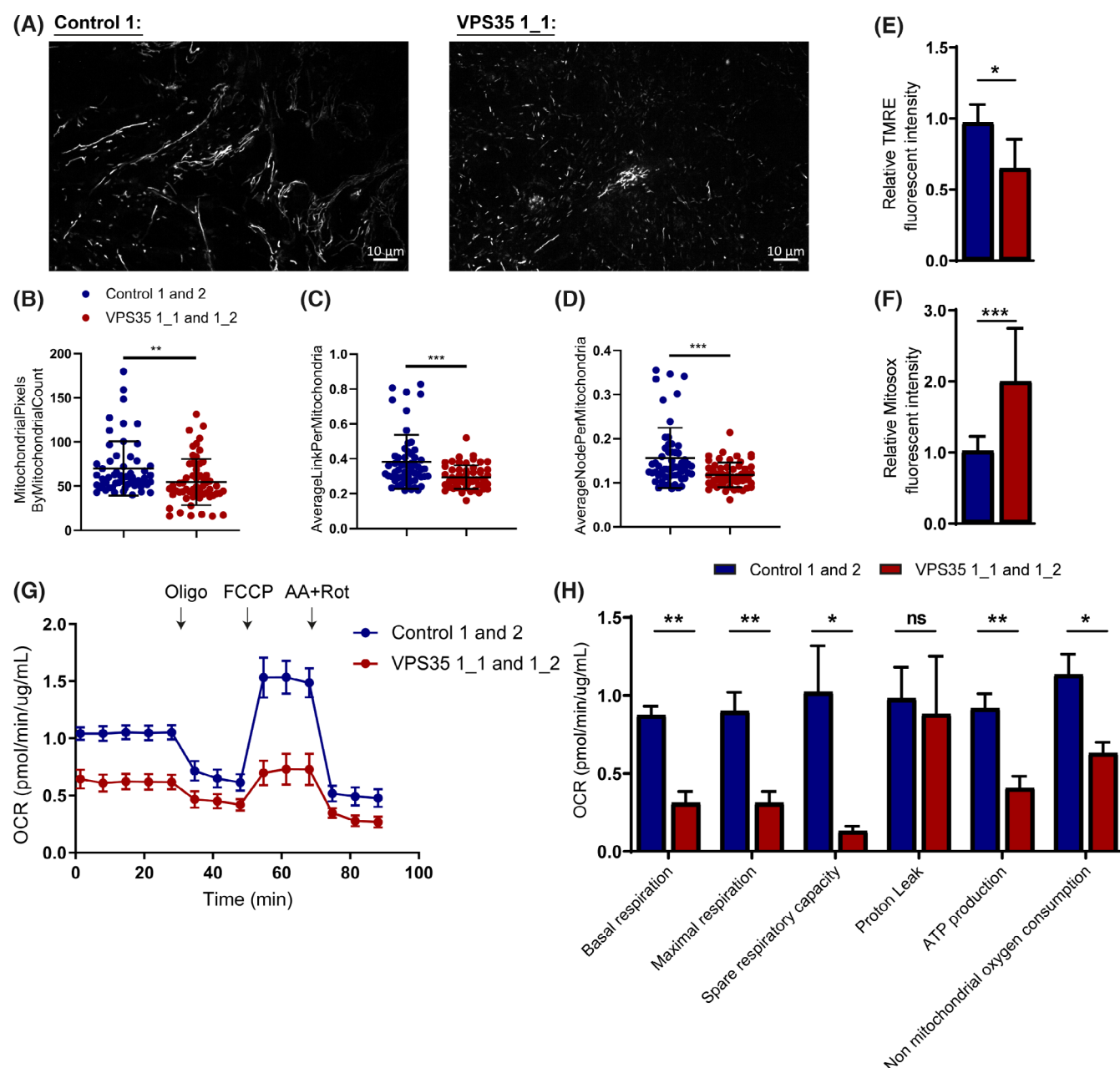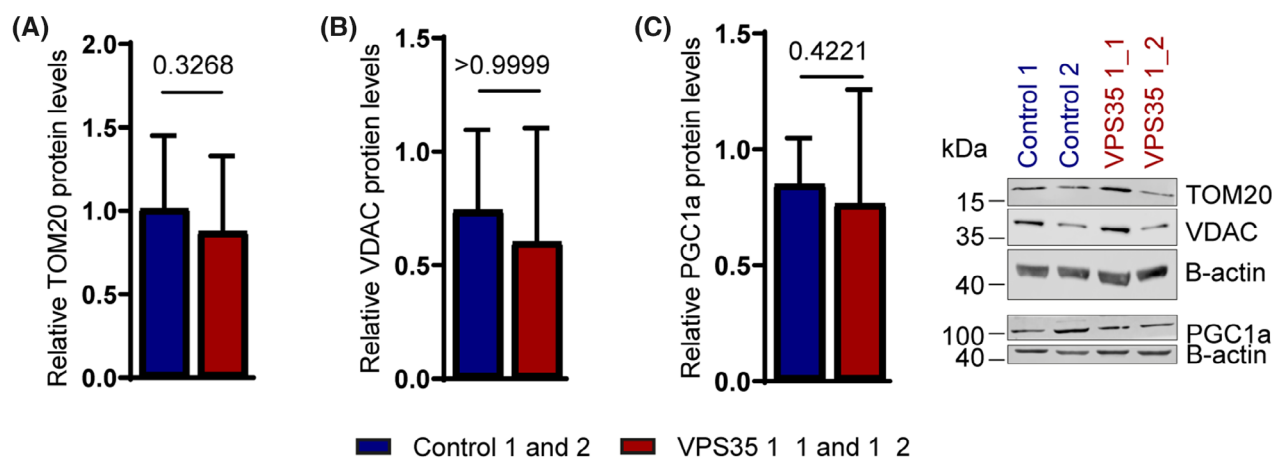
FIG. 2. Mitochondrial dysfunction in VPS35 mutant induced pluripotent stem cell (IPSC)-derived neurons. (**A**) Representative image of mitochondria stained with MitoTracker Green FM and evaluation of mitochondrial size (**B**), average links per mitochondrion (**C**), and average nodes per mitochondrion (**D**) in control (Control 1 and 2) and VPS35 D620N mutant (VPS35 clones 1_1 and 1_2) neurons in culture medium without antioxidants (without B27 and ascorbic acid) for 24 hours (n = 4). (**E**) Mitochondrial membrane potential measured by tetramethylrhodamine ethyl ester (TMRE) mean fluorescence intensity and (**F**) mitochondrial reactive oxygen species measured by MitoSOX mean fluorescence intensity by flow cytometry in control (Control 1 and 2) and VPS35 D620N mutant (VPS35 clones 1_1 and 1_2) neurons in culture medium without antioxidants (without B27 and ascorbic acid) for 4 hours (n = 4). (**G**) Mean average oxygen consumption rate (OCR) of control (Control 1 and 2) and VPS35 D620N mutant (VPS35 clones 1_1 and 1_2) neurons over a time course. Measurement of basal OCR is followed by the addition of oligomycin (oligo) 2 μM final concentration, FCCP 250 nM final concentration, and antimycin A (AA) 5 μM final concentration and rotenone (rot) 5 μM final concentration (n = 4). (**H**) Calculated basal respiration, maximal respiration, spare respiratory capacity, proton leak, ATP production, and non-mitochondrial oxygen consumption (n = 4). All statistical tests were Mann–Whitney tests to compare groups. Error bars show standard deviation and ns $P > 0.05$; *$P < 0.05$; **$P < 0.01$; ***$P < 0.001$. [Color figure can be viewed at wileyonlinelibrary.com]

However, the difference between patient and control cells becomes significant at 8 hours and 24 hours, as the number of mitochondria inside autophagosomes decreased in control-derived neurons and stayed elevated in patient-derived neurons.

Lysosomal Clearance Dysfunction and α-Synuclein Accumulation in p.D620N VPS35 Patient-Derived Neurons

The link between the retromer and macroautophagy has been identified by the sorting of ATG9, an
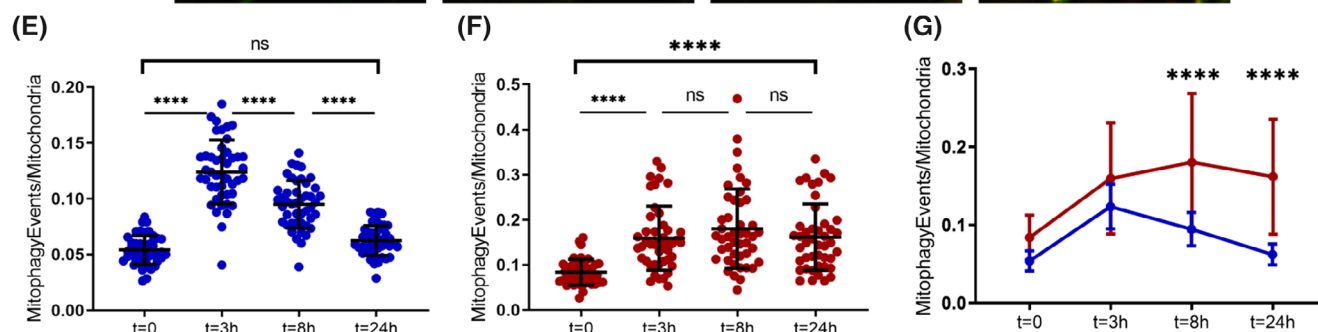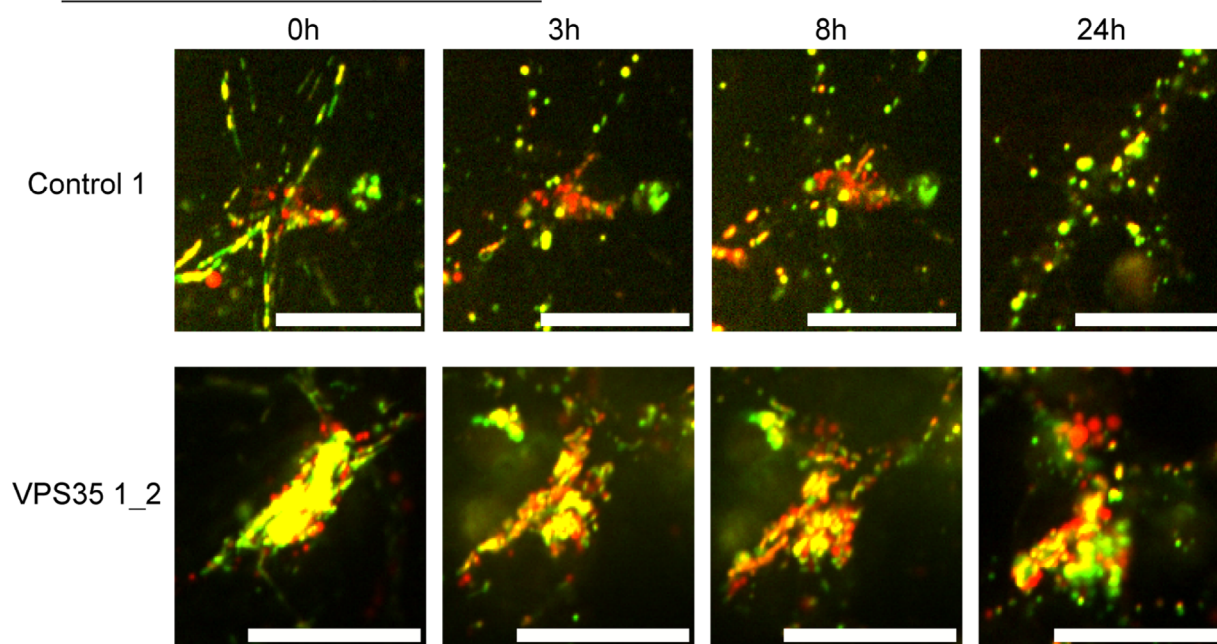
FIG. 3. Mitophagy clearance impairment in VPS35 mutant induced pluripotent stem cell (IPSC)-derived neurons after CCCP (carbonyl cyanide 3-chlorophenylhydrazone) treatment. (**A,B,C**) Western blot analysis of TOM20 (**A**), VDAC (**B**), PGC1α (**C**), and β-actin (loading control) of control (Control 1 and 2) and VPS35 D620N mutant (VPS35 clones 1_1 and 1_2) neurons under basal culture condition (n = 4). (**D**) Representative image of mitochondria and mitophagy events under CCCP treatment over a time course. The scale bar represents 20 μm. Calculated mitophagic events by mitochondria count in Control 1 (**E**) and mutant VPS35 1_2 (**F**) from three independent differentiations of control (Control 1) and VPS35 D620N mutant (VPS35 clone 1_2) neurons expressing ATP5C1-RFP-pHluorin protein in culture medium without antioxidants (without B27 and ascorbic acid) and treated with CCCP 10 μM for 0, 3, 8, and 24 hours. Each time point is compared with the previous one (n = 3). (**G**) Comparison of both lines. All statistical tests were Mann–Whitney tests or one-way ANOVA followed by Sidak's multiple comparisons tests to compare groups and conditions. Error bars show standard deviation and ns $P > 0.05$; *$P < 0.05$; **$P < 0.01$; ***$P < 0.001$; ****$P < 0.0001$. [Color figure can be viewed at wileyonlinelibrary.com]
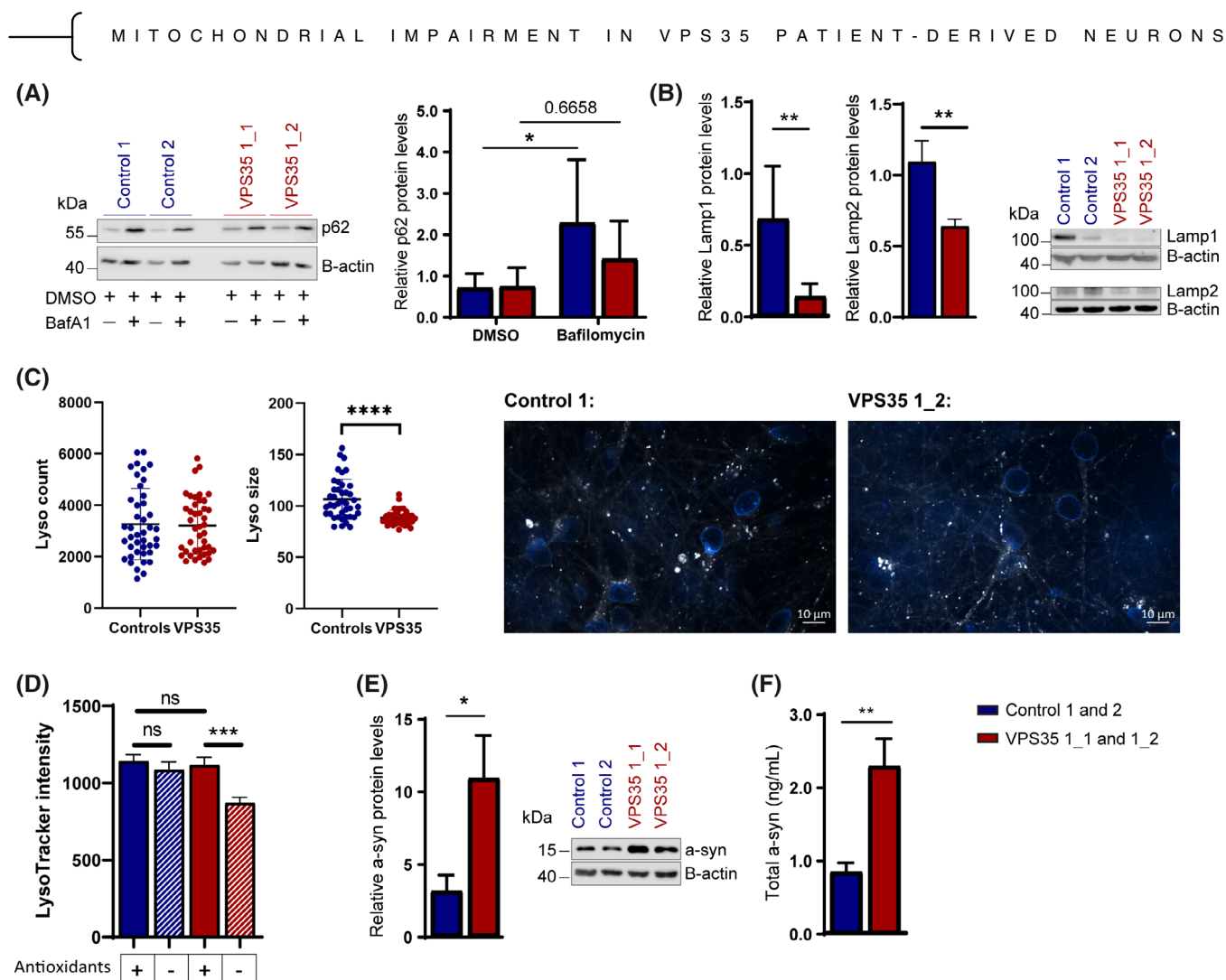
FIG. 4. Impaired lysosomal clearance and α-synuclein accumulation in VPS35 mutant induced pluripotent stem cell (IPSC)-derived neurons. (A) Western blot analysis of p62 and β-actin (loading control) in control (Control 1 and 2) and VPS35 D620N mutant (VPS35 clones 1_1 and 1_2) neurons under basal culture condition and Bafilomycin A1 (BafA1) 100 nM treatment for 24 hours (n = 5). (B) Western blot analysis of Lamp1, Lamp2, and β-actin (loading control) in control (Control 1 and 2) and VPS35 D620N mutant (VPS35 clones 1_1 and 1_2) neurons under basal culture condition (n = 4). (C) Left: evaluation of lysosomal size and number by LysoTracker staining in control (Control 1 and 2) and VPS35 D620N mutant (VPS35 clones 1_1 and 1_2) neurons under basal culture condition (n = 3). Right: representative images of lysosomes stained with LysoTracker Deep Red (white). Nucleus are stained with Hoechst. (D) Evaluation of LysoTracker Deep Red staining intensity in control (Control 1 and 2) and VPS35 D620N mutant (VPS35 clones 1_1 and 1_2) neurons under basal culture condition and mild stress (antioxidant removal) (n = 3). (E) Western blot analysis of α-synuclein (α-syn) and β-actin (loading control) in control (Control 1 and 2) and VPS35 D620N mutant (VPS35 clones 1_1 and 1_2) neurons under basal culture condition (n = 4). (F) Time-resolved fluorescence energy transfer (TR-FRET) measurement of total α-synuclein (α-syn) amount in control (Control 1 and 2) and VPS35 D620N mutant (VPS35 clones 1_1 and 1_2) neurons under basal culture condition (n = 4). All statistical tests were Mann–Whitney tests or one-way ANOVA followed by Sidak's multiple comparisons tests to compare groups and conditions. Error bars show standard deviation and *P < 0.05; **P < 0.01; ***P < 0.001; ****P < 0.0001. [Color figure can be viewed at wileyonlinelibrary.com]

important protein for induction of autophagy with the retromer.[27] Additionally, in cells overexpressing the mutant p.D620N VPS35 it was shown that ATG9 was missorted, which is thought to lead to impaired autophagy.[8] Here, we measured the steady-state level of the autophagy protein p62 (Fig. 4A), which was not differing between patient and control-derived neurons. Upon treatment with Bafilomycin A1, which blocks autophagy by inhibiting the lysosomal v-ATPase, p62 was accumulating in the controls, as shown by an increase compared to the untreated state. However, p62 did not significantly increase in the patient neurons

after Bafilomycin A1 treatment, showing an impaired autophagic flux. Moreover, compared to control-derived neurons, we found reduced Lamp1 and Lamp2 steady-state protein levels in the patient neurons (Fig. 4B), suggesting a lower late-endosome/lysosome mass compared to controls. This decrease in Lamp1 and Lamp2 levels was accompanied by the presence of smaller lysosomes in patient-derived neurons, while the number of lysosomes was comparable between groups (Fig. 4C). This reduction in content and size of lysosome is implying an impaired functionality[13] which is also revealed by a decreased intensity of the acidotropic probe,
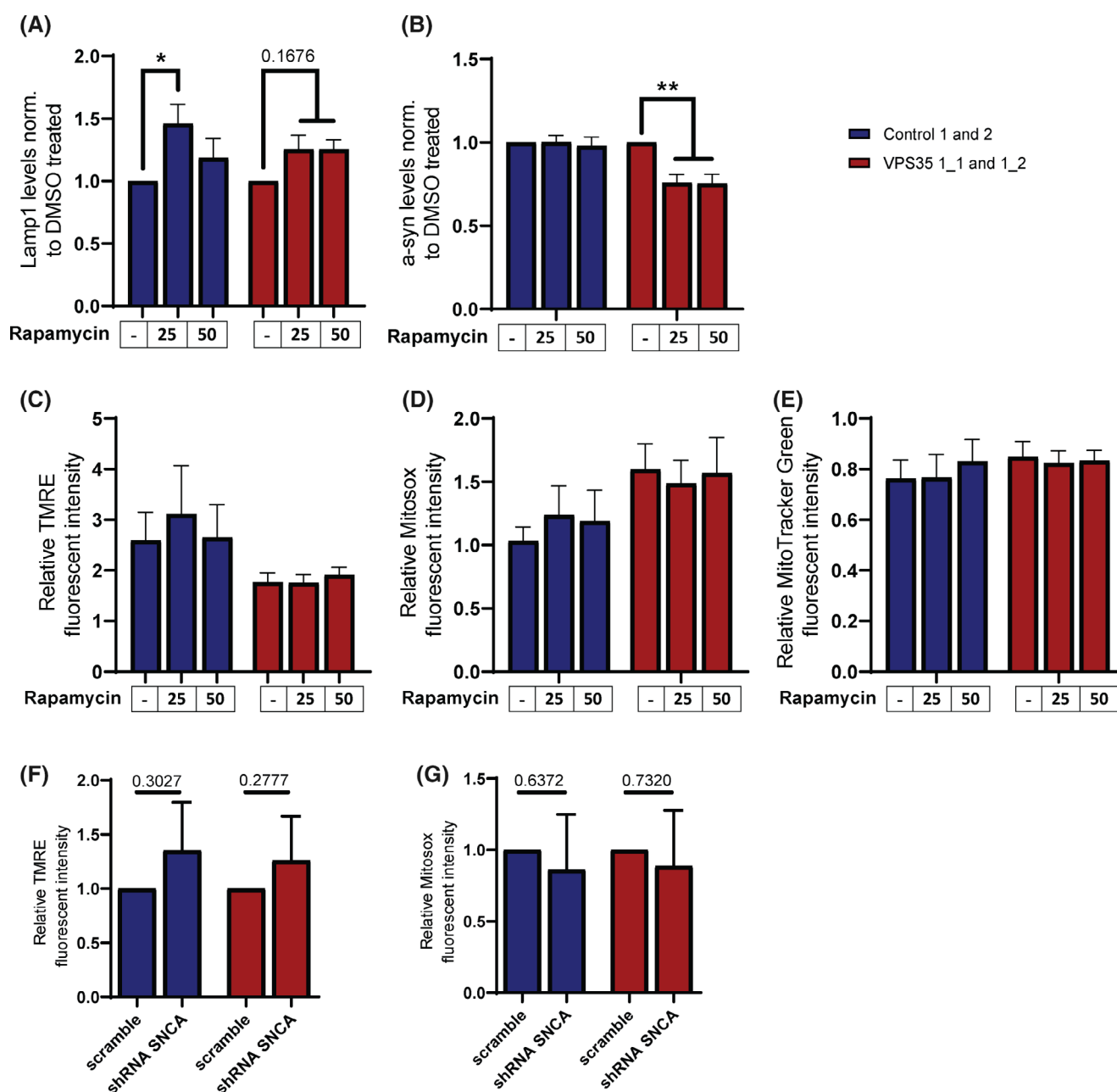
FIG. 5. Autophagy enhancement and α-synuclein knockdown are not sufficient to alleviate mitochondrial dysfunction. (**A,B**) Western blot analysis of Lamp1 (**A**) and α-synuclein (**B**) of control and VPS35 D620N mutant neurons after 24 hours of treatment with DMSO (50 nM) or rapamycin (25 or 50 nM) (n = 5). Values are normalized to DMSO-treated line respectively. (**C**) Mitochondrial membrane potential measured by tetramethylrhodamine ethyl ester (TMRE) mean fluorescence intensity, (**D**) mitochondrial reactive oxygen species measured by MitoSOX mean fluorescence intensity, and (**E**) mitochondrial mass measured by MitoTracker Green FM mean fluorescence intensity by flow cytometry in control and VPS35 D620N mutant neurons after 24 hours of treatment with DMSO (50 nM) or rapamycin (25 or 50 nM) (n = 5). Values are normalized to DMSO-treated Control 1. (**F**) Mitochondrial membrane potential measured by TMRE mean fluorescence intensity and (**G**) mitochondrial reactive oxygen species measured by MitoSOX mean fluorescence intensity by flow cytometry in control and VPS35 D620N mutant neurons transduced with scramble shRNA and shRNA against α-synuclein (n = 3). Values are normalized to scramble transduced line respectively. All statistical tests were Mann–Whitney tests or one-way ANOVA followed by Sidak's multiple comparisons tests to compare groups and conditions. Error bars show standard deviation and *$P < 0.05$; **$P < 0.01$. [Color figure can be viewed at wileyonlinelibrary.com]

LysoTracker, in patient-derived neurons when exposed to mild oxidative stress (antioxidant removal) (Fig. 4D) as already described in other genetic models of PD.[28]

The impaired lysosomal clearance was accompanied by an increase of the amount of α-synuclein in patient-derived neurons as demonstrated by western blotting for the monomeric form of α-synuclein (Fig. 4E) and validated by time-resolved fluorescence energy transfer (TR-FRET) assessing total α-synuclein amount (Fig. 4F).

α-Synuclein Accumulation is not the Main Cause of Mitochondrial Impairment in pD620N VPS35 Neurons

In patient-derived neurons carrying a triplication of the *SNCA* gene locus, extensive mitochondrial defects are found.[29, 30] Consequently, we hypothesized that the mitochondrial impairment seen in our patient-derived neurons could be due to both a general impairment of the autophagy machinery and to α-synuclein accumulation. Therefore, we used a pharmacological approach to rescue autophagy with rapamycin.[31] Rapamycin has been shown to increase lysosomal biogenesis and to enhance mitophagy in cellular models of PD.[32, 33] After 24 hours of treatment, Lamp1 levels were increased in both control- and patient-derived neurons (Fig. 5A) and this led to a moderate decrease of α-synuclein levels in patient-derived neurons (Fig. 5B). We evaluated the effect of this treatment on mitochondrial dysfunction but did not observe a rescue of the decreased MMP nor of the increased ROS levels in patient-derived lines (Fig. 5C,D). Of note, mitochondrial mass was not affected (Fig. 5E), which shows that rapamycin did not enhance basal mitophagy in these experimental conditions. We hypothesized that a more efficient decrease of α-synuclein levels might influence the mitochondrial impairment. We knocked-down α-synuclein in both control- and patient-derived neurons with shRNA against *SNCA*.[34] After transduction, we detected a reduction of the levels of α-synuclein in patient-derived neurons to the physiological levels of α-synuclein (Fig. S5A,B). Using the same technique as previously, we found that the reduction of α-synuclein protein levels did not rescue the loss of MMP (Fig. 5F) nor the increased ROS level (Fig. 5G).

Discussion

The increasing importance of endosomal trafficking pathways in PD pathogenesis has been widely recognized besides established pathways such as mitochondrial impairment, lysosomal dysfunction, protein aggregation, and synaptic dysfunction.[35] Indeed, numerous *PARK* genes (*DNAJC13*, *LRRK2*, and *SNCA*) are implicated in this pathway and there is a growing interest in finding other disease-relevant endosomal trafficking genes.[36]

VPS35 deficiency has been previously linked to mitochondrial and lysosomal clearance impairment in multiple cellular models such as dopaminergic neurons from mice carrying a heterozygous loss of VPS35, rat cortical neurons overexpressing p.D620N VPS35, and patient fibroblasts carrying the p.D620N VPS35 mutation. These studies consistently report fragmented mitochondria with decreased MMP and impaired respiration.[14-16] Moreover, decreased autophagic flux together with impaired cathepsin D and Lamp2a trafficking was also previously described in other models.[5] In this study, we demonstrate for the first time in patient-specific iPSC-derived neurons that the PD-causing mutation p.D620N in *VPS35* leads to fragmented and impaired mitochondria with decreased size and branching, decreased membrane potential, increased mitochondrial ROS, and dysfunctional respiration (Fig. 2). These defects were linked to dysfunctional mitochondrial clearance with accumulation of mitophagic events under mitochondrial stress without completion of the full mitophagic process (Fig. 3). Lysosomal clearance was also more globally impaired with decreased autophagic flux, decreased late-endosome/lysosome mass and size, and impaired acidification (Fig. 4A–D). Possibly linked to the lysosomal dysfunction, we observed an accumulation of α-synuclein in patient-derived neurons (Fig. 4E,F).

We hypothesize that mitochondrial impairment in iPSC-derived neurons carrying the p.D620N VPS35 mutation is caused by a substantially impaired mitochondrial quality control linked to a more general autophagy defect. Improving autophagic function by rapamycin treatment reduced α-synuclein levels in patient-derived neurons, showing the involvement of lysosomal dysfunction in α-synuclein accumulation, but the mitochondrial dysfunction remained (Fig. 5A–D). As it is known that the induction of autophagy via rapamycin is only mild in mammalian cells, for example, compared to yeast cells,[37] we used a more stringent reduction of α-synuclein levels via RNA knockdown. However, also this was not sufficient to significantly improve mitochondrial function (Fig. 5F,G) and shows that α-synuclein accumulation is not the main cause of mitochondrial impairment in p.D620N VPS35 neurons.

Further pharmacological and genetic modification of the lysosome, as well as alternative organellar degradation pathways, may help to better understand the link between lysosomal dysfunction and mitochondrial impairment. Indeed, previous studies also reported that VPS35 and the retromer are involved in an alternative subtype of mitochondrial quality control, via the formation of mitochondria-derived vesicles (MDVs).[38] Two cargos have been identified trafficking towards the lysosome or the peroxisome for degradation, namely Drp1[14] and MAPL (mitochondrial-associated protein ligase).[15,38] MAPL is known to stabilize Drp1, a mitochondrial fission protein, and degrade Mfn2, a mitochondrial fusion protein. By trafficking both proteins, VPS35 seems to stabilize the mitochondrial network in a fused state. In cells overexpressing p.D620N VPS35, the retromer does not correctly transport Drp1 and MAPL, which leads to increased MAPL and Drp1 protein levels and a decreased Mfn2 protein level. This subsequently leads to a fragmented mitochondrial network,[14,15] also observed in patient-derived neurons in our study. Interestingly, treatment of cells overexpressing p.D620N VPS35 and patient fibroblasts

carrying the p.D620N VPS35 variant with Mdivi1, a Drp1 inhibitor, rescues the mitochondrial functional impairment.[14,16] This suggests that mitochondrial functional impairment is at least in part caused by the mistrafficking of Drp1 and MAPL by the retromer-containing mutant p.D620N VPS35.

Although providing evidence for novel cellular phenotypes related to mutant VPS35 in patient-derived neurons, our study has limitations towards the specificity of these findings for the dopaminergic pathway. In order to directly assess a specific role of mutations of VPS35 on dopaminergic neurons, single-cell analyses of these neurons within a mixed culture including glial cells or a cell-sorting of dopaminergic neurons for enrichment prior to experiments would allow evaluation of the specific contribution of these observed cellular phenotypes for dopaminergic neurons. Previous findings on iPSC-derived neurons with heterozygous VPS35 mutations[39] suggested that the p.D620N VPS35 mutation acts by a loss-of-function mechanism, while animal models using overexpression of human mutant VPS35 tend to support a toxic gain-of-function or a dominant-negative mechanism.[40,41] The present data show conserved levels of VPS35 protein and suggest an impairment of physiological functions of VPS35. The next steps to better qualify the p.D620N mutation would include the investigation of the described phenotypes on a larger panel of patient-derived VPS35 D620N lines as well as overexpression of the wild-type and mutant protein in different cell types. Also, the inclusion of isogenic controls would allow dissection of the specific contribution of the p.D620N VPS35 mutation within the individual genetic background of the controls and the patient, which may influence the disease phenotype by itself. Taken together, our findings provide the first evidence for mitochondrial impairment, lysosomal degradation defects, and α-synuclein accumulation in patient-derived neurons, which confirm the implication of the p.D620N VPS35 mutation in the typical pathophysiology of PD. ●

References

1. Krüger R, Klucken J, Weiss D, Tönges L, Kolber P, Unterecker S, et al. Classification of advanced stages of Parkinson's disease: translation into stratified treatments. J Neural Trans 2017;124(8):1015–1027.

2. Vilariño-Güell C, Wider C, Ross OA, Dachsel JC, Kachergus JM, Lincoln SJ, et al. VPS35 mutations in Parkinson disease. Am J Hum Genet 2011;89(1):162–167. https://www.unfpa.org/sites/default/files/pub-pdf/De-linkingFGMfromIslamfinalreport.pdf. Accessed February 17, 2020.

3. Zimprich A, Benet-Pagès A, Struhal W, Graf E, Eck SH, Offman MN, et al. A mutation in VPS35, encoding a subunit of the retromer complex, causes late-onset Parkinson disease. Am J Hum Genet. 2011;89(1):168–175. http://www.ncbi.nlm.nih.gov/pubmed/21763483. Accessed February 17, 2020.

4. Deng H, Gao K, Jankovic J. The VPS35 gene and Parkinson's disease. Mov Disord 2013;28(5):569–575. http://www.ncbi.nlm.nih.gov/pubmed/23536430. Accessed February 17, 2020.

5. Mohan M, Mellick GD. Role of the VPS35 D620N mutation in Parkinson's disease. Parkinsonism Relat Disord 2017;36:10–18. http://www.ncbi.nlm.nih.gov/pubmed/27964832. Accessed February 17, 2020.

6. MacLeod DA, Rhinn H, Kuwahara T, Zolin A, Di Paolo G, McCabe BD, et al. RAB7L1 interacts with LRRK2 to modify intraneuronal protein sorting and Parkinson's disease risk. Neuron 2013;77(3):425–439. https://linkinghub.elsevier.com/retrieve/pii/S0896627312011208. Accessed June 12, 2020.

7. Seaman MN, McCaffery JM, Emr SD. A membrane coat complex essential for endosome-to-Golgi retrograde transport in yeast. J Cell Biol 1998;142(3):665–681. http://www.ncbi.nlm.nih.gov/pubmed/9700157. Accessed February 17, 2020.

8. Zavodszky E, Seaman MNJ, Moreau K, Jimenez-Sanchez M, Breusegem SY, Harbour ME, et al. Mutation in VPS35 associated with Parkinson's disease impairs WASH complex association and inhibits autophagy. Nat Commun 2014;5:3828. http://www.ncbi.nlm.nih.gov/pubmed/24819384. Accessed February 17, 2020.

9. Arighi CN, Harmell LM, Aguilar RC, Haft CR, Bonifacino JS. Role of the mammalian retromer in sorting of the cation-independent mannose 6-phosphate receptor. J Cell Biol 2004;165(1):123–133.

10. Follett J, Norwood SJ, Hamilton NA, Mohan M, Kovtun O, Tay S, et al. The Vps35 D620N mutation linked to Parkinson's disease disrupts the cargo sorting function of retromer. Traffic 2014;15(2):230–244. http://www.ncbi.nlm.nih.gov/pubmed/24152121. Accessed February 17, 2020.

11. McGough IJ, Steinberg F, Jia D, Barbuti PA, McMillan KJ, Heesom KJ, et al. Retromer binding to FAM21 and the WASH complex is perturbed by the Parkinson disease-linked VPS35(D620N) mutation. Curr Biol 2014;24(14):1670–1676. http://www.ncbi.nlm.nih.gov/pubmed/24980502. Accessed February 17, 2020.

12. Miura E, Hasegawa T, Konno M, Suzuki M, Sugeno N, Fujikake N, et al. VPS35 dysfunction impairs lysosomal degradation of α-synuclein and exacerbates neurotoxicity in a drosophila model of Parkinson's disease. Neurobiol Dis 2014;71:1–13.

13. Tang F-L, Erion JR, Tian Y, Liu W, Yin D-M, Ye J, et al. VPS35 in dopamine neurons is required for endosome-to-golgi retrieval of Lamp2a, a receptor of chaperone-mediated autophagy that is critical for α-synuclein degradation and prevention of pathogenesis of Parkinson's disease. J Neurosci 2015;35(29):10613–10628.

14. Wang W, Wang X, Fujioka H, Hoppel C, Whone AL, Caldwell MA, et al. Parkinson's disease-associated mutant VPS35 causes mitochondrial dysfunction by recycling DLP1 complexes. Nat Med 2016;22(1):54–63.

15. Tang FL, Liu W, Hu JX, Erion JR, Ye J, Mei L, et al. VPS35 deficiency or mutation causes dopaminergic neuronal loss by impairing mitochondrial fusion and function. Cell Rep 2015;12(10):1631–1643.

16. Zhou L, Wang W, Hoppel C, Liu J, Zhu X. Parkinson's disease-associated pathogenic VPS35 mutation causes complex I deficits. Biochim Biophys Acta Mol Basis Dis 2017;1863(11):2791–2795. http://www.ncbi.nlm.nih.gov/pubmed/28765075. Accessed February 17, 2020.

17. Larsen SB, Hanss Z, Krüger R. The genetic architecture of mitochondrial dysfunction in Parkinson's disease. Cell Tissue Res 2018;373(1):21–37. http://www.ncbi.nlm.nih.gov/pubmed/29372317. Accessed June 13, 2019.

18. Reinhardt P, Glatza M, Hemmer K, Tsytsyura Y, Thiel CS, Höing S, et al. Derivation and expansion using only small molecules of human neural progenitors for neurodegenerative disease modeling. PLoS One 2013;8(3):e59252 http://www.ncbi.nlm.nih.gov/pubmed/23533608. Accessed February 17, 2020.

19. Baumuratov AS, Antony PMA, Ostaszewski M, He F, Salamanca L, Antunes L, et al. Enteric neurons from Parkinson's disease patients display ex vivo aberrations in mitochondrial structure. Sci Rep 2016;6:33117. http://www.ncbi.nlm.nih.gov/pubmed/27624977. Accessed February 17, 2020.

20. Zanin M, Santos BFR, Antony PMA, Berenguer-Escuder C, Larsen SB, Hanss Z, et al. Mitochondria-mitochondria interaction networks show altered topological patterns in Parkinson's disease. bioRxiv 2020;984195. https://doi.org/10.1038/s41540-020-00156-4. Accessed March 10, 2020.

21. Arias-Fuenzalida J, Jarazo J, Walter J, Gomez-Giro G, Forster JI, Krueger R, et al. Automated high-throughput high-content autophagy and mitophagy analysis platform. Sci Rep 2019;9(1):9455. http://www.ncbi.nlm.nih.gov/pubmed/31263238. Accessed February 17, 2020.

22. Hockemeyer D, Soldner F, Beard C, Gao Q, Mitalipova M, DeKelver RC, et al. Efficient targeting of expressed and silent genes in human ESCs and iPSCs using zinc-finger nucleases. Nat Biotechnol 2009;27(9):851–857.

23. Cong L, Ran FA, Cox D, Lin S, Barretto R, Habib N, et al. Multiplex genome engineering using CRISPR/Cas systems. Science 2013;339(6121):819–823. http://www.ncbi.nlm.nih.gov/pubmed/23287718. Accessed July 9, 2019.

24. Mali P, Yang L, Esvelt KM, Aach J, Guell M, DiCarlo JE, et al. RNA-guided human genome engineering via Cas9. Science 2013;339(6121):823–826.

25. Bentley SR, Bortnick S, Guella I, Fowdar JY, Silburn PA, Wood SA, et al. Pipeline to gene discovery—analysing familial parkinsonism in the Queensland Parkinson's project. Park Relat Disord 2018;49:34–41. http://www.ncbi.nlm.nih.gov/pubmed/29329938. Accessed February 17, 2020.

26. Larsen SB, Hanss Z, Cruciani G, Massart F, Barbuti PA, Mellick G, et al. Induced pluripotent stem cell line (LCSBi001-a) derived from a patient with Parkinson's disease carrying the p.D620N mutation in VPS35. Stem Cell Res 2020;45:101776. https://doi.org/10.1016/j.scr.2020.101776

27. Popovic D, Dikic I. TBC1D5 and the AP2 complex regulate ATG9 trafficking and initiation of autophagy. EMBO Rep 2014;15(4):392–401. http://www.ncbi.nlm.nih.gov/pubmed/24603492. Accessed February 17, 2020.

28. Krebiehl G, Ruckerbauer S, Burbulla LF, Kieper N, Maurer B, Waak J, et al. Reduced basal autophagy and impaired mitochondrial dynamics due to loss of Parkinson's disease-associated protein DJ-1. Petrucelli L, editor. PLoS One 2010;5(2):e9367. http://www.ncbi.nlm.nih.gov/pubmed/20186336. Accessed February 23, 2010.

29. Zambon F, Cherubini M, Fernandes HJR, Lang C, Ryan BJ, Volpato V, et al. Cellular α-synuclein pathology is associated with bioenergetic dysfunction in Parkinson's iPSC-derived dopamine neurons. Hum Mol Genet 2019;28(12):2001–2013. http://www.ncbi.nlm.nih.gov/pubmed/30753527. Accessed August 2, 2019.

30. Little D, Luft C, Mosaku O, Lorvellec M, Yao Z, Paillusson S, et al. A single cell high content assay detects mitochondrial dysfunction in iPSC-derived neurons with mutations in SNCA. Sci Rep 2018;8(1):9033. https://pubmed.ncbi.nlm.nih.gov/29899557/. Accessed July 23, 2020.

31. Sarkar S, Ravikumar B, Floto RA, Rubinsztein DC. Rapamycin and mTOR-independent autophagy inducers ameliorate toxicity of polyglutamine-expanded huntingtin and related proteinopathies. Cell Death Differ 2009;16:46–56. https://pubmed.ncbi.nlm.nih.gov/18636076/. Accessed July 23, 2020.

32. Dehay B, Bové J, Rodríguez-Muela N, Perier C, Recasens A, Boya P, et al. Pathogenic lysosomal depletion in Parkinson's disease. J Neurosci 2010;30(37):12535–12544.

33. Burbulla LF, Fitzgerald JC, Stegen K, Westermeier J, Thost A-K, Kato H, et al. Mitochondrial proteolytic stress induced by loss of mortalin function is rescued by Parkin and PINK1. Cell Death Dis 2014;5(4):e1180. http://www.nature.com/doifinder/10.1038/cddis.2014.103

34. Mazzulli JR, Zunke F, Isacson O, Studer L, Krainc D. α-Synuclein-induced lysosomal dysfunction occurs through disruptions in protein trafficking in human midbrain synucleinopathy models. Proc Natl Acad Sci USA 2016;113(7):1931–1936.

35. Perrett RM, Alexopoulou Z, Tofaris GK. The endosomal pathway in Parkinson's disease. Mol Cell Neurosci 2015;66 (Pt A):21–28. http://www.ncbi.nlm.nih.gov/pubmed/25701813. Accessed February 17, 2020.

36. Bandres-Ciga S, Saez-Atienzar S, Bonet-Ponce L, Billingsley K, Vitale D, Blauwendraat C, et al. The endocytic membrane trafficking pathway plays a major role in the risk of Parkinson's disease. Mov Disord 2019;34(4):460–468.

37. Thoreen CC, Sabatini DM. Rapamycin inhibits mTORC1, but not completely. Autophagy. Taylor and Francis Inc. 2009;5:725–726. https://pubmed.ncbi.nlm.nih.gov/19395872/. Accessed July 31, 2020.

38. Braschi E, Zunino R, HM MB. MAPL is a new mitochondrial SUMO E3 ligase that regulates mitochondrial fission. EMBO Rep 2009;10(7):748–754. http://www.ncbi.nlm.nih.gov/pubmed/19407830. Accessed February 17, 2020.

39. Munsie LN, Milnerwood AJ, Seibler P, Beccano-Kelly DA, Tatarnikov I, Khinda J, et al. Retromer-dependent neurotransmitter receptor trafficking to synapses is altered by the Parkinson's disease VPS35 mutation p.D620N. Hum Mol Genet 2015;24(6):1691–1703.

40. Tsika E, Glauser L, Moser R, Fiser A, Daniel G, Sheerin UM, et al. Parkinson's disease-linked mutations in VPS35 induce dopaminergic neurodegeneration. Hum Mol Genet 2014;23(17):4621–4638.

41. Chen X, Kordich JK, Williams ET, Levine N, Cole-Strauss A, Marshall L, et al. Parkinson's disease-linked D620N VPS35 knockin mice manifest tau neuropathology and dopaminergic neurodegeneration. Proc Natl Acad Sci USA 2019;116(12):5765–5774.

Supporting Data

Additional Supporting Information may be found in the online version of this article at the publisher's web-site.

Manuscript VII

GDAP1 loss of function inhibits the mitochondrial pyruvate dehydrogenase complex by altering the actin cytoskeleton

Wolf et al. 2021

Status:

Published in Communications Biology 03.06.2022

Preface

I contributed to the following manuscript by analysing mass spectrometry data using a computational pipeline in R, which I established during my PhD.

communications
biology

ARTICLE

OPEN

Check for updates

GDAP1 loss of function inhibits the mitochondrial pyruvate dehydrogenase complex by altering the actin cytoskeleton

Christina Wolf[1], Alireza Pouya [1], Sara Bitar[1], Annika Pfeiffer [1], Diones Bueno [1], Liliana Rojas-Charry[1], Sabine Arndt [2], David Gomez-Zepeda[2], Stefan Tenzer [2], Federica Dal Bello[1,3,4], Caterina Vianello [1,3,4], Sandra Ritz[5], Jonas Schwirz[5], Kristina Dobrindt[6], Michael Peitz [6,7], Eva-Maria Hanschmann[8], Pauline Mencke[9], Ibrahim Boussaad [9,10], Marion Silies [11], Oliver Brüstle[6], Marta Giacomello [3,4], Rejko Krüger[9,12] & Axel Methner [1✉]

Charcot-Marie-Tooth (CMT) disease 4A is an autosomal-recessive polyneuropathy caused by mutations of ganglioside-induced differentiation-associated protein 1 (GDAP1), a putative glutathione transferase, which affects mitochondrial shape and alters cellular Ca^{2+} homeostasis. Here, we identify the underlying mechanism. We found that patient-derived motoneurons and *GDAP1* knockdown SH-SY5Y cells display two phenotypes: more tubular mitochondria and a metabolism characterized by glutamine dependence and fewer cytosolic lipid droplets. GDAP1 interacts with the actin-depolymerizing protein Cofilin-1 and beta-tubulin in a redox-dependent manner, suggesting a role for actin signaling. Consistently, GDAP1 loss causes less F-actin close to mitochondria, which restricts mitochondrial localization of the fission factor dynamin-related protein 1, instigating tubularity. GDAP1 silencing also disrupts mitochondria-ER contact sites. These changes result in lower mitochondrial Ca^{2+} levels and inhibition of the pyruvate dehydrogenase complex, explaining the metabolic changes upon GDAP1 loss of function. Together, our findings reconcile GDAP1-associated phenotypes and implicate disrupted actin signaling in CMT4A pathophysiology.

[1] Institute of Molecular Medicine, University Medical Center Mainz, Mainz, Germany. [2] Institute for Immunology, University Medical Center Mainz, Mainz, Germany. [3] Department of Biology, University of Padova, Padova, Italy. [4] Department of Biomedical Sciences, University of Padova, Padova, Italy. [5] Institute of Molecular Biology (IMB) gGmbH, Mainz, Germany. [6] Institute of Reconstructive Neurobiology, University of Bonn Medical Faculty and University Hospital Bonn, Bonn, Germany. [7] Cell Programming Core Facility, University of Bonn School of Medicine, Bonn, Germany. [8] Department of Neurology, Medical Faculty, Heinrich-Heine University, Düsseldorf, Germany. [9] Translational Neuroscience, Luxembourg Centre for Systems Biomedicine (LCSB), University of Luxembourg, Belvaux, Luxembourg. [10] Disease Modeling and Screening Platform (DMSP), Luxembourg Centre of Systems Biomedicine (Biomedicine), University of Luxembourg and Luxembourg Institute of Health (LIH), Belvaux, Luxembourg. [11] Institute of Development Biology and Neurobiology, Johannes Gutenberg-University Mainz, Mainz, Germany. [12] Transversal Translational Medicine, Luxembourg Institute of Health (LIH), Strassen, Luxembourg. ✉email: axel.methner@gmail.com

Charcot-Marie-Tooth (CMT) disease is the most frequently inherited peripheral neuropathy in humans and affects one in 2500 people. Clinically, this group of diseases can be distinguished by mode of inheritance, age of onset, and by electrophysiological characteristics that distinguish demyelinating and axonal forms. Mutations in the gene *GDAP1* (ganglioside-induced differentiation-associated protein 1) cause various forms of CMT: the most frequent recessively inherited demyelinating subtype CMT4A[1], the axonal-recessive (AR)-CMT2[2], the intermediate-recessive subtype CMTRIA[3], and the dominant subtype CMT2K[4].

GDAP1 is located in the mitochondrial outer membrane facing the cytosol. It possesses two glutathione transferase (GST)-like domains[2,5,6] and a C-terminal hydrophobic anchor which crosses the outer mitochondrial membrane[7]. Whether GDAP1 is a catalytically active GST remains controversial[6,8–10], but it appears clear that GDAP1 can bind GST substrates[9,10].

One potential mechanism of GDAP1 action that has been connected to CMT4A disease is mitochondrial dynamics. Overexpression of GDAP1, but not over-expression of GDAP1 bearing recessive disease-causing mutations, results in more fragmented mitochondria, whereas a GDAP1 knockdown (KD) results in mitochondrial elongation[11]. This GDAP1-mediated mitochondrial fragmentation depends on the activity of dynamin-related protein 1 (DRP1), the major mitochondrial fission factor[12,13]. The mechanism behind this is unknown. DRP1 is a cytosolic protein which, when recruited to mitochondria, promotes fission by forming ring-like oligomers that constrict and divide mitochondria[14]. The recruitment of DRP1 to mitochondria depends on the presence of ER tubules[15] and filamentous actin (F-actin)[16] at the sites of constriction. The ER-protein inverted formin 2 (INF2) promotes actin polymerization which occurs before DRP1-driven constriction[17]. INF2-mediated actin polymerization also increases mitochondria-ER contact sites (MERCS)[18]. This further connects actin polymerization and GDAP1 function as mitochondrial and ER marker proteins colocalize less frequently in *GDAP1 KD* cells[19]. Interestingly, INF2 mutations also cause CMT disease (CMTDIE)[20], implying that actin polymerization is important for the survival of peripheral nervous system neurons, similar to GDAP1 function. Another protein at the interface of F-actin polymerization and DRP1 recruitment is Cofilin-1. Cofilin-1 binds to monomeric actin and F-actin and controls cytoskeletal dynamics mostly by actin depolymerization. Cofilin-1 deletion results in DRP1 accumulation at mitochondria and fragmentation[21]. In summary, defective actin polymerization affects the same mitochondrial fission pathway upstream of DRP1 and results in a clinical phenotype similar to GDAP1 mutation. Whether F-actin polymerization and its regulation play a role in CMT4A is still poorly understood.

Another process that is affected by loss of *GDAP1* is cellular Ca^{2+} homeostasis. Neuronal *GDAP1* KD reduces Ca^{2+} influx from the extracellular space that follows depletion of the ER Ca^{2+} stores, so-called store-operated Ca^{2+} entry (SOCE), possibly due to an impaired mitochondrial localization at subplasmalemmal microdomains[19]. *GDAP1* KD also blunts the Ca^{2+}-dependent increase of mitochondrial respiration upon SOCE[22]. Mitochondrial Ca^{2+} levels increase the activity of several enzymes of the tricarboxylic acid cycle (TCA) like pyruvate dehydrogenase (PDH)[23], the key enzyme of the pyruvate dehydrogenase complex (PDC) which catalyzes the conversion of pyruvate to acetyl-CoA and links glycolysis to the TCA. This connection between Ca^{2+} and TCA activity is thought to connect mitochondrial activity to ATP demand. Changes in the activity of the PDC have not been studied yet in CMT4A or in cells with perturbed GDAP1 expression but, interestingly, a pathogenic mutation of pyruvate dehydrogenase kinase isoenzyme 3 (PDK3) that inhibits the PDC also causes CMT disease, CMTX6[24]. How GDAP1-mediated changes of the mitochondrial Ca^{2+} homeostasis are connected to its fission activity is still unclear.

In this study, we used motoneurons obtained from CMT4A-patient-derived induced-pluripotent stem cells and neuronal *GDAP1* KD cells to study the pathophysiology of CMT4A. We found that GDAP1 interacts with actin-binding Cofilin-1. Loss of GDAP1 results in a reduction of F-actin fibers in mitochondrial proximity, which restricts DRP1 access to mitochondrial constriction sites and disrupts mitochondria-ER contact sites. This reduces mitochondrial Ca^{2+} levels and inhibits the PDC resulting in a rewired cellular metabolism characterized by glutamine dependence and increased consumption of fatty acids. Together, these findings implicate disrupted F-actin signaling in CMT4A pathophysiology.
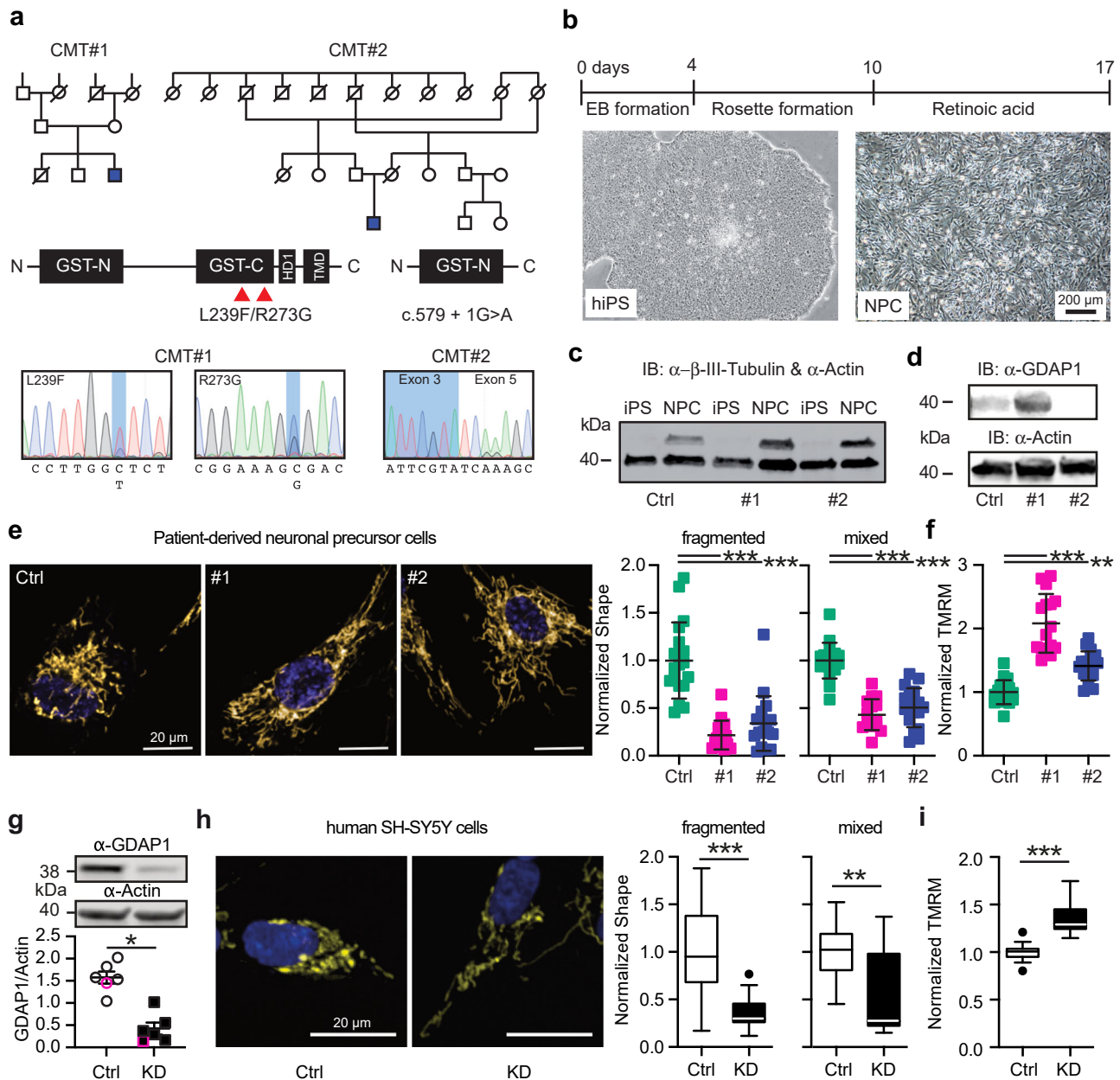
Results

More tubular mitochondria and an increased mitochondrial membrane potential in CMT4A patient-derived neuronal cells and GDAP1 knockdown cells. To establish a model for CMT4A, we compared *GDAP1* KD SH-SY5Y cells[19,25] with neuronal cells derived from CMT4A patients. Patient CMT#1 is a 25-year-old ambulant male with a compound heterozygosity (L239F/R273G) of mutations in the C-terminal GST domain of GDAP1 and patient CMT#2 is a 40-year-old wheelchair-bound male with a homozygous mutation of the intron 4 splice donor site (c.579 + 1G>A). This mutation causes skipping of exon 4 leading to a frameshift and a truncated protein lacking the C-terminal GST and the transmembrane domain of GDAP1 (Fig. 1a).

We generated induced-pluripotent stem cells from fibroblast cell lines[26] from these patients using non-integrative expression of the Yamanaka factors and differentiated them to neuronal precursor cells (NPCs) (Fig. 1b) that express the neuronal marker protein β-III tubulin (Fig. 1c). In contrast to fibroblasts[26], control and CMT#1 NPCs express GDAP1 detectable by immunoblotting (Fig. 1d). NPCs from CMT#2 lacked GDAP1 expression (Fig. 1d). Because the polyclonal antiserum targets an antigen which should still be present in the patient, this is probably due to nonsense-mediated mRNA decay or degradation of the truncated protein.

We quantified mitochondrial shape and membrane potential (Δψm) using automated high-content confocal microscopy analysis of cells simultaneously stained with the fluorescent dyes mitotracker and tetramethylrhodamine methyl ester (TMRM). Patient-derived neuronal cells contained significantly more tubular mitochondria (Fig. 1e) with a more negative mitochondrial membrane potential (Fig. 1f). Applying the same methodology to *GDAP1* KD cells (Fig. 1g), we found similar changes; more elongated mitochondria (Fig. 1h) and a significantly more negative membrane potential (Fig. 1i). The consistency between the phenotypes of patient-derived cells and *GDAP1* KD cells suggests that *GDAP1* KD cells are a suitable model to study CMT4A disease.

GDAP1 knockdown uncouples mitochondrial respiration from ATP generation. Mitochondria produce ATP by consuming oxygen and the energetic electron donors NADH and $FADH_2$ in a process called oxidative phosphorylation. NADH is provided by the TCA, PDH and β-oxidation. To assess the effect of *GDAP1* KD on this all-important process, we measured mitochondrial oxygen consumption using high-resolution respirometry and found a higher mitochondrial routine respiration in *GDAP1* KD cells (Fig. 2a). The maximal capacity of the electron transfer system (ETS), determined by titrating in the uncoupler FCCP, was however similar in both cell lines (Fig. 2a). Normalization of the respiratory states to the maximum ETS capacity, the so-called flux control ratio, revealed that the *GDAP1* KD cells use a higher

Fig. 1 More tubular mitochondria and an increased mitochondrial membrane potential in CMT4A patient-derived neuronal cells and GDAP1 knockdown cells. a Pedigree and GDAP1 DNA sequences from two patients suffering from autosomal-recessive CMT4A disease. **b** Differentiation protocol to obtain neuronal precursor cells from induced-pluripotent stem cells (iPSCs). **c** Immunoblot demonstrating expression of the neuronal marker β-tubulin III in the NPCs but not in iPSCs. **d** Control and CMT#1 but not CMT#2 neuronal cells express GDAP1 shown by immunoblotting. Size is indicated, Actin served as loading control. **e, h** Representative images of automated high-content confocal microscopy analysis of mitochondrial shape (MitoTracker) in patient-derived (**e**) and *GDAP1* KD (**h**) cells demonstrating elongated mitochondria in GDAP1 loss-of-function cells. **f, i** Increased mitochondrial membrane potential (TMRM) in patient-derived (**f**) and *GDAP1* KD (**i**) cells. The values obtained in control cells were set as 1. **g** GDAP1 immunoblot and quantification demonstrating successful knockdown. Size is indicated, Actin served as loading control. Data in e and f are from 3 independent experiments with 4–8 replicates per experiment with a range of 74 to 1908 cells per well. Data in (**h**) and (**i**) are from 4 independent experiments with 4–8 replicates with a range of 343 to 4977 cells per well. Statistical variation is shown as scatter plot (**e–g**) or Tukey boxplot (**h, i**) and significance calculated using one-way ANOVA (**e, f**) or Mann–Whitney (**g–i**) tests, *$p < 0.05$, **$p < 0.001$, ***$p < 0.0001$.

fraction of their maximal capacity for routine, leak and phosphorylating respiration (Fig. 2a′). An increased ratio between non-phosphorylating leak respiration (electron flow coupled to proton pumping to compensate for proton leaks) and ETS capacity suggests intrinsic uncoupling or dysfunction in *GDAP1* KD cells. Quantification of ATP content using the ratiometric reporters BTeam targeted either to the cytosol or to the mitochondrial matrix[27] also demonstrated a reduced mitochondrial ATP

generation in *GDAP1* KD cells despite the increased Δψm and routine respiration (Fig. 2b). Taken together, these data suggest that *GDAP1* KD results in the uncoupling of mitochondrial respiration and ATP generation via oxidative phosphorylation.

GDAP1 knockdown shifts cellular metabolism towards glutaminolysis. To identify metabolic pathways in *GDAP1* KD cells
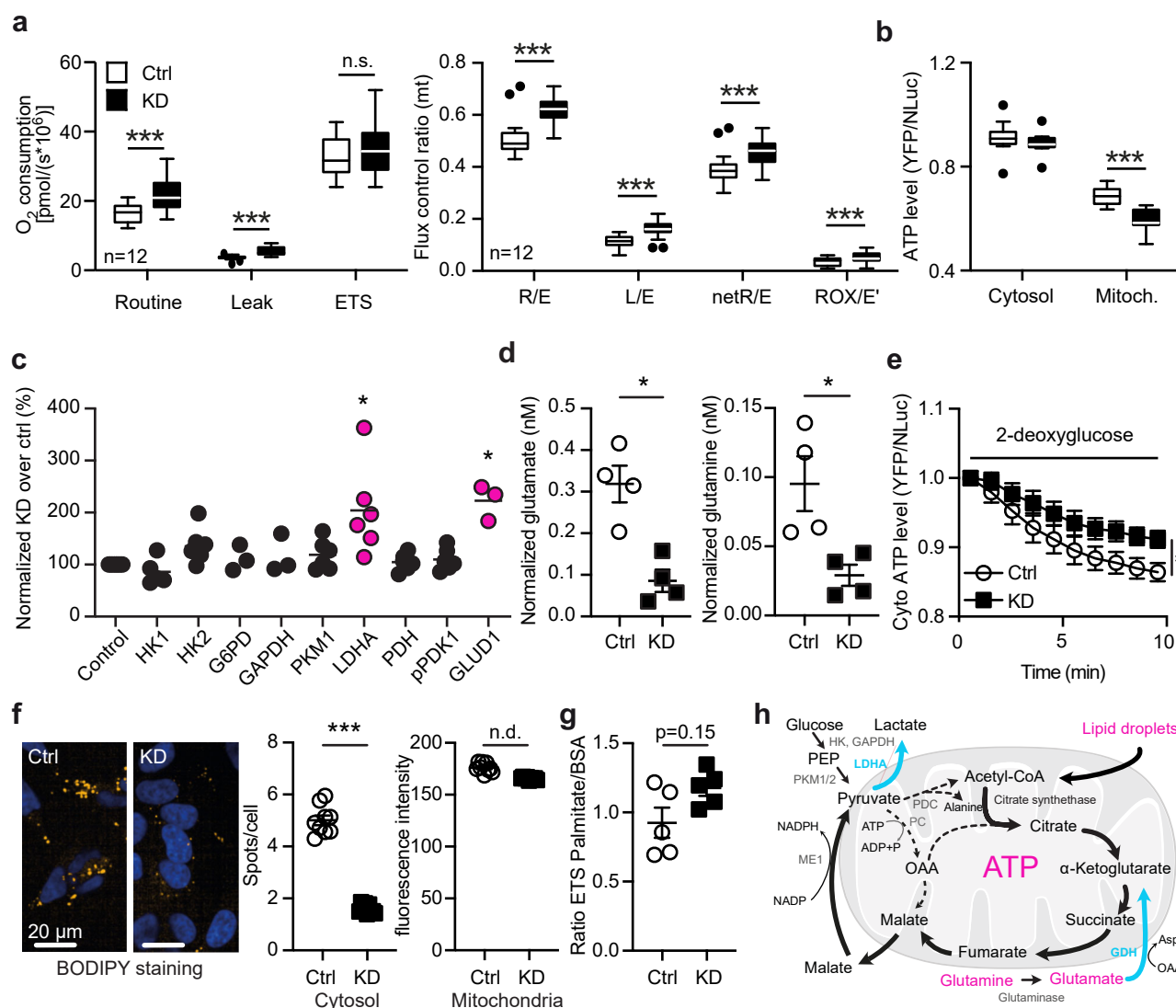
Fig. 2 GDAP1 knockdown uncouples mitochondrial respiration from ATP generation and shifts metabolism towards glutaminolysis. a Mitochondrial oxygen consumption of intact cells in regular growth medium measured by high-resolution respirometry and corrected for ROX. ETS, electron transfer system; L, leak respiration; R, routine respiration; E, ETS capacity; ROX, residual oxygen consumption; netR, oxygen consumption minus ROX. Calculation of flux control ratios. **b** Comparison of cytosolic and mitochondrial ATP content using the genetically encoded ATP sensor BTeam. Calculation of BTeam YFP/ NLuc emission ratios under basal conditions revealed reduced mitochondrial ATP levels. **c** Immunoblot quantification of proteins involved in glycolysis in Ctrl and KD cells shows an increase in lactate dehydrogenase A (LDHA) and glutamate dehydrogenase 1 (GLUD1) levels. HK, Hexokinase; G6PD, glucose-6-phosphate dehydrogenase; GAPDH, Glyceraldehyde 3-phosphate dehydrogenase; PKM1, pyruvate kinase M1; PDH, pyruvate dehydrogenase; pPDK1, phospho-pyruvate dehydrogenase kinase. Actin expression served as loading control. **d** Diminished glutamate and glutamine levels determined by a luminescence-based assay. **e** Comparison of cytosolic ATP content using the genetically encoded ATP sensor BTeam. BTeam YFP/NLuc emission ratios after treatment with 25 µM 2-deoxyglucose reveals increased non-glucose dependent ATP generation capacity in KD cells. **f** Automated high-content confocal microscopy analysis of BODIPY-stained fatty acids demonstrating less lipid droplets in KD cells identified by Höchst staining of nuclei. Lipid droplets close to mitochondria were identified by MitoTracker staining. **g** ETS capacity in the presence of palmitate or BSA as substrates measured by high-resolution respirometry. **h** Schematic illustration of metabolic changes observed in *GDAP1* KD cells. Upregulation is shown in blue and bold lines; downregulation in magenta and dashed lines. ME, malic enzyme 1; PDC, pyruvate dehydrogenase complex; PKM1/2, pyruvate kinase M1/2; OAA, oxaloacetate. Data in (**a**) and (**a'**) are from 12 independent experiments performed in duplicate. Data in (**b**) are from 4 independent experiments performed in triplicates. Data in (**e**) are from 6 independent experiments performed in triplicates. Data in (**f**) were from >10,000 cells in total and were analyzed in 3 independent experiments performed in triplicates. Statistical variation is shown as Tukey's boxplots in (**a**) and (**b**), **XY** graph in (**c**), scatter plots in (**d**) and (**f**), mean ± SEM in (**e**). Significance was calculated using the student's *t* test in (**a**), 2-way ANOVA in b, the non-parametric Kruskal–Wallis test in (**c**), the Mann–Whitney test in (**d**–**g**), *$p < 0.05$, **$p < 0.001$, ***$p < 0.0001$.

that compensate for the diminished capacity for oxidative phosphorylation, we quantified the expression levels of various metabolic enzymes in control and KD cells by immunoblotting. This revealed a significant higher protein levels of lactate dehydrogenase (LDHA) and glutamate dehydrogenase 1 (GLUD1) in

GDAP1 KD cells (Fig. 2c, Supplementary Fig. 1). LDHA catalyzes the interconversion of pyruvate to lactate. GLUD1, in contrast, converts glutamate to α-ketoglutarate, the precursor of succinyl-CoA in the TCA. In line with the increased expression of GLUD1, *GDAP1* KD cells consume significantly more glutamate, the
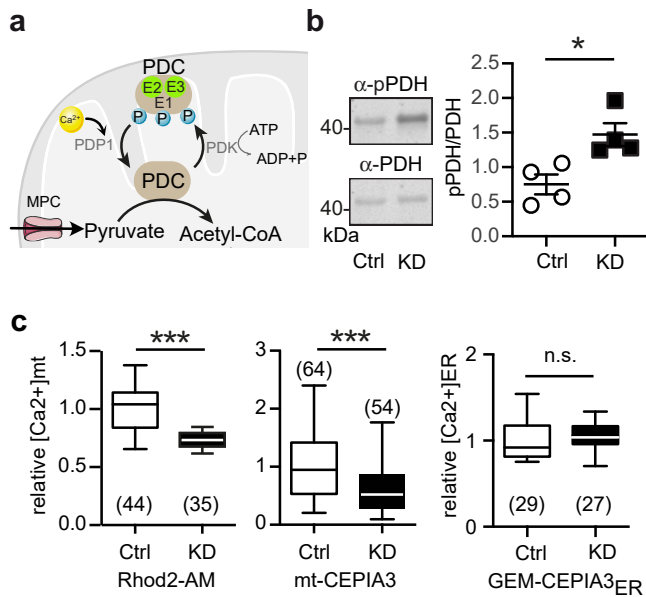
Fig. 3 Hyperphosphorylated pyruvate dehydrogenase and reduced mitochondrial Ca^{2+} levels in *GDAP1* KD cells. a Scheme showing the regulation of the pyruvate dehydrogenase complex (PDC). The PDC E1 subunit can be phosphorylated by the catalytic activity of the PDH kinase (PDK). The PDH phosphatase subunit 1 (PDP1) in turn dephosphorylates the serine residues upon activation by Ca^{2+}. MPC, mitochondrial pyruvate carrier; PDK1, pyruvate dehydrogenase kinase 1. **b** Immunoblots from whole cell lysates for quantification of PDH E1 phosphorylation (serine 293), normalized to total PDH E1 levels revealed increased phosphorylation of PDH in *GDAP1* KD cells. **c** Mitochondrial Ca^{2+} measured with the fluorescent dye Rhod2-AM or mito-CEPIA normalized to mito-FarRed indicated reduced mt[Ca^{2+}] levels. ER[Ca^{2+}] levels measured with the genetically encoded Ca^{2+} sensor GEM-CEPIA3$_{ER}$ did not show any variation between the cell lines. Data in (**c**) were from 3 independent experiments with the indicated number of cells. Data for GEM-CEPIA3$_{ER}$ were from 2 independent experiments. Statistical variation is shown as scatter plots in (**b**) and Tukey boxplots in (**c**). Significance was calculated using the non-parametric Mann–Whitney in (**b**) and Student's *t* test in (**c**), *$p < 0.05$, **$p < 0.001$, ***$p < 0.0001$.
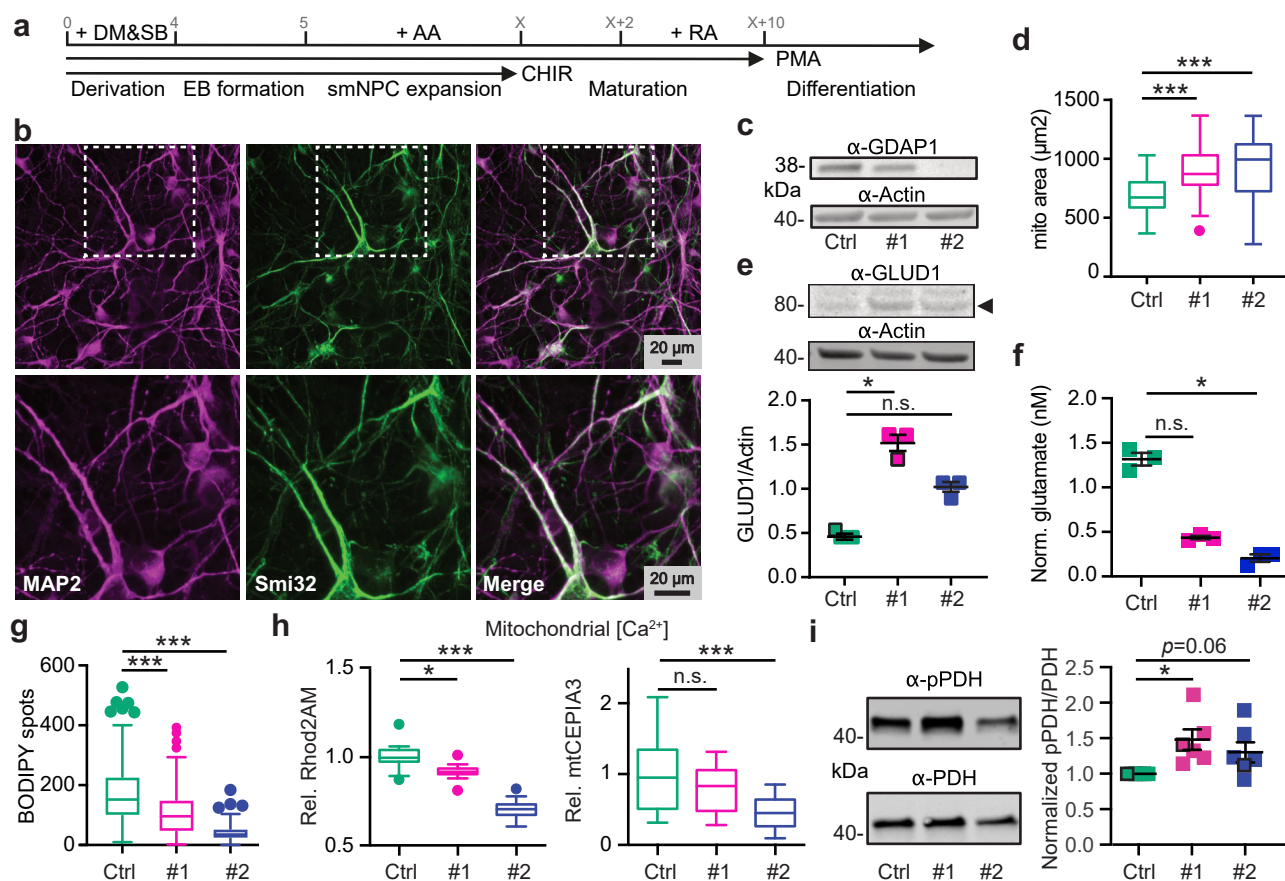
mechanisms, clearly pointing towards a dysfunction of the TCA cycle in *GDAP1* KD cells at the level of the PDC (summarized in Fig. 2h).

Hyperphosphorylated pyruvate dehydrogenase and reduced mitochondrial Ca^{2+} levels in *GDAP1* KD cells. Increased mitochondrial Ca^{2+} levels activate the PDC by stimulating PDH phosphatase[28]. Ca^{2+} also activates isocitrate dehydrogenase which is upstream of α-ketoglutarate, the product of GLUD1, and α-ketoglutarate dehydrogenase[29]. Based on the reported attenuated mitochondrial respiration upon SOCE in *GDAP1* KD cells[22], we suspected altered PDH phosphorylation levels driven by changes in mitochondrial Ca^{2+} content as the reason for PDC inhibition (see scheme in Fig. 3a). To test this idea, we probed phosphorylation of serine 293 of the E1 PDH subunit, which has been directly linked to PDC activity[30]. Immunoblotting showed a significantly increased phosphorylation of PDH E1 serine 293 in *GDAP1* KD cells as compared to total E1 PDH (Fig. 3b). This is in line with a decreased activity of the PDC. We then measured mitochondrial Ca^{2+} levels by imaging live cells stained with Rhod2-AM or expressing the genetically encoded mitochondrial Ca^{2+} sensor mito-CEPIA[31] normalized to mito-FarRed. The Ca^{2+} sensor GEM-CEPIA1er targeted to the ER served as a control. Both methods revealed a reduction in steady-state mitochondrial Ca^{2+} levels in *GDAP1* KD cells, whereas ER calcium levels were not affected (Fig. 3c). We conclude that the PDC malfunction in *GDAP1* KD cells is likely caused by a reduction in mitochondrial Ca^{2+} levels resulting in an increased phosphorylation of PDH.

Patient-derived cells are similarly characterized by increased glutaminolysis, reduced lipid droplets and reduced mitochondrial Ca^{2+} levels. We next tested whether the findings of reduced mitochondrial Ca^{2+} levels and increased glutaminolysis also apply to patient-derived cells. We set out to specifically test this in motoneurons, a cell type affected by CMT4A. Motoneurons were differentiated from NPCs following established protocols (Fig. 4a) and motoneuronal identity was confirmed by immunostaining against the dendrite marker MAP2 and the motoneuronal neurofilament H marker antibody Smi32 (Fig. 4b). Control and patient-derived motoneurons stained similarly for these markers as shown by high-content imaging (Supplementary Fig. 2). These motoneurons express GDAP1 similar to NPCs with cells from patient CMT#2 lacking GDAP1 expression (Fig. 4c). High-content microscopy of MitoTracker-stained cells revealed an increased area occupied by mitochondria (Fig. 4d). Immunoblotting reproduced the increased expression of GLUD1 seen upon *GDAP1* KD (Figs. 4e, 2c). Motoneurons differentiated from patient-derived cells also increased the consumption of the GLUD1-substrate glutamate (Figs. 4f, 2d) and its precursor glutamine. Furthermore, motoneurons showed a decrease in lipid droplets normalized to the nuclear area (Fig. 4g), indicative of increased fatty acid consumption. Together, these data further highlight the similarity between patient-derived cells and *GDAP1* KD cells.

Because motoneuronal cells showed a low transfection efficiency which made it difficult to identify single neurons in the cultures, we reverted to the patient-derived NPCs instead of fully differentiated motoneurons to assess the mitochondrial Ca^{2+} phenotype. We measured lower resting Ca^{2+} levels with Rhod2-AM and mito-CEPIA (Fig. 4h) in NPCs, similar to KD cells. Patient-derived NPCs also had increased levels of pPDH as compared to total PDH levels (Fig. 4i). We conclude that neuronal cells from patients with GDAP1 mutation not only have the same changes in mitochondrial shape and membrane

substrate of GLUD1, and more glutamine which can be converted to glutamate by glutaminase (Fig. 2d). We also observed an attenuated decline in cytosolic ATP content in KD cells after treatment with the glucose antimetabolite 2-deoxyglucose (Fig. 2e) in line with a reduced use of glucose as the major fuel for the TCA cycle. The TCA metabolite upstream of α-ketoglutarate is citrate, which is produced by the transfer of acetyl-CoA to oxaloacetate. Acetyl-CoA is the product of the PDC in the mitochondrial matrix or of mitochondrial β-oxidation. We suspected a dysfunction of the TCA cycle in *GDAP1* KD cells at the level of the PDC and therefore quantified the amount of lipid droplets as alternative sources for acetyl-CoA via β-oxidation in *GDAP1* KD cells. We quantified the amount of lipid droplets by BODIPY C$_{12}$ staining and indeed found decreased cytosolic lipid droplet levels in *GDAP1* KD cells, whereas lipid droplets associated with mitochondria were unchanged (Fig. 2f). Maximum oxygen consumption of *GDAP1* KD cells indeed tended to be higher in the presence of the fatty acid oxidation substrate palmitate (Fig. 2g). Together, these results are in line with a high lipid catabolism that serves to replenish fatty acids and consequently acetyl-CoA levels in the TCA cycle. We posit that the increased demand of glutamine and fatty acids in *GDAP1* KD probably serve as compensatory

Fig. 4 Patient-derived cells are similarly characterized by an anaplerotic state and reduced mitochondrial Ca^{2+} levels. a Differentiation protocol to obtain motoneurons (MN) from induced-pluripotent stem cells (iPSCs) and (**b**) confirmatory immunocytochemistry by staining against dendrite marker MAP2 and motoneuronal neurofilament Smi32. **c** Immunoblot of total MN cell lysates for validation of GDAP1 expression, actin served as loading control, size is indicated. **d** Automated high-content microscopy analysis of MitoTracker-stained mitochondria revealed an increased total mitochondrial mass per well. **e** Immunoblot of total MN cell lysates demonstrated increased glutamate dehydrogenase (GLUD1, arrowhead) in patient-derived MNs, actin served as loading control. **f** Reduced glutamate levels in CMT4A patient-derived MN determined by a luminescence-based assay indicating increased glutamine consumption compared to Ctrl. **g** Automated high-content microscopy analysis of BODIPY-positive spots normalized to the nuclei area in MN revealed a reduced number of lipid droplets in CMT4A patient-derived cells. **h** Reduced relative mt[Ca^{2+}] levels of NPCs determined by confocal microscopy with Rhod2-AM and mito-CEPIA3. **i** Immunoblots and quantification demonstrating increased phosphorylation of PDH E1 serine 293, normalized to total PDH E1 levels and control cells. Data in (**d**–**g**) were from 3 independent differentiations and data in (**d**, **g**) were obtained from $n > 40{,}000$ cells in quadruplicate, experiments in (**f**) were performed in duplicate. Data in (**h**) were from 20–22 Rhod2-AM-stained cells and 22–33 cells mitoCEPIA3 transfected from three independent experiments. Data in (**i**) were from 6 different passages. Data points corresponding to the example blots are highlighted. Statistical variation is shown as Tukey boxplots in (**d**, **e**) or scatter plots in (**i**) with mean ± SEM indicated. Significance was calculated using the non-parametric Kruskal–Wallis test, *$p < 0.05$, **$p < 0.001$, ***$p < 0.0001$.

potential as *GDAP1* KD cells (Fig. 1) but also feature the same metabolic changes and alterations of Ca^{2+} levels. Together this suggests that GDAP1-mediated CMT4A is caused by inhibition of PDH activity resulting in an anaplerotic state.

GDAP1 knockdown reduces the number of contact sites between mitochondria and the endoplasmic reticulum. We suspected that changes in MERCS might underlie the changes in mitochondrial Ca^{2+} levels especially as a reduced colocalization of ER and mitochondrial markers hint to changes in MERCS, as shown previously[19]. MERCS are hot spots of interactions between the ER and mitochondria defined by a distance of mitochondrial and ER membranes between ~10 and ~50 nm[32] and are important signaling hubs (reviewed in ref. [33]). Using transmission electron microscopy, we indeed found (i) a decrease in MERCS in *GDAP1* KD cells defined as the percentage of mitochondrial perimeter covered by the ER, (ii) a decreased number of MERCS

per mitochondrion, (iii) a decreased length of MERCS (Fig. 5a) and (iv) an increased width between the ER and mitochondria (Fig. 5a, b). As an additional readout to quantify the distance between mitochondria and the ER, we used a well-established assay based on Förster resonance emission transfer (FRET) between two fluorescent proteins targeted to the surface of mitochondria and the ER, both facing the cytosol[34,35]. The lower FRET ratio (Fig. 5c) confirmed the data obtained by the morphometric analysis with an increased width between the organelles in *GDAP1* KD cells. Comparing the amount of ER protein present in mitochondrial cell fractions using immunoblotting of the membrane ER protein Sec62 and the mitochondrial protein Cox4 also confirmed the reduction in contact sites (Fig. 5d). Such a reduction and increased distance should result in decreased Ca^{2+} transfer from the ER to the mitochondrial matrix. We studied this by triggering ER Ca^{2+} release with the cholinergic agent carbachol, which activates inositol trisphosphate receptors (IP3Rs) leading to Ca^{2+} release into the cytosol, generating Ca^{2+}
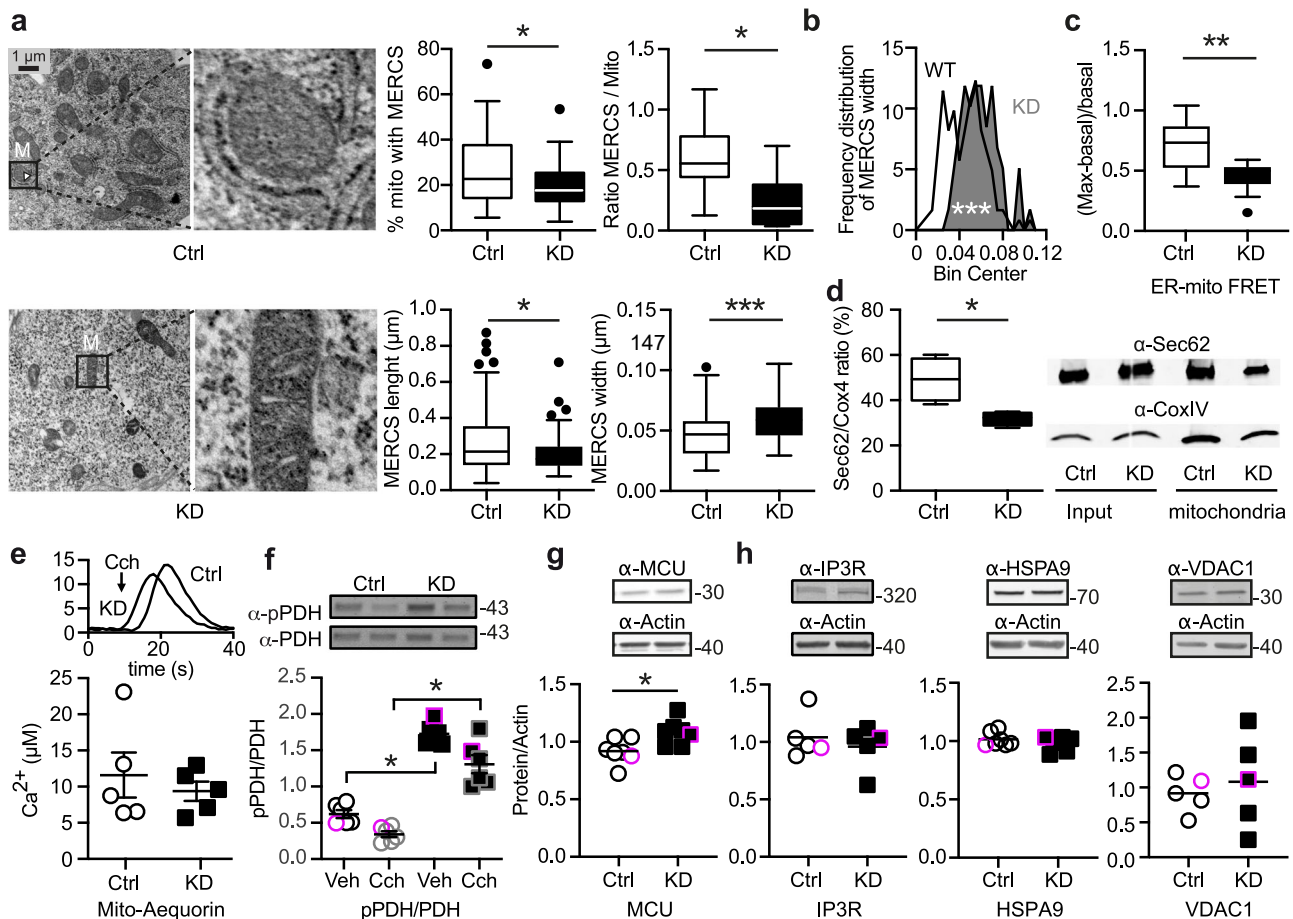
Fig. 5 GDAP1 knockdown reduces the number of contact sites between mitochondria and the endoplasmic reticulum. a Transmission electron microscopy of knockdown (KD) and control (Ctrl) cells. The indicated parameters were quantified using ImageJ by a blinded investigator. M, mitochondrion. **b** Histogram showing the distribution of MERCS' widths, and an increased distance in KD cells between the ER and mitochondria. **c** Proximity of ER and mitochondria was measured using a FRET-FEMP sensor comprising ER CFP-Sac1 and mitochondrial YFP-Akap1. Proximity leads to high intensity of YFP-FRET-emission (410-430/520-560 ex/em). 100 nM rapamycine was added to achieve the closest possible distance, and the measurement of FRET ratio was calculated as $(FRET_{max}-FRET_{basal})/FRET_{basal}$. **d** Quantification of ER membrane (Sec62) and mitochondrial (Cox4) proteins in mitochondrial fractions. **e** Representative curve for the aequorin Ca^{2+} measurement and quantification of mitochondrial Ca^{2+} levels after addition of 200 μM carbachol (CCH), which releases Ca^{2+} from the ER by activation of a G-protein-coupled receptor. **f)** Immunoblot of Ctrl and KD cells lysed 10 min after 200 μM CCH addition to quantify the PDH phosphorylation ($pPDH/(PDH_{total})$ after Ca^{2+} release into the MERCS and mitochondria. **g, h** Immunoblot of total cell lysates of Ctrl and KD cells showing increased expression levels of MCU but not pan-IP3R, HSPA9 or VDAC1, actin served as loading control, size is indicated. Data in (**a**) were obtained from 11 (Ctrl) and 9 (KD) cells, in (**b**) from 4 independent experiments in triplicate or quintuplicate with a range of 162–818 cells per experiment, and in (**d**) from 4 independent experiments. Data in (**e**) from 5 independent experiments performed in triplicates. Data points corresponding to the example blots are highlighted. Statistical variation is shown as Tukey boxplots or scatter plots with the indication of mean ± SEM and significance was calculated using the non-parametric Mann–Whitney test, *$p < 0.05$, **$p < 0.001$, ***$p < 0.0001$.

microdomains at MERCS, which sustain rapid Ca^{2+} uptake by mitochondria[34,36]. Surprisingly, we did not observe a difference in mitochondrial Ca^{2+} uptake measured by mitochondrially-targeted aequorin upon treatment with carbachol (Fig. 5e). The direct reducing effect of carbachol on PDH E1 phosphorylation was also similar in both cell lines while the baseline levels were significantly increased in *GDAP1* KD cells (Fig. 5f). Apparently, upregulated MCU levels (Fig. 5g) and hyperpolarization (see Fig. 1I) can compensate for the increased distance between the organelles under conditions of high Ca^{2+} influx. The other components of the ER-mitochondrial Ca^{2+} uptake complex[37], the IP3R ER Ca^{2+} release channels, the molecular chaperone glucose-regulated protein 75 (Grp75, official name Heat Shock Protein Family A (Hsp70) Member (HSPA)), and the mito-chondrial voltage-dependent anion channel 1 (VDAC1) at the outer mitochondrial membrane were however similarly expressed in *GDAP1* KD and control cells (Fig. 5h). Taken together our

findings support altered MERCS with an increased distance between the ER and mitochondria in *GDAP1* KD cells.

Increased levels of proteins involved in β-oxidation in *GDAP1* KD cells. To clarify how *GDAP1* KD affects MERCS and mito-chondrial Ca^{2+} levels, we next set out to identify proteins that are dysregulated in KD cells by label-free quantitative liquid chro-matography coupled to mass spectrometry (LC-MS)[38]. Compar-ing the proteome of control and *GDAP1* KD cells identified 985 significantly dysregulated proteins out of 3914 proteins—456 proteins were found to be less abundant and 529 to be more abundant (Fig. 6a). Then, we submitted the list of upregulated proteins to STRING[39] and observed that the following KEGG (Kyoto Encyclopedia of Genes and Genomes) pathways were over-represented with an false-detection rate below 2×10^{-4}: protein processing in the ER, lysosome, regulation of the actin cytoskeleton, endocytosis, fatty acid degradation and citrate cycle
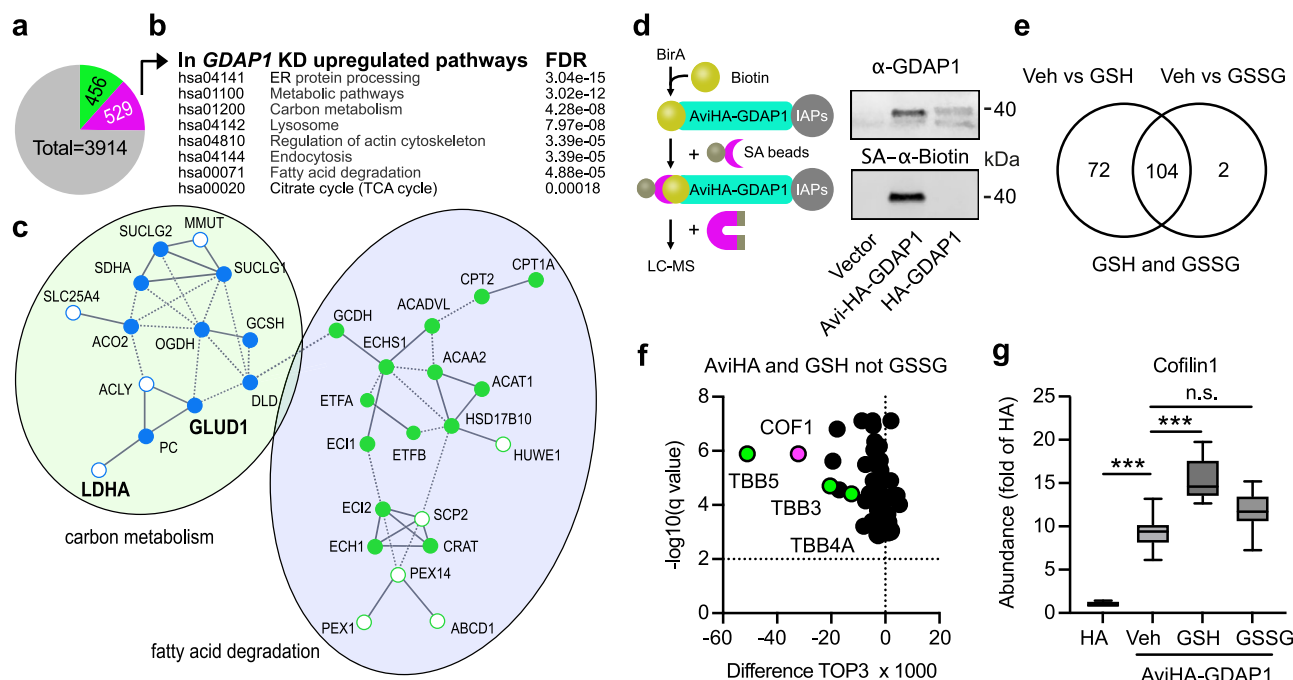
Fig. 6 LC-MS proteomics identifies proteins involved in β-oxidation as being more abundant in *GDAP1* KD cells and hints to alterations of the actin cytoskeleton mediated by redox-dependent interactions with GDAP1. a Number of proteins dysregulated in *GDAP1* KD cells identified by label-free proteomics from three independent experiments, measured in quadruplicates, green less abundant, magenta more abundant. Statistical significance was determined by Student's *t* test with Bonferroni correction. **b** KEGG pathways significantly altered in proteins more abundant in *GDAP1* KD cells. **c** Section of a STRING analysis of proteins more abundant in *GDAP1* KD cells corroborating altered carbon metabolism (blue) and fatty acid degradation (green) in these cells. Open dots correspond to more abundant interacting proteins that do not fall directly into these categories. Proteins in bold were found to be more abundant independently using immunoblotting. **d** Schematic illustration showing the biotinylation of the AviTag fused to GDAP1 protein and subsequent pulldown and enrichment of biotinylated GDAP1 protein via streptavidin-labeled magnetic beads. Immunoblot of cell lysates prior to pulldown of biotinylated GDAP1 stained against GDAP1 and Biotin with an infrared-labeled streptavidin (SA) dye shows an overlap of biotinylation and GDAP1 protein. Streptavidin pulldown was performed with primary neuronal cultures from BirA-expressing E16 mouse embryos. **e** Results from label-free quantitative proteomics performed with GSH or GSSG added to the preparation, (**f**) shows the 72 proteins with an altered expression after addition of GSH but not GSSG. **g** TOP3 quantification of Cofilin-1 abundance and increased Cofilin-1 abundance upon GSH, but not GSSG addition indicated an interaction with GDAP1 in a redox-dependent manner. Statistical significance in g was determined by one-way ANOVA and the Tukey test, ***$p < 0.0001$.

(Fig. 6b). The analysis corroborated the increased levels of LDHA and GLUD1 observed by immunoblotting (Fig. 2c). It also demonstrated increased levels of proteins involved in β-oxidation (Fig. 6c) like carnitine palmitoyltransferase 1 (CPT1A) which catalyzes the transfer of the acyl group of long-chain fatty acid-CoA conjugates onto carnitine to transport the resulting acyl-carnitine long-chain fatty acids inside the mitochondria. These results suggest that the decrease in lipid droplets observed in *GDAP1* KD cells (Fig. 2f) indeed reflects a high lipid catabolism that serves to provide the TCA cycle with acetyl-CoA.

GDAP1 interacts with proteins of the actin cytoskeleton in a redox-dependent manner. We then used label-free proteomics to identify GDAP1-interacting proteins to get a more complete picture of how GDAP1 loss of function affects cellular metabolism. We transduced primary cortical cultures from mice expressing the biotin ligase BirA[40] with adeno-associated viruses expressing GDAP1 tagged with an Avi-tag, a specific substrate for BirA[41]. Only Avi-HA-tagged GDAP1 but not the HA-tagged control was biotinylated (Fig. 6d). By treating the mitochondrial preparations with GSH or GSSG as described[42], we further aimed to identify proteins whose interaction is affected by their specific redox state. This was driven by the fact that GDAP1 can bind potential GST substrates[9,10] and the assumption that such an interaction might depend on the local redox environment. A total of 268 proteins were pulled down from Avi-HA but not or less from HA-GDAP1-transduced cultures. 176 of these proteins

showed a statistically different abundance in preparations treated with GSH compared to vehicle and 106 in preparations treated with GSSG. For 72 proteins the interaction with GDAP1 was altered only by GSH and not by GSSG treatment (Fig. 6e). Interestingly, the most strongly and most significantly regulated proteins can be linked to the cytoskeleton like tubulins (Fig. 6f, green), crucial components of the cytoskeleton that can serve as a scaffold for mitochondrial transport[43]. This is consistent with regulation of the actin cytoskeleton being one of the top hits in the KEGG analysis of proteins upregulated in *GDAP1* KD cells (Fig. 6b, Supplementary fig. 3). In addition, an interaction between GDAP1 and β-tubulin TUBB has been reported in a yeast-two-hybrid experiment[44]. This led us to further concentrate our subsequent analysis on a potential misregulation in actin dynamics in CMT4A-disease models.

GDAP1 knockdown reduces Cofilin-1 abundance at mitochondria. The actin-regulatory protein Cofilin-1 (Fig. 6g) specifically caught our attention because it affects mitochondrial shape by inducing depolymerization of actin filaments in mitochondrial proximity which restricts access of DRP1 to mitochondria[21]. Its antagonist is the ER-anchored INF2, which also causes CMT disease when mutated[20]. We further explored the identified interaction between GDAP1 and Cofilin-1, and hypothesized that GDAP1 alters actin abundance, polymerization or both at mitochondrial sites by interacting with Cofilin-1. The actin-binding ability of Cofilin-1 is inhibited by phosphorylation of serine 3
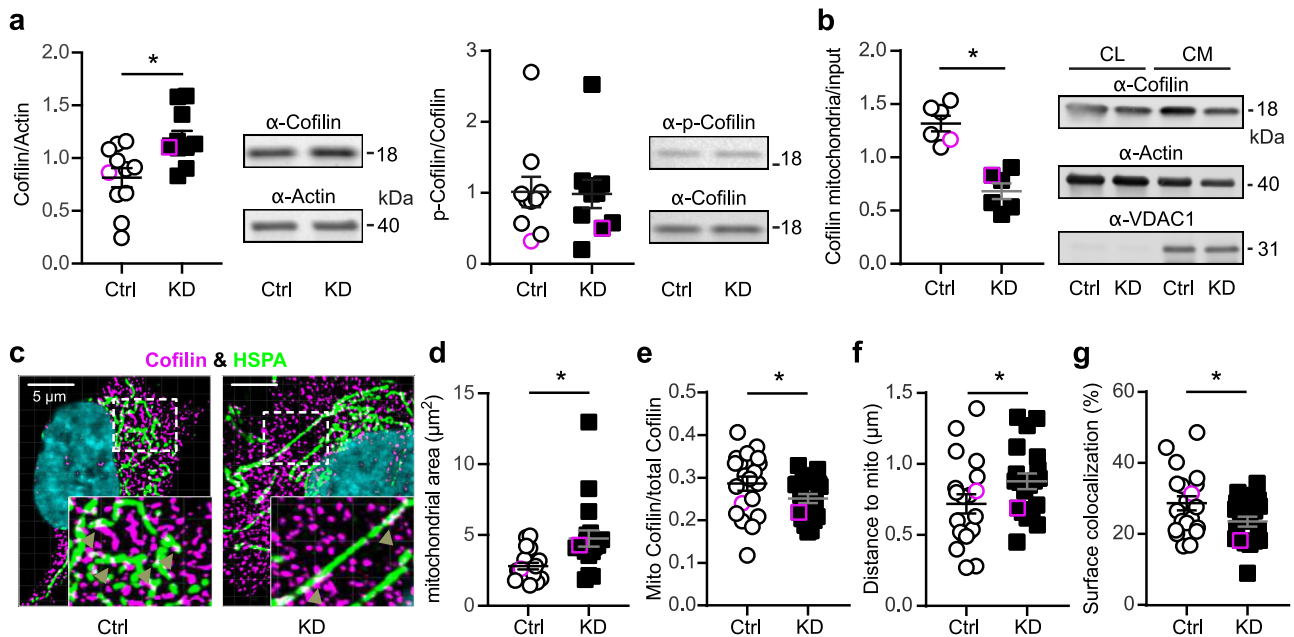
Fig. 7 Reduced presence of Cofilin-1 at mitochondria. a Immunoblot of whole cell lysates and quantification of Cofilin-1 and p-Cofilin-1 (S3) protein levels. Actin served as loading control. **b** Analysis of Cofilin-1 abundance at the mitochondria after fractionation of crude mitochondria (CM) normalized to Cofilin-1 levels in whole cell lysates (CL). **c** Immunostaining of Ctrl and *GDAP1* KD cells for Cofilin-1 and HSPA9 as mitochondrial protein. Nuclei were counterstained with DAPI. Imaris analysis confirmed (**d**) the increased mitochondrial area in KD cells and (**e**) a reduction of mitochondrially-located Cofilin-1 (white, arrowheads) concomitant with (**f**) an increased distance between mitochondria and cofilin-1. Conversion of the structures into surfaces using contact XTension demonstrated (**g**) that the proportion of the mitochondrial surface area in contact with Cofilin-1 was significantly reduced. **d, f** Data are from a total of $n = 20$ cells per cell line from three independent experiments. Data points corresponding to the example are highlighted. Statistical variation is shown as scatter plots with the indication of mean ± SEM and significance calculated using the non-parametric Mann–Whitney test, *$p < 0.05$.

which is controlled by the presence of intramolecular disulfide bridges[45,46] or protein glutathionylation[47] and could thus be a target of GDAP1's GST activity. Alternatively, GDAP1 could just recruit Cofilin-1 to the mitochondrial surface in a redox-dependent manner. We studied Cofilin-1 abundance and intra-cellular localization and phosphorylation in *GDAP1* KD and control cells. *GDAP1* KD increased the total abundance of Cofilin-1 but did not affect phosphorylation (Fig. 7a). However, when we compared the protein levels in mitochondrial fractions, we observed the opposite, a significant reduction in *GDAP1* KD cells (Fig. 7b). To further test for the amount and localization of Cofilin-1 close to mitochondria, we used HSPA9, a mitochondrial matrix protein, as a marker as it was not regulated in *GDAP1* KD cells (Fig. 5h) and plays a role in ER-mitochondrial Ca^{2+} transfer[37]. Confocal microscopy demonstrated an increase in the area covered by mitochondria (Fig. 7c and d) in line with the more tubular network in *GDAP1* KD cells (Fig. 1h) and a reduction of mitochondrial Cofilin-1 compared to total Cofilin-1 in *GDAP1* KD cells (Fig. 7e), in line with the fractionation assays. In addition, the distance of Cofilin-1 spots from mitochondria was significantly increased (Fig. 7f) and the colocalization of the surfaces of Cofilin-1 and HSPA9-expressing structures was reduced (Fig. 7g). These results imply that GDAP1 controls the presence of Cofilin-1 in proximity to the mitochondrial surface, possibly at MERCS.

GDAP1 KD reduces F-actin fibers at mitochondrial surfaces and restricts access of DRP1 to the mitochondria resulting in less DRP1 and MFF. Because Cofilin-1 is an actin-binding pro-tein, we suspected less actin in the proximity of mitochondria in *GDAP1* KD cells. We quantitated F-actin levels and its colocali-zation with mitochondria in living cells by transiently transfecting control and *GDAP1* KD cells with GFP-tagged F-tractin and

labeling of mitochondria with mitotracker red. F-tractin does not perturb actin rearrangement[48–50] and was previously used to study the effects of INF2 perturbation on mitochondrial dynamics[18,51]. Our data revealed a significant reduction of surface colocalization between F-actin and mitochondria in *GDAP1* KD cells (Fig. 8a) in line with our hypothesis. As expected from previous work[17], this severely reduced DRP1 localization in mitochondrial fractions (Fig. 8b). The decreased colocalization of DRP1 with mitochondria was also evident when we over-expressed GFP-tagged DRP1 in control and *GDAP1* KD cells (Fig. 8c). Interestingly, DRP1 also covered less space in *GDAP1* KD cells (Fig. 8d). To rule out that this is caused by a reduced transfection efficiency, we quantified total endogenous DRP1. This also revealed a reduced abundance of DRP1 and its receptor at the mitochondrial surface, mitochondrial fission factor (MFF) (Fig. 8e). In summary, these findings imply that in the absence of GDAP1, F-actin fibers are less present at the mitochondrial surface which restricts the access of ER tubules and DRP1 to sites of mitochondrial constriction and decreased levels of DRP1 and its receptor MFF resulting in a dysfunction of mitochondrial dynamics (Fig. 8f).

Discussion
In this work, we used neuronal *GDAP1* KD in human SH-SY5Y neuroblastoma cells and patient-derived cells to study the pathophysiology of CMT4A. We found that GDAP1 interacts with the actin-interacting protein Cofilin-1 and that loss of GDAP1 results in a reduction of F-actin fibers in mitochondrial proximity. This limits the access of ER tubules to mitochondria which connects two processes: it impedes DRP1 recruitment to mitochondrial constriction sites resulting in more tubular mito-chondria and it disrupts mitochondria-ER contact sites causing reduced mitochondrial Ca^{2+} levels. The reduced mitochondrial
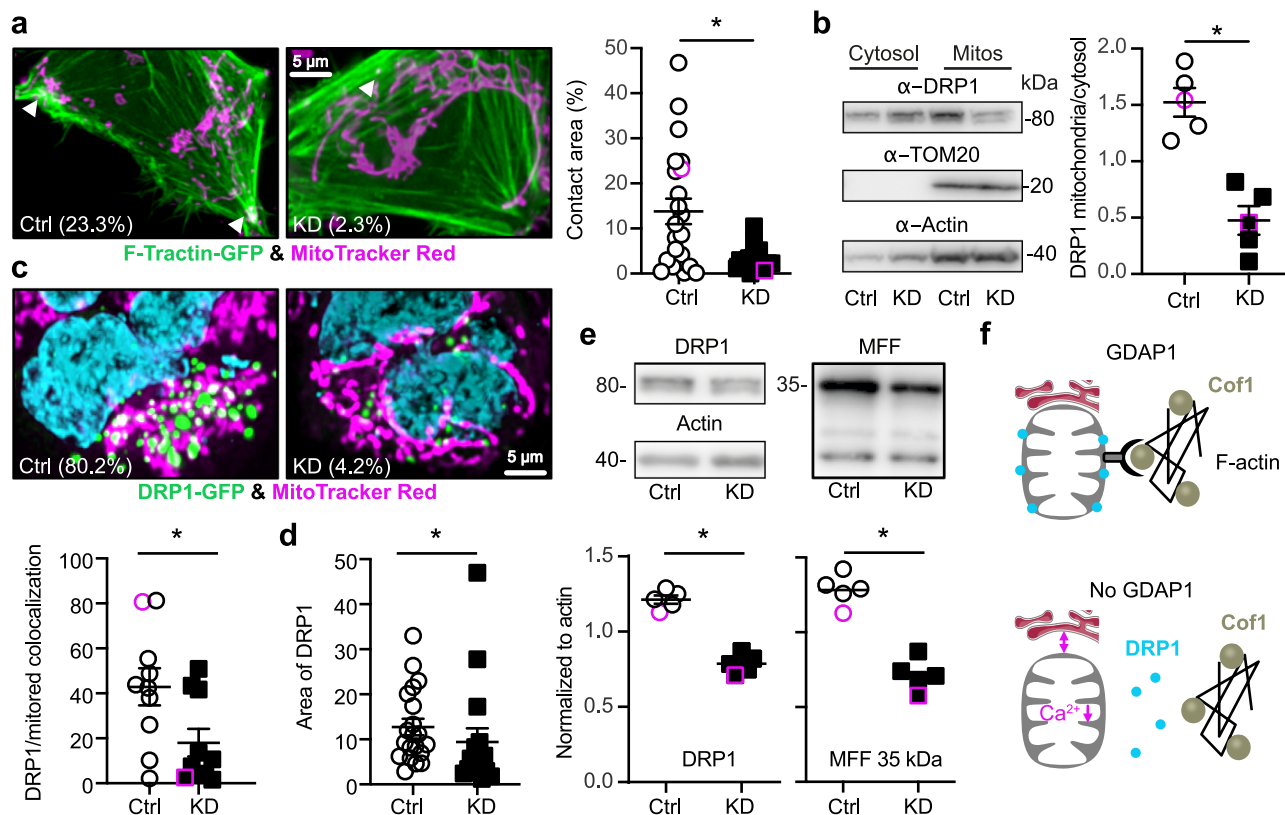
Fig. 8 GDAP1 KD reduces F-actin fibers at mitochondrial surfaces and restricts access of DRP1 to the mitochondria resulting in less DRP1 and MFF.
a Live cell imaging of GFP-F-tractin transfected cells. Mitochondria were stained with MitoTracker and images analyzed for contact area using Imaris.
b Immunoblot of DRP1 in cytosolic and mitochondrial fractions demonstrating a reduced DRP1 abundance in mitochondrial fractions. TOM20 and actin served as loading controls, size is indicated. **c, d** Live cell imaging of GFP-DRP1 transfected cells. Mitochondria were stained with MitoTracker and images analyzed for (**c**) colocalization and (**d**) area. **e** Immunoblot of total DRP1 and MFF demonstrating a reduced abundance of both proteins. Actin served as loading control, size is indicated. **f** Scheme depicting our findings. Cof1, Cofilin-1. In the absence of GDAP1 mitochondrial F-actin is reduced resulting in an increased distance between ER and mitochondria, reduced mitochondrial Ca^{2+} levels, and a reduced presence of DRP1 at mitochondrial constriction sites. Data from (**a**) are from $n = 19$ cells per cell line from three independent experiments performed in triplicates. Data from (**c**) are from $n = 10$ and (**d**) from $n = 16$ cells per cell line from three independent experiments. Data points corresponding to the examples are highlighted. Statistical variation is shown as scatter plots with the indication of mean ± SEM and significance calculated using the non-parametric Mann–Whitney test, $*p < 0.05$.

Ca^{2+} levels inhibit the PDC and result in a rewired cellular metabolism characterized by dependence on glutamine and fatty acids to compensate for an impaired TCA cycle. We therefore conclude that the reduction in F-actin presence at mitochondria caused by GDAP1 loss of function represents the probable cause of autosomal-recessive CMT4A.

The reduced mitochondrial Ca^{2+} levels in GDAP1 KD and GDAP1-loss-of-function NPCs are difficult to understand because over-expression of the MCU was shown previously to increase the matrix Ca^{2+} concentration[52]. Other, unchanged components of the ER-mitochondrial complex that regulate Ca^{2+} transfer, such as the ER release channels, the mitochondrial VDAC1 channels and the linking protein HSPA9 (Grp75)[37] (Fig. 5h) might account for this. In addition, the amount and stoichiometry of the MCU-interacting proteins MICU1 and MICU1, which are regulatory subunits of the large protein complex which mediates mitochondrial Ca^{2+} uptake, also affect the matrix Ca^{2+} concentration[52] and were not further studied here as it is difficult to fathom how the outer mitochondrial membrane protein GDAP1 could affect or modify these proteins. Despite the reduction in MERCs in GDAP1 KD cells, agonist-induced increases in mitochondrial Ca^{2+} levels were unchanged. Such Ca^{2+} transients are believed to instigate the increase in PDC activity[28,29]. We therefore have to conclude that the reported blunting of the Ca^{2+}-dependent increase of mitochondrial respiration upon SOCE[22] also affects PDC activity. In line with this, it was recently shown that in mouse *Gdap1−/−* moto-neurons, glutamate treatment results in a decreased decay of the Ca^{2+} signal and a reduction in respiration[53]. The authors attributed this to defects in mitochondrial movement resulting in a lack of correct positioning of mitochondria at sites where an intense stimulation of ATP production by oxidative phosphorylation is required like the plasma membrane. Interestingly, the actin cytoskeleton is essential for short-distance mitochondrial movements and for immobilization of mitochondria at the actin cortex, a specialized layer of cytoplasmic proteins on the inner face of the cell membrane (reviewed in[54]) suggesting that the changes described here could also underlie these defects in mitochondrial positioning. Alternatively, other yet unknown mechanisms exist that link the actin cytoskeleton to steady-state mitochondrial Ca^{2+} levels.

We found that GDAP1 interacts with Cofilin-1 in a redox-dependent manner and restricts its presence at the mitochondrial surface. This was shown by confocal microscopy using HSPA9 as a marker protein. HSPA9 (Grp75) is recognized to be enriched in MERCS. An enrichment of Cofilin-1 in MERCs has not been reported yet and we reproduced the reduced abundance of Cofilin-1 in *GDAP1* KD cells in fractions containing crude mitochondria (Fig. 7b). We therefore conclude that the reduction of Cofilin-1 at mitochondrial surfaces is not restricted to MERCS.

Very recently, Cofilin-1 was shown to affect mitochondrial shape and function[55]. Theoretically, GDAP1 could affect Cofilin-1 function through its still unresolved potential GST-like enzymatic activity[6,8–10] because Cofilin-1 contains four potential GST target cysteine residues at the positions 39, 80, 139 and 147. Cysteines 39 and 80 are buried inside the protein while cysteines 139 and 147 are located on the surface of the protein[56]. Redox-mediated modifications of these cysteine residues clearly affect the function of Cofilin-1. Treatment with hydrogen peroxide leads to the formation of an intramolecular disulfide bond resulting in a conformational change that prevents phosphorylation and thereby actin polymerization[45]. Moreover, intermolecular disulfides and oligomeric forms of Cofilin-1 have been described. Monomeric Cofilin-1 possesses severing activity, whereas the dimeric and oligomeric forms have actin-bundling activity[57]. Interestingly, only monomeric Cofilin-1 is phosphorylated[58] which represents the most-studied post-translational modification of Cofilin-1 to date. Cofilin-1 can be post-translationally modified by phosphorylation of serine 3. Increased phosphorylation inhibits the actin-binding ability of Cofilin-1[59]; dephosphorylated Cofilin-1 preferentially localizes to mitochondria, whereas a mutation mimicking the phosphorylated protein prevents translocation from the cytosol to mitochondria[60]. We found no changes in Cofilin-1 phosphorylation in whole cell lysates and no phosphorylated Cofilin-1 in mitochondrial fractions. Upon oxidation of all four cysteine residues and dephosphorylation at serine 3, Cofilin-1 loses its affinity for actin, translocates from the cytosol to mitochondria and induces apoptosis[60,61]. Oxidation of methionine 115 apparently also prevents its actin depolymerization activity and induces forced mitochondrial translocation and apoptosis[62]. In addition, Cofilin-1 can be glutathionylated, which represents the presumed enzymatic activity of GDAP1. Glutathionylation of Cofilin-1 was demonstrated in lymphocytes treated with the thiol-oxidizing reagent diamide[63] and in cells of the rat nucleus accumbens during cued cocaine seeking in the absence of cocaine[47]. Interestingly, glutathionylation reduces cofilin-1-dependent depolymerization of F-actin, implying regulatory functions in cell signaling[47]. It remains to be clarified whether GDAP1 affects the redox state and function of Cofilin-1 by specific glutathionylation.

Mutations in other proteins that target the same pathway also cause CMT disease. Mutated PDK3 also inhibits the PDC by hyperphosphorylation of the PDH E1α subunit similar to GDAP1 loss of function. This causes CMTX6[24]. Loss of function of the actin-polymerizing protein INF2 alters mitochondrial shape by changing DRP1 access to mitochondria similar to GDAP1 KD[17]. INF2 is also implicated in the abundance of MERCS and changes in mitochondrial Ca^{2+} dynamics[18] which we also observed in GDAP1 loss-of-function cells. Mutations in INF2 also cause CMT disease, CMTDIE[20]. Mutations in Dynamin-2 (DNM2), a ubiquitously expressed large GTPase that interacts tightly with the actin and microtubule network[64,65] also cause CMT disease, dominant intermediate CMT (CMTDIB)[66] and autosomal-dominant CMT2M[67]. Similar to GDAP1, DNM2 works in concert with DRP1 to orchestrate mitochondrial constriction events that result in division[68]. DNM2 therefore directly interferes with the same processes that we found to be affected by GDAP1 loss of function. Finally mutations in BSCL2 (Bernardinelli-Seip Congenital Lipodystrophy Type 2) also known as seipin cause a distal hereditary motor neuronopathy (HMN5C) which can present with features of axonal CMT2[69]. BSCL2 is an ER protein crucial in the formation of lipid droplets[70,71]. BSCL2 also interacts with the adaptor protein YWHAB (14-3-3-beta) which then recruits cofilin-1 to remodel the actin cytoskeleton for adipocyte differentiation[72].

In summary, our results shed light on the pathophysiology of CMT4A and highlight the importance of GDAP1 and actin for mitochondrial function. The fact that mutations in diverse proteins that all interact with the overarching mechanisms described here—metabolic and mitochondrial remodeling caused by changes in the the interaction of the actin cytoskeleton with mitochondria—cause CMT disease strengthens the importance of this mechanism for the health of the peripheral nervous system.

Methods

Generation of iPSCs. iPSC lines from two CMT4A patients and one healthy donor were generated with Sendai virus (CytoTune, DNAVEC Corporation) coding for POU5F1, SOX2, KLF4 and MYC. All subjects gave written informed consent prior and the study was approved by the local ethics committee at the Universities of Warsaw (patient #1), Düsseldorf (patient #2) and Bonn (healthy donor). In brief, Sendai virus-infected primary fibroblasts were immediately centrifuged for 45 min at 32 °C with 1500 g (spinfection) and cultivated in Advanced DMEM containing 5% fetal calf serum (FCS) and 1% GlutaMAX™ (all from Life Technologies). On the following day the virus-containing medium was replaced with fresh culture medium. Five days post infection (d5), transduced fibroblasts were trypsinized and seeded onto mouse feeder-coated dishes in DMEM/F-12 containing 10% Knock-Out™ Serum Replacement, 1% nonessential amino acids (NEAA), 1% GlutaMAX™, 1% pyruvate, 0.1 mM β-mercaptoethanol and 10 ng/ml basic fibroblast growth factor (bFGF) (all from Life Technologies). Medium was changed every other day until clonal iPSC colonies were manually picked and adapted to feeder-free culture conditions. Several clonal lines were subjected to SNP genotyping in order to identify iPSC clones with normal karyotype.

SNP analysis of iPSC lines. Genomic DNA was prepared using the DNeasy Blood & Tissue Kit (Qiagen). Whole-genome single nucleotide polymorphism (SNP) genotyping was performed at the Institute of Human Genetics at the University of Bonn. Genomic DNA at a concentration of 60 ng/μL was used for whole-genome amplification. Afterwards, the amplified DNA was fragmented and hybridized to sequence-specific oligomers bound to beads on an Illumina HumanOmniExpress-12v1.0 chip. Data were analyzed using Illumina Bead Studio.

Differentiation of hiPSCs into neural cells. Induced-pluripotent stem cells were grown using mTeSR™1 medium (Stemcell Tech., 05850) on matrigel (Corning, 354277). Human iPS cells were detached from matrigel using ReLeSR™ (Stemcell Tech., 05872), resuspended in medium consisting of Dulbecco's modified Eagle's medium/ F12 supplemented with 10% knockout serum (Invitrogen, 10828-028), 1% N2 supplement (Gibco, 17502-048), 0.05% B27 (Gibco, 17504-044), 20 ng/ml epidermal growth factor (Sigma, E9644) and 10 ng/ml basic fibroblast growth factor (Gibco, PHG0024), and plated within a low-attachment petri dish to induce embryoid body (EB) formation for 4 days. The EBs were plated on polyornithine (Sigma, P3655)/laminin (Sigma, L2020)-coated dishes for additional 6 days to induce the formation of neural rosettes. Neural rosettes were then manually removed, dissociated with accutase (Stemcell Tech., 07920), plated on poly-L-ornithine/laminin-coated dishes, and then treated with 3 μM retinoic acid for 7 days. The medium was changed daily and cultures were passaged weekly by accutase and plated on matrigel-coated dishes in the above-mentioned neural medium.

Small molecule differentiation of hiPSCs into motoneurons. iPSCs differentiation was performed by the addition of small molecules adapted from a previously described protocol[73]. Briefly, for neuronal induction, iPSCs were seeded as colonies resuspended in E8 medium 2 days prior differentiation. To start the differentiation, medium was changed to N2B27 medium (50% Neurobasal medium/ 50% DMEM-F12 medium with 1:200 N2 supplement, 1:100 B27 supplement without vitamin A and 1% penicillin, streptomycin and L-glutamine respectively) supplemented with the small molecules 10 μM SB-431542 (SB), 1 μM dorsomorphin (DM), 3 μM CHIR 99021 and 0.5 μM PMA for four days. Subsequently, SB and DM were replaced by 150 μM Ascorbic Acid (AA), and cells were fed daily until epithelium-like structures emerged. Neural epithelial structures were picked, dissociated mechanically and plated on 12-well plates, which were coated with Matrigel (1:100 in DMEM/F12) overnight. After around five passages the smNPC cells reached a high purity and were further kept in culture on Matrigel-coated plates and N2B27 medium supplemented with CHIR, PMS and AA. Detaching of the cells for passaging was performed with accutase. Starting from smNPC passage 13, differentiation to MN could be initiated. N2B27 medium with 1 μM PMA was added 3 days after passaging. After two more days, 1 μM retinoic acid (RA) and 1 μM PMA were supplemented to the medium for the following 8 days, until culturing in maturation medium began, consisting of N2B27 medium with BDNF, GDNF and dbcAMP for two more weeks.

Immunoblotting. Denatured total cellular protein samples were separated on SDS polyacrylamide gels 4-15% Mini-PROTEAN® TGX Stain-Free™ gels (Bio-Rad) and transferred onto a nitrocellulose membrane using the Trans-Blot® Turbo™ Transfer System (Bio-Rad). Membranes were blocked with 3% (w/v) milk powder in PBS-T

or TBS-T (1x PBS or TBS, 0.05% (v/v) Tween 20) for 1 h at room temperature (RT). Chameleon Duo Pre-stained Protein Ladder (Li-Cor Biosciences) was used as a molecular weight standard. Primary antibodies were anti-actin mAB (clone C4, 1:4000; Millipore MAB1501), anti-Cofilin-1 mAB (clone D3F9, 1:1000, Cell Signaling, 5175), anti-p-Cofilin-1 mAB (Ser3, clone 77G2, 1:1000, Cell Signaling 3313), anti-DRP1 mAB (clone 4E11B11, 1:1000, Cell Signaling 14647), anti-GDAP1 (1:750, Sigma HPA014266), anti-G6PD mAB (clone D5D2, 1:1000, Cell Signaling 12263), anti-GAPDH mAB (clone 14C10, 1:2000, Cell Signaling 2118), anti-GLUD1 mAB (clone D9F7P, 1:1000, Cell Signaling 12793), anti-HK1 mAB (clone C35C4, 1:1000; Cell Signaling 2024), anti-HK2 mAB (clone C64G5, 1:1000, Cell Signaling 2687), anti-HSPA9 (clone N52A/42, 1:1000, UC Davis/NIH NeuroMab Facility, Davis, USA, 73-127), anti-LDHA mAB (clone C4B5, 1:1000, Cell Signaling 3582), anti-MCU (1:1000, Sigma HPA016480), anti-MFF (1:1000, Proteintech 17090-1-AP), anti-MFN2 mAB (clone M03, 1:500; Abnova H00009927-M03), anti-Nestin mAB (clone rat-401, 1:1000, Merck chemicals MAB353), anti-PDH mAb (E1α, clone C54G1, 1:1000, Cell Signaling 3205), anti-PDH mAB (E2,E3bp, clone 13G2AE2BH5, 1:1000, Abcam, ab110333) anti-p-PDH (Ser293, 1:1000, Cell Signaling 31866), anti-PKM1/2 mAb (clone C103A3, 1:1000, Cell Signaling 3582), anti-TOM20 (1:1000, Sigma HPA011562), anti-βIII-Tubulin mAB (clone TuJ-1, 1:1000, R&D Systems MAB1195), anti-VDAC1 (clone 20B12AF2, 1:1000, Abcam ab14734). The membranes were incubated with the primary antibodies overnight at 4 °C. For visualization, membranes were incubated with an infrared fluorescence IRDye® 680RD Streptavidin for biotinylation staining or IRDye 800-conjugated anti-mouse, 800-conjugated anti-rabbit, or 680-conjugated anti-mouse IgG secondary antibody (1:15,000; Licor), for 1 h at RT and detected with the Odyssey Infrared Imaging System (Licor). Western Blots were analyzed with the Image Studio Lite Software (Li-Cor Biosciences).

Immunocytochemistry. Neuronal cells were grown on matrigel-coated μ-Slide 8 Well, ibiTreat (Ibidi, 80826), fixed with 4% paraformaldehyde (PFA) (CarlROTH, 3105.2) and permeabilized by 0.25% (v/v) Triton X-100 in PBS. Unspecific binding of antibodies was blocked with 1X Roti®-Block (CarlROTH, A151.4) for 30 min. Primary antibodies anti-Nestin (1:100, Ebioscience, 14-9843-82), anti-MAP2 (1:500, Synaptic Systems, 188004), anti-Smi32 (Clone SMI32, 1:1000, Biolegend 801702), anti-beta-III tubulin (1:1000, R&D Systems, MAB1195) were treated in 1X Roti®-Block at 4 °C overnight. The cells were washed three times with PBS and incubated with the fluorescent conjugated secondary antibody (Molecular Probes, A-11001) in 1X Roti®-Block for 1 h at RT. Subsequently, three PBS washing steps were done. Nuclei were stained with 300 nM 4′,6-diamidino-2-phenylindole (DAPI). Pictures were taken with a Leica TCS SP5 inverted confocal microscope with a 63x/NA1.4 oil immersion objective, a BX51 Fluorescence microscope (Olympus) with a 20x objective or an Opera PhenixTM spinning disc high-content screening microscope (Perkin Elmer, USA) equipped with two 16-bit sCMOS cameras and a 40x, 1.1 NA water immersion objective. For Cofilin-1 evaluations, SH-SY5Y cells were grown on 12 mm glass cover slides. Primary antibodies were anti-Cofilin-1 mAB (clone D3F9, 1:100, Cell Signaling, 5175), anti-GRP75 mAB (clone N52A/42, 1:20, Neuromab 75-127). Pictures were taken with a Leica TCS SP8 inverted confocal microscope with a 63x/1.4 NA oil immersion objective in z-stacks. Images were analyzed in Imaris 9.5.1 (Bitplane). For motoneurons analysis, images were imported into marcopolo columbus database and underwent batch analysis that determined the fluorescence intensity of each marker. The signal intensities of Smi32 and MAP2 were normalized to β-tubulinIII each.

Confocal microscopy and image analysis. High-content light microscopy analysis was conducted with the Opera PhenixTM spinning disc microscope. Fluorescence (Ex/Em) for Hoechst, MitoTrackerTM Green FM and tetramethylrhodamine methyl ester perchlorate (TMRM) was measured at 405/435-480, 488/500-550 and 561/570-630 nm ex/em, respectively. BODIPY™ 558/568 C12 was added to the cells in parallel to MitoTracker in a final concentration of 1 μM for 15 min and subsequently, cells were incubated with normal growth medium. The images were analyzed with the software packages Harmony (version 4.5) and Columbus (version 2.7.1) containing the PhenoLOGICTM machine learning plugin (Perkin Elmer). Cells were selected via nuclear staining with HOECHST, but the cytosol region was defined using the mitochondrial stain. Within this selection, mitochondria and LDs were defined as isolated populations and analyzed respectively for their area and intensity. For mitochondria-associated LDs, the intensity of BODIPY™ 558/568 C12 staining was determined within the mitochondrial area. The complete image analysis sequences are available upon request. Live-cell imaging of actin filament analysis was conducted two days after transfection of GFP-F-tractin (gift of Henry N. Higgs, Dartmouth University) and together with staining of mitochondria with 100 nM MitoTracker™ Red CMXRos. Cells were imaged using the Leica TCS SP8 inverted confocal microscope with a 63x/1.4 NA oil immersion objective in z-stacks. Cells were captured at 1024×1024 with sequential image capturing. Step size was set at 0.25 μm. Images from confocal microscopy for Cofilin-1, HSPA9 and actin filament quantification were analyzed in Imaris 9.5.1 (Bitplane). To improve the signal-to-noise ratio, iterative deconvolution was performed (Huygens Essential 20.10). The software then created 3D surfaces of mitochondria and Cofilin-1 spots to measure the surface area and to determine the shortest distance from the Cofilin-1 surface to the mitochondrial surface. Colocalizing Cofilin-1/actin with a distance ≤ 0 μm was duplicated to a

new surface and taken for the Imaris surface-surface contact XTension to quantify the contact area, defined as the percentage of mitochondrial surface contacting Cofilin-1. Similarly, 3D surfaces of Actin and the mitochondria were created. The software computed the contact area between the two surfaces as well as the shortest distance between the actin and mitochondria surfaces. Live-cell imaging of DRP1 surface analysis was conducted two days after transfection of pcDNA3-GFP-DRP1 (gift of Prof. Dr. Culmsee, Philipps-Universität Marburg) and together with staining of mitochondria with 100 nM MitoTracker™ RedCMXRos. Images were captured in a similar manner using the Leica TCS SP8 inverted confocal microscope. Images were then imported to and analyzed in Imaris 9.7.2 (Bitplane) where 3D surfaces of Actin and the mitochondria were created. The software computed the contact area between the two surfaces as well as colocalization XTension to quantify the colocalized voxels between the Drp1 surface and the mitochondrial surface.

Cell culture and generation of stable cell lines. SH-SY5Y cell lines were grown in DMEM/F12 medium (Gibco) supplemented with 10% (v/v) fetal calf serum (FCS; Thermo Scientific), 2 mM L-glutamine (Gibco), 1 x MEM non-essential amino acids, 100 U/ml penicillin and 100 μg/ml streptomycin (Gibco) in a humidified incubator at 37 °C, 5% CO_2 and 95% air. The SH-SY5Y cell lines pLKO-NT (control) and G4 (knockdown) were a kind gift of David Pla-Martin and Francesc Palau[19] and were grown in growth medium containing 2 μg/ml puromycin (InvivoGen).

Measurement of mitochondrial oxygen consumption. Mitochondrial respiration and oxygen consumption were analyzed using the Oxygraph-2k (Oroboros Instruments). Cells in suspension at a density of 1.5–2.0 × 10^6 cells/ml were analyzed under continuous stirring at 750 rpm and 37 °C. All chemicals with the exception of palmitate-BSA were purchased from Sigma. Palmitate-BSA was purchased from Biomol. In a phosphorylation-control-protocol, the routine respiration of cells in their general growth medium was measured following the addition of 2 μg/ml oligomycin to inhibit the ATP synthase and measure leak respiration. By titration of the protonophore carbonyl cyanide 4-(trifluoromethoxy) phenylhydrazone in 0.5 μM steps the respiration was stimulated up to a maximum oxygen flow and the electron transfer system capacity was determined. By the addition of 0.5 μM rotenone and 2.5 μM antimycin A the respiration was inhibited and the non-mitochondrial residual oxygen consumption was measured. In 2 s intervals, the oxygen concentration and the oxygen flow per cells were recorded using the DatLab software 5.1 (Oroboros Instruments). All measurements were performed after daily calibration of the polarographic oxygen sensors and using instrumental background correction. The measured respiratory states were analyzed after correction with ROX to compare only mitochondrial oxygen consumption.

ATP measurements. Cytosolic and mitochondrial ATP levels were quantified as described[27]. Cells were transiently transfected with plasmids carrying the bioluminescence energy transfer (BRET)-based ATP biosensor BTeam without targeting signal sequence (for cyto-ATP determination) or targeted to mitochondria (for mito-ATP determination) using TurboFectin reagent (OriGene). The plasmids were a kind gift of Hiroshi Imamura, University of Kyoto. 48 h later, the cells were incubated for 30 min in phenol red-free medium supplemented with 30 μM NanoLuciferase (NLuc) inhibitor to avoid disturbance from the BTeam released from dead cells. Afterwards, NLuc substrate (Promega) was added to the medium and the plate incubated for 20 min. Subsequently, luminescent emissions from the cells were measured at 37 °C at 520/560 nm (Yellow Fluorescent Protein (YFP) emission) and at 430/470 nm (NLuc emission) using a Tecan Spark® Multimode Microplate Reader.

Glutamine and glutamate measurements. The glutamine-glutamate-glo assay (Promega, # J8021) was performed according to manufacturer's instructions to determine intracellular glutamine and glutamate concentrations. Briefly, 20,000 cells of the SH-SY5Y cell line and 100,000 motoneurons were plated in triplicates per experiment on white 96-well plates (Greiner, # 655083) two or seven days prior to the experiment, respectively. On the day of the experiment, cells were washed twice with PBS and 30 μl of PBS as well as 15 μl of 0.3 HCl solution was added to the cells and mixed for 5 min. 15 μl of 450 mM Tris solution, pH 8.0 was added and incubated for further 60 sec. From each lysate, 25 μl was transferred into a new white 96-well plate for I) glutamine plus glutamate and II) glutamate only measurement. Glutaminase was only added to the first set of wells and incubated for 30 min at RT. The detection reagent composed of Luciferin detection solution, reductase, reductase substrate, GLUD1 and NAD was added to all wells and incubated for 60 min at RT before luminescence detection in a Tecan Infinite 200 pro plate reader. Concentrations were calculated with glutamine and glutamate standard curves (0.78 to 50 μM) and a blank was included to remove any assay background signal. Glutamate levels were calculated by subtracting the glutamate-only signal from the signal containing glutamate and glutamine levels together.

Electron microscopy and analysis. Cells were pelleted by centrifugation at 1300 rpm for 3 min and fixed in 3% glutaraldehyde overnight. Following several

rinses in 0.2 M sodium cacodylate buffer (pH 7.3), the samples were postfixed in 1% osmium tetroxide in cacodylate buffer for 2 h, dehydrated through an ascending series of ethanol concentrations and embedded in resin with propylene oxide as an intermediary. Semi-thin (0.65 µm) sections for light microscopy and ultrathin (50 nm) sections for electron microscopy were cut on a Leica Ultracut UCT ultramicrotome. Semi-thin sections were stained with methylene blue. Ultrathin sections were stained with an alcoholic solution of 1% uranyl acetate and lead citrate in sodium hydroxide and examined with a Zeiss EM-910 transmission electron microscope. For morphometric and quantitative analysis, representative cells were photographed at a magnification of 10,000 and 18,000. Analyses were done with ImageJ. MERCs were defined by a distance of mitochondrial and ER membranes between ~10 and ~50 nm. The frequency distribution of the MERCs width was calculated using GraphPad.

Biochemical analysis of mitochondria-ER contact sites. Cells were detached using trypsin/ETDA and resuspended in 1–2 ml of a buffer containing 0.32 M sucrose, 10 mM Tris-HCl, 1 mM EDTA and protease (Roche Diagnostics, 04693124001) and phosphatase (Roche Diagnostics, 04906845001) inhibitors. Cells were disrupted by a nitrogen decompression instrument (Parr Instrument Company, 4639) and centrifuged (2000 g, 10 min). The supernatant was transferred to a new microtube, centrifuged at 10,000 g for 10 min and the cell pellet resuspended in 1 ml of the same buffer containing the same components as above except 0.5 M sucrose. Finally, mitochondria were sedimented by centrifugation at 10,000 g for 10 min and resolved in an appropriate amount of RIPA buffer for the subsequent experiments.

FRET-based FEMP probe to quantify mitochondria-ER contact sites. MERCS were quantified with a FRET-based sensor indicating the proximity between the ER and mitochondria. The plasmid encodes for a YFP-linked outer mitochondrial membrane protein Akap1 and a CFP-conjugated ER-protein Sac1, as well as a fused FKBP and FRB domain respectively and is available from Marta Giacomello, University of Padova. These domains can form heterodimers upon rapamycin treatment. The specific localization of these proteins is ensured by the introduction of a self-cleavable Tav2A sequence[34,35]. The FEMP plasmid (FRET-based ER-mitochondria probe) was transfected with GenJet. 48 h later, images were taken with the Perkin Elmer Operetta High-Content Imaging System acquiring the CFP-(410-430/460-500 ex/em), YFP- (490-510/520-560 ex/em) and YFP$_{FRET}$-emission (410-430/520-560 ex/em) with a ×40 water objective for determination of the basal distances between the organelles. Subsequently, the cells were treated with 100 nM rapamycine for 15 min for FKBP-FRB dimerization induction and to reach a maximum of YFP$_{FRET}$ signal. Cells were fixed for another 20 min with 1% PFA and imaging was performed again with equal microscopy settings. For the analysis, the Harmony software was used. First, the cells were identified using the YFP channel. Within each cell and region of interest (ROI), the intensities of the three acquired channels were calculated, including background subtraction. FRET basal and FRET max were calculated as: (FYFP-FRETcell-FYFP-FRET$_{background}$)/ (FCFPcell-FCFP$_{background}$); FRET Ratio was calculated as (FRET$_{max}$–FRET$_{basal}$)/FRET$_{basal}$.

Mitochondrial Ca^{2+} measurement. Dye: Cells were plated (20,000 cells/cm^2) in 8-well µ-slides ibiTreat (ibidi, 80826) and treated with 5 µM of Rhod2-AM (Molecular Probes, R1245MP) in culture medium without FBS for 60 min at 37 °C the next day. Rhod2-AM fluorescent signals were analyzed at (Ex/Em) 549/578 nm wavelengths using a Leica SP5 confocal microscope and analyzed by ImageJ. Genetically encoded reporter: Cells were transfected with the genetically encoded reporters and analyzed two days later in an inverted TCS-SP5 confocal microscope (Leica) with appropriate excitation/emission wavelengths as reported for CEPIA3mt (Addgene, 58219) and GEM-CEPIA1er (Addgene, 58217)[31]. The CEPIA3mt construct was co-transfected and normalized to mito-TurboFarRed.

Aequorin Ca^{2+} measurements. For Ca^{2+} measurements, the biosensor aequorin (AEQ) was used, which is a 22 kDa calcium-binding photoprotein isolated from jellyfish Aequorea Victoria. The plasmid is available from Marta Giacomello, University of Padova. SH-SY5Y cells were grown on 12 mm glass coverslips to a confluence of 40–50% and transfected with cytosolic or mitochondria-targeted AEQ (cytAEQ/mtAEQ) using GenJet. On the day of the experiment, the cells were treated with 5 µM coelenterazine-N-AM (Santa Cruz Biotechnology sc-205904) in basic saline solution (BS, 135 mM NaCl, 5 mM KCl, 0.4 mM KH$_2$PO$_4$, 1 mM MgSO$_4$ x 7 H$_2$O, 20 mM HEPES, 0.1% (w/v) glucose, pH 7.4 adjustment at 37 °C with NaOH 10 N) containing 1 mM CaCl$_2$ for 2 h at 37 °C and 5% CO$_2$. Coelenterazine served as a substrate for AEQ. Cover slides were then placed in the luminometer with constant buffer perfusion with BS supplemented with I) 1 mM Ca^{2+} (30 s) II) 200 µM EGTA (30 s) III) 200 µM Carbachol (CCH) + 200 µM EGTA (120 s) IV) 100 µM Digitonin + 5 mM CaCl$_2$ (220 s).

Precipitation of biotinylated Avi-GDAP1. Primary cortical neuron cultures were prepared from embryos (E16) from the transgenic mouse line Gt(ROSA) 26Sortm1(birA)Mejr (ROSA26-BirA) of a C57BL/6 N background. In this mouse strain, the biotin ligase BirA was inserted into the gene locus of the ROSA26 promoter[40]. Cortical neurons were cultured on poly-D-lysine coated plates

(0.05 mg/ml) in Neurobasal medium (NBM, Life Technologies, 21103049) supplemented with 2% (v/v) B-27 supplement (Life Technologies, 17504-044), 1% (v/v) L-glutamine (Sigma-Aldrich, G1251) and 100 U/ml penicillin and 100 µg/ml streptomycin (Sigma-Aldrich, P0781). Medium change was performed at day 1 and day 4 after isolation. For transduction of the primary neurons, viruses were added in a volume that equaled 6 × 10^7–8 × 10^7 copies/µl per well of a 6 well plate containing 4 ml of NBM and neurons on day 4 after isolation. Neurons were cultured for further 7 days. Cells were harvested, washed with PBS and lysed in RIPA buffer supplemented with protease inhibitors. The samples were centrifuged at 21,000 g for 30 min at 4 °C, the proteins concentration was determined via BC-Assay and 20 µg protein lysate was removed as input-control. Protein lysates were either directly incubated with Dynabeads™ MyOne™ Streptavidin T1 according to the manufacturer's protocol or taken for GSH or GSSG incubation (5 mM GSH or GSSG in 10 mM HEPES pH 7.4, 35 mM sucrose, 40 mM KCl, 0.25 mM EGTA, 2 mM Mg(CH$_3$COO)$_2$, 0.5 mM GTP, 1 mM ATP (K$^+$), 5 mM Na-succinate, 0.08 mM ADP, 2 mM K$_2$HPO$_4$ for 30 min at 37 °C). Dynabeads™ MyOne™ Streptavidin T1 was incubated for 45 min at RT on a shaker. Dynabeads were washed three times with RIPA buffer and once with PBS and stored at −80 °C until further processing for LC-MS.

Protein elution, lysis and digestion. Bound proteins were eluted from Dynabeads in 10 mM Tris pH 8.0, 2% SDS, 1 mM Biotin at 80 °C. Whole cells were lysed in 5 µl of 10% SDS at 95 °C for 5 min. Protein samples were digested using the SP3 ("Single-Pot Solid-Phase-Enhanced Sample Preparation") protocol[74] with modifications[75]. Proteins were reduced by adding 5 µl of 200 mM Dithiothreitol (DTT) per 100 µl lysate (45 °C, 30 min). Free cysteines were subsequently alkylated by adding 10 µl 100 mM Iodoacetamide (IAA) per 100 µl lysate (RT, 30 min, in the dark). Subsequently, remaining IAA was quenched by adding 10 µl 200 mM DTT per 100 µl lysate. Magnetic carboxylate modified particles Beads (SpeedBeads, Sigma) were used for protein clean-up and acetonitrile (ACN), in a final concentration of 70%, was added to the samples to induce the binding of the proteins to the beads by hydrophilic interactions (18 min RT). By incubating the bead-protein mixture on a magnetic stand for 2 min, the sample was bound to the magnet and the supernatant removed, followed by two washing steps with 70% ethanol (EtOH), addition of 180 µl ACN, incubation for 15 s and removal of the solvent. Finally, 5 µl digest buffer (50 mM ammonium bicarbonate, 1:25 w/w trypsin:protein ratio) was added to the air-dried bead-protein mixtures and incubated overnight at 37 °C. To purify peptides after digestion, ACN was added to a final concentration of 95%. After another washing step. the beads were resuspended in 10 µl 2% DMSO (in water), put into an ultrasonic bath for 1 min and then shortly centrifuged. 10 µl of the resulting supernatant was mixed with 5 µl 100 fmol/µl Enolase digest (Waters Corporation) and acidified with 5 µl 1% formic acid (FA).

LC-MS analysis. Liquid chromatography (LC) of tryptic peptides was performed on a NanoAQUITY UPLC system (Waters Corporation) equipped with 75 µM × 250 mm HSS-T3 C18 column (Waters corporation). Mobile phase A was 0.1% (v/v) formic acid (FA) and 3% (v/v) DMSO in water. Mobile phase B was 0.1% (v/v) FA and 3% (v/v) DMSO in ACN. Peptides were separated running a gradient from 5 to 40% (v/v) mobile phase B at a flow rate of 300 nL/ min over 90 min. The column was heated to 55 °C. MS analysis of eluting peptides was performed by ion-mobility enhanced data-independent acquisition (UDMS^E). Precursor ion information was collected in low-energy MS mode at a constant collision energy of 4 eV. Fragment ion information was obtained in the elevated energy scan applying drift-time specific collision energies. The spectral acquisition time in each mode was 0.7 s with a 0.05 s interscan delay resulting in an overall cycle time of 1.5 s for the acquisition of one cycle of low and elevated energy data. [Glu1]-fibrinopeptide was used as lock mass at 100 fmol/µL and sampled every 30 s into the mass spectrometer via the reference sprayer of the NanoLockSpray source. All samples were analyzed in three technical replicates.

Data processing and label-free protein quantification. UDMS^E data processing and database search was performed using ProteinLynx Global Server (PLGS, ver. 3.0.2, Waters Corporation). The resulting proteins were searched against the UniProt proteome database (species: Mus musculus, UniProtK-Swissprot release 2019_05, 17.051 entries; Homo sapiens, UniProtK-Swissprot release 2019_10, 20367 entries) supplemented with a list of common contaminants. The database search was specified by trypsin as enzyme for digestion and peptides with up to two missed cleavages were included. Carbamidomethyl cysteine was set as fixed modification and oxidized methionine as variable modification. False discovery rate assessment for peptide and protein identification was done using the target-decoy strategy by searching a reverse database and was set to 0.01 for database search in PLGS. Retention time alignment, exact mass retention time (EMRT), as well as normalization and filtering were performed in ISOQuant ver.1.8. By using TOP3 quantification, absolute in-sample amounts of proteins were calculated.

Statistics and reproducibility. Normal distribution was tested using the D'Agostino-Pearson omnibus normality test. Statistical significance was then verified using appropriate parametric (Student's t test or ANOVA) or non-parametric

tests (Mann–Whitney and Kruskal–Wallis tests) followed by multiple comparison tests as indicated. The Wilcoxon signed rank test was used when normalization to 100% was necessary as indicated. Statistical analysis of mass spectrometry data was performed using two-tailed, paired t-tests and subsequent Bonferroni correction. Here, a corrected $p < 0.01$ was considered significant for the biotinylated Avi-GDAP1 pulldown experiment and $p < 0.05$ for whole cell lysates. In all other data a $p < 0.05$ was considered to be statistically significant. Pathway over-representation analysis was performed using the STRING database with default parameters[39]. KEGG pathway visualization was performed using the R package clusterProfiler[76].

Reporting summary. Further information on research design is available in the Nature Research Reporting Summary linked to this article.

Data availability

References

1. Baxter, R. V. et al. Ganglioside-induced differentiation-associated protein-1 is mutant in Charcot-Marie-Tooth disease type 4A/8q21. *Nat. Genet.* **30**, 21–22 (2002).
2. Cuesta, A. et al. The gene encoding ganglioside-induced differentiation-associated protein 1 is mutated in axonal Charcot-Marie-Tooth type 4A disease. *Nat. Genet.* **30**, 22–25 (2002).
3. Senderek, J. et al. Mutations in the ganglioside-induced differentiation-associated protein-1 (GDAP1) gene in intermediate type autosomal recessive Charcot-Marie-Tooth neuropathy. *Brain* **126**, 642–649 (2003).
4. Chung, K. W. et al. A novel GDAP1 Q218E mutation in autosomal dominant Charcot-Marie-Tooth disease. *J. Hum. Genet.* **53**, 360–364 (2008).
5. Marco, A., Cuesta, A., Pedrola, L., Palau, F. & Marín, I. Evolutionary and structural analyses of GDAP1, involved in Charcot-Marie-Tooth disease, characterize a novel class of glutathione transferase-related genes. *Mol. Biol. Evol.* **21**, 176–187 (2004).
6. Shield, A. J., Murray, T. P. & Board, P. G. Functional characterisation of ganglioside-induced differentiation-associated protein 1 as a glutathione transferase. *Biochem. Biophys. Res. Commun.* **347**, 859–866 (2006).
7. Wagner, K. M., Rüegg, M., Niemann, A. & Suter, U. Targeting and function of the mitochondrial fission factor GDAP1 are dependent on its tail-anchor. *PLoS ONE* **4**, e5160 (2009).
8. Pedrola, L. et al. GDAP1, the protein causing Charcot-Marie-Tooth disease type 4A, is expressed in neurons and is associated with mitochondria. *Hum. Mol. Genet.* **14**, 1087–1094 (2005).
9. Huber, N. et al. Glutathione-conjugating and membrane-remodeling activity of GDAP1 relies on amphipathic C-terminal domain. *Sci. Rep.* **6**, 36930 (2016).
10. Googins, M. R. et al. Structural and functional divergence of GDAP1 from the glutathione S-transferase superfamily. *FASEB J.* **34**, 7192–7207 (2020).
11. Niemann, A., Ruegg, M., La Padula, V., Schenone, A. & Suter, U. Ganglioside-induced differentiation associated protein 1 is a regulator of the mitochondrial network: new implications for Charcot-Marie-Tooth disease. *J. Cell Biol.* **170**, 1067–1078 (2005).
12. Huber, N., Guimaraes, S., Schrader, M., Suter, U. & Niemann, A. Charcot-Marie-Tooth disease-associated mutants of GDAP1 dissociate its roles in peroxisomal and mitochondrial fission. *EMBO Rep.* **14**, 545–552 (2013).
13. Niemann, A., Wagner, K. M., Ruegg, M. & Suter, U. GDAP1 mutations differ in their effects on mitochondrial dynamics and apoptosis depending on the mode of inheritance. *Neurobiol. Dis.* **36**, 509–520 (2009).
14. Ingerman, E. et al. Dnm1 forms spirals that are structurally tailored to fit mitochondria. *J. Cell Biol.* **170**, 1021–1027 (2005).
15. Friedman, J. R. et al. ER tubules mark sites of mitochondrial division. *Science* **334**, 358–362 (2011).
16. De Vos, K. J., Allan, V. J., Grierson, A. J. & Sheetz, M. P. Mitochondrial function and actin regulate dynamin-related protein 1-dependent mitochondrial fission. *Curr. Biol.* **15**, 678–683 (2005).
17. Korobova, F., Ramabhadran, V. & Higgs, H. N. An actin-dependent step in mitochondrial fission mediated by the ER-associated formin INF2. *Science* **339**, 464–467 (2013).
18. Chakrabarti, R. et al. INF2-mediated actin polymerization at the ER stimulates mitochondrial calcium uptake, inner membrane constriction, and division. *J. Cell Biol.* **217**, 251–268 (2018).
19. Pla-Martín, D. et al. Silencing of the Charcot-Marie-Tooth disease-associated gene GDAP1 induces abnormal mitochondrial distribution and affects Ca2+ homeostasis by reducing store-operated Ca2+ entry. *Neurobiol. Dis.* **55**, 140–151 (2013).
20. Boyer, O. et al. INF2 mutations in Charcot-Marie-Tooth disease with glomerulopathy. *N. Engl. J. Med.* **365**, 2377–2388 (2011).
21. Rehklau, K. et al. Cofilin1-dependent actin dynamics control DRP1-mediated mitochondrial fission. *Cell Death Dis.* **8**, e3063 (2017).
22. González-Sánchez, P. et al. CMT-linked loss-of-function mutations in GDAP1 impair store-operated Ca2+ entry-stimulated respiration. *Sci. Rep.* **7**, 42993 (2017).
23. Chance, B. The energy-linked reaction of calcium with mitochondria. *J. Biol. Chem.* **240**, 2729–2748 (1965).
24. Kennerson, M. L. et al. A new locus for X-linked dominant Charcot-Marie-Tooth disease (CMTX6) is caused by mutations in the pyruvate dehydrogenase kinase isoenzyme 3 (PDK3) gene. *Hum. Mol. Genet.* **22**, 1404–1416 (2013).
25. Pla-Martín, D. et al. Junctophilin-1 is a modifier gene of GDAP1-related Charcot-Marie-Tooth disease. *Hum. Mol. Genet.* **24**, 213–229 (2015).
26. Noack, R. et al. Charcot-Marie-Tooth disease CMT4A: GDAP1 increases cellular glutathione and the mitochondrial membrane potential. *Hum. Mol. Genet.* **21**, 150–162 (2012).
27. Yoshida, T., Kakizuka, A. & Imamura, H. BTeam, a novel BRET-based biosensor for the accurate quantification of ATP concentration within living cells. *Sci. Rep.* **6**, 39618 (2016).
28. Denton, R. M., Randle, P. J. & Martin, B. R. Stimulation by calcium ions of pyruvate dehydrogenase phosphate phosphatase. *Biochem. J.* **128**, 161–163 (1972).
29. Denton, R. M., Richards, D. A. & Chin, J. G. Calcium ions and the regulation of NAD+-linked isocitrate dehydrogenase from the mitochondria of rat heart and other tissues. *Biochem. J.* **176**, 899–906 (1978).
30. Zhao, Y. et al. Site-directed mutagenesis of phosphorylation sites of the branched chain alpha-ketoacid dehydrogenase complex. *J. Biol. Chem.* **269**, 18583–18587 (1994).
31. Suzuki, J. et al. Imaging intraorganellar Ca2+ at subcellular resolution using CEPIA. *Nat. Commun.* **5**, 4153 (2014).
32. Giacomello, M. & Pellegrini, L. The coming of age of the mitochondria-ER contact: a matter of thickness. *Cell Death Differ.* **23**, 1417–1427 (2016).
33. Marchi, S., Patergnani, S. & Pinton, P. The endoplasmic reticulum-mitochondria connection: one touch, multiple functions. *Biochim. Biophys. Acta* **1837**, 461–469 (2014).
34. Csordás, G. et al. Imaging interorganelle contacts and local calcium dynamics at the ER-mitochondrial interface. *Mol. Cell* **39**, 121–132 (2010).
35. Naon, D. et al. Critical reappraisal confirms that Mitofusin 2 is an endoplasmic reticulum-mitochondria tether. *Proc. Natl Acad. Sci. USA* **113**, 11249–11254 (2016).
36. Giacomello, M. et al. Ca2+ hot spots on the mitochondrial surface are generated by Ca2+ mobilization from stores, but not by activation of store-operated Ca2+ channels. *Mol. Cell* **38**, 280–290 (2010).
37. Szabadkai, G. et al. Chaperone-mediated coupling of endoplasmic reticulum and mitochondrial Ca2+ channels. *J. Cell Biol.* **175**, 901–911 (2006).
38. Tenzer, S. et al. Proteome-wide characterization of the RNA-binding protein RALY-interactome using the in vivo-biotinylation-pulldown-quant (iBioPQ) approach. *J. Proteome Res.* **12**, 2869–2884 (2013).
39. Szklarczyk, D. et al. The STRING database in 2021: customizable protein–protein networks, and functional characterization of user-uploaded gene/measurement sets. *Nucleic Acids Res.* **49**, D605–D612 (2020).
40. Driegen, S. et al. A generic tool for biotinylation of tagged proteins in transgenic mice. *Transgenic Res.* **14**, 477–482 (2005).
41. Cull, M. G. & Schatz, P. J. Biotinylation of proteins in vivo and in vitro using small peptide tags. *Methods Enzymol.* **326**, 430–440 (2000).
42. Shutt, T., Geoffrion, M., Milne, R. & McBride, H. M. The intracellular redox state is a core determinant of mitochondrial fusion. *EMBO Rep.* **13**, 909–915 (2012).
43. Bittermann, E. et al. Differential requirements of tubulin genes in mammalian forebrain development. *PLoS Genet.* **15**, e1008243 (2019).
44. Estela, A., Pla-Martín, D., Sánchez-Piris, M., Sesaki, H. & Palau, F. Charcot-Marie-Tooth-related gene GDAP1 complements cell cycle delay at G2/M phase in Saccharomyces cerevisiae fis1 gene-defective cells. *J. Biol. Chem.* **286**, 36777–36786 (2011).
45. Klemke, M. et al. Oxidation of cofilin mediates T cell hyporesponsiveness under oxidative stress conditions. *Immunity* **29**, 404–413 (2008).

166

46. Gellert, M., Hanschmann, E.-M., Lepka, K., Berndt, C. & Lillig, C. H. Redox regulation of cytoskeletal dynamics during differentiation and de-differentiation. *Biochim. Biophys. Acta* **1850**, 1575–1587 (2015).

47. Kruyer, A., Ball, L. E., Townsend, D. M., Kalivas, P. W. & Uys, J. D. Post-translational S-glutathionylation of cofilin increases actin cycling during cocaine seeking. *PLoS ONE* **14**, e0223037 (2019).

48. Melak, M., Plessner, M. & Grosse, R. Actin visualization at a glance. *J. Cell Sci.* **130**, 525–530 (2017).

49. Bunnell, T. M., Burbach, B. J., Shimizu, Y. & Ervasti, J. M. β-Actin specifically controls cell growth, migration, and the G-actin pool. *Mol. Biol. Cell* **22**, 4047–4058 (2011).

50. McGough, A., Pope, B., Chiu, W. & Weeds, A. Cofilin changes the twist of F-actin: implications for actin filament dynamics and cellular function. *J. Cell Biol.* **138**, 771–781 (1997).

51. Ji, W.-K., Hatch, A. L., Merrill, R. A., Strack, S. & Higgs, H. N. Actin filaments target the oligomeric maturation of the dynamin GTPase Drp1 to mitochondrial fission sites. *Elife* **4**, e11553 (2015).

52. Patron, M. et al. MICU1 and MICU2 finely tune the mitochondrial Ca2+ uniporter by exerting opposite effects on MCU activity. *Mol. Cell* **53**, 726–737 (2014).

53. Civera-Tregón, A. et al. Mitochondria and calcium defects correlate with axonal dysfunction in GDAP1-related Charcot-Marie-Tooth mouse model. *Neurobiol. Dis.* **152**, 105300 (2021).

54. Boldogh, I. R. & Pon, L. A. Interactions of mitochondria with the actin cytoskeleton. *Biochim. Biophys. Acta* **1763**, 450–462 (2006).

55. Hoffmann, L. et al. Cofilin1 oxidation links oxidative distress to mitochondrial demise and neuronal cell death. *Cell Death Dis.* **12**, 953 (2021).

56. Pope, B. J., Zierler-Gould, K. M., Kühne, R., Weeds, A. G. & Ball, L. J. Solution structure of human cofilin: actin binding, pH sensitivity, and relationship to actin-depolymerizing factor. *J. Biol. Chem.* **279**, 4840–4848 (2004).

57. Pfannstiel, J. et al. Human cofilin forms oligomers exhibiting actin bundling activity. *J. Biol. Chem.* **276**, 49476–49484 (2001).

58. Goyal, P. et al. Cofilin oligomer formation occurs in vivo and is regulated by cofilin phosphorylation. *PLoS ONE* **8**, e71769 (2013).

59. Siudeja, K., Grzeschik, N. A., Rana, A., de Jong, J. & Sibon, O. C. M. Cofilin/Twinstar phosphorylation levels increase in response to impaired coenzyme a metabolism. *PLoS ONE* **7**, e43145 (2012).

60. Chua, B. T. et al. Mitochondrial translocation of cofilin is an early step in apoptosis induction. *Nat. Cell Biol.* **5**, 1083–1089 (2003).

61. Klamt, F. et al. Oxidant-induced apoptosis is mediated by oxidation of the actin-regulatory protein cofilin. *Nat. Cell Biol.* **11**, 1241–1246 (2009).

62. Luo, S., Uehara, H. & Shacter, E. Taurine chloramine-induced inactivation of cofilin protein through methionine oxidation. *Free Radic. Biol. Med.* **75**, 84–94 (2014).

63. Fratelli, M. et al. Identification by redox proteomics of glutathionylated proteins in oxidatively stressed human T lymphocytes. *Proc. Natl Acad. Sci. USA* **99**, 3505–3510 (2002).

64. Orth, J. D., Krueger, E. W., Cao, H. & McNiven, M. A. The large GTPase dynamin regulates actin comet formation and movement in living cells. *Proc. Natl Acad. Sci. USA* **99**, 167–172 (2002).

65. Lee, E. & De Camilli, P. Dynamin at actin tails. *Proc. Natl Acad. Sci. USA* **99**, 161–166 (2002).

66. Züchner, S. et al. Mutations in the pleckstrin homology domain of dynamin 2 cause dominant intermediate Charcot-Marie-Tooth disease. *Nat. Genet.* **37**, 289–294 (2005).

67. Fabrizi, G. M. et al. Two novel mutations in dynamin-2 cause axonal Charcot-Marie-Tooth disease. *Neurology* **69**, 291–295 (2007).

68. Lee, J. E., Westrate, L. M., Wu, H., Page, C. & Voeltz, G. K. Multiple dynamin family members collaborate to drive mitochondrial division. *Nature* **540**, 139–143 (2016).

69. Luigetti, M. et al. Seipin S90L mutation in an Italian family with CMT2/dHMN and pyramidal signs. *Muscle Nerve* **42**, 448–451 (2010).

70. Boutet, E. et al. Seipin deficiency alters fatty acid Delta9 desaturation and lipid droplet formation in Berardinelli-Seip congenital lipodystrophy. *Biochimie* **91**, 796–803 (2009).

71. Tian, Y. et al. Tissue-autonomous function of Drosophila seipin in preventing ectopic lipid droplet formation. *PLoS Genet.* **7**, e1001364 (2011).

72. Yang, W. et al. BSCL2/seipin regulates adipogenesis through actin cytoskeleton remodelling. *Hum. Mol. Genet.* **23**, 502–513 (2014).

73. Reinhardt, P. et al. Derivation and expansion using only small molecules of human neural progenitors for neurodegenerative disease modeling. *PLoS ONE* **8**, e59252 (2013).

74. Hughes, C. S. et al. Ultrasensitive proteome analysis using paramagnetic bead technology. *Mol. Syst. Biol.* **10**, 757 (2014).

75. Sielaff, M. et al. Evaluation of FASP, SP3, and iST Protocols for Proteomic Sample Preparation in the Low Microgram Range. *J. Proteome Res.* **16**, 4060–4072 (2017).

76. Wu, T. et al. clusterProfiler 4.0: A universal enrichment tool for interpreting omics data. *Innov. J.* **2**, 100141 (2021).

77. Vizcaíno, J. A. et al. The PRoteomics IDEntifications (PRIDE) database and associated tools: status in 2013. *Nucleic Acids Res.* **41**, D1063–D1069 (2013).

Acknowledgements

Author contributions

C.W., A.P., S.B., AnnP, D.B., P.M., F.d.B., C.V., I.B., D.G., P.M. carried out experiments; K.D., M.P., and O.B. generated the iPS cells; J.S. and S.R. helped establishing high-content microscopy; S.A., D.G., and S.T. analyzed quantitative proteomic analyses; M.G. supervised and analyzed the FEMP and aequorin measurements; R.K. supervised and analyzed the experiments with human motoneurons; C.W., M.S., and E.M.H. analyzed data and helped writing the manuscript; A.M. devised experiments, analyzed data and wrote the manuscript.

Funding

Competing interests

The authors declare no competing interests.

Additional information

Supplementary information The online version contains supplementary material available at https://doi.org/10.1038/s42003-022-03487-6.

Correspondence and requests for materials should be addressed to Axel Methner.

Peer review information This manuscript has been previously reviewed at another Nature Portfolio journal. The manuscript was considered suitable for publication without further review at *Communications Biology*. Primary Handling Editors: Eve Rogers.

Reprints and permission information is available at http://www.nature.com/reprints

Publisher's note Springer Nature remains neutral with regard to jurisdictional claims in published maps and institutional affiliations.

Bibliography

1. Ibáñez, K., Boullosa, C., Tabarés-Seisdedos, R., Baudot, A. & Valencia, A. Molecular Evidence for the Inverse Comorbidity between Central Nervous System Disorders and Cancers Detected by Transcriptomic Meta-analyses. *PLoS Genet.* **10**, 1–7 (2014).

2. Klus, P., Cirillo, D., Botta Orfila, T. & Gaetano Tartaglia, G. Neurodegeneration and cancer: where the disorder prevails. *Sci. Rep.* **5**, 1–7 (2015).

3. Wahabi, K., Perwez, A. & Rizvi, M. A. Parkin in Parkinson's Disease and Cancer: a Double-Edged Sword. *Mol. Neurobiol.* **55**, 6788–6800 (2018).

4. Mhyre, T. R., Nw, R., Boyd, J. T., Hall, G. & Room, C. *Parkinson's Disease*. vol. 65 (2012).

5. Kim, C. Y. & Alcalay, R. N. Genetic Forms of Parkinson 's Disease. (2017).

6. Jin, S. *et al.* MicroRNA-544 inhibits glioma proliferation, invasion and migration but induces cell apoptosis by targeting PARK7. *Am. J. Transl. Res.* **8**, 1826–1837 (2016).

7. Alifieris, C. & Trafalis, D. T. Glioblastoma multiforme: Pathogenesis and treatment. *Pharmacol. Ther.* **152**, 63–82 (2015).

8. Goffart, N., Kroonen, J. & Rogister, B. Glioblastoma-initiating cells: Relationship with neural stem cells and the micro-environment. *Cancers (Basel).* **5**, 1049–1071 (2013).

9. Devine, M. J., Plun-Favreau, H. & Wood, N. W. Parkinson's disease and cancer: Two wars, one front. *Nat. Rev. Cancer* **11**, 812–823 (2011).

10. Feng, D. D., Cai, W. & Chen, X. The associations between Parkinson's disease and cancer: The plot thickens. *Transl. Neurodegener.* **4**, (2015).

11. Klus, P., Cirillo, D., Botta Orfila, T. & Gaetano Tartaglia, G. Neurodegeneration and cancer: where the disorder prevails. *Sci. Rep.* **5**, 1–7 (2015).

12. Takahashi, K. & Yamanaka, S. Induction of Pluripotent Stem Cells from Mouse Embryonic and Adult Fibroblast Cultures by Defined Factors. *Cell* **126**, 663–676 (2006).

13. Avior, Y., Sagi, I. & Benvenisty, N. Pluripotent stem cells in disease modelling and drug discovery. *Nat. Rev. Mol. Cell Biol.* **17**, 170–182 (2016).

14. Jinek, M. *et al.* A Programmable Dual-RNA–Guided DNA Endonuclease in Adaptive Bacterial Immunity. **337**, 816–822 (2012).

15. Jarazo, J., Qing, X. & Schwamborn, J. C. Guidelines for fluorescent guided biallelic HDR targeting selection with PiggyBac system removal for gene editing. *Front. Genet.* **10**, 1–12 (2019).

16. Bonifati, V. *et al.* Mutations in the DJ-1 gene associated with autosomal recessive early-onset parkinsonism. *Science (80-.).* **299**, 256–259 (2003).

17. Wang, C. *et al.* The positive correlation between DJ-1 and β-catenin expression shows prognostic value for patients with glioma. *Neuropathology* **33**, 628–636

(2013).

18. Booth, H. D. E., Hirst, W. D. & Wade-Martins, R. The Role of Astrocyte Dysfunction in Parkinson's Disease Pathogenesis. *Trends Neurosci.* **40**, 358–370 (2017).

19. Neumann, M. *et al.* Pathological properties of the Parkinson's disease-associated protein DJ-1 in α-synucleinopathies and tauopathies: Relevance for multiple system atrophy and Pick's disease. *Acta Neuropathol.* **107**, 489–496 (2004).

20. Bandopadhyay, R. *et al.* The expression of DJ-1 (PARK7) in normal human CNS and idiopathic Parkinson's disease. *Brain* **127**, 420–430 (2004).

21. Hinkle, D. A., Mullett, S. J., Gabris, B. E. & Hamilton, R. L. DJ-1 expression in glioblastomas shows positive correlation with p53 expression and negative correlation with epidermal growth factor receptor amplification. *Neuropathology* **31**, 29–37 (2011).

22. Oh, S. E. & Mouradian, M. M. *Regulation of signal transduction by DJ-1*. *Advances in Experimental Medicine and Biology* vol. 1037 (2017).

23. Ariga, H. *et al.* Neuroprotective Function of DJ-1 in Parkinson ' s Disease. **2013**, (2013).

24. Kacem, K., Lacombe, P., Seylaz, J. & Bonvento, G. Structural organization of the perivascular astrocyte endfeet and their relationship with the endothelial glucose transporter: A confocal microscopy study. *Glia* **23**, 1–10 (1998).

25. Prebil, M., Jensen, J., Zorec, R. & Kreft, M. Astrocytes and energy metabolism. *Arch. Physiol. Biochem.* **117**, 64–69 (2011).

26. Papouin, T., Dunphy, J., Tolman, M., Foley, J. C. & Haydon, P. G. Astrocytic control of synaptic function. *Philos. Trans. R. Soc. B Biol. Sci.* **372**, (2017).

27. Rose, J., Brian, C., Pappa, A., Panayiotidis, M. I. & Franco, R. Mitochondrial Metabolism in Astrocytes Regulates Brain Bioenergetics, Neurotransmission and Redox Balance. *Front. Neurosci.* **14**, 1–20 (2020).

28. Mahmoud, S., Gharagozloo, M., Simard, C. & Gris, D. Astrocytes maintain glutamate homeostasis in the cns by controlling the balance between glutamate uptake and release. *Cells* **8**, 1–27 (2019).

29. Turner, D. A. & Adamson, D. C. Neuronal-astrocyte metabolic interactions: Understanding the transition into abnormal astrocytoma metabolism. *J. Neuropathol. Exp. Neurol.* **70**, 167–176 (2011).

30. Vicente-Gutierrez, C. *et al.* Astrocytic mitochondrial ROS modulate brain metabolism and mouse behaviour. *Nat. Metab.* **1**, 201–211 (2019).

31. Hertz, L., Dringen, R., Schousboe, A. & Robinson, S. R. Astrocytes: Glutamate producers for neurons. *J. Neurosci. Res.* **57**, 417–428 (1999).

32. Meiser, J. *et al.* Loss of DJ-impairs antioxidant response by altered glutamine and serine metabolism. *Neurobiol. Dis.* **89**, 112–125 (2016).

33. Kim, K. S. *et al.* DJ-1 associates with lipid rafts by palmitoylation and regulates lipid rafts-dependent endocytosis in astrocytes. *Hum. Mol. Genet.* **22**, 4805–4817 (2013).

34. Zhou, W. & Freed, C. R. DJ-1 up-regulates glutathione synthesis during oxidative stress and inhibits A53T α-synuclein toxicity. *J. Biol. Chem.* **280**, 43150–43158 (2005).

35. Peng, L. *et al.* Effect of DJ-1 on the neuroprotection of astrocytes subjected to cerebral ischemia/reperfusion injury. *J. Mol. Med.* **97**, 189–199 (2019).

36. Lopez-Fabuel, I. *et al.* Complex I assembly into supercomplexes determines differential mitochondrial ROS production in neurons and astrocytes. *Proc. Natl. Acad. Sci. U. S. A.* **113**, 13063–13068 (2016).

37. Waak, J. *et al.* Regulation of astrocyte inflammatory responses by the Parkinson's disease-associated gene DJ-1. *FASEB J.* **23**, 2478–2489 (2009).

38. Kim, J. hyeon *et al.* DJ-1 facilitates the interaction between STAT1 and its phosphatase, SHP-1, in brain microglia and astrocytes: A novel anti-inflammatory function of DJ-1. *Neurobiol. Dis.* **60**, 1–10 (2013).

39. Simon, M. C. Coming up for air: HIF-1 and mitochondrial oxygen consumption. *Cell Metab.* **3**, 148–150 (2006).

40. Chen, X., Song, M., Zhang, B. & Zhang, Y. Reactive Oxygen Species Regulate T Cell Immune Response in the Tumor Microenvironment. *Oxid. Med. Cell. Longev.* **2016**, 11–16 (2016).

41. Tavassolifar, M. J., Vodjgani, M., Salehi, Z. & Izad, M. The Influence of Reactive Oxygen Species in the Immune System and Pathogenesis of Multiple Sclerosis. *Autoimmune Dis.* **2020**, (2020).

42. Yang, Z., Min, Z. & Yu, B. Reactive oxygen species and immune regulation. *Int. Rev. Immunol.* **39**, 292–298 (2020).

43. Naik, E. & Dixit, V. M. Mitochondrial reactive oxygen species drive proinflammatory cytokine production. *J. Exp. Med.* **208**, 417–420 (2011).

44. Belikov, A. V., Schraven, B. & Simeoni, L. T cells and reactive oxygen species. *J. Biomed. Sci.* **22**, 1–11 (2015).

45. Colombo, E. & Farina, C. Astrocytes: Key Regulators of Neuroinflammation. *Trends Immunol.* **37**, 608–620 (2016).

46. Liu, T., Zhang, L., Joo, D. & Sun, S. C. NF-κB signaling in inflammation. *Signal Transduct. Target. Ther.* **2**, (2017).

47. Hayden, M. S., West, A. P. & Ghosh, S. NF-κB and the immune response. *Oncogene* **25**, 6758–6780 (2006).

48. Moynagh, P. N. The interleukin-1 signalling pathway in astrocytes: A key contributor to inflammation in the brain. *J. Anat.* **207**, 265–269 (2005).

49. Lebovic, D. I., Chao, V. A., Martini, J. F. & Taylor, R. N. IL-1β induction of RANTES (regulated upon activation, normal T cell expressed and secreted) chemokine gene expression in endometriotic stromal cells depends on a nuclear factor-κB site in the proximal promoter. *J. Clin. Endocrinol. Metab.* **86**, 4759–4764 (2001).

50. Taipa, R. *et al.* DJ-1 linked parkinsonism (PARK7) is associated with Lewy body pathology. *Brain* **139**, 1680–1687 (2016).

51. Kam, T. I., Hinkle, J. T., Dawson, T. M. & Dawson, V. L. Microglia and astrocyte dysfunction in parkinson's disease. *Neurobiol. Dis.* **144**, 105028 (2020).

52. Sonninen, T. M. *et al.* Metabolic alterations in Parkinson's disease astrocytes. *Sci. Rep.* **10**, (2020).

53. Choi, D. J. *et al.* Critical roles of astrocytic-CCL2-dependent monocyte infiltration in a DJ-1 knockout mouse model of delayed brain repair. *Glia* **68**, 2086–2101 (2020).

54. Ashley, A. K., Hinds, A. I., Hanneman, W. H., Tjalkens, R. B. & Legare, M. E. DJ-1 mutation decreases astroglial release of inflammatory mediators. *Neurotoxicology* **52**, 198–203 (2016).

55. Frøyset, A. K. *et al.* Astroglial DJ-1 over-expression up-regulates proteins involved in redox regulation and is neuroprotective in vivo. *Redox Biol.* **16**, 237–247 (2018).

56. Crawford, A., Angelosanto, J. M., Nadwodny, K. L., Blackburn, S. D. & Wherry, E. J. A role for the chemokine RANTES in regulating CD8 T cell responses during chronic viral infection. *PLoS Pathog.* **7**, (2011).

57. Thapa, P. & Farber, D. L. The Role of the Thymus in the Immune Response. *Thorac. Surg. Clin.* **29**, 123–131 (2019).

58. Tansey, M. G. *et al.* Inflammation and immune dysfunction in Parkinson disease. *Nat. Rev. Immunol.* **0123456789**, (2022).

59. Brochard, V. *et al.* Infiltration of CD4+ lymphocytes into the brain contributes to neurodegeneration in a mouse model of Parkinson disease. *J. Clin. Invest.* **119**, 182–192 (2009).

60. Yanagida, T. *et al.* Oxidative stress induction of DJ-1 protein in reactive astrocytes scavenges free radicals and reduces cell injury. *Oxid. Med. Cell. Longev.* **2**, 36–42 (2009).

61. Cao, J., Chen, X., Ying, M., He, Q. & Yang, B. DJ-1 as a therapeutic target against cancer. *Adv. Exp. Med. Biol.* **1037**, 203–222 (2017).

62. Cao, J., Lou, S., Ying, M. & Yang, B. DJ-1 as a human oncogene and potential therapeutic target. *Biochem. Pharmacol.* **93**, 241–250 (2015).

63. Nagakubo, D. *et al.* DJ-1, a novel oncogene which transforms mouse NIH3T3 cells in cooperation with ras. *Biochem. Biophys. Res. Commun.* **231**, 509–513 (1997).

64. Hernández, A., Domènech, M., Muñoz-Mármol, A. M., Carrato, C. & Balana, C. Glioblastoma: Relationship between metabolism and immunosuppressive microenvironment. *Cells* **10**, (2021).

65. Wesseling, P. & Capper, D. WHO 2016 Classification of gliomas. *Neuropathol. Appl. Neurobiol.* **44**, 139–150 (2018).

66. S., C., Lourenco, T., Xavier-Magalhaes, A., Pojo, M. & M., B. Mechanisms of Aggressiveness in Glioblastoma: Prognostic and Potential Therapeutic Insights. *Evol. Mol. Biol. Brain Tumors Ther. Implic.* (2013) doi:10.5772/52361.

67. Wenger, A. *et al.* Intratumor DNA methylation heterogeneity in glioblastoma: Implications for DNA methylation-based classification. *Neuro. Oncol.* **21**, 616–627 (2019).

68.   Wank, M. *et al.* Human glioma migration and infiltration properties as a target for personalized radiation medicine. *Cancers (Basel).* **10**, (2018).

69.   Garcia, J. H., Jain, S. & Aghi, M. K. Metabolic Drivers of Invasion in Glioblastoma. *Front. Cell Dev. Biol.* **9**, 1–16 (2021).

70.   Bélanger, M., Allaman, I. & Magistretti, P. J. Brain energy metabolism: Focus on Astrocyte-neuron metabolic cooperation. *Cell Metab.* **14**, 724–738 (2011).

71.   Tardito, S. *et al.* Glutamine synthetase activity fuels nucleotide biosynthesis and supports growth of glutamine-restricted glioblastoma. *Nat. Cell Biol.* **17**, 1556–1568 (2015).

72.   Marin-Valencia, I. *et al.* Analysis of tumor metabolism reveals mitochondrial glucose oxidation in genetically diverse human glioblastomas in the mouse brain in vivo. *Cell Metab.* **15**, 827–837 (2012).

73.   Natarajan, S. K. & Venneti, S. Glutamine metabolism in brain tumors. *Cancers (Basel).* **11**, (2019).

74.   Cruzat, V., Rogero, M. M., Keane, K. N., Curi, R. & Newsholme, P. Glutamine: Metabolism and immune function, supplementation and clinical translation. *Nutrients* **10**, 1–31 (2018).

75.   Yarosz, E. L. & Chang, C. H. Role of reactive oxygen species in regulating T cell-mediated immunity and disease. *Immune Netw.* **18**, 1–15 (2018).

76.   Peng, H. Y. *et al.* Metabolic Reprogramming and Reactive Oxygen Species in T Cell Immunity. *Front. Immunol.* **12**, 1–10 (2021).

77.   Kamiński, M. M. *et al.* Mitochondrial Reactive Oxygen Species Control T Cell Activation by Regulating IL-2 and IL-4 Expression: Mechanism of Ciprofloxacin-Mediated Immunosuppression. *J. Immunol.* **184**, 4827–4841 (2010).

78.   Frossi, B., De Carli, M., Piemonte, M. & Pucillo, C. Oxidative microenvironment exerts an opposite regulatory effect on cytokine production by Th1 and Th2 cells. *Mol. Immunol.* **45**, 58–64 (2008).

79.   Stanke, K. M., Wilson, C. & Kidambi, S. High Expression of Glycolytic Genes in Clinical Glioblastoma Patients Correlates With Lower Survival. *Front. Mol. Biosci.* **8**, 1–12 (2021).

80.   Singh, K. *et al.* Enhancing t cell chemotaxis and infiltration in glioblastoma. *Cancers (Basel).* **13**, (2021).

81.   Antunes, A. R. P. *et al.* Understanding the glioblastoma immune microenvironment as basis for the development of new immunotherapeutic strategies. *Elife* **9**, 1–16 (2020).

82.   Zhang, X. N. *et al.* Pericytes augment glioblastoma cell resistance to temozolomide through CCL5-CCR5 paracrine signaling. *Cell Res.* **31**, 1072–1087 (2021).

83.   Gong, D. *et al.* TGFβ signaling plays a critical role in promoting alternative macrophage activation. *BMC Immunol.* **13**, 1 (2012).

84.   Vitkovic, L., Maeda, S. & Sternberg, E. Anti-inflammatory cytokines: Expression and action in the brain. *Neuroimmunomodulation* **9**, 295–312 (2001).

85. Mullett, S. J. & Hinkle, D. A. DJ-1 knock-down in astrocytes impairs astrocyte-mediated neuroprotection against rotenone. *Neurobiol. Dis.* **33**, 28–36 (2009).

86. Lev, N. *et al.* Knocking out DJ-1 attenuates astrocytes neuroprotection against 6-hydroxydopamine toxicity. *J. Mol. Neurosci.* **50**, 542–550 (2013).

87. Mullett, S. J., Di Maio, R., Greenamyre, J. T. & Hinkle, D. A. DJ-1 Expression Modulates Astrocyte-Mediated Protection Against Neuronal Oxidative Stress. *J. Mol. Neurosci.* **49**, 507–511 (2013).

88. Wang, H. *et al.* Different T-cell subsets in glioblastoma multiforme and targeted immunotherapy. *Cancer Lett.* **496**, 134–143 (2021).

89. Mohan, A. A. *et al.* Targeting Immunometabolism in Glioblastoma. *Front. Oncol.* **11**, 1–16 (2021).

90. Nobusawa, S., Watanabe, T., Kleihues, P. & Ohgaki, H. IDH1 mutations as molecular signature and predictive factor of secondary glioblastomas. *Clin. Cancer Res.* **15**, 6002–6007 (2009).

91. Han, S. *et al.* IDH mutation in glioma: molecular mechanisms and potential therapeutic targets. *Br. J. Cancer* **122**, 1580–1589 (2020).

92. Seltzer, M. J. *et al.* Inhibition of glutaminase preferentially slows growth of glioma cells with mutant IDH1. **70**, 8981–8987 (2011).

93. Tommasini-Ghelfi, S. *et al.* Cancer-associated mutation and beyond: The emerging biology of isocitrate dehydrogenases in human disease. *Sci. Adv.* **5**, 1–18 (2019).

94. Yang, J. *et al.* Isocitrate protects DJ-1 null dopaminergic cells from oxidative stress through NADP+-dependent isocitrate dehydrogenase (IDH). *PLoS Genet.* **13**, 1–26 (2017).

Affidavit

I hereby confirm that the PhD thesis entitled "Examination of role and function of DJ-1 in Parkinsons`s disease and Glioblastoma" has been written independently and without any other sources than cited.

Luxembourg, the 26.01.2023

Name

P. Menike

Acknowledgements